

## University of Southampton Research Repository

Copyright © and Moral Rights for this thesis and, where applicable, any accompanying data are retained by the author and/or other copyright owners. A copy can be downloaded for personal non-commercial research or study, without prior permission or charge. This thesis and the accompanying data cannot be reproduced or quoted extensively from without first obtaining permission in writing from the copyright holder/s. The content of the thesis and accompanying research data (where applicable) must not be changed in any way or sold commercially in any format or medium without the formal permission of the copyright holder/s.

When referring to this thesis and any accompanying data, full bibliographic details must be given, e.g.

Thesis: Author (Year of Submission) "Full thesis title", University of Southampton, name of the University Faculty or School or Department, PhD Thesis, pagination.

Data: Author (Year) Title. URI [dataset]

## University of Southampton

Faculty of Engineering and Physical Sciences Institute of Sound and Vibration Research

# Characterization and source separation of turbofan broadband noise using intra-stage measurements

by

Ram Kumar Venkateswaran

ORCiD: [0000-0003-0389-1841]

A thesis for the degree of Doctor of Philosophy

June 2025

#### University of Southampton

#### **Abstract**

Faculty of Engineering and Physical Sciences
Institute of Sound and Vibration Research

## Doctor of Philosophy

# Characterization and source separation of turbofan broadband noise using intra-stage measurements

by Ram Kumar Venkateswaran

The broadband (BB) noise generated in the fan stage is a significant contributor to the total engine noise with the dominant noise generation mechanisms attributed to the self-noise at the trailing edges (TE) of the fan blades and the rotor-stator interaction noise at the leading edges (LE) of the outlet guide vanes (OGV). Despite more than 50 years of research, the fan BB noise is not properly understood, and its rotor (fan) and stator (OGV) components haven't been properly quantified. The noise measurements in the engine intra-stage between the fan TE and OGV LE permit a direct comparison between the BB noise characteristics and the relative levels generated by the fan and OGV, unlike the engine intake and bypass sections, wherein the noise from the fan and OGV arrive simultaneously in one direction and suffer some degree of acoustic blockage due to one another. In this thesis, we exclusively focus on the noise measurements made in the intra-stage region to identify and reveal the fundamental characteristics of the fan BB noise and develop suitable phased array techniques to overcome the measurement challenges and accomplish the desired source separation.

In our present work, we propose a theoretical point source model for the engine intrastage with empirically determined source parameters, which effectively reproduces the measured relative BB modal pressure distribution characteristics due to the fan and OGV. The consistency of these source parameters is demonstrated across different turbofan rigs and operating conditions to bring out their universality. The problem of acoustic mode detection and wave splitting in the engine intra-stage are systematically investigated with suitable phased array methods developed and implemented, which reveal the OGV to dominate the fan noise spectrum by more than 6 dB at both approach and cutback. The concept of modal axial group velocity is investigated for ducted swirling flows, based on which modal sound power distributions have been estimated for measured intra-stage noise data at approach and cutback, which show conformity as well as deviation from the ideal equal-power-per-mode concept.

# **Contents**

D	eclara	ation of Authorship	xi
A	cknov	wledgements	xiii
Li	st of	Abbreviations	xvii
Li	st of	Symbols	xix
1	Intr	oduction	1
	1.1	Aircraft noise	1
	1.2	Turbofan noise sources	3
	1.3	An overview of the fan noise	6
		1.3.1 Fan tonal noise	7
		1.3.1.1 Rotor-locked tones: <i>Rotor-alone</i> tones	7
		1.3.1.2 Rotor-locked tones: Buzz saw tones (multiple pure tones)	7
		1.3.1.3 Rotor-stator interaction tones	8
		1.3.2 Fan broadband noise	8
	1.4	Scope and objectives of the Ph.D. project	10
	1.5	Original contributions	11
	1.6	Outline of the thesis	14
2	Lite	rature Review	15
	2.1	Previous work on Fan BB noise characterization	17
		2.1.1 The significance of the modal cut-on ratio	18
		2.1.2 Characterizing the broadband multimodal sound structure	20
		2.1.3 In-duct source location techniques	21
	2.2	An overview of the mode detection methods	23
		2.2.1 Modal analysis of a tonal sound field	23
		2.2.2 Modal analysis of a broadband sound field	25
		2.2.2.1 Techniques measuring the discrete modal spectra	26
		2.2.2.2 Asymptotic wavenumber distribution approaches	27
	2.3	Relevance to the engine intra-stage	28
3	Mod	dal Transmission	31
	3.1	Uniform axial flow in a rigid cylindrical duct	31
		3.1.1 Acoustic eigenmodes	32
		3.1.2 Acoustic Green's function for pressure	34
	2.2	Non uniform equipling flow in an annular dust	24

vi *CONTENTS* 

		3.2.1	Acoustic analogy in a swirling flow	36
			3.2.1.1 Swirling base flow	36
			3.2.1.2 Acoustic boundary condition	37
			3.2.1.3 Evaluation of the eigenmodes, and Green's function	38
	3.3	Rigid l	body swirl model for acoustic propagation in a swirling flow	40
		3.3.1	Suitability of the rotating coordinate approximation	41
4	Fan	broadb	and noise characterization using engine intra-stage measurements	43
	4.1		cterizing the broadband intra-stage sound field	44
		4.1.1	Modal propagation in the intra-stage duct	44
		4.1.2	Equivalent point source model for rotor and stator noise	45
	4.2	Noise	metrics	45
		4.2.1	Normalized mean squared spinning mode amplitude, $\overline{a_m^2}(\omega)$	46
		4.2.2	Relative modal split, $\sigma_{\pm m}(\omega)$	47
		4.2.3	Normalized mean squared spinning mode amplitude distribu-	
			tion, $\overline{a^2}(\gamma)$	47
			4.2.3.1 Multi-frequency implementation	50
		4.2.4	Normalized mean squared mode amplitude distribution, $\overline{a^2}(\zeta)$ .	51
	4.3	Evider	nce for separability of the intra-stage broadband sound field	54
	4.4	Limita	tions of the standard method for estimating rotor-alone noise by	
		OGV r	removal	55
	4.5	Descri	ption of the three fan rigs	56
		4.5.1	The intra-stage geometry, and acoustic instrumentation	56
			4.5.1.1 The modular NASA 22-inch fan rig simulator	56
			4.5.1.2 ACAT1 fan	57
			4.5.1.3 Rolls-Royce Low Speed Fan for Research (RR-LSF)	58
		4.5.2	Intra-stage flow profiles	58
		4.5.3	Test matrix	59
	4.6		SDT modal spectra	60
		4.6.1	Wall pressure modal spectra	60
		4.6.2	Determining the equivalent point rotor $(\varphi_r)$ and OGV $(\varphi_o)$ dipole	<i>(</i> 1
			orientation	61
			4.6.2.1 Measured vs computed $\overline{a_m^2}(\omega)$	63
			4.6.2.2 Measured vs computed $\sigma_{+m}(\omega)$	64
		4.60	4.6.2.3 Measured vs computed $\langle \overline{a^2}(\gamma) \rangle$	65
		4.6.3	Interpretation of the modal pressure distributions due to rotor	(7
			and OGV	67 68
			4.6.3.2 OGV	69
	4.7	Invocti	igations using the ACAT1 turbofan rig	69
	4.7	4.7.1	Comparison between the measured and computed $\overline{a^2}(\zeta)$ distri-	09
		4.7.1	butions	69
			4.7.1.1 The modal overlap	70
	4.8	Investi	igations using the RR-LSF test rig	71
	4.9		ading remarks	73
			<u> </u>	
5	Broa	adband	acoustic mode detection in swirling flows	75

*CONTENTS* vii

	5.1	Moda	l overlap in a swirling flow	76
		5.1.1	Impact of the modal overlap on the mode detection capability of	
			existing methods	77
	5.2		lation of the modal overlap phenomenon using the rigid body swirl	
			1	79
		5.2.1	Higher order $(+m, n)$ modes	80
		5.2.2	Higher order $(-m, n)$ modes	80
		5.2.3	Inferences and their validation	81
	5.3		vavenumber distribution approaches for enhanced wave splitting	
			wirling flow	82
		5.3.1	2-D multi- <i>ka</i> wavenumber distribution methods	82
		5.3.2	2-D single- <i>ka</i> wavenumber distribution methods	84
			5.3.2.1 Response function of a generic $n_c$ -ring beamformer	85
			5.3.2.2 1-ring beamformer array	
			5.3.2.3 2-ring beamformer arrays	87
	5.4		sment of the mode detection capability of the 2-D wavenumber	
			oution approaches	88
		5.4.1	2-D multi- <i>ka</i> techniques	89
		5.4.2	2-D single- <i>ka</i> beamformers	
			5.4.2.1 1-ring beamformer	89
			5.4.2.2 2-ring beamformer	90
		5.4.3	Comparison of the relative source balance predicted using the 2-	
			D multi- <i>ka</i> and single- <i>ka</i> techniques	91
	5.5	Concl	uding remarks	91
6	Feti	mation	of the relative balance between the rotor and OGV broadban	d
U	nois		of the relative balance between the fotor and od v broadban	93
	6.1		tigation of the relative importance of secondary noise sources	93
		6.1.1	Acoustic near-field	94
		6.1.2	Rotor hydrodynamic near-field	95
		6.1.3	Nearly convected hydrodynamic disturbances	
		6.1.4	Incoherent boundary layer noise	
		6.1.5	Turbulent flow noise	97
	6.2		cation of the different phased array techniques on the ACAT1 intra-	
			noise data at approach	98
		6.2.1	Application of the two-microphone method	98
		6.2.2	Application of the axial beamformer method	100
		6.2.3	Application of the 1- <i>ring</i> -1- <i>mic</i> method	101
	6.3	Invest	tigations using the RR-LSF intra-stage noise data	102
		6.3.1	Application of the 1-ring-1-mic method	102
	6.4	Source	e separation of the fan BB noise of the ACAT1 intra-stage at approac	h103
		6.4.1	Comparison of the relative source balance predicted using the	
			different methods	103
		6.4.2		103 104
	6.5		different methods	104
		Concl	different methods	104 104
7		Concl	different methods	104

viii CONTENTS

		7.1.1	Two-microphone technique, and the modal overlap	108
	7.2	Applie	cation of the 1-ring-1-mic method to separate the fan and OGV mode	s109
	7.3	Source	e separation of the fan BB noise of the ACAT1 intra-stage at cutback	110
		7.3.1	Predicted relative source balance	110
		7.3.2	Final noise breakdown	111
	7.4	Concl	uding remarks	112
			O	
8			l group velocity in ducted swirling flows and its relevance to intra	
	stag		measurements	113
	8.1		etical interpretation of the axial group velocity in a swirling flow .	114
	8.2	Invest	igations considering simple rigid body swirling flows	116
		8.2.1	$\vartheta$ versus $\zeta$ behavior	117
		8.2.2	$\alpha$ versus $\zeta$ behavior	118
		8.2.3	Ambiguity in the usage of $\alpha$ in a swirling flow	119
	8.3		igations considering realistic intra-stage swirling flows	120
	8.4	$\vartheta$ in th	ne measurement of intra-stage duct mode amplitudes	121
		8.4.1	Modal distribution function in $\vartheta$	122
		8.4.2	Acoustic mode detection in $\vartheta$	123
	8.5	Corres	spondence of $\vartheta$ with the modal sound power distributions in the	
		engine	e intra-stage	124
		8.5.1	Modal sound power in a swirling flow	125
			8.5.1.1 Calculations based on a generalized definition of the	
			acoustic intensity	126
			8.5.1.2 Calculations based on the RBS approximation	126
		8.5.2	Modal sound power distributions for the ACAT1 intra-stage noise	
			data at approach and cutback	127
	8.6	Concl	uding remarks	128
9	Con	clusior	ns and future work	131
	9.1	Concl	usions	131
	9.2	Avenu	ues for future research	134
		9.2.1	Investigating the modal transmission from the intra-stage region	
			to the intake and bypass sections	135
		9.2.2	A targeted intra-stage liner design	135
		9.2.3	Suitable surface treatments of the OGV to mitigate its dominant	
			co-rotating modes	136
Ar	ppend	dix A	Brief summary of the two existing asymptotic wavenumber distri	_
r	-		roaches	137
			A.1 The axial beamformer	137
			A.2 The two-microphone method	
	11		1	
Αŗ	_		Numerical procedure to calculating the eigenmodes, and Green's	
			a ducted swirling flow	141
			3.1 Numerical eigenmodes	141
	App	endix I	3.2 Numerical Green's function	142
Αŗ	peno	dix C	Assessment of the suitability of the rigid body swirl model	145

*CONTENTS* ix

Appendix	C.1 Comparison of the cut-on $m$ -range, and $N_{\omega}$		145
Appendix	C.2 Accuracy of the $\zeta_{mn}$ estimations		146
Appendix	C.3 Mode amplitude distributions, $\overline{A^2}(\zeta)$		147
Appendix	C.4 Radial mode shape variation, $\psi_{mn}(r)$		147
	Aeroacoustic equivalence of a single source at the two-thion to an incoherent distribution of sources	rds annu	- 149
* *	Sensitivity of the modal pressure distribution characteris rce position	tics to the	e 153
	Relative modal splits, $\sigma_{+m}^{\pm}(\omega)$ , at the approach and cutbale ACAT1 intra-stage	ıck condi	- 155
References			157

## **Declaration of Authorship**

I declare that this thesis and the work presented in it is my own and has been generated by me as the result of my own original research.

#### I confirm that:

- 1. This work was done wholly or mainly while in candidature for a research degree at this University;
- 2. Where any part of this thesis has previously been submitted for a degree or any other qualification at this University or any other institution, this has been clearly stated;
- 3. Where I have consulted the published work of others, this is always clearly attributed;
- 4. Where I have quoted from the work of others, the source is always given. With the exception of such quotations, this thesis is entirely my own work;
- 5. I have acknowledged all main sources of help;
- 6. Where the thesis is based on work done by myself jointly with others, I have made clear exactly what was done by others and what I have contributed myself;
- 7. Parts of this work have been published as:
  - V. Ram Kumar, P. Joseph, and P. Chaitanya, "High-frequency ducted broadband acoustic mode detection in the swirling flows", in 28<sup>th</sup> AIAA/CEAS Aeroacoustics 2022 Conference, doi: 10.2514/6.2022-3016. An abridged version was shortlisted and presented at the finals of the Peter Watson Prize 2022.
  - V. Ram Kumar, P. Joseph, and P. Chaitanya, "Modal axial group velocity in ducted swirling flows and its application to the detection of broadband acoustic modes", in 28<sup>th</sup> AIAA/CEAS Aeroacoustics 2022 Conference, doi: 10.2514/6.2022-3017.
  - V. Ram Kumar, P. Joseph, and P. Chaitanya, "Estimation of the relative balance between the rotor and the OGV broadband noise", in AIAA AVIATION 2023 Forum, doi: 10.2514/6.2023-3208. Won the 2023 AIAA/CEAS Aeroacoustics Student Paper award.

xii CONTENTS

• V. Ram Kumar, P. Joseph, and P. Chaitanya, "Generalized microphone array geometries for source separation in engine intra-stages", in AIAA AVI-ATION 2023 Forum, doi: 10.2514/6.2023-3816.

• V. Ram Kumar, P. Joseph, and P. Chaitanya, "Characterizing Fan Broadband Noise Using Engine Intra-Stage Measurements", in 30<sup>th</sup> AIAA/CEAS Aeroacoustics 2024 Conference, doi: 10.2514/6.2024-3115. Finalist in the 2024 AIAA/CEAS Aeroacoustics student paper competition.

Signed:	Date:

## Acknowledgements

First and foremost, I am grateful to Prof. Madhu Ganesh (currently at the Karunya Institute of Technology and Sciences) for introducing me to fluid mechanics during my undergraduate studies, and for instilling in me the confidence to pursue a research career. I am profoundly indebted to Prof. (Emeritus) M. L. Munjal of the Indian Institute of Science for his outstanding monograph on mufflers, and for handholding me through the process of achieving my first publication. I extend my sincere thanks to Dr. Chaitanya Paruchuri for taking me into this research project and recommending me for the research studentship, which has enabled me to expand my skills and contribute to an important area of research. I deeply appreciate the supervision of Prof. Phil Joseph, whose insightful discussions, expertise, and lighthearted banter made my work engaging and enjoyable. I hope I have successfully implemented his advice on concise writing in this thesis, which I am pleased to have completed at the time of his well-deserved CEAS Aeroacoustics Award.

I would like to express my gratitude to Rolls-Royce PLC for their financial and technical support through the Rolls-Royce University Technology Centre (UTC) in Propulsion Systems Noise at the ISVR. I also extend my thanks to Dr. Juan Vera, Dr. Kevin Britchford, and Dr. Christoph Richter from the Noise Engineering team at Rolls-Royce for sharing their LSF intra-stage noise data, which provided valuable input to my thesis.

I am sincerely grateful to Dr. David Stephens, Dr. Dan Sutliff, and Dr. Ed Envia of the Acoustics Research branch at the NASA Glenn Research Center for their prompt and seamless response to my request for the measured data from the NASA Source Diagnostic Test (SDT). I gained valuable insights from the post-processing of the SDT noise data, the results of which form a crucial part of my research.

I am also thankful to Prof. Alan McAlpine for his constructive feedback during my progression reviews. A special thanks to the wonderful people I met here at the ISVR, including Suresh, Deepak, Ramesh, Amin, Ivan, Sergi, Long, Joe, and many others.

Before I conclude, I must mention my dad, to whom I am deeply grateful for his unwavering moral support in my decision to pursue a PhD. He was overjoyed when I received the research studentship, and I hope to make him even prouder with the successful outcomes of my thesis.

```
To simplify things, we need an O\ R\ D\ E\ R.
```

## **List of Abbreviations**

ACAT AneCom AeroTest GmbH

**ANECOM** Aeroacoustic and Noise Engine Consortium

**AST** Advanced Subsonic Technology

**BB** BroadBand

**BL** Boundary Layer

**BPF** Blade Passage Frequency

**BR** Bypass Ratio

**CEAS** Council of European Aerospace Societies

**CFD** Computational Fluid Dynamics

**CHB** Circular Harmonics Beamforming

CSD Cross Spectral Density

**CSM** Cross Spectral Matrix

**EEpM** Equal-Energy-per-Mode

**EEDpM** Equal-Energy-Density-per-Mode

**EO** Engine Order

**EPNL** Effective Perceived Noise Level

**EU** European Union

**FFT** Fast Fourier Transform

FT Fourier Transform

HBR High Bypass Ratio

iBIA iterative Bayesian Inverse Approach

**IFT** Inverse Fourier Transform

IL Insertion Loss

**LDV** Laser Doppler Velocimetry

LE Leading Edge

LG Long-Gap

xviii CONTENTS

**LSWT** Low Speed Wind Tunnel

MBR Medium Bypass Ratio

NASA National Aeronautics and Space Administration

**OGV** Outlet Guide Vanes

**PSD** Power Spectral Density

**RBS** Rigid Body Swirl

**RPCA** Robust Principal Component Analysis

**RR-LSF** Rolls-Royce Low Speed Fan for Research

SD Standard Deviation

**SDT** Source Diagnostic Test

**SNR** Signal-to-Noise Ratio

**SPL** Sound Pressure Level

TE Trailing Edge

**UFFA** Universal Fan Facility for Acoustics

UHBR Ultra High Bypass Ratio

**UTC** University Technology Centre

WKB Wentzel-Kramers-Brillouin

## **List of Symbols**

## Latin lower case

```
а
                   normalised modal amplitude (no units) or duct tip-radius (m)
b
                   duct radius at the hub (m)
                   sound speed (m \cdot s^{-1})
C.
                   frequency (Hz) or modal density function (no units)
                   complex source strength (N)
                   rotational frequency of the fan shaft (Hz)
f_s
                   hub-to-tip ratio of the annular duct (no units)
h
                   imaginary unit
k
                   acoustic wavenumber (m^{-1})
                   azimuthal number (no units)
m
                   harmonic order or radial mode order (no units)
п
\hat{\boldsymbol{n}} = [\hat{z}_s, \hat{r}_s, \hat{\theta}_s]
                   unit vector along the direction of the fluctuating dipole loading
                   number of axial microphones
                   number of sensor rings
n_c
                   acoustic pressure (Pa)
p
                   radial duct coordinate
                   two-thirds annular radius (m)
r_{2/3}
                   observer time (s)
                   velocity along the duct axial coordinate (m \cdot s^{-1})
                   velocity along the duct radial coordinate (m \cdot s^{-1})
v
                   velocity along the duct angular coordinate (m \cdot s^{-1})
w
\mathbf{x} = (z, r, \theta)
                   observer coordinates along the duct
x_a = (z, a, \theta)
                   observer position at the duct wall, r = a
\mathbf{y} = (z_s, r_s, \theta_s)
                   source coordinates along the duct
```

XX CONTENTS

z axial duct coordinate

## Latin upper case

A	complex modal pressure amplitude (Pa)			
$B_{mn} \& C_{mn}$	coefficients of the Bessel functions in the radial mode shape func-			
	tion (no units)			
$\mathcal{C}$	pressure coherence (no units)			
$D_{mn}$	dipole directivity $(m^{-1})$			
E	acoustic energy per unit volume $(N \cdot m^{-2})$			
$E_s$	acoustic source or sink term in the acoustic energy conservation equation $(\mathbf{N}\cdot m^{-2}\cdot \mathbf{s}^{-1})$			
F	pressure-power conversion factor $(m^3 \cdot s^{-1} \cdot Pa^{-1})$			
$\hat{G}_{\omega}$	frequency domain acoustic Green's function for pressure $(m^{-1})$			
I	acoustic intensity vector $(W \cdot m^{-2} \cdot Hz^{-1})$			
$J_m$	Bessel's function of the first kind (no units)			
$M_{ heta}$	swirling flow Mach number (no units)			
$M_z$	axial flow Mach number (no units)			
N	number of circumferential microphones or number of fan blades			
$N_m$	number of cut-on azimuthal mode orders at the analysis frequency			
$N_{\omega}$	total number of cut-on modes at the analysis frequency			
S	duct's cross-sectional area (m <sup>2</sup> )			
T	periodogram length (s)			
$U = U_z$	mean flow velocity along the duct axial coordinate $(m \cdot s^{-1})$			
V	number of stator vanes (no units) or mean flow velocity along the duct radial coordinate $(m\cdot s^{-1})$			
$W=U_{ heta}$	mean flow velocity along the duct angular coordinate $(\mathbf{m}\cdot\mathbf{s}^{-1})$			
$\overline{W}$	modal sound power $(W \cdot Hz^{-1})$			
$\overline{\mathcal{W}}$	normalized modal sound power (no units)			
$W_1$	exit velocity relative to the fan blade TE $(m\cdot s^{-1})$			
$Y_m$	Bessel's function of the second kind (no units)			
Z	complex acoustic impedance $(Pa \cdot m^{-1} \cdot s)$			

CONTENTS xxi

## Greek lower case

α	modal cut-on ratio (no units)
$\beta = \sqrt{1 - M_z^2}$	Doppler factor (no units)
$\gamma = m/ka$	normalized azimuthal wavenumber at the duct wall, $r=a$ (no units)
$\gamma_b$	look-up value of the normalized modal transverse wavenumber in the inverse problem (no units) $ \\$
δ	delta function
$\epsilon_m = m\Omega/\omega$	relative phase shift (no units)
$\zeta = \kappa/k$	normalized modal axial wavenumber (no units)
$\zeta_b$	look-up value of the normalized modal axial wavenumber in the inverse problem (no units) $ \\$
$\zeta_i$	inner cut-on bound of the normalized axial wavenumber spec-
	trum (no units)
η	relative spatial cross-spectrum of the sound field (no units)
$\theta$	angular duct coordinate
l	response function of the inverse approach (no units)
κ	$\   \text{modal axial wavenumber} \ (\mathbf{m}^{-1})$
μ	modal axial group velocity $(m \cdot s^{-1})$
ξ	modal cut-off ratio (no units)
ρ	air density $(kg \cdot m^{-3})$
$\sigma$	relative modal split (no units)
ς	combined radial-transverse wavenumber $(m^{-1})$
$\tau = \kappa a$	non-dimensional modal axial wavenumber (no units)
$\vartheta = \mu/c$	normalized modal axial group velocity (no units)
$\varphi$	angle of the fluctuating point force vector relative to the duct axis
χ	blade stagger angle
$\psi$	normalized radial mode shape function (no units)
$\omega$	circular frequency $(rad \cdot s^{-1})$

## Greek upper case

 $\Gamma \hspace{1cm} \text{ratio of the specific heat capacities (no units)} \\$ 

xxii CONTENTS

$\Delta z$	separation distance between the adjacent pair of axial micro-
<i>∆</i> 2	phones (m)
$\Delta\gamma_b$	azimuthal wavenumber resolution of the single-ka beamformer
	(no units)
$\Delta {\cal \zeta}_b$	axial wavenumber resolution of the single-ka beamformer
	(no units)
$\Delta \zeta_o$	bandwidth of the modal overlap region (no units)
$\phi$	in-duct modal propagation angle
Ω	angular velocity of rotation of the fluid or the sound source (rad $\cdot$ $\ensuremath{s^{-1}})$
Superscripts	
.+	downstream mode
	upstream mode
.′	perturbation, or denotes a different observer position and/or
	modal index
*	complex conjugation
.0	non-dimensionalized and quantified for the steady base (mean) flow
-	denotes an averaging operation - either across the periodogram
	blocks or duct cross-section
÷	non-dimensionalized variable
·+ <i>m</i>	related to the subset of co-rotating modes
-m	related to the subset of contra-rotating modes
Subscripts	
m	quantified for a spinning mode order $m$
mn	quantified for an $(m, n)$ duct mode
0	quantified for the steady base (mean) flow
+	denotes the dimensionless form of a variable
$\epsilon$	denotes the Doppler-shifted quantity in the RBS model
r	related to the fan
0	related to the OGV
+m	related to the subset of co-rotating modes
-m	related to the subset of contra-rotating modes

## Chapter 1

## Introduction

## 1.1 Aircraft noise

CIVIL aviation has continuously risen over the past few decades and has been critical in developing the global economy. However, the continued expansion of the aerospace sector is limited by its environmental impacts of noise and emission footprints. The European Commission has drafted Flightpath 2050 as Europe's Vision for Aviation with goals to develop technologies and systems to allow a 75% reduction in the CO<sub>2</sub> emissions per passenger kilometer, a 90% reduction in the NO<sub>x</sub> emissions, and a 65% decrease in the perceived noise emissions of a flying aircraft by 2050. Sustainable air transport calls for achieving the noise benefits without compromising on the fuel burn and emissions.

Noise is an important aspect of aircraft design consideration. Every new aircraft before entering service must be certified for its noisiness - the metric used for which is the Effective Perceived Noise Level (EPNL). It is predicted at three reference certification points during an airplane pass-by event: the *approach* (or landing) reference point is located 120 *m* below the flight path, at a distance of 2000 *m* from the runway threshold, as the airplane lands steadily at 3° glide angle at about 50% of the full engine power; the *sideline* (or lateral) reference point is located at 450 *m* to the side of the flight path as the airplane climbs steeply at full engine power; and the *cutback* (or flyover) reference point is situated below the flight path at a distance of 6500 *m* from the runway threshold at which the airplane cuts back to approximately 80% of the full engine power. The noise regulations limit the cumulative noise to be within certain EPNL targets based on the number of engines and maximum take-off weight. The whole aircraft noise is an amalgamation of the noise radiated from the airframe and the engine noise sources. The engine is the loudest component at all the three certification points, with the airframe noise contributing comparably (but still lesser) to the engine at *approach* alone

<sup>&</sup>lt;sup>1</sup>The targets mentioned are relative to the capabilities of a baseline aircraft of year 2000.

(Astley (2010)). Characterizing and reducing the noise emitted from the airframe and the engines has been an enormous engineering challenge.

The airframe noise results from the unsteady flow of air around the airframe structures such as the landing gears and the high lift devices (slats and flaps). Additionally, there may be noise due to installation effects such as the engine inlet flow distortion (Rienstra (2015)) and the jet-surface interaction (Zante et al. (2017)). The propulsion system noise (engine noise) emanates from the turbomachinery components, the combustion system, and the mixing noise at the shear layers due to the expansion of the high-speed jets from the engine exhaust. The gas turbine engines used in the 1950s were the turbojets comprising of a compressor stage, the combustor, and the turbine stages. In these jet engines, the thrust is entirely generated by the high-temperature and high-velocity jet stream ejected out of the exhaust nozzle. The turbofan variants were introduced in the 1960s which included a fan at the front to suck the air into the system, wherein only a small portion of this intake air passes through the core region (or, the gas generator) comprising of the compressor stage, the combustor, and the turbine stages, and a major portion bypasses the core. A unique design factor of the turbofans is their bypass ratio (BR) defined as the ratio of the air mass bypassing the core to the air mass entering the core. Table 1.1 below presents the range of bypass ratios for different classifications of turbofans.

TABLE 1.1: Range and classification of bypass ratios for different generation of turbofans

Classification	Low BR	Medium BR	High BR	Ultra High BR
BR	< 2	2 - 7	7 - 10	> 10

The bypassed air stream exits out as slow-speed cold jet mixing with the hot high-speed gas generating out from the core exhaust. As a result, the net exhaust jet velocity is decreased with an increase in the total air mass flow, resulting in the same thrust levels within the same total energy supply. The net thrust produced by a turbofan is the summation of the individual thrusts generated by the fan and the core, with the fan producing most of the thrust. As a result, increasing the BRs has resulted in more efficient engines that consume less fuel and consequently emit fewer pollutants. Driven by the considerations of enhanced propulsion efficiency, the shift towards higher BRs, alongside the incremental advances in engine designs and noise reduction concepts, has also contributed to tremendous noise benefits resulting in significantly quieter aircrafts powered by the subsequent generations of turbofan engines, as shown below in Fig. 1.1.

A striking feature to be noticed however is the change in the relative dominance of the different engine noise sources, as indicated by the representative lobes whose size and orientation correspond to the relative magnitude and the far-field sound directivity, respectively. As the jet noise scales with the 8<sup>th</sup> power of velocity (Glegg and Devenport

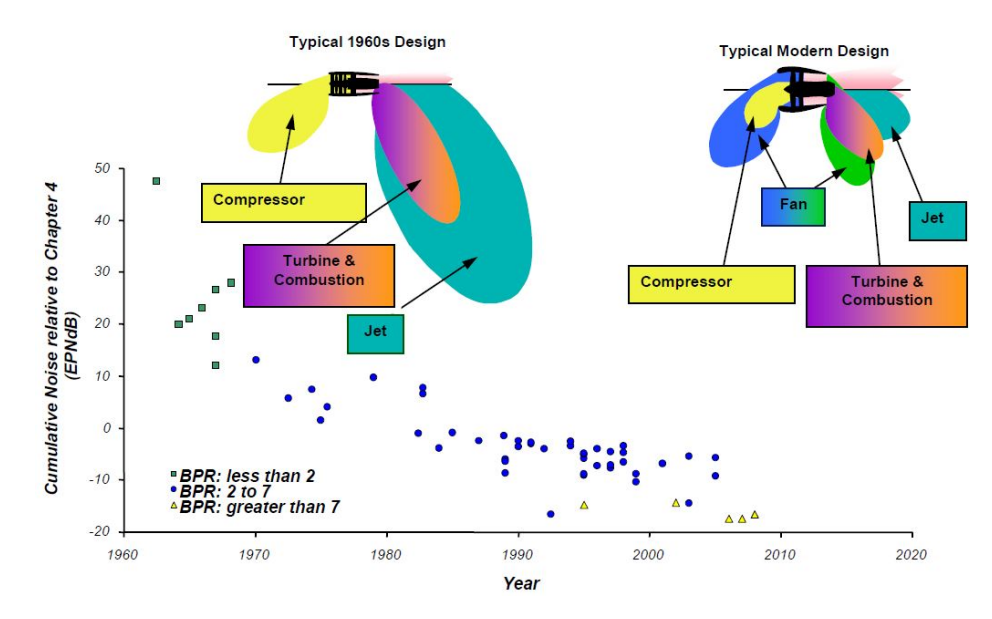


FIGURE 1.1: Reducing trend of the aircraft noise levels over the years (taken from Kempton (2011)).

(2017)), the reduction in the net jet velocity with increasing BRs explains the reduction in the jet noise levels. The turbofan engines include a fan stage comprising a rotor component consisting of the rotating fan blades, and a stator component consisting of a set of stationary outlet guide vanes (OGV). The OGV serves to undo the swirling flow generated in the wake of the fan to recover the energy lost in the angular momentum. Referring to Fig. 1.1, the noise from the fan stage (or more generally, the fan noise), generated from both the rotor and the stator components, is radiated both forward and aft of the engine. The diminishing preponderance of the jet noise is accompanied by the increased relative dominance of the fan noise with increasing BRs. Consequently, for a high bypass ratio (HBR) turbofan aircraft, targeting the fan noise is crucial to reducing the cumulative EPNL and meeting the stringent noise regulations.

## 1.2 Turbofan noise sources

The engine noise spectrum comprises contributions from the fan stage and the core noise sources. Fig. 1.2 below comprehensively showcases the core section, and the component duct sections of the fan stage, which include the intake, the intra-stage, and the bypass, through the cutaway view of a modern turbofan engine. We may note here that the investigations reported in this thesis exclusively consider the noise measurements made in the engine intra-stage, which is the duct section between the fan trailing edge (TE) and the OGV leading edge (LE).

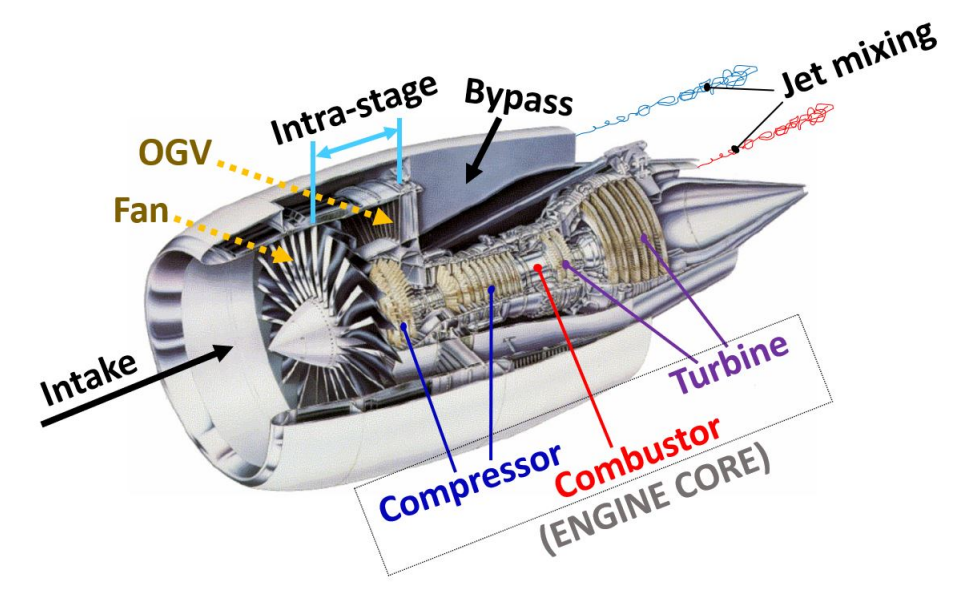
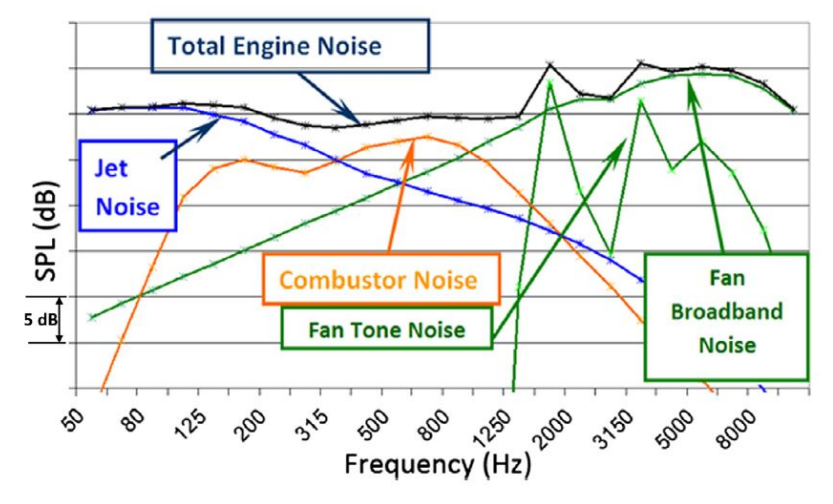


FIGURE 1.2: A cutaway section of a turbofan engine depicting the core and the fan stage. The above image corresponds to the GE90 engine taken from Reed et al. (2003).

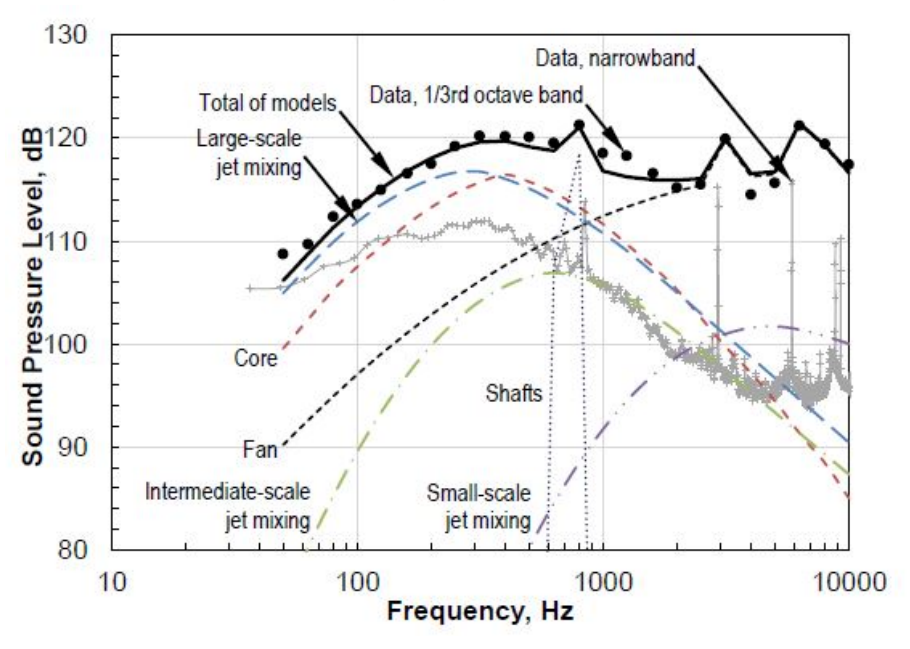
The relative importance of the different engine noise sources depends on the turbofan design configuration, frequency, and operating condition. To enable a good appreciation, Fig. 1.3 below compares the noise measurements of a modern HBR turbofan (Dowling and Mahmoudi (2015)) and a geared turbofan (Berton (2015)) at selected operating conditions with the individual plots inclusive of a breakdown of the component noise spectrum of the different engine sources predicted using appropriate scaling laws and empirical models. It may be noted here that the core noise in Fig. 1.3b solely refers to the combustion noise, albeit in a general sense, the core noise encompasses the noise from the compressor, the combustor, the turbine, and the jet noise sources.

The superposed acoustic signatures of the component noise sources reveal useful insights:

- The broadband (BB) jet mixing noise is dominant at lower frequencies. The noise levels increase with higher overall jet velocities at higher engine speeds, increasing the relative contributions to the overall engine noise at *cutback* and *sideline*.
- The combustion noise is primarily generated by two important mechanisms direct combustion noise that is generated by the unsteady combustion process it-self and indirect combustion noise (or, the entropy noise) generated by the acceleration of the temperature inhomogeneities (entropy perturbations) through the turbine stages. The combustion noise (the totality of the direct and the indirect noise mechanisms) is broadband in nature and is important in the low-to-mid frequency range, typically between 300 Hz to less than 1000 Hz. In modern HBR turbofans, the combustion noise is the third important noise source after the fan and the jet noise sources. However, for future engine architectures with reduced



(A) HBR turbofan at approach, taken from Dowling and Mahmoudi (2015).



(B) Geared turbofan at 96% shaft speed, taken from Berton (2015).

FIGURE 1.3: Typical noise contributions of different sources within a turbofan engine.

overall jet velocities and novel lean burn combustion systems (with more air-to-fuel ratio, which would make the combustion process more turbulent and unsteady (Garcia (2013))), the low-frequency prominence of the combustion noise is expected to increase, rendering it dominant to the jet noise at *approach* and *cutback* (Dowling and Mahmoudi (2015) and Zante et al. (2017)). Comparison of the noise breakdown of Figs. 1.3a and 1.3b reveals that the combustion noise and the jet noise may contribute equally in the case of a geared turbofan with reduced jet velocities (even at the maximum engine power) as opposed to a typical HBR turbofan at reduced engine power.

The fan noise, composed of both tonal and broadband components, is dominant

in the mid-to-high frequency range typically spanning from 1000~Hz to 10000~Hz. For a typical modern HBR turbofan, the total engine noise is uniquely dominated by the fan noise at *approach*, with comparable contributions from the jet noise at *cutback* and *sideline*. For future Ultra High Bypass Ratio (UHBR) engine concepts (Zante et al. (2017) and Palani (2022)) characterized by a bigger nacelle diameter (therefore further reduced jet velocities), a decreased fan blade count, and lower fan *rpms*, the preponderance of the fan noise spectrum is expected to widen with the fan tonal components shifted to further lower frequencies (< 1000~Hz) and the BB component still expected to dominate the higher frequencies.

• The turbine and compressor comprise multiple rows of stators and rotors, and consequently their noise signatures are dominated by multiple interaction tonal components with discrete acoustic modes that cut-on<sup>2</sup> and radiate notably at very high frequencies (Astley (2010) and Berton (2015)). However, for the evaluation of the EPNL, the noise regulations set the upper-limit of the one-third octave band center frequency to 10000 *Hz*, which is much less than the frequencies relevant for the turbines and compressors. Consequently, these turbomachinery noise sources do not garner significant attention concerning the aircraft noise metrics.

## 1.3 An overview of the fan noise

Since the EPNL depends on the tones as well as the frequency content, attention to the tonal and broadband characteristics of the fan noise is important. The fan tonal noise is present at discrete frequencies, which are either the harmonics of the fundamental frequency of the fan shaft's rotation,  $f_s$  rps with rps here denoting the revolutions-persecond where 1 rps = 1 Hz, or the harmonics of the blade passage frequency (BPF) at  $Nf_s$  Hz where N is the number of fan blades. Fig. 1.4 below depicts the tonal and BB spectral breakdown of one of the wall microphone signals in the engine intra-stage of an HBR turbofan test rig (Kumar et al. (2023)). The tonal and BB noise separation has been accomplished through the rotor phase-locked time domain averaging method (Rademaker et al. (2001) and Sijtsma (2010)) using a 1-p signal (one pulse per revolution of the shaft, or more generally the tacho signal).

For a rotor system of 20 fan blades and a steady fan speed of  $3750 \, rpm$ , the rotor-locked tones corresponding to the shaft harmonics (or, more commonly the Engine orders (EO)) exist at multiples of  $62.5 \, Hz$  and the BPF harmonics peak at multiples of  $1250 \, Hz$ . We may note from Fig. 1.4 that except for the narrow-band BPF harmonics, the broadband noise dictates the total fan noise spectrum. In the subsequent sub-sections, we

<sup>&</sup>lt;sup>2</sup>"Acoustically cut-off" signifies that the modal sound waves decay exponentially as they propagate along the duct. On the other hand, "acoustically cut-on" modes do not undergo any exponential attenuation.

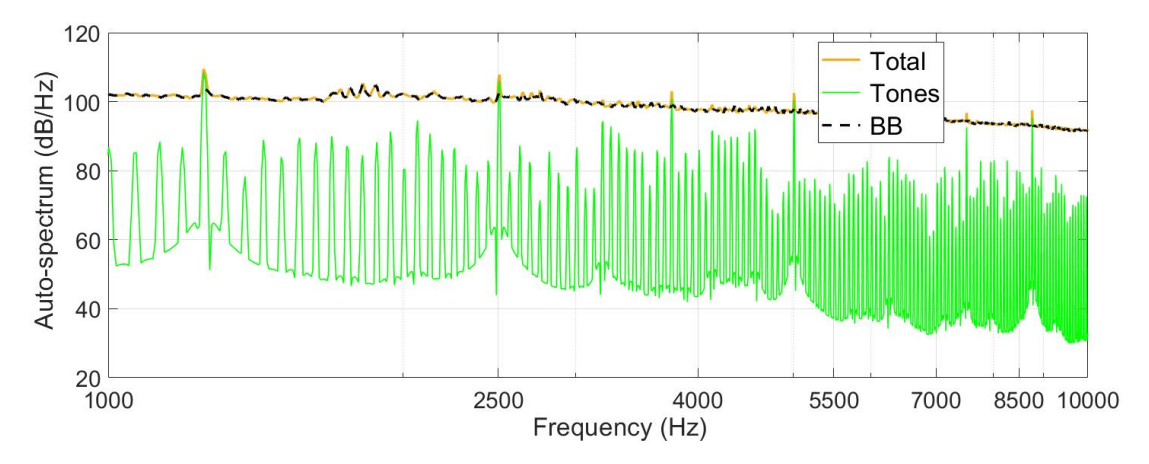


FIGURE 1.4: Separation of the tonal and the BB noise components from the total pressure signal sensed at the wall of an intra-stage in a scaled HBR turbofan.

summarize the underlying noise generation mechanisms of the tonal and BB fan noise, including the standard and future noise abatement strategies to mitigate them.

#### 1.3.1 Fan tonal noise

#### 1.3.1.1 Rotor-locked tones: Rotor-alone tones

As the name indicates, the rotor-locked pressure field is steady (implying no time dependence) in the rotor's frame of reference. Assuming identical fan blades, the *rotor-alone* sound field that is stationary but azimuthally periodic at integer multiples of the number of fan blades is accordingly Doppler-shifted in the observer's frame of reference at harmonics of the BPF carrying the time dependence of the rotor. The azimuthal periodicity of the rotor-locked pressure field is given by  $e^{jm\theta}$ , where  $\theta$  is the angular duct coordinate, and m is the azimuthal number (or the spinning mode order) corresponding to the number of nodal diameters (Rienstra (2015)). For *rotor-alone* tones at BPF harmonics, m = nN where n denotes the harmonic order. The *rotor-alone* tones are cut-off at subsonic fan tip speeds, wherein these exponentially attenuate before radiation to the far-field.

## 1.3.1.2 Rotor-locked tones: *Buzz saw* tones (multiple pure tones)

At supersonic fan tip speeds, stand-off shocks develop on the blades leading to non-linear wave propagation in the intake duct with the pressure field depicting a saw-tooth waveform (McAlpine et al. (2012)). Unlike the *rotor-alone* tones, the buzz saw tones are sensitive to the manufacturing inaccuracies from blade to blade and are therefore not periodic with the blade spacing. These are still rotor-locked but at EO harmonics with the azimuthal periodicity given by m = EO. The *buzz saw* tones are cut-on at supersonic

fan tip-speeds and dominate the forward arc engine noise spectrum at *sideline* rendering a peaky distribution. Their impact can be mitigated by designing the blade profile to reduce the aerodynamic shock strength (such as providing the sweep and lean on the fan blades) or blade shuffling to arrive at an optimized blade arrangement (Astley (2010)).

#### 1.3.1.3 Rotor-stator interaction tones

When stators are present behind the rotor, interaction tones are generated when a rotor-coherent pressure field encounters the stator vanes. This rotor-coherent field could either correspond to the *rotor-alone* pressure field discussed in Sec. 1.3.1.1 or the rotating wakes from the fan blades (Maldonado (2016)), which are scattered from the OGV carrying the time dependence of the blade rotation as well as the periodicity of the stator vane spacing, resulting in a sequence of interaction modes (Tyler and Sofrin (1962)) at harmonics of the BPF with the azimuthal periodicity given by  $m = n_1N + n_2V$ , where  $n_1$  denotes the harmonic order,  $n_2$  is any integer, and V is the number of stator vanes.

Unlike the *rotor-alone* tones, the *rotor-stator interaction* modes are not locked to the fan shaft, and could be cut-on even at subsonic tip speeds, thereby propagating unattenuated. A design strategy to mitigate this sound is the "Tyler-Sofrin selection rule" which is based on a clever choice of N and V so that the interaction mode is acoustically cut-off at the desired frequency (Tyler and Sofrin (1962)). As a rule-of-thumb, V > 2N ensures that the interaction mode at the  $1^{st}$  BPF is cut-off, which is a common observation in most of the modern turbofan engines. This is termed as "cut-off" design.

#### 1.3.2 Fan broadband noise

The fan BB noise is a random event generated by the unsteadiness in the flow field, attributed to the turbulent flow structures, interacting with the fan blades and OGV, inducing a fluctuating loading that emits sound. There are numerous possible sources of BB noise in the fan stage (Ganz et al. (1998)) with the underlying turbulent structures either corresponding to the rotor wakes, boundary layer (BL) developed in the casing wall/blades/vanes, or the tip vortices from the fan. Ganz et al. (1998) published a report detailing their systematic investigation using a modular fan rig, capable of operating with and without the OGV, which employs a sophisticated boundary layer (BL) suction system (to suck out the intake BL when required), thereby allowing the confounding noise effects due to the intake boundary layer, and the OGV interaction to be isolated. The report identifies three primary BB noise generation mechanisms:

• **Rotor self-noise** (trailing edge noise) due to the interaction of the convecting turbulent eddies in the blade boundary layer (BL) with the fan trailing edge (TE),

- **Rotor tip-Boundary layer interaction noise** due to the interaction of the fan blade tips with the turbulence in the casing wall boundary layer, and
- **Rotor-stator interaction BB noise** (leading edge noise) due to the impingement of the turbulent rotor wakes on the leading edges of the OGV.

For a better illustration, Fig. 1.5a below schematically depicts the potential BB noise generation mechanisms in the fan stage. Ganz et al. (1998) performed a sub-component level source extraction using their modular test rig to predict the BB noise spectrum due to each of the three aforementioned source mechanisms. The results of the source decomposition obtained using the rear arc noise measurements have been reproduced and plotted alongside in Fig. 1.5b.

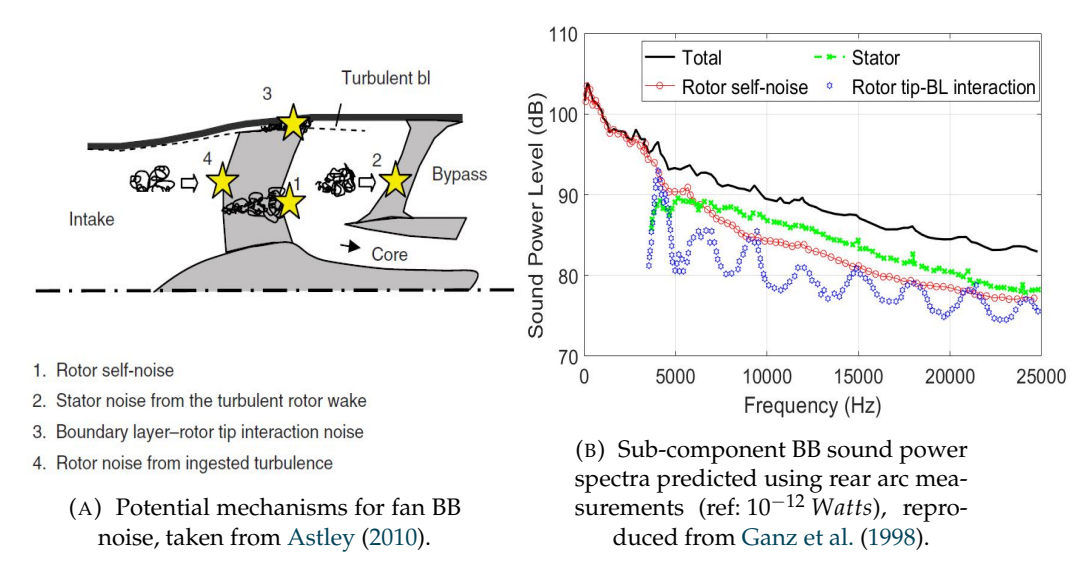


FIGURE 1.5: Sources of fan BB noise, and their radiated sound power levels obtained via sub-component level source extraction using a modular fan rig (Ganz et al. (1998)).

The report of Ganz et al. (1998) presents a detailed work considering the measurements made in-duct and in the far-field (both forward and aft of the fan) across various operation and design parameters such as fan loading and tip-clearance. The extracted spectra for each component noise source were averaged over fan loading and tip clearance variations for the comparative study, and the complete set of results suggests that the stator-bound noise dominates the rotor-bound noise sources only by a small margin (not exceeding 3 *dB*). The relative dominance of the rotor-bound tip and self-noise sources is not decisive from their sub-component level extractions (Ganz et al. (1998)) since the rotor tip-BL interaction noise spectrum was predicted to be higher than the rotor self-noise in the measurements upstream of the fan (i.e.: the intake duct and forward arc), whereas the fan self-noise was predicted to be stronger in the aft duct and rear arc noise measurements. However, over the years, the rotor self-noise (TE noise) and the rotor-stator interaction BB noise (LE noise), attributed to the fan and OGV, respectively, have been extensively studied through experiments and computations (Kissner et al.

(2020), Guérin et al. (2020), Masson et al. (2016), Posson and Peake (2012), and Morin (2010), Glegg and Jochault (1998)) considering their relevance even in un-ducted fan systems facilitating investigations using isolated airfoils (Amiet (1975), Amiet (1976), Brooks et al. (1989), Chaitanya Paruchuri (2017)).

The standard attenuation strategy for the fan BB noise is the placement of acoustic absorption liners along the engine intake and bypass ducts to attenuate the propagating waves before their radiation to the far-field. Since the liners also mitigate the fan tones, optimizing the liner design (Rice (1976a), Rice (1976b), Walsh (2016)) and investigating novel liner concepts (Palani (2022), Subramanyam et al. (2024), Cabré (2021)) have been vital areas of research in turbofan acoustics targeted at obtaining as much Insertion loss (IL) as possible within the available liner area. Over the years, however, active noise control strategies have been explored that attempt to control or modify the turbulence characteristics to achieve a reduction in the aerofoil BB noise. Some of these include the provision of serrated profiles on the fan trailing edge (Pereira et al. (2023)) and OGV leading edge (Chaitanya Paruchuri (2017)), Trailing edge blowing (TEB) to minimize the velocity deficit in the fan wake (Sutliff et al. (2002)), soft blade/vane concept (Fernandez et al. (2016)) wherein a short section along the aerofoil span is perforated, and swept and leaned OGVs (Premo and Joppa (2002) and Walsh (2016)). Finally, we may note here that investigations have also been directed at a noise-focused nacelle design such as spliceless liners (Walsh (2016)), negatively scarfed intakes (Envia (2002)), radial/circumferential lined splitters in the bypass, and extended intake lip liners. More details on the advanced turbofan noise reduction concepts may be referred to from Envia (2002), Astley (2010), and Zante et al. (2017).

## 1.4 Scope and objectives of the Ph.D. project

The fan broadband noise is not properly understood. Unlike the fan tones, the BB noise, at its every narrow-band frequency component, comprises all the acoustically cut-on duct modes, roughly increasing in number as the square of frequency (Rice (1976c)). It may be noted that all the propagating modes are not equally excited by the fan and OGV, and there is a characteristic modal pressure distribution (Ganz et al. (1998) and Premo and Joppa (2002)). Therefore, characterizing the fan BB noise entails investigating the sound propagation characteristics due to the fan and OGV. Also, despite more than 50 years of research into fan noise, the relative balance between the rotor-based and stator-based BB noise sources has never been properly established.<sup>3</sup> In this thesis, we address these important aspects using the noise measurements made in the engine intra-stage.

<sup>&</sup>lt;sup>3</sup>The sub-component level source extraction, as discussed in Sec. 1.3.2, is not representative of the relative source levels since the fan aerodynamics (and consequently its acoustic source strength distribution) is different in the presence of the OGV (Venkateswaran et al. (2024) and Hughes et al. (2002)).

So far, the acoustic analysis of the fan BB noise has predominantly focused on the measurements made in the engine intake and bypass ducts mainly because these sections transmit the in-duct propagating noise to the far-field. However, the drawback of measurements in these sections is that the noise from the fan and OGV arrive simultaneously in one direction and suffer some degree of acoustic blockage due to one another, which does not permit the prediction of the relative source contributions. However, the engine intra-stage effectively circumvents this challenge by permitting an analysis on a first approximation considering the upstream waves (propagating against the direction of the mean axial flow) to be solely originating from the OGV and the downstream waves (propagating in the direction of the mean axial flow) to be solely originating from the fan, ignoring any acoustical reflection/scattering as secondary effects.

As discussed in Sec. 1.3.2, the prominent BB noise sources in the fan stage are the rotor self-noise at the trailing edges (TE) of the fan blades and the rotor-stator interaction noise at the leading edges (LE) of the stator vanes. Therefore, the fan BB noise is primarily generated in the engine intra-stage making this region particularly suitable for predicting the relative source contribution and gathering insights into the noise generation and propagation characteristics of the fan and OGV BB noise sources. However, despite its appropriateness, the intra-stage has been a less explored region primarily because it is a hostile environment for acoustic measurements owing to:

- the inherent space restriction to mount large microphone arrays,
- the acoustic and hydrodynamic near-fields,
- high levels of turbulent flow noise, and
- high levels of swirling flow.

In this thesis, we exclusively focus on the measurements made in the intra-stage region to identify and reveal the fundamental characteristics of the BB noise generated within the fan stage and develop measurement techniques that overcome the foregoing challenges and accomplish the desired source separation.

## 1.5 Original contributions

This thesis reports the investigations conducted using the intra-stage noise data obtained from three different turbofans across a wide range of operating conditions. The novel contributions borne out of our research have been organized into five chapters of the thesis. In the following, we present the subject matter and key highlights of each of these chapters.

- 1. Fan BB noise characterization using engine intra-stage measurements
  - Sound propagation characteristics of the fan and OGV are investigated by developing and measuring suitable normalized mode distribution metrics that reveal the underlying multimodal sound structure.
  - An equivalent point source model for the engine intra-stage is conceptualized wherein the fan and OGV BB noise sources are effectively reduced to singular point dipoles. The source parameters of this simplistic model are empirically determined such that it generates near-identical BB noise characteristics as the measured distributions for the fan and OGV. The consistency of the source parameters is demonstrated across different turbofans and operating conditions, thereby rendering these as "engine constants".
  - The establishment of the equivalent point source model is shown to permit: (i) an interpretation of the measured relative modal pressure distribution due to the fan and OGV, (ii) the illustration of the physical existence of the modal overlap region in which high-amplitude modes of the fan and OGV share the same axial wavenumber and are inseparable using the existing mode detection methods, and (iii) the demonstration of the preponderance of the OGV as the dominant BB noise source.

#### 2. Broadband acoustic mode detection in swirling flows

- Using synthesized datasets, the region of modal overlap is shown to present
  a unique challenge to wave splitting at higher fan speeds by rendering the
  existing phased array techniques unsuitable for predicting the relative source
  contributions of the upstream propagating (OGV-based) and downstream
  propagating (fan-based) modes.
- The occurrence of the modal overlap region is elucidated, wherein it is shown that the overlap bandwidth could be reasonably characterized by co-rotating upstream modes and contra-rotating downstream modes.
- A generalized modal analysis framework for the engine intra-stage is proposed that not only overcomes the challenge due to modal overlap but also enables a systematic fitment of modal analysis methods for any given intra-stage microphone array geometry.
- 3. Estimation of the relative balance between the rotor and OGV broadband noise
  - The intra-stage noise data of two turbofan rigs with different intra-stage lengths is systematically analyzed to examine the relative influence of different secondary noise sources due to acoustic and hydrodynamic near-fields, hydrodynamic modes, and turbulent flow noise.
  - The investigations across the two turbofans have unanimously detected the presence of a turbulent flow noise structure of short correlation length scale

- to significantly influence the axial pressure coherence rendering several of the potential phased array techniques unreliable for acoustic mode measurements in the engine intra-stage.
- By the use of techniques that permit a suitable spatial-filtering-and-averaging, the pseudo-noise contributions are removed resulting in the extraction of the acoustical modal distributions. The final predictions obtained using the intra-stage noise data at approach for a scaled HBR turbofan reveal the OGV to be dominant by about 8 *dB* across the BB frequency range.
- 4. Source separation of the fan broadband noise at higher engine speeds
  - At higher fan speeds, the phenomenon of modal overlap kicks in, entrapping the high-amplitude modes of the fan and OGV within its bandwidth.
     The investigations on the modal overlap presented in Chapter 5 using an appropriate synthesized dataset for the cutback operating point of a scaled HBR turbofan are demonstrated using the measured dataset in this chapter.
  - The predictions of the mode amplitude distributions and the relative source balance obtained using the measured noise data are shown to be in good agreement with the corresponding results obtained using the synthesized dataset.
  - The final predictions reveal an almost flat noise spectrum for the fan and the OGV, with the OGV dominant by about 6 *dB* across the BB frequency range
- 5. Modal axial group velocity in ducted swirling flows and its relevance to intra-stage noise measurements
  - A theoretical interpretation of the modal axial group velocity in the swirling flows is developed, the appropriateness of which is verified across ideal rigid body swirling flows and realistic intra-stage swirling flows.
  - The modal axial group velocity is demonstrated to be a more relevant parameter to the classical cut-on ratio in a swirling flow. The suitability of the axial group velocity towards modal detection is also investigated using measured intra-stage noise data.
  - The extent of definiteness of the axial group velocity in a swirling flow governs the relevancy of defining modal sound powers based on which the modal sound power distributions are estimated for measured intra-stage noise data at the approach and the cutback operating conditions of a scaled HBR turbofan, which exhibit conformity as well as deviation from the ideal equal-power-per-mode concept.

### 1.6 Outline of the thesis

Following this introduction chapter, Chapter 2 focuses on the literature review. This chapter has been essentially split into two parts with the first part focusing on some of the important works carried out on the fan BB noise characterization. Here, we shall discuss the different strategies employed to understand the noise generation mechanisms, the in-duct modal sound structure, and propagation characteristics.

The second part then reviews the different modal measurement techniques for quantifying the tonal and BB sound fields. Here, we examine the different phased array approaches considering their underlying framework, the complexity of acoustic instrumentation, the inherent assumptions, and more importantly, their suitability for implementation in the engine intra-stage.

Chapter 3 presents a brief theoretical background on the fundamental concepts governing acoustic propagation in a ducted flow. We begin with presenting the principal concepts of the acoustic eigenmodes, and Green's function for an ideal uniform axial flow (Glegg and Devenport (2017)) which is a good approximation for the engine intake and bypass ducts (Mathews et al. (2018), Premo and Joppa (2002)), following which we present the acoustic analogy in a swirling flow (Mathews (2016), Posson and Peake (2013)) which forms the basis of the numerical solver *GreenSwirl* used through this research for numerical calculations of the eigenmodes, and Green's function in the swirling flows. This chapter also discusses the usefulness of the analytical *rigid body swirl* model (Morfey (1971a)) for understanding the acoustic propagation in swirling flows.

Chapters 4-8 present the novel contributions of our research, which we had briefly introduced above in Sec. 1.5.

Finally, the conclusions and ideas for future work are presented in Chapter 9.

# **Chapter 2**

# Literature Review

Ducts, also known as waveguides, effectively transmit sound waves over large distances. When the ducts are narrow and the frequencies of interest are small, as with the commercial automotive exhaust systems (Munjal (2014)), only the plane wave propagates effectively. However, in large turbofan ducts, where the cross-dimensions are larger compared to the wavelength at the frequencies of interest, the noise propagates in a complicated manner with numerous simultaneously propagating modes eventually radiating from the engine to the ground. The three duct sections comprising the fan stage are near-cylindrical making the in-duct sound field azimuthally periodic, thereby allowing for the Fourier series representation:

$$p(\mathbf{x},\omega) = \sum_{m=-\infty}^{\infty} p_m(z,r,\omega) e^{jm\theta}, \qquad (2.1)$$

where p is the complex acoustic pressure (phasor),  $x = (z, r, \theta)$  denotes the duct coordinates with z, r, and  $\theta$  being the axial, radial, and angular coordinates, respectively, and  $\omega$  is the circular frequency in rad/s. Note that the  $e^{-j\omega t}$  time dependence is implicit in Eq. (2.1). The azimuthal and temporal dependence together account for the spin of the constituent Fourier harmonics, thereby rendering these as  $spinning\ modes$ . Therefore, the index m above denotes the azimuthal number or the spinning mode order. Modes spinning in the direction of the fan are termed co-rotating modes (m > 0) whereas the contra-rotating modes (m < 0) spin opposite to the fan. Each of the spinning mode harmonics,  $p_m$ , in turn, can be expressed as a summation across the radial mode orders, n, as:

$$p_{m}(z,r,\omega) = \sum_{n=1}^{\infty} \left( A_{mn}^{-}(\omega) \psi_{mn}^{-}(r) e^{j\kappa_{mn}^{-}z} + A_{mn}^{+}(\omega) \psi_{mn}^{+}(r) e^{j\kappa_{mn}^{+}z} \right), \tag{2.2}$$

where  $A_{mn}^{\pm}$  is the modal pressure amplitude,  $\psi_{mn}^{\pm}(r)$  is the normalised radial mode shape function, and  $\kappa_{mn}^{\pm}$  is the modal axial wavenumber with the superscripts  $(\pm)$  denoting the downstream running (+) modes and upstream running (-) modes, respectively. It may be noted here that the radial mode index, n, physically corresponds to the number of nodal circles (Rienstra  $(2015))^1$ . The subscripts (m,n) in Eq. 2.2 above denote the particular mode order index and in most of this thesis, for reasons of brevity, we would delete the (m,n) subscripts and the  $\pm$  superscripts while referring to the modal quantities. From Eq. (2.2), we understand that each of the spinning mode harmonics accounts for the contributions from the upstream and downstream modal components. As far as the fan stage is concerned, it is appropriate to assume the *intake* sound field to be constituted by upstream propagating modes, the *bypass* sound field to be constituted by downstream propagating modes, and the *intra-stage* sound field as a superposition of upstream (OGV-bound) and downstream (rotor-bound) modes. Despite several years of investigations into the fan noise, the noise transmission from the intra-stage region to the intake and bypass ducts has never been properly understood.

The pioneering works aimed at the source diagnostics of the fan BB noise include the test campaigns under the AST (Advanced Subsonic Technology) program, carried out in the 1990s, on the Boeing 18-inch fan rig (Ganz et al. (1998)), and the NASA 22-inch SDT (Source Diagnostic Test) fan rig (Premo and Joppa (2002)). Both the fan rigs only constitute an HBR fan stage (with a single air stream) in a modular test set-up to permit the experiments with and without the stator. The investigations using the Boeing fan rig (Ganz et al. (1998)) were aimed at identifying and quantifying the different BB noise mechanisms and conducting a parametric study under different operation and design parameters. Premo and Joppa (2002) investigated the wall pressure measurements of the SDT fan rig at the intake, intra-stage, and bypass to produce suitable spinning mode order plots, which depict the distribution of the wall pressure spectra across the azimuthal constituents over the BB frequency range, for fan stage configurations with and without OGV to gather some insights on the modal transmission and propagation characteristics. Over the years, numerous investigations have been dedicated to characterizing and measuring the fan BB noise. Characterization of the fan BB noise involves a qualitative understanding of the BB sound field by:

- developing suitable in-duct source location methods (Sijtsma (2010) and Sijtsma (2012)) to identify the dominant noise generation mechanisms.
- simplifying the analysis of a multimodal sound field in terms of a characteristic modal propagation parameter (Rice (1976a), Rice (1976c) and Joseph et al. (2003)),
- predicting the multimodal sound structure (Rice (1978) and Venkateswaran et al. (2024)).

 $<sup>^{1}</sup>$ The index n begins from 1 instead of 0 to correspond with the count of the radial mode within each azimuthal number (Munjal (2014)).

Understanding the multimodal noise propagation in large turbofan ducts would involve deducing the distribution of the in-duct sound pressures and powers into the numerous propagating modal components, which consists of determining the relative modal magnitudes using phased microphone arrays. The estimated modal amplitudes:

- 1. are fundamental to predicting the in-duct sound power transmitted from the microphone array measurements (Joseph et al. (2003)).
- 2. enable the design of efficient sound absorbers as the optimum liner impedance varies for each mode (Rice (1976a), Rice (1976b), J. Cuenca and R. Hallez and B. Peeters (2013)).
- 3. can be used as input to a radiation model to predict the far-field mean square pressure directivity in situations where direct measurement of the far-field directivity is difficult and acoustic measurements are restricted to within the duct (Joseph (2017), Lowis et al. (2010), Sinayoko et al. (2010), Melling et al. (2017)).
- 4. provide insights into the source diagnostics as the underlying modal structure differs for different sound excitation mechanisms (Joppa (1987), Tapken et al. (2012), Venkateswaran et al. (2024)).

Therefore, the primary objective of the different mode measurement techniques is to predict the modal amplitudes. The complexity and suitability of the different measurement techniques depend upon the nature of the sound source (tonal or broadband) and the parameters of the modal distribution used for the analysis. Control of noise from turbofan ducts requires investigating its generation and propagation characteristics. Below, we structure our literature review into two broad sections, with the first one discussing the diverse approaches employed to understand the fan BB noise in terms of its source mechanisms, in-duct modal sound structure, and propagation characteristics. The second part then presents a systematic survey of the different mode measurement approaches for quantifying the tonal and BB sound fields.

### 2.1 Previous work on Fan BB noise characterization

Research on fan noise gained precedence in the 1970s-80s with the advent of the medium bypass ratio (MBR) turbofans, which were shown to accomplish a higher reduction in the perceived noise levels than the then-used low bypass ratio architectures (Kramer (1971)). The key emphasis was on:

- 1. an improved understanding of the fan noise generation process,
- 2. the radiation directivity pattern of the duct acoustic modes, and

3. the development of nacelle acoustic linings to attenuate the fan modes.

The primary focus was on the engine intake and bypass ducts transmitting the ducted sound to the far-field. These duct sections were approximated as cylindrical ducts with circular (intake) and annular (bypass) cross-sections carrying uniform axial flow (with a thin boundary layer that was accounted for in the assessment of the liner performance (Rice (1976a) and Rice (1976b))). In cylindrical ducts with a uniform flow, the radial mode shape function (or, commonly the radial eigenfunction) of Eq. (2.2) is simply a linear combination of the Bessel's functions (Rienstra (2015)) and the corresponding modal eigenvalues, which for a hard-walled circular duct are the stationary points of the Bessel's functions (Rienstra (2015)), were shown to be related to the peak pressure in the modal far-field directivity (Homicz and Lordi (1975)). In Sec. 2.1.1 that follows below, we discuss how Rice came up with a characteristic modal propagation parameter based on the eigen values, and developed simple correlation equations to analyze the sound propagation in lined ducts (Rice (1976a,b)), rigid ducts (Rice (1976c); Rice et al. (1979)), and its radiation to the far-field (Rice (1978)).

# 2.1.1 The significance of the modal cut-on ratio

The modal cut-on ratio ( $\alpha_{mn}$ ), which was originally defined as the modal cut-off ratio ( $\xi_{mn}$ ) by Rice (Rice (1976a)), is directly related to the modal eigenvalues and defines the modal axial wavenumber in an ideal uniform axial flow. In a cylindrical duct carrying a uniform axial flow of Mach number,  $M_z$ , the modal cut-off ratio is defined following Rice (1976a) as  $\xi_{mn} = k/\left(\xi_{mn}\sqrt{1-M_z^2}\right)$ , where  $\xi_{mn}$  is the modal eigenvalue (refer to Sec. 3.1.1). The modal cut-on ratio ( $\alpha_{mn}$ ) is related to  $\xi_{mn}$  as  $\alpha_{mn} = \sqrt{1-1/\xi_{mn}^2}$ , and is unanimously defined for any arbitrary ducted flow as (Morfey (1971a) and Mathews et al. (2018)):

$$\alpha_{mn} = \pm \sqrt{1 - \left(\frac{\omega_{mn}}{\omega}\right)^2},\tag{2.3}$$

where  $\omega_{mn}$  is the modal cut-on frequency (or, the resonance frequency beyond which a duct mode propagates unattenuated (Rienstra (2015))) that intrinsically incorporates the modal eigenvalues, flow Mach number dependence, and the duct cross-dimensions. The cut-on ratio is a well-defined parameter for the ideal case of a rigid cylindrical duct carrying a uniform axial flow where the modal eigenvalues are real (Rice (1976a)). Simply put,  $\alpha_{mn}$  is a normalized measure of the extent to which an (m,n) acoustic mode propagating at a frequency  $\omega$  is excited (or cut-on) above its resonance frequency. For the cut-on modes,  $\alpha$  is real and is bounded within [-1,1] with  $\alpha \to 0$  corresponding to the modes near cut-off.<sup>2</sup> In a rigid duct, the cut-on modes propagate unattenuated, whereas the cut-off modes have an imaginary  $\alpha$  and are exponentially attenuated as they propagate along the duct. It may be noted that the sign of  $\alpha$  corresponds to the

<sup>&</sup>lt;sup>2</sup>In terms of  $\xi$ , the cut-on modes have  $1 < \xi < \infty$  with  $\xi \le 1$  corresponding to the cut-off modes.

direction of the energy propagation (Morfey (1971a)) with a positive sign for the downstream going modes (along the mean axial flow) and a negative sign for the upstream going modes. In this section, we only briefly introduce the concept of  $\alpha$ . For more clarity, please refer to the governing equations presented in Sec. 3.1.1 of Chapter 3.

The concept of the modal cut-off ratio ( $\xi$ ) emerged when Rice (Rice (1976a)) was investigating the optimum impedance for the intake duct modes (upstream propagating) and discovered that the normalized resistance and the normalized reactance, estimated for a broad range of (m, n) modes reveal a characteristic contour with the modes having different indices grouped. These coincident modes were found to have nearly the same  $\xi$  value, thereby revealing that the optimum impedance is solely a function of the modal cut-off ratio, enabling the dependency on the modal indices to be removed. Further, Rice (Rice (1976b)) showed that the maximum sound power attenuation at the optimum impedance is approximately a function of the cut-off ratio, thereby facilitating the modal analysis and the liner design as a one-dimensional problem in terms of  $\xi$  removing the dependency on the individual (m, n) modal identity. Such a simplified analysis would befit the higher frequencies (typically from the 1<sup>st</sup> BPF) with more cut-on modes.

At that time, the in-duct phased array measurements were not as robustly developed, and the relative ease of making far-field measurements allowed an understanding of the in-duct modal sound structure (such as equal-amplitude-per-mode or equal-powerper-mode) by comparing the measured and predicted far-field pressure directivity patterns (Saule (1976) and Rice (1978)). With explicit expressions for individual modal acoustic radiation patterns (Saule (1976) and Homicz and Lordi (1975)) and the direct correspondence of the duct eigen values with the location of the far-field peak pressure (Homicz and Lordi (1975)), Rice (Rice (1978)) developed approximate equations for the individual and multimodal far-field relative pressure directivity for different classes of modal sound power distribution models by employing legitimate simplifications. With the cut-off ratio established, the in-duct sound field could be approximated from the double summation over the modal indices to integration over  $\xi$ . Rice (Rice (1976c)) developed a simple equation to estimate the total number of cut-on modes from  $\infty$  to a particular value of  $\xi$ , and thence estimated the modal population density to predict the acoustic power and the far-field pressure (Rice (1978)) concentrated within a narrow  $\xi$ -range. These concepts shall complement the far-field pressure measurements to enable a robust prediction of the acoustic power produced by a turbofan as a function of  $\xi$  allowing for an acoustic assessment of candidate liner designs.

Rice (Rice et al. (1979)) went on to develop approximate expressions for the in-duct propagation angles of the local modal wavefronts in terms of  $\xi$  for a cylindrical duct, and studied the effect of convective drifts due to the internal and external uniform flow Mach numbers. These approximate expressions are however valid only at the duct wall, which is also physically the most relevant region where the microphones

are installed and the bulk of the acoustic intensity is concentrated. The approximate expressions were handy in correlating the in-duct axial propagation angle to the location of the principal lobe peak in the far-field radiation for static (no external flow) and in-flight (with external flow) engine tests. Additionally, it was also shown that the radial propagation angle (i.e.: the angle of incidence at the duct wall) is almost uniquely a function of  $\xi$  such that the near cut-off modes are almost incident normally at the duct wall, with the well cut-on modes possessing more axially normal wavefronts. The pioneering works of Rice (Rice (1976a,b,c, 1978); Rice et al. (1979)) had established the cut-on ratio as a modal behavioral index to suitably analyze the in-duct propagation, liner performance, and the far-field radiation characteristics. Joseph (Joseph (2017); Lowis et al. (2010); Melling et al. (2017)) later developed in-duct phased array techniques to suitably predict the mode amplitude distribution as a function of  $\alpha$  using a limited number of wall flush-mounted axial microphones for high-frequency BB sound fields.

# 2.1.2 Characterizing the broadband multimodal sound structure

Knowledge of the relative modal pressure distribution characteristics would complement the phased array measurements and help develop robust noise prediction models. The investigations using the forerunner MBR turbofans in the 1970s - 80s predominantly focused on the engine intake where the fan noise dominated the forward radiating compressor noise and also the intake section lent a relative ease of conducting indoor measurements unlike the bypass, which was ducted away. The fan BB noise generation mechanisms were not understood back then, and it was considered important to characterize the intake multimodal sound structure to corroborate the forward arc measurements and thence estimate the total acoustic power produced by a turbofan. Concepts of equal-amplitude-per-mode and equal-acoustic-power-per-mode were investigated by Saule (1976), who showed that the relative far-field pressure pattern estimated using the equal energy model agrees very well with the forward arc measurements. Later, Rice (Rice (1978)) presented qualitative comparisons in his paper employing a  $\xi$ —weighted modal pressure distribution model to corroborate the measured relative polar pressure pattern for several contemporary MBR turbofans. His analysis revealed that whilst the uniform power distribution model is usually satisfactory, unequal power distributions could also exist.

Joseph (Joseph et al. (2003); Joseph and Morfey (1999)) extended the idea of Rice (Rice (1978)) to express the mean squared mode amplitudes in terms of  $\alpha$  for a class of physically important source distributions in uniform axial flows to study the multimodal radiation (Joseph and Morfey (1999)) and in-duct propagation (Joseph et al. (2003)) characteristics. Such idealized mode amplitude distributions were useful in understanding certain source-independent characteristics of a BB sound field (Joseph et al. (2003)) and

developing in-duct mode measurement approaches for shorter linear microphone arrays (Lowis et al. (2010); Joseph (2017); Melling et al. (2017)). Recently, Pereira (Pereira and Jacob (2022)) evaluated the suitability of the equal-energy-per-mode (EEpM) and equal-energy-density-per-mode (EEDpM) distribution models on the intake and bypass broadband noise data and showed that the uniform modal power distribution concept is reasonably justified in both the sections.

# 2.1.3 In-duct source location techniques

With the advent of the HBR concepts in the 1990s, the fan BB noise became even more significant and was radiated comparably both forward and aft of the engine. The sub-component level investigations conducted in the AST program (Ganz et al. (1998); Premo and Joppa (2002)) attempt to identify and quantify the different BB noise mechanisms. Despite delivering useful insights, a sub-component level source breakdown is still immature in classifying the fan BB noise sources, calling for suitable beamforming methods to locate and quantify the aeroacoustic sources on the fan and OGV.

Beamforming is a classical method employing an array of microphones to locate and quantify the sound sources in a free-field environment (de Santana (2017); Sijtsma et al. (2001)). A beamforming algorithm typically consists of a source-receiver transfer model to incorporate the phase delay, and a delay-and-sum averaging to predict the source amplitudes. Conventionally, the Green's function (free-field or tailored) has been used to provide the steering vectors to relate the different source points with the receiver microphones for the delay-and-sum algorithm. In the context of aircraft noise, phased array beamforming approaches had been developed for airframe noise (Mendoza et al. (2002); Hutcheson and Brooks (2002)), wind tunnel tests of scaled aircraft models (Oerlemans and Sijtsma (2004)), and flyover measurements (Guérin et al. (2005)), but not for ducted sound sources within a turbofan. Lowis and Joseph (2006) pioneered the investigations for a focused beamformer with a rotating and stationary focus to locate and quantify the rotor- and stator-bound BB noise sources, respectively, making use of tailored Green's function for duct modes (satisfying the hard wall boundary conditions). The intention was to separate the relative contributions due to the fan and OGV using measurements in the engine intake by employing numerous wall microphone rings. The functionality of the focused beamformer was demonstrated numerically with the rotor and stator BB noise mechanisms represented by a radial array of incoherent axial dipoles of unit source strength. The difference in the beam and source speeds was shown to be crucial in separating the rotor-based and stator-based BB noise sources.

Sijtsma (2010) presented an advanced beamforming analysis by producing source maps of the fan and OGV to enable a visualization of the BB noise mechanisms. Unlike the approach of Lowis and Joseph (2006), Sijtsma (2010) makes use of free-field Green's function (ignoring the duct wall reflections), which was shown to work well with acoustic

liners installed between the source and the sensors (Sijtsma (2006)). Since the measured noise data was available only from a ring-shaped array in the intake and bypass, the scan planes were restricted to the rotor and stator LEs for intake, and the stator TE for the bypass. The beamformed results were summed up to one-third octave bands and by the mismatch between the source and beam speeds (Lowis and Joseph (2006)), sources were visualized on the fan and OGV. The beamformed source maps were appropriately normalized by the peak value, and an additional deconvolution step (Sijtsma (2017)) was incorporated to filter out the correlated source areas for mapping of tonal and broadband noise sources. The source maps obtained using the intake measurements vaguely revealed tip sources at the rotor (attributable to the rotor tip-BL interaction noise), whereas the bypass results depict a continuous distribution of sources along the span of the OGV instead of concentration around its tip. The utility of the beamformed source maps was confirmed by the correct number of fan blades and stator vanes detected in the analysis. Importantly, no large-scale coherent source distribution was revealed from the deconvoluted BB source maps.

Sijtsma (Sijtsma (2012); Brouwer and Sijtsma (2019)) later employed the circular harmonics beamforming (CHB) using an axisymmetric microphone set-up as an alternative to conventional beamforming (Sijtsma (2010)) for ducted sources. Here, the steering vector comprises the circumferential harmonics of the tailored Green's function, and the method was tested using the measured noise data of the intake (Sijtsma (2012)) and intra-stage (Brouwer and Sijtsma (2019)) to locate the rotating and stationary sources. The intake beamforming results detected tip sources on the fan, whereas the CHB technique was not very successful on the intra-stage data with the reasons attributed to the plausible variation in the flow profiles along the duct axis and the deviation from an ideal axisymmetric annular profile for the intra-stage duct. To tackle these uncertainty issues, Pieter (Sijtsma et al. (2023)) proposed a ray tracing-based beamforming scheme to localize the sound sources in the intra-stage duct. The new beamforming approach is based in the frequency domain with the steering vector comprised of the time delay between the microphones and the source grid points, which is calculated iteratively using the ray tracing technique. The new approach was demonstrated using numerically synthesized raw data to localize a stationary monopole source.

We may note here that the in-duct source beamforming approaches are useful to visualize the noise sources and infer the dominant noise mechanisms and their usefulness could be extended with suitable deconvolution methods (Sijtsma (2017); Brooks and Humphreys (2006)) to minimize the array artifacts and deliver cleaner source maps. But these inevitably suffer from poor axial resolution (say, in distinguishing between the LE and TE noise sources of fan/OGV) due to a limited number of sensor rings. Furthermore, the intra-stage is a very hostile and noisy environment, and the new ray tracing approach (Sijtsma et al. (2023)) despite tackling the uncertainties in duct axisymmetry and flow profile variation, restricts the number of usable sensor positions

per scan point owing to a reduced number of direct acoustic eigen rays connecting a source point to the wall receiver positions, which is attributed to the presence of the core duct. This would mean a reduced number of wall microphones per source grid point, and consequently, poor flow noise suppression, which is not desirable for the intra-stage region, which is already shorter with low sensor density. Also, from the source maps of Sijtsma (2010), it is evident that the source detection techniques suffer from acoustic blockage of the fan and OGV due to one another and cannot estimate the relative balance between the two noise sources. This calls for developing robust mode detection techniques for the intra-stage to estimate the total upstream (OGV) and downstream (fan) modal levels. The next section reviews the different phased array techniques to predict the duct mode amplitudes.

# 2.2 An overview of the mode detection methods

# 2.2.1 Modal analysis of a tonal sound field

The modal analysis of the fan tones is generally carried out at selected BPF harmonics with the dominant modes relatable to the explicable blade row interactions (Tyler and Sofrin (1962)). The analysis framework here attempts to measure the individual (m,n) modal constituents by inverting a system of linear equations relating the measured pressures to the modal amplitudes. Pioneering work in modal decomposition was undertaken by Bolleter and Crocker (1972) who measured the mode amplitude and power spectra of the first nine cut-on modes from the pressure cross-spectral density (CSD) measurements between two well-spaced-out microphone locations. Their approach does not consider axial standing waves and consists of writing down the Fourier-transformed pressure solution into separate co-rotating and counter-rotating parts considering the modal interaction terms (modal cross-correlations) amongst solving for the unknowns. Solving the linear acoustics problem then required CSD measurements at different pairs of microphone positions to obtain a statistically determinate set of equations which would be inverted to deduce the modal amplitudes.

A more systematic approach was demonstrated by Moore (1979), whose technique first consists of deducing the spinning mode amplitudes at a set of radial points by the discrete Fourier transformation of sound pressure phasors in a duct cross-section. Note here that the maximum azimuthal number resolved is one less than half the number of azimuthal sensing points (Sijtsma and Zillmann (2007)). Moore then proposes three approaches to deduce the radial mode contributions:

a) *Integration method* based on the orthogonality of the modal shape functions (or eigen functions) for simple no-flow and uniform axial flows,

- b) *Matrix Inversion* that comprises of inverting a matrix of modal shape functions, and
- c) *Least squares fitting* to deduce the radial mode amplitudes by minimizing the total mean squared error at all the measured radial points.

The three methods were first tested numerically by considering artificial modal distributions before implementation on intake fan rig measurements, and it was concluded that the *least squares fitting* is the best analysis method.

The least squares fitting procedure has since been extensively used for measuring the modal signature of the fan harmonics in large-scale test beds and production engines with sophisticated instrumentation (such as radial rakes of sensors (Tapken et al. (2012)) and continuously rotating rake of radial microphones (Sutliff et al. (2012); Heidelberg and Hall (1995))) to obtain a sufficient number of measurement points for modal decomposition. The principle was also extended by Thomas et al. (1999) and Farassat et al. (2001) to deduce the radiated duct modes from the measurements of the far-field pressure directivity. As these approaches primarily rely on estimating the spinning mode order spectra from a circular array of microphones, investigations have been directed at improved signal processing (Sijtsma and Zillmann (2007)), array optimization (Rademaker et al. (2001)), mode amplitude prediction (Behn et al. (2016); Behn and Tapken (2019)), and deconvolution approaches (Sijtsma and Brouwer (2018)) to enhance the azimuthal mode detection capability. However, decomposing the constituent radial modes by a direct measurement of the radial sound structure via in-duct microphone intrusion suffers several drawbacks such as increased complexity of instrumentation, flow noise contamination, and potential wake generation mechanisms. An alternative to the insertion of microphones is having longitudinal arrays of wall flush-mounted microphone rings (Tapken et al. (2012); J. Cuenca and R. Hallez and B. Peeters (2013)), in which case the number of axial measurement planes required should at least equal the largest radial mode order to be detected. This approach also involves the same least squares fitting procedure, which finally reduces to computing the Moore-Penrose inverse (pseudo-inverse) of the modal matrix constructed from a known modal basis.

Despite several improvements and modifications, the applicability of the *least squares fitting* procedure relies on using a sufficient number of measurement points and the condition number of the modal matrix to be inverted. The matrix conditioning could be improved by optimizing the sensor locations and increasing their numbers (Tapken et al. (2012); Moore (1979)). Typically, the number of microphones required is at least twice the number of propagating modes to be measured. Also, since the inversion procedure involves fitting the measured pressure distribution to a set of duct modes, it requires the measurement uncertainties to be minimal. Consequently, its numerical stability is impacted by any modeling inaccuracies such as excluded mode orders (whose contributions are comparable), measurement noise, uncertainties in the flow

field, or installation tolerances, all of which increase the noise floor (error) of the mode detection procedure. The analysis quality could be improved by applying some regularisation techniques (Kim and Nelson (2004)).

# 2.2.2 Modal analysis of a broadband sound field

The fan broadband (BB) noise is a stochastic phenomenon. Thus, for modal analysis of a BB sound field, we deal with statistical quantities such as auto-spectra and crossspectra as opposed to deterministic quantities such as pressure at a point. Working with statistical quantities ensures that the pressure time series data is suitably time-averaged (ensemble averaged) to obtain a time-invariant (mean) BB sound field to deliver statistical evidence. A BB signal is distributed over a broad frequency range, and the sound field at every narrow-band frequency component comprises of all possible cuton modes which are assumed to be mutually incoherent (Joseph et al. (2003); Sijtsma and Brouwer (2018)). For the rotor-coherent tonal noise, the associated modes are wellcorrelated with each other and the source. In the case of fan BB noise, we can assume that there are numerous statistically uncorrelated source mechanisms that in total exceed the number of cut-on modes in any narrow-band frequency component (Enghardt et al. (2007)). These aeroacoustic BB noise sources are considered to be separated by a distance larger than the statistical correlation length scale of the associated turbulent structures (Lowis and Joseph (2006); Sijtsma (2010); de Santana (2017)). Therefore, for a BB sound field, it can be assumed that the point-to-point coherence in space and time is too short to be captured experimentally to effect an incoherent analysis (Dougherty (2016)). It may be noted here that incoherent modes simplify calculations (and technique development) as the modal interaction effects (cross-terms) can be ignored.

As a BB sound field comprises a larger number of cut-on modes, which roughly increase as the square of frequency (Rice (1976c)), there have been different approaches to BB modal measurements. These can be broadly classified into two categories depending on the fundamental way the BB sound field is modeled:

- (i) **Techniques measuring the discrete modal spectra**: Here, the methods aim at measuring the individual (m, n) modal components.
- (ii) **Asymptotic wavenumber distribution approaches**: Here, the BB sound field is regarded as a continuum of modes such that the double summation over the (m,n) mode orders may be approximated by integration over a suitable modal parameter such as the modal cut-on ratio<sup>3</sup> or the normalized axial wavenumber,  $\zeta = \kappa/k$ , where  $k = \omega/c$  is the acoustic wavenumber with c being the isentropic sound speed, thereby suppressing the discrete modal identity. The assumption

 $<sup>^{3}</sup>$ Eq. 3.10 shows that  $\alpha$  is a flow-drifted normalized axial wavenumber

of a modal continuum is valid in the high-frequency (asymptotic) limit, which theoretically corresponds to  $\omega \to \infty$ , but is suitable beyond ka=10 (Joseph et al. (2003)), which covers the mid-to-high frequency range from the  $1^{st}$  BPF onwards with a greater number of cut-on modes. Here, ka is the non-dimensional Helmholtz number with r=a being the duct tip-radius.

### 2.2.2.1 Techniques measuring the discrete modal spectra

For a BB sound field, the techniques measuring the discrete modal spectra typically involve a spatial cross-correlation of microphone signals in conjunction with a beamforming or inversion approach. Enghardt et al. (2007) employs the conventional beamforming (de Santana (2017)) approach based on the duct modes, wherein the steering vectors incorporate the radial, azimuthal, and axial wave functions of the different (m, n) mode pairs (refer to Eqs. 2.1 & 2.2) to finally produce a vector of mode amplitude coupling terms (comprising the modal auto- & cross-sepctra). The beamforming approach was demonstrated on several synthesized BB sound fields in a no-flow test bench excited using a suitable arrangement of wall flush-mounted axisymmetric rings of loudspeakers, each of which was independently fed with random white noise signals to generate a desired sound field with varying levels of inter-modal coherency. The modal analysis approach required a dense cage array of multiple wall-mounted microphone rings to measure the mean squared amplitudes (and thence the acoustic power) of the individual (m, n) modes to determine the total transmitted (downstream propagating) and reflected (upstream propagating) sound power along the duct. Tapken et al. (2014) adopt a similar no-flow bench set-up to investigate their mode detection method. However, their analysis assumes uncorrelated duct modes, which permits a modal decomposition using a cross array (instead of a cage array) comprising a microphone ring and an axial line of wall microphones. The measurement approach here comprises the prediction of azimuthal constituents of the cross-spectra of the circumferential microphones with the individual microphones of the axial array from which the constituent (radial) mode amplitude spectra are estimated by a simple Moore-Penrose matrix inversion.

Later, Dougherty and Bozak (2018) proposed a robust adaptive beamforming algorithm, combined with a specialized regularisation technique, which offers a higher resolution and dynamic range compared to the classical beamforming. Their approach consists of constructing the steering vectors from a 2-D wavenumber grid in the  $m-\zeta$  plane instead of the theoretical duct mode values. The duct mode processing then consists of identifying the peaks in the beamformer maps and assigning them to the appropriate radial orders in each m. The beamformer output is the mean squared modal pressure at the duct wall, which is subsequently used to estimate the modal sound powers (Morfey (1971a)). The method assumes incoherent duct modes and was implemented using a cross-array (similar to that of Tapken et al. (2014) but of larger size)

to estimate the total sound powers radiating forward of a single rotor-operated fan-rig (Zante et al. (2007)) up to 10 kHz.

We may note here that the beamforming or inverse approaches are generalized classes of minimization problems. Pereira and Jacob (2022) extended this idea to come up with an iterative Bayesian inverse approach (iBIA) to decompose the BB modal spectra in terms of: 1) the (m,n) mode orders (Eq. 2.2), 2) the m harmonics (Eq. 2.1), and 3) distribution of axial wavenumbers (similar to the approaches discussed below in Sec. 2.2.2.2) from generalized matrix algebraic equations relating the vector of measured pressures to the vector of desired modal coefficients. The solution framework of the iBIA is iterative with an intrinsic regularization procedure. The iBIA is a sparsity-based reconstruction algorithm (with a parameter to control the degree of modal sparsity for tonal & BB sound fields) and therefore has reduced sidelobe effects compared to the conventional least squares beamforming. The iBIA approach was implemented on the measured BB noise data of a scaled turbofan (Kissner et al. (2020); Guérin et al. (2020); Kumar et al. (2023)) at its intake and bypass to accomplish a modal decomposition up to  $10 \ KHz$ .

# 2.2.2.2 Asymptotic wavenumber distribution approaches

The techniques under this category do not seek to detect the individual (m,n) duct modes. Rather, these attempt to predict the modal levels as a continuous distribution over the modal wavenumbers. As a consequence, similar modes are grouped which circumvents the need for a complete modal breakdown. One of the earliest works in this direction was by Joppa (1987), who measured the modal propagation using a wall-mounted cross-array of axial and circumferential sensors. Joppa (1987) separately measures the axial and circumferential propagations by appropriate Fourier transformation to plot the relative modal levels in the axial and circumferential wavenumber domains, respectively. The SPL (sound pressure level) spectra in the two wavenumber domains are collectively studied to detect the dominant modes and thereby identify the respective source mechanisms. This wavenumber distribution approach was found to be more robust and numerically stable since it doesn't involve any modal fitting procedure, thereby allowing some degree of measurement uncertainty. However, Joppa (1987) only measures the relative modal pressure levels and doesn't estimate the modal sound powers, which would require a knowledge of the relative mode amplitude distribution.

The high-ka limit allows the double summation over the (m,n) modal indices to be approximated by integration over a characteristic modal parameter which is treated to be a continuous variable with well-defined bounds. For uniform axial flows, Joseph (Joseph et al. (2003); Joseph and Morfey (1999)) chooses the modal cut-on ratio  $(\alpha)$ , which from Sec. 2.1.1, may be understood to characterize the modal propagation in

lined ducts, rigid ducts, and the far-field radiation. Presently, there are two asymptotic wavenumber distribution approaches developed by Joseph, namely the axial beamformer (Lowis et al. (2010)) and the two-microphone technique (Joseph (2017); Melling et al. (2017)), which predict the BB modal amplitudes as a function of  $\alpha$  assuming uniform axial flow and incoherent duct modes. The axial beamformer (Lowis et al. (2010)) consists of using a linear array of equi-spaced wall microphones and is a simple implementation of the conventional delay-and-sum algorithm with a steering vector to steer the beamformer's look-up to the desired modal value. The two-microphone technique (Joseph (2017); Melling et al. (2017)) estimates the mode amplitude distribution from the measurements of the complex coherence function between two closely spaced axial microphones on the duct wall. The formulations of the two techniques have been summarized in Appendix A.

# 2.3 Relevance to the engine intra-stage

The investigations concerning the engine intra-stage have so far exclusively focused on numerical schemes to predict the pressure solution (Cooper and Peake (2005)), the Green's function (Mathews (2016); Posson and Peake (2013)), and studying the hydrodynamic instabilities (Heaton and Peake (2006)). Works of direct relevance include the development of predictive models for the rotor self-noise (Posson and Peake (2012)) and rotor-OGV interaction BB noise (Masson et al. (2016); Kissner et al. (2020); Guérin et al. (2020)). It may be worth mentioning here that very few publications have been concerned with the modal measurements in the intra-stage but these are limited to the detection of azimuthal modes (Behn and Tapken (2019); Brouwer and Sijtsma (2019); Ganz et al. (1998); Premo and Joppa (2002)). However, referring to Eq. 2.2, the measurement of the azimuthal mode spectra doesn't convey the direction of the modal propagation. This was the motivation behind the recent test expedition of the EU project, TurboNoiseBB (Kissner et al. (2020); Guérin et al. (2020)), wherein the acoustic instrumentation in the intra-stage comprises an axial line of wall microphones alongside two circular rings to allow the decomposition of the total pressure signal into its upstream (OGV) and downstream (fan) components for estimating the relative source balance.

Owing to its shorter length and microphone sparsity, the engine intra-stage would befit an asymptotic wavenumber distribution approach. The latest work by Mathews et al. (2018) presents a numerical investigation into the concept of the modal cut-on ratio ( $\alpha$ ) for non-uniform swirling flows prevalent in the engine intra-stage, and demonstrates  $\alpha$  to be ambiguous in its meaning and usage with deviations from an idealized uniform axial flow condition. The paper suggests the use of the normalized modal axial wavenumber ( $\zeta$ ) over  $\alpha$  for duct mode measurements in the intra-stage. In our thesis, we exclusively consider the noise data measured in the intra-stages of three turbofans to:

- identify and reveal the BB multimodal characteristics due to the rotor self-noise and rotor-OGV interaction BB noise,
- develop suitable asymptotic wavenumber distribution techniques to separate the relative contributions due to the fan and OGV BB noise sources, and also
- produce modal sound power distribution plots for the intra-stage at different operating conditions, which have been shown to obey as well as deviate from the ideal equal-power-per-mode concept for the turbofans.

# Chapter 3

# **Modal Transmission**

In this chapter, we review the fundamental concepts governing acoustic propagation in a ducted flow. We begin with the principal equations for a uniform axial flow, where we discuss the concept of the eigenmodes, and Green's function (Glegg and Devenport (2017); Goldstein (1976)). We subsequently present the acoustic analogy in a swirling flow (Posson and Peake (2013); Mathews and Peake (2017)), which forms the basis of the swirling flow calculations throughout our research. In the final section of this chapter, we discuss the rotating coordinate approximation for acoustic propagation in a swirling flow, which is the analytical *rigid body swirl* (RBS) model (Morfey (1971a)).

# 3.1 Uniform axial flow in a rigid cylindrical duct

Fig. 3.1 below depicts simple sketches of an annular duct and a circular duct with indicated coordinate directions.

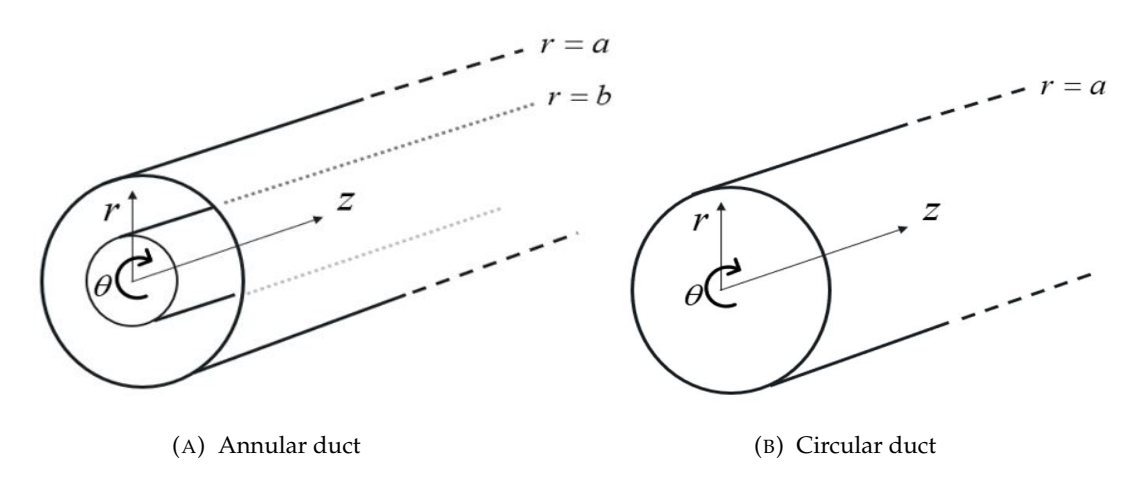


FIGURE 3.1: Simple sketches of rigid semi-infinite cylindrical ducts.

Considering sound propagation in a uniform medium, the acoustic pressure p' must satisfy the homogeneous convected wave equation:

$$\mathbb{L}(p') = 0,\tag{3.1}$$

where the linear operator L is defined as:

$$\mathbb{L} = \left(\frac{1}{c^2} \frac{D_0^2}{Dt^2} - \nabla^2\right),\tag{3.2}$$

where  $\frac{D_o}{Dt} = \frac{\partial}{\partial t} + U_z \frac{\partial}{\partial z}$  is the substantial derivative with t denoting the time, and  $U_z$  being the uniform axial flow speed.

Assuming a harmonic time dependence, the single-frequency pressure solution may be expressed as  $p' = \Re(p(x,\omega)e^{-j\omega t})$ . For axially uniform ducts (i.e.: constant cross-section and an axially independent wall boundary condition), the in-duct pressure field can be expressed as a series summation of a countable and an infinite set of solutions called modes [43]. Referring to Eqs. 2.1 & 2.2, the Fourier transformed pressure may be expressed as the (m,n) modal expansion:

$$p(\mathbf{x},\omega) = \sum_{m,n} A_{mn}(\omega) \,\hat{\Psi}_{mn}(r,\theta) \, e^{j\kappa_{mn}z}, \qquad (3.3)$$

where  $\hat{\Psi}_{mn}(r,\theta)$  is the modal eigenfunction (more commonly, the modal shape function). In the two sub-sections that follow, we present the eigenmodes, and Green's function for the operator  $\mathbb{L}$  of Eq. 3.2.

### 3.1.1 Acoustic eigenmodes

Substitution of Eqns. 3.2 & 3.3 into Eq. 3.1 renders the eigen value problem for each (m, n) modal constituent as:

$$(\nabla_{\perp}^{2} + \zeta_{mn}^{2})\hat{\Psi}_{mn}(r,\theta) = 0, \tag{3.4}$$

where  $\nabla_{\perp}^2$  denotes the Laplacian in  $r \& \theta$ , and  $\varsigma_{mn}$  is the modal eigenvalue (or the combined radial-transverse wavenumber (Rice et al. (1979))) satisfying the modal dispersion relation:

$$\varsigma_{mn}^2 + \kappa_{mn}^2 = (k - M_z \kappa_{mn})^2, \tag{3.5}$$

where  $M_z = U_z/c$  is the uniform axial flow Mach number. As the duct and the flow field are axisymmetric, the sound field should be periodic in  $\theta$ . So, we write the modal eigen function in its variable separable form as:

$$\hat{\Psi}_{mn}(r,\theta) = \psi_{mn}(r)e^{jm\theta},\tag{3.6}$$

where the radial mode shape function,  $\psi_{mn}(r)$ , is a linear combination of the Bessel's functions:

$$\psi_{mn}(r) = B_{mn} J_m(\varsigma_{mn} r) + C_{mn} Y_m(\varsigma_{mn} r), \tag{3.7}$$

where  $J_m$  and  $Y_m$  are the Bessel's functions of the first and second kind, respectively, of order m, with the corresponding coefficients,  $B_{mn}$  and  $C_{mn}$ , obtained such that the modal eigen function is normalized to have an area-average of unity, i.e.:

$$\frac{1}{S} \int_{S} \hat{\Psi}_{mn}(r,\theta) \hat{\Psi}_{mn}^{*}(r,\theta) dS = 1, \tag{3.8}$$

where S is the duct's cross-sectional area and the \* denotes complex conjugation. For circular ducts, with no central tube, the finiteness of acoustic pressure at r=0 will result in  $C_{mn}=0$ . It may be noted that  $\varsigma_{mn}$  only takes discrete values as governed by the appropriate wall boundary conditions, which for hard walls is the radial particle velocity (or, the radial pressure gradient) becoming zero. Once the modal eigenvalues are deduced, the corresponding axial wavenumbers can be estimated using the dispersion relation of Eq. 3.5 as:

$$\kappa_{mn} = \frac{-kM_z \pm \sqrt{k^2 - \varsigma_{mn}^2 \beta^2}}{\beta^2},\tag{3.9}$$

where  $\beta = \sqrt{1 - M_z^2}$  is the Doppler factor. Eq. 3.9 is more commonly expressed as (Morfey (1971a); Joseph et al. (2003)):

$$\zeta_{mn} = \frac{-M_z + \alpha_{mn}}{\beta^2},\tag{3.10}$$

where the cut-on ratio,  $\alpha_{mn}$ , is defined using Eq. 3.9 as:

$$\alpha_{mn} = \pm \sqrt{1 - \frac{\varsigma_{mn}^2 \beta^2}{k^2}} = \pm \sqrt{1 - \left(\frac{\omega_{mn}}{\omega}\right)^2} = \pm \sqrt{1 - \left(\frac{1}{\xi}\right)^2},\tag{3.11}$$

where  $\xi$  is the original modal cut-off ratio (Rice (1976a,b,c)) discussed in Sec. 2.1.1. In Eq. 3.11, the positive and negative values of the radical shall correspond to the downstream and upstream propagating (m, n) mode, respectively.

# 3.1.2 Acoustic Green's function for pressure

The frequency domain Green's function,  $\hat{G}_{\omega}(x|y)$ , for the linear operator  $\mathbb{L}$  of Eq. 3.2 solves for:

$$k^{2}\hat{G}_{\omega}\left(x|y\right)+2jkM_{z}\frac{\partial}{\partial z}\hat{G}_{\omega}\left(x|y\right)+\nabla^{2}\hat{G}_{\omega}\left(x|y\right)-M_{z}^{2}\frac{\partial^{2}}{\partial z^{2}}\hat{G}_{\omega}\left(x|y\right)=-\delta\left(x-y\right),$$
 (3.12)

where  $y = (z_s, r_s, \theta_s)$  is the source position from some origin. The tailored Green's function satisfying the hard-wall boundary conditions can be expressed as the infinite (m, n) eigen expansion (similar to Eq. 3.3) as:

$$\hat{G}_{\omega}\left(x|y\right) = \sum_{m=-\infty}^{\infty} \sum_{n=1}^{\infty} \mathring{A}_{mn}\left(y_{s},\omega\right) \psi_{mn}\left(r\right) e^{j\kappa_{mn}\left(z-z_{s}\right)} e^{jm\theta},\tag{3.13}$$

where  $y_s = (r_s, \theta_s)$ . The above equation assumes that the waveguide is infinitely long (no end reflections). Thus, the modal propagation from the source will be unidirectional such that  $z - z_s < 0$  corresponds to the upstream propagation and  $z - z_s > 0$  corresponds to the downstream propagation. The mode amplitude due to a monopole source at  $y_s = (r_s, \theta_s)$  is expressed as (Glegg and Devenport (2017)):

$$\mathring{A}_{mn}\left(\mathbf{y}_{s},\omega\right) = \frac{j\psi_{mn}^{*}\left(r_{s}\right)e^{-jm\theta_{s}}}{2Sk\alpha_{mn}}.$$
(3.14)

Refer to Chapter 17 of Glegg and Devenport (2017) for a detailed and systematic derivation.

# 3.2 Non-uniform swirling flow in an annular duct

The rotating fan generates an azimuthal flow component in the intra-stage which cannot be neglected while studying the sound propagation. Mean flow measurements in the engine intra-stage (Kumar et al. (2023); Venkateswaran et al. (2024); Guérin et al. (2020)) have revealed comparable levels of the axial and swirling flows, with a relatively insignificant radial flow component. Thus, the modeling of the intra-stage section assumes an annular duct with only axial and azimuthal mean flow components (Mathews (2016); Posson and Peake (2013); Cooper and Peake (2005)) which are considered to be only radially varying with zero gradients in the axial and circumferential directions.

In the case of a uniform axial flow, the propagating unsteady disturbances can be classified as:

- (i) *acoustical waves*: these are pressure-dominated and attributed to the isentropic compression and expansion of the fluid element.
- (ii) *vortical waves*: these correspond to the unsteadiness in the vorticity that is convected with the mean flow. The vortical waves do not carry any pressure or density fluctuations.
- (iii) *entropy waves*: these manifest as wave patches of low and high density transported by the mean flow. They do not carry any pressure or velocity fluctuations.

For intra-stage purposes, we consider a homentropic base flow (so no entropy waves). The unsteady disturbances in a homentropic swirling flow (Posson and Peake (2013)) are classified into acoustic modes (sonic), nearly-convected modes (vortical waves), and the critical layer (continuous spectrum of purely convected non-modal perturbations). The hydrodynamic part comprises the nearly-convected modes and the critical layer, which group in the complex axial wavenumber plane (Maldonado (2016); Posson and Peake (2013); Heaton and Peake (2006)). The nearly-convected modes comprise a discrete set of modes related to the swirl in the mean flow and carry a small pressure component. These convect at a similar speed (although not the same) as the mean axial flow speed. The critical layer is a result of the non-uniformity in the mean flow. The contributions from the hydrodynamic part are present only in the downstream propagation and are smaller than those from the acoustic modes unless we go far too downstream of the source where the hydrodynamic part may grow unstable (Heaton and Peake (2006)). Since the intra-stage section is short, the contributions from the hydrodynamic part can be ignored, and the in-duct pressure field may be regarded as an infinite summation over the sonic modes.

Solving the acoustic propagation in a duct with non-uniform flow is not analytically straightforward since the resulting differential equation has variable coefficients (unlike the uniform axial flow case) and one must resort to sophisticated methods to find a solution. Cooper and Peake (2005) considered solving the homogeneous convected Helmholtz equation (no source terms) for a radially-varying axial and swirling flow in a rigid annular duct in the high-frequency (asymptotic) limit, which enabled the use of the WKB (Wentzel–Kramers–Brillouin) method to find an approximate solution. Their asymptotic analysis ( $ka \gg 1$ ) was solely restricted to the acoustic part ignoring any hydrodynamic contributions. We may note here that understanding the acoustic propagation and making noise predictions would consist of knowing both the eigenmodes, and Green's function. Posson and Peake (2013) developed an acoustic analogy for swirling flow in an annular duct by combining the linearised Euler equations into a sixth-order differential equation acting on the pressure perturbation. The eigenmodes,

and Green's function were numerically computed for the sixth-order linear operator. Later, Mathews and Peake (2017) extended the sixth-order analogy by computing the eigenmodes, and Green's function using high-frequency asymptotics and comparing their predictions against the numerical results (Posson and Peake (2013)).

The numerical procedure discussed in Posson and Peake (2013) and Mathews and Peake (2017) had been MATLAB-coded as a numerical solver named *GreenSwirl*, presently licensed by the University of Cambridge. Throughout this research, the numerical calculations of the eigenmodes, and pressure field in complex swirling flows have been performed using *GreenSwirl*. In the next section, we present the acoustic analogy in a swirling flow (Posson and Peake (2013); Mathews and Peake (2017)) with the corresponding numerical procedure summarized in Appendix B.

# 3.2.1 Acoustic analogy in a swirling flow

# 3.2.1.1 Swirling base flow

We consider the annular duct of Fig. 3.1a. The formulation is done in the dimensionless form with the values at the tip-radius (r=a) chosen as the reference. Therefore, all the distances are non-dimensionalized by the tip-radius, velocities by the speed of sound at the tip (c(a)), frequencies by c(a)/a, and time by a/c(a). The density is normalized by the mean density,  $\rho_0(a)$ , at the duct tip, and the pressure is normalized by  $\rho_0(a)c(a)^2$ . The dimensionless inner and outer wall radii are  $r_+ = h$  and  $r_+ = 1$ , respectively, with h being the hub-to-tip ratio. In the below equations, the dagger + on the subscript shall denote the dimensionless form of the variable. We split the inviscid total flow (underlined) into a steady base (mean) flow (superscripted by 0) plus small amplitude perturbations (superscripted by +) as:

$$\begin{pmatrix}
\underline{u}_{\dagger} \\
\underline{v}_{\dagger} \\
\underline{w}_{\dagger} \\
\underline{\rho}_{-\dagger} \\
p_{+}
\end{pmatrix} = \begin{pmatrix}
U_{\dagger}^{0} \\
V_{\dagger}^{0} \\
W_{\dagger}^{0} \\
\rho_{\dagger}^{0} \\
p_{\dagger}^{0}
\end{pmatrix} + \begin{pmatrix}
u_{\dagger}' \\
v_{\dagger}' \\
w_{\dagger}' \\
\rho_{\dagger}' \\
p_{\dagger}' \\
p_{\dagger}'
\end{pmatrix},$$
(3.15)

where  $(\underline{u}_{\dagger}, \underline{v}_{\dagger}, \underline{w}_{\dagger})$  are the total velocities along the  $(z, r, \theta)$  coordinates, respectively, with  $\underline{\rho}_{\dagger}$  and  $\underline{p}_{\dagger}$  being the total density and total pressure quantities, respectively. Note here that the normalized mean flow velocities  $(U_{\dagger}^0, V_{\dagger}^0, W_{\dagger}^0)$  would correspond to the mean flow Mach numbers along the respective coordinates. For a homentropic fluid

 $p'_{+}=c_{+}^{2}\rho'_{+}$ . We solve for the Euler equations (continuity of mass, momentum, and energy) considering a perfect gas as the working fluid:

$$\frac{\partial \underline{\rho}_{\dagger}}{\partial t_{\dagger}} + \nabla_{\dagger} \cdot \left(\underline{\rho}_{\dagger} \underline{u}_{\dagger}\right) = 0, \tag{3.16a}$$

$$\underline{\rho}_{+} \left( \frac{\partial \underline{u}_{+}}{\partial t_{+}} + \underline{u}_{+} \cdot \nabla_{+} \underline{u}_{+} \right) = \underline{\rho}_{+} \frac{d}{dt_{+}} \left( \underline{u}_{+} \right) = -\nabla_{+} \underline{p}_{+'}$$
 (3.16b)

$$\frac{d\underline{p}_{\dagger}}{dt_{\dagger}} = \frac{\Gamma\underline{p}_{\dagger}}{\rho_{+}} \frac{d\underline{\rho}_{\dagger}}{dt_{\dagger}} = c_{\dagger}^{2} \frac{d\underline{\rho}_{\dagger}}{dt_{\dagger}}, \tag{3.16c}$$

where  $\Gamma$  is the ratio of the specific heat capacities (taking the value of 1.4 for air),  $\underline{u}_{\dagger} = (\underline{u}_{\dagger}, \underline{v}_{\dagger}, \underline{w}_{\dagger})$ , and  $c_{\dagger}$  is the local (non-dimensional) isentropic sound speed. Combining the Eqns. 3.16a and 3.16c for mass continuity and isentropicity (energy), we obtain the combined mass and energy equation:

$$\frac{d\underline{p}_{\dagger}}{dt_{\dagger}} + \Gamma\underline{p}_{\dagger} \left( \nabla_{\dagger} \cdot \underline{\boldsymbol{u}}_{\dagger} \right) = 0. \tag{3.17}$$

We define the base flow as:

$$(U_{+}^{0}, V_{+}^{0}, W_{+}^{0}) = (M_{z}(r_{+}), 0, M_{\theta}(r_{+})), \qquad (3.18)$$

where the Mach numbers,  $M_z(r_{\dagger})$  and  $M_{\theta}(r_{\dagger})$ , are obtained from CFD calculations or measurements. In the presence of a homentropic swirling flow, the mean pressure, mean density, and sound speed exhibit radial variations as (Mathews and Peake (2017); Posson and Peake (2013)):

$$c_{+}^{2}(r_{+}) = c_{+}^{2}(1) - (\Gamma - 1) \int_{r_{+}}^{1} \frac{M_{\theta}^{2}(s)}{s} ds,$$
 (3.19a)

$$p_{+}^{0}(r_{+}) = \left[c_{+}^{2}(r_{+})\right]^{\frac{\Gamma}{(\Gamma-1)}},$$
 (3.19b)

$$\rho_{+}^{0}(r_{+}) = \left[c_{+}^{2}(r_{+})\right]^{\frac{1}{(\Gamma-1)}}.$$
(3.19c)

Eqns. 3.19a, 3.19b, and 3.19c reveal that from a knowledge of the swirling flow profile, the radial variation of the mean pressure, mean density, and sound speed can be evaluated.

### 3.2.1.2 Acoustic boundary condition

The inviscid flow assumption allows slip flow at the duct wall (no boundary layer). For modeling purposes, the effect of the boundary layer (vortex sheet) on the wall acoustic

impedance is accounted for using the standard Myers boundary condition (allowing for slip flow at the duct wall assuming a vanishingly thin boundary layer) as (Rienstra (2015); Mathews and Peake (2017))<sup>1</sup>:

$$v'_{+}.\hat{r} = \left(-j\omega_{+} + M_{z}(r_{+})\frac{\partial}{\partial z_{+}} + \frac{M_{\theta}(r_{+})}{r_{+}}\frac{\partial}{\partial \theta}\right) \frac{p'_{+}}{-j\omega_{+}Z_{+}(r_{+})}, \text{ for } r_{+} = \{h, 1\}, \qquad (3.20)$$

where  $\hat{r}$  is the unit outward normal on the duct surface (acting along the radial coordinate). For rigid ducts,  $Z_{\dagger} = \infty$  at  $r_{\dagger} = \{h, 1\}$ , which renders  $v'_{+}(h) = v'_{+}(1) = 0$ .

### 3.2.1.3 Evaluation of the eigenmodes, and Green's function

The Green's function is a fundamental solution to the acoustic propagation problem. It is the impulse response of the acoustic field. Therefore, evaluating the sound field in a ducted swirling flow necessitates a knowledge of the tailored Green's function, and the first step in computing the Green's function is to determine the allowed eigenmodes of the system.

Unlike the case of the uniform axial flow, the presence of the swirling flow (and the consequent non-uniform mean pressure and density distributions) no longer renders a simple second-order (Bessel's) differential equation to be solved. Therefore, for a swirling flow, the eigenmodes, and Green's function are computed numerically (Posson and Peake (2013); Mathews and Peake (2017)), with the corresponding numerical methods presented in Appendix B.1 and B.2, respectively. It is worth noting here that in a swirling flow, the eigenvalues computed are the modal axial wavenumbers  $\tau_{+}(=\kappa_{mn}a)$ , unlike the case of the uniform axial flow, where the combined radial-transverse wavenumbers (Eq. 3.4) are the eigenvalues of the problem. The predicted eigenvalues correspond to both the acoustic and hydrodynamic modes. *GreenSwirl* first predicts the continuous spectrum of critical layer by solving  $D_0/Dt_+=0$  (referring to Eqs. 3.22 & 3.23 below). The eigen values grouping close to the critical layer are identified as hydrodynamic and ignored. The acoustic modes comprise upstream and downstream components and therefore possess a symmetry, allowing their eigenvalues to be easily identified and retained.

The acoustic analogy in a swirling flow, considered in Mathews and Peake (2017); Posson and Peake (2013), consists of rearranging the linearised Euler equations into a single sixth-order linear differential equation on the pressure perturbation. The analogy is given as:

$$\mathbb{F}(p_{\dagger}') = \mathbb{S},\tag{3.21}$$

 $<sup>^{1}</sup>$ Masson et al. (2018) propose using a correction to the classical Ingard-Myers boundary condition in the presence of the swirling flow

where S is the source term accounting for the non-linear effects, viscosity effects, and rotor-stator geometry. The source term S can be referred from Posson and Peake (2013) and not stated here. The differential operator  $\mathbb{F}$  is defined as:

$$\mathbb{F} = \left(\frac{1}{c_{+}^{2}} \frac{D_{0}^{2}}{Dt_{+}^{2}} - \frac{\partial^{2}}{\partial z_{+}^{2}} - \frac{1}{r_{+}^{2}} \frac{\partial^{2}}{\partial \theta^{2}}\right) \mathcal{R}^{2} + \left(\frac{1}{r_{+}} \frac{D_{0}}{Dt_{+}} - \frac{dM_{z}}{dr} \frac{\partial}{\partial z_{+}} - \left(\frac{M_{\theta}}{r_{+}^{2}} + \frac{1}{r_{+}} \frac{dM_{\theta}}{dr_{+}}\right) \frac{\partial}{\partial \theta}\right) \mathcal{R}\mathcal{T} + \mathcal{R} \frac{D_{0}}{Dt_{+}} \frac{\partial}{\partial r_{+}} \mathcal{T} - \frac{D_{0}}{Dt_{+}} \left[2\frac{dM_{z}}{dr_{+}} \frac{\partial}{\partial z_{+}} \frac{D_{0}}{Dt_{+}} + 2\left(\frac{d}{dr_{+}} \left(\frac{M_{\theta}}{r}\right)\right) \frac{\partial}{\partial \theta} \frac{D_{0}}{Dt_{+}} + \frac{d\mathcal{U}_{\theta}}{dr_{+}}\right] \mathcal{T},$$

$$(3.22)$$

where

$$\frac{D_0}{Dt_{\dagger}} = \frac{\partial}{\partial t_{\dagger}} + M_z \frac{\partial}{\partial z_{\dagger}} + \frac{M_{\theta}}{r_{\dagger}} \frac{\partial}{\partial \theta}; \quad \mathcal{R} = \frac{D_0^2}{Dt_{\dagger}^2} + \mathcal{U}_{\theta};$$

$$\mathcal{T} = -\frac{D_0}{Dt_{\dagger}} \frac{\partial}{\partial r_{\dagger}} - \frac{2M_{\theta}}{r_{\dagger}^2} \frac{\partial}{\partial \theta} + \frac{M_{\theta}^2}{r_{\dagger}c_{\dagger}^2} \frac{D_0}{Dt_{\dagger}}; \quad \text{and} \quad \mathcal{U}_{\theta}(r_{\dagger}) = \frac{2M_{\theta}}{r_{\dagger}} \left(\frac{M_{\theta}}{r_{\dagger}} + \frac{dM_{\theta}}{dr_{\dagger}}\right).$$
(3.23)

We look for a Green's function,  $\hat{G}_{\omega}(x_{\dagger}|y_{\dagger})$ , which solves:

$$\mathbb{F}\left(\hat{G}_{\omega}(\mathbf{x}_{\dagger}|\mathbf{y}_{\dagger})e^{-j\omega t}\right) = \frac{1}{2\pi} \frac{D_{0}^{2}}{Dt_{+}^{2}} \mathcal{R}\left(\delta\left(\mathbf{x}_{\dagger} - \mathbf{y}_{\dagger}\right)e^{-j\omega t}\right). \tag{3.24}$$

Eq. 3.24 reduces to computing the Green's function for the convected wave equation for the limiting case of a uniform axial flow. As we consider an axisymmetric flow,  $\hat{G}_{\omega}(x_{\dagger}|y_{\dagger})$  is expressed as the Fourier series:

$$\hat{G}_{\omega}\left(\mathbf{x}_{\dagger}|\mathbf{y}_{\dagger}\right) = \frac{1}{4\pi^{2}} \sum_{m=-\infty}^{\infty} \mathcal{G}_{m} e^{jm(\theta-\theta_{s})},\tag{3.25}$$

with the spinning mode amplitude,  $G_m$ , expressed as the Fourier integral over the domain of axial wavenumber ( $\tau_{+}$ ) as (Posson and Peake (2013); Mathews and Peake (2017)):

$$G_{m} = \int_{-\infty}^{\infty} g_{m} \left( r_{\dagger} | r_{\dagger}^{s}; \tau_{\dagger}, \omega \right) e^{j\tau_{\dagger}(z_{\dagger} - z_{\dagger}^{s})} d\tau_{\dagger}, \tag{3.26}$$

where  $r_+^s$  and  $z_+^s$  are respectively the non-dimensional radial and axial coordinates of the single monopole source, and  $g_m$  solves a second-order ordinary differential equation (refer to Eq. B.8 in B.2). Note that the factor of  $(4\pi^2)$  in the denominator of Eq. 3.25 arises due to the Fourier transformation from the temporal and axial coordinates. It may be noted that the eigenmodes occur as the poles of  $g_m$  such that by Cauchy's residue theorem the integral over the domain of axial wavenumbers reduces to the conventional summation over the radial indices as (Posson and Peake (2013); Mathews and Peake (2017)):

$$\mathcal{G}_{m} = \int_{-\infty}^{\infty} g_{m} (r_{+} | r_{+}^{s}; \tau, \omega) e^{j\tau_{+}(z_{+}-z_{+}^{s})} d\tau_{+} 
= (2\pi j) \sum_{n} \operatorname{Res} \left( g_{m} (r_{+} | r_{+}^{s}; \tau_{+}(n), \omega) e^{j\tau_{+}(n)(z_{+}-z_{+}^{s})} \right),$$
(3.27)

*GreenSwirl* computes the eigenmodes  $\tau_{+} = \tau_{mn}$ , and the residue of Eq. 3.27 numerically using the Chebfun (Driscoll et al. (2014)) in MATLAB, which is an open-source package and an integral part of the solver. The calculations in the swirling flows, reported in Chapters 4-8, are performed using the *GreenSwirl* solver.

# 3.3 Rigid body swirl model for acoustic propagation in a swirling flow

The *rigid body swirl* (RBS) model assumes a 2-D flow comprised of a rigid body rotation and a uniform axial flow. The modal propagation here is studied in a coordinate system rotating with the fluid such that the relative circumferential phase speed of a (m, n) mode will be:

$$\frac{\omega_{\epsilon}a}{m} = \frac{\omega a}{m} - a\Omega,\tag{3.28}$$

$$\implies \omega_{\epsilon} = \omega - m\Omega,$$
 (3.29)

where  $\omega_{\epsilon}$  is the Doppler-shifted radian frequency, and  $\Omega$  is the uniform angular velocity of the fluid rotation. Eq. 3.29 implies that for an absolute frequency,  $\omega$ , in the stationary duct-fixed reference frame, each mode propagates at a Doppler-shifted frequency,  $\omega_{\epsilon}$ , in the rotating reference frame depending upon its m-order. The corresponding modal axial wavenumbers would then be derived as:

$$\kappa_{mn}^{\pm} = \frac{-k_{\epsilon} M_z \pm \sqrt{k_{\epsilon}^2 - \zeta_{mn}^2 \beta^2}}{\beta^2},$$
(3.30)

where  $k_{\epsilon}(=\omega_{\epsilon}/c)$  is the Doppler-shifted acoustic wavenumber related to the free-space acoustic wavenumber as:

$$k_{\epsilon} = \frac{\omega_{\epsilon}}{c} = k \left( 1 - \frac{m\Omega}{\omega} \right) = k \left( 1 - \epsilon_m \right),$$
 (3.31)

where  $\epsilon_m$  is defined here as the relative phase shift and is a comprehensive parameter encapsulating the swirl velocity, azimuthal number, and absolute propagation frequency. Eq. 3.30 may be further simplified to yield a Doppler-shifted linear relation between  $\zeta_{mn}$  and  $\alpha_{mn}$  as:

$$\zeta_{mn} = (1 - \epsilon_m) \frac{-M_z + \alpha_{mn}}{\beta^2},\tag{3.32}$$

where  $\alpha_{mn}=\pm\sqrt{1-\frac{\varsigma_{mn}^2\beta^2}{k_c^2}}$  is the modal cut-on ratio calculated using  $\omega_{\epsilon}$ . It may therefore be understood that depending upon the value of  $\omega_{\epsilon}$ , a (m,n) mode cut-off in an ideal uniform axial flow may be acoustically cut-on in a swirling flow and vice-versa. For non-uniform fluid rotation, the results are generalized to uniform fluid rotation by defining an averaged angular velocity  $(\overline{\Omega})$  as:

$$\overline{\Omega} = \frac{\int_r \Omega(r) r^3 dr}{\int_r r^3 dr},\tag{3.33}$$

which corresponds to the angular momentum average of  $\Omega(r)$  if the mean density were uniform (Morfey (1971a)). The radially varying axial flow may be approximated by a plug flow of area-averaged axial Mach number  $(\overline{M_z})$ , which is not a major approximation considering that the typical mean flow profiles in an intra-stage reveal an almost radially uniform axial flow component (refer to Chapter 4).

Morfey (1971a) suggests that for subsonic rotation with:

$$\overline{\Omega} \ll \omega$$
 (3.34)

the modal cut-on frequencies, relative to the mean swirl  $(\overline{\Omega})$ , can be sufficiently predicted using the Doppler-frequency correction. The same condition also ensures the continuity of acoustic energy and Morfey (1971a) extends the RBS model to show that the mean swirl  $(\overline{\Omega})$  simply alters the classical modal power expression in a uniform axial flow by a multiplicative factor of  $(\omega/\omega_{\varepsilon})$ . We may note that the simplistic RBS model ignores the radial variations in the mean density, mean pressure, and sound speed, and also the coupling between the unsteady pressure (acoustics) and vorticity fields. Simply put, the foregoing analytical approximation inherently assumes that at a Doppler-shifted frequency, the sound propagates relative to the mean swirl in the same way as in a non-rotating uniform axial flow.

# 3.3.1 Suitability of the rotating coordinate approximation

Studying the modal propagation in a rotating coordinate is a fairly reasonable approach since it is comprehensible that the sound pressures and wavelengths (thus the wavenumbers) remain the same in both the moving and fixed reference frames with the frequency alone being appropriately Doppler-shifted in the former. Evidence of this phenomenon is in the understanding of the *rotor-alone* fan tones of Sec. 1.3.1.1 where we noted that the stationary pressure field in the rotor frame of reference is manifested as temporal variations in the stationary duct-fixed reference frame at integer multiples of

the BPF. However, in the case of a homentropic uniform flow, the acoustic and vortical disturbances are rigorously separated unlike with the swirling flow, where the two are coupled because of the Coriolis and Centrifugal forces induced by the mean swirling flow (Posson and Peake (2013)). In this respect, the Doppler-frequency correction is not exact and can incur potential errors when applied to realistic non-uniform swirling flow profiles typically encountered in the engine intra-stage (Posson and Peake (2013)).

However, our primary objective with the RBS model is not to approximate the eigenvalue calculations but rather employ it to understand the modal physics in swirling flows. The analytical nature of the model enables us to develop simple utilitarian expressions and physical interpretations - the accuracy and suitability of which can be investigated and verified via exact numerical calculations using *GreenSwirl*. Appendix C compares the analytical estimations of the RBS model against the corresponding *GreenSwirl* calculations for idealized cases of uniform axial flow accompanied by a rigid body swirl. We may observe that the analytical approximation is reasonably accurate in its predictions of the total number of cut-on modes, modal wavenumbers (i.e.: the axial and azimuthal wavenumbers), radial mode shape variation ( $\psi_{mn}(r)$ ), and modal pressure amplitudes, which gives confidence in employing the RBS model to derive valuable physical insights concerning the general characteristics of the modal distributions in swirling flows.

# **Chapter 4**

# Fan broadband noise characterization using engine intra-stage measurements

This chapter is concerned with the noise measurements made in the intra-stage region to characterize the broadband noise due to the fan and OGV. These measurements will allow a qualitative understanding of the broadband sound field aimed at improved liner design, obtaining an estimation of the balance between fan and OGV noise, and developing low-fidelity noise prediction models. Intra-stage noise measurements from three turbofan rigs, namely the NASA Fan Noise Source Diagnostic Test (NASA SDT), the ACAT1 fan investigated in the EU project TurboNoiseBB, and the Rolls-Royce LSF (low speed fan for research) will be analyzed in detail to extract the general behavior of the broadband sound field. In particular, we aim to:

- Propose new quantities for characterizing the distinct modal structure of the broadband sound field generated in the engine intra-stage by the rotor and OGV.
- Interpret the modal broadband sound field in terms of basic equations of sound generation in flow ducts.
- Illustrate the existence of the modal overlap region in which different upstream
  and downstream propagating modes share the same axial wavenumber, leading
  to ambiguity in mode detection methods.
- Investigate the relative dominance of the fan and OGV BB noise sources.
- Investigate the suitability of a point source model for the engine intra-stage that can generate near-identical broadband noise characteristics to the measured noise from the rotor and OGV, which is useful for the development of source location techniques, liner design, and low-fidelity noise prediction models.

# 4.1 Characterizing the broadband intra-stage sound field

We first review the basic equations governing the sound generation in ducts with arbitrary swirling flow profiles due to a point force, which will form the basis of the noise metrics proposed in Sec. 4.2 below and assist in the interpretation of the measured modal spectra presented in Secs. 4.6, 4.7, and 4.8. The simple model presented below assumes that the dominant sources of broadband noise are generated by the unsteady blade loading at the rotor trailing edges and OGV leading edges. The former is the result of the scattering of the turbulent boundary layer convecting past the trailing edge, while the latter is the result of rotor wake turbulence impinging upon the OGV leading edge.

# 4.1.1 Modal propagation in the intra-stage duct

The fluctuating forces at the fan and OGV could be appropriately represented by dipole sources as shown in Fig. 4.1 below.

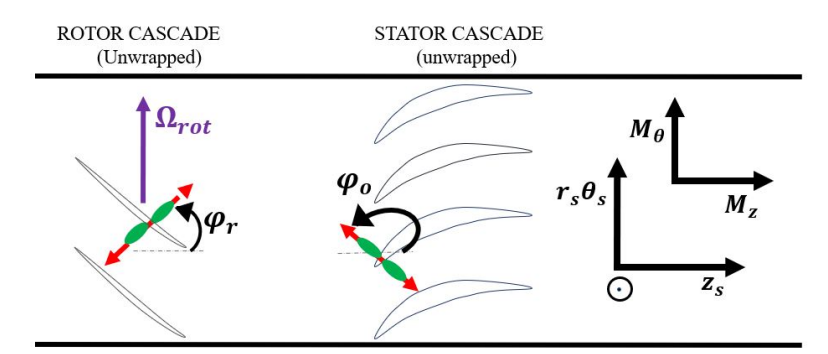


FIGURE 4.1: Schematic of the engine intra-stage carrying a 2-*D* flow field with unwrapped cascades of the fan and OGV with the fluctuating loading represented by singular dipole sources of appropriate orientation relative to the engine axis.

A dipole source with complex source strength  $\hat{f}(\omega)$  located at  $y = (z_s, r_s, \theta_s)$  from some origin and oriented in the  $z - \theta$  plane at an angle  $\varphi$  to the duct axis has the unit vector  $\hat{n}(y)$  with components,  $\hat{n}(y) = [\hat{z}_s, \hat{r}_s, \hat{\theta}_s] = [\cos\varphi, 0, \sin\varphi]$ . The pressure field at position x in the duct due to the point dipole source can then be calculated from:

$$p^{\pm}(\mathbf{x},\omega) = \hat{f}(\omega)\hat{\mathbf{n}}(\mathbf{y}).\nabla_{s}\left(\hat{G}_{\omega}^{\pm}(\mathbf{x}|\mathbf{y})\right), \tag{4.1}$$

where  $\nabla_s = \hat{z}_s \partial/\partial z_s + (\hat{\theta}_s/r_s)\partial/\partial \theta_s$  and  $\hat{G}^{\pm}_{\omega}(x|y)$  is the Green's function for the duct, which can be expressed as a summation over azimuthal modes of order m and radial modes of order n,  $\hat{G}^{\pm}_{\omega}(x|y) = \sum_{m=-\infty}^{\infty} \sum_{n=-\infty}^{\infty} \hat{G}^{\pm}_{mn}(x|y)$ , where the modal basis functions may be expressed following Eq. 3.13 as:

$$\hat{G}_{mn}^{\pm}(\boldsymbol{x}|\boldsymbol{y}) = \mathring{A}_{mn}^{\pm}(\omega)\psi_{mn}^{\pm}(r)e^{jm\theta}e^{j\kappa_{mn}^{\pm}z}.$$
(4.2)

4.2. Noise metrics 45

Following differentiation, the dependence of the dipole angle on the acoustic pressure can be made explicit,

$$p^{\pm}(\mathbf{x},\omega) = \sum_{m=-\infty}^{\infty} \sum_{n=1}^{\infty} \hat{f}(\omega) D_{mn}^{\pm}(\varphi) \hat{G}_{mn}^{\pm}(\mathbf{x}|\mathbf{y}), \tag{4.3}$$

where

$$D_{mn}^{\pm}(\varphi) = \left(\frac{-jm}{r_s}\right) \sin\varphi - j\kappa_{mn}^{\pm} \cos\varphi \tag{4.4}$$

is referred to here as the dipole directivity. For complex intra-stage swirling flows, the Green's function amplitudes, eigenfunctions  $\psi_{mn}^{\pm}(r)$ , and the eigenvalues  $\kappa_{mn}^{\pm}$  are computed using the numerical solver, *GreenSwirl*, summarized in Sec. 3.2.1.

# 4.1.2 Equivalent point source model for rotor and stator noise

The theory outlined in section 4.1.1 above describes the underlying theory for sound generation due to a point dipole source. However, in practice broadband noise in the engine duct is generated by a continuous distribution of sources along the rotor trailing edge and stator leading edge, with a particular correlation length. In this chapter, we demonstrate using measured noise data that the relative mode amplitude distributions due to the fan and OGV can be reproduced, to good accuracy, by a single point dipole source located at two-thirds the annular radius,  $r_{2/3} = b + 2/3(a - b)$ , with orientation  $\varphi_r$  and  $\varphi_0$  normal to the metal angles of the rotor blade twist and OGV leading edge angle, respectively, as sketched in Fig. 4.10 in Sec. 4.6.2. Evidence to support this simplification is presented in Appendices D and E. This single-source representation will be used to provide greater insight into the sound field. We note that in this equivalent point force model we assume that the rotor generates only downstream-traveling modes while the OGV generates only upstream-traveling modes and hence modal scattering from the rotor and OGV is ignored.

# 4.2 Noise metrics

In this section, we introduce four metrics that characterize different aspects of the modal distribution of the broadband sound field generated in the engine intra-stage. We now introduce the hypothesis that in the high-frequency limit (ka>10) the broadband noise cross-spectral density  $E\left[p(x_a,\omega)p^*(x_a',\omega)\right]$  between any two points on the wall of the engine duct,  $x_a=(z,a,\theta)$  and  $x_a'=(z',a,\theta')$ , can be separated into the product of a frequency pressure spectral density  $\overline{p^2}(\omega)$  at the duct wall and a non-dimensional frequency-independent factor  $\eta\left(x_a,x_a'\right)$  that quantifies the relative spatial

cross-spectrum of the sound field, i.e.,

$$\lim_{T \to \infty} \frac{1}{T} E[p(\mathbf{x}_a, \omega) p^*(\mathbf{x}'_a, \omega)] = \overline{p^2}(\omega) \eta(\mathbf{x}_a, \mathbf{x}'_a), \tag{4.5}$$

such that

$$\eta(x_a, x_a') = \lim_{T \to \infty} \frac{1}{T} E[\hat{p}(x_a, \omega) \hat{p}^*(x_a', \omega)], \tag{4.6}$$

where  $E[\ ]$  denotes the expectation, T is the time duration (periodogram length) over which the Fast Fourier transform (FFT) of the pressure time series is performed,  $\hat{p}(x_a) = p(x_a,\omega)/\sqrt{\overline{p^2}(\omega)}$ , and  $\eta(x_a=x_a')=1$ , with  $\overline{p^2}(\omega)$  assumed to be independent of position on the duct wall. The four metrics proposed below therefore aim to characterize  $\eta(x_a,x_a')$ , which we shall demonstrate are normalized functions in terms of their modal

components  $a_m$  and  $a_{mn}$  at the duct wall such that  $\hat{p}(x_a, \omega) = \sum_{m=m_{min}(\omega)}^{m_{max}(\omega)} a_m(\omega) e^{jm\theta}$  with

 $a_m = \sum_n a_{mn} e^{j\kappa_{mn}z}$ , wherein we restrict each summation to only cut-on acoustic modes.  $a_{mn}$  is related to the pressure mode amplitudes  $A_{mn}$  defined in Eq. 2.2 above by:

$$a_{mn} = \frac{A_{mn}\psi_{mn}(a)}{\sqrt{\overline{p^2}(\omega)}}. (4.7)$$

Evidence to support the separability hypothesis of Eq. 4.5 is provided below in Sec. 4.3. This factorization follows from the form of Eq. 4.3 for the acoustic pressure due to a point force in which the frequency and spatial dependence of the sound field may be separated. At high frequencies, the spatial variation of the sound field tends to an asymptotic limit that is weakly dependent on frequency. This separability assumption is implicitly assumed in the mode distribution proposed by Rice (1978) and, more recently in an experimental study by Melling et al. (2017).

# **4.2.1** Normalized mean squared spinning mode amplitude, $\overline{a_m^2}(\omega)$

We first consider the decomposition of the non-dimensional pressure cross spectrum  $\eta\left(x_a, x_a'\right)$  at the duct wall into its mean square spinning modal components  $a_m$ . At a single axial position, z = z',  $\eta\left(x_a, x_a'\right)$  at the duct wall is of the form

$$\eta\left(\mathbf{x}_{a}, \mathbf{x}_{a}^{\prime}\right) = \sum_{m=m_{min}(\omega)}^{m_{max}(\omega)} \sum_{m^{\prime}=m_{min}(\omega)}^{m_{max}(\omega)} E\left[a_{m}(\omega)a_{m^{\prime}}^{*}(\omega)\right] e^{j(m\theta-m^{\prime}\theta^{\prime})},\tag{4.8}$$

where  $a_m$  is the non-dimensional spinning mode pressure amplitude. For the idealized case in which the spinning mode amplitudes are uncorrelated, i.e.  $E\left[a_m(\omega)a_{m'}^*(\omega)\right] = \overline{a_m^2}(\omega)\delta_{mm'}$ ,

4.2. Noise metrics 47

$$\eta\left(x_{a}, x_{a}'\right) = \sum_{m=m_{min}(\omega)}^{m_{max}(\omega)} \overline{a_{m}^{2}}(\omega) e^{jm(\theta-\theta')}$$
(4.9)

The normalization property  $\eta(x_a = x_a') = 1$  applied to the above equation yields the normalization condition:

$$\sum_{m=m_{min}(\omega)}^{m_{max}(\omega)} \overline{a_m^2}(\omega) = 1.$$
(4.10)

In the general case of correlated modes, the cross-spectrum of mode amplitudes  $E\left[a_m(\omega)a_{m'}^*(\omega)\right]$ , and hence  $\overline{a_m^2}(\omega)$ , can be obtained by direct inversion of Eq. 4.8,

$$E[a_m(\omega)a_{m'}(\omega)] = N^{-2} \sum_{l=1}^{N} \sum_{s=1}^{N} e^{-jm\theta_l} \eta(\theta_l, \theta_s) e^{jm'\theta_s}. \tag{4.11}$$

Modal distributions that depict the mean squared spinning mode amplitudes across frequencies,  $\overline{A_m^2}(\omega) = \overline{p^2}(\omega)\overline{a_m^2}(\omega)$ , are conventionally called as *Joppa* plots. The modal distribution,  $\overline{a_m^2}(\omega)$ , may be regarded as a non-dimensional and normalized *Joppa* plot and has the advantage that it focuses on the relative (not absolute) mode decomposition of the sound field at a given frequency.

# **4.2.2** Relative modal split, $\sigma_{\pm m}(\omega)$

The second metric quantifies the ratio of the mean squared pressure at the duct wall associated with the co- and counter-rotating modes, to the mean square pressure  $\overline{p^2}(\omega)$  due to all propagating modes. The relative modal split is estimated separately for the rotor (+) and OGV (-) noise, and is obtained for the co-rotating modes,  $\sigma^{\pm}_{+m}(\omega)$ , and contra-rotating modes,  $\sigma^{\pm}_{-m}(\omega)$ , as:

$$\sigma_{+m}^{\pm}(\omega) = \sum_{m>0} \overline{a_m^2}^{\pm}(\omega); \quad \sigma_{-m}^{\pm}(\omega) = \sum_{m<0} \overline{a_m^2}^{\pm}(\omega), \tag{4.12}$$

such that  $\sigma_{+m}^{\pm}(\omega) + \sigma_{-m}^{\pm}(\omega) = 1$  is separately satisfied for the upstream and down-stream propagations. This metric, as a function of frequency, will be shown to be highly sensitive to the effective dipole orientation  $(\varphi_r/\varphi_o)$ . It will, therefore, exhibit different behavior for the rotor and OGV and can, therefore, help in source diagnostics.

# **4.2.3** Normalized mean squared spinning mode amplitude distribution, $\overline{a^2}(\gamma)$

In this section, we propose a new metric that aims to decompose the normalized pressure cross spectrum  $\eta(x_a, x_a')$  at the wall into its normalized transverse wavenumber components,  $\gamma = m/ka$ . The rationale for this decomposition is (i) the mean squared

mode amplitude spectrum  $\overline{a^2}(\gamma)$  collapses asymptotically with increasing frequency ka, (ii) it is sensitive to the dipole orientation and is therefore useful in source diagnostics, (iii)  $1/\gamma$  corresponds to the circumferential phase speed of the mode normalized on the free space sound speed, and (iv)  $\gamma$  tends to the transverse propagation angle in the low Mach number limit (Rice et al. (1979)). The first point follows automatically from the separability assumption of Eq. 4.6.

At a single frequency, following Eq. 2.1, the non-dimensional acoustic pressure  $\hat{p}(x_a, \omega)$  at the duct wall is expressed as the Fourier sum of the circumferential duct modes with phase  $e^{jm\theta}$ . This modal expansion may be re-written in terms of the new variables,  $\gamma_m = m/ka$  and  $\hat{\theta} = ka\theta$  as the new conjugate pairs, and hence,

$$\hat{p}(\theta_i) = \sum_{m=m_{min}}^{m_{max}} a_m(\omega) e^{jm\theta} = \sum_{m=m_{min}}^{m_{max}} a_{\gamma_m}(\omega) e^{j\gamma_m \hat{\theta}}.$$
 (4.13)

The non-dimensional wavenumber  $\gamma_m = m/ka$  may also be expressed as  $\gamma_m = cm/\omega a$ . Noting that  $\omega a/m$  is the circumferential phase speeds of the spinning mode,  $\gamma_m$  also has the alternative interpretation as the inverse of the non-dimensional spinning mode phase speed.

Note that in a non-swirling flow, the range of propagating modes is nearly characterized by  $-1 \le \gamma_m \le 1$ . However, this condition is violated in a swirling flow with a greater cut-on range for the contra-rotating modes. Nevertheless, the propagating range of  $\gamma$  is bounded within limits,  $[\gamma_{min}, \gamma_{max}]$ , which are found to converge asymptotically in the high-ka limit,  $ka \to \infty$ . Therefore, at suitably high frequencies, the discrete summation of Eq. 4.10 may be approximated by the integration over a continuum of modes as follows:

$$\sum_{m=m_{min}(\omega)}^{m_{max}(\omega)} \overline{a_m^2}(\omega) = \frac{\sum_{m=m_{min}(\omega)}^{m_{max}(\omega)} \overline{A_m^2}(\omega)}{\overline{p^2}(\omega)} = 1,$$
(4.14)

where  $\overline{A_m^2}(\omega)$  is the dimensional azimuthal modal spectra predicted by the discrete inverse Fourier Transform of the wall pressures as:

$$\overline{A_m^2}(\omega) = \overline{p^2}(\omega) N^{-2} \sum_{l=1}^N \sum_{s=1}^N e^{-jm\theta_l} \eta(\theta_l, \theta_s) e^{jm\theta_s}. \tag{4.15}$$

In the high-*ka* limit, following the change of variables as in Eq. 4.13, Eq. 4.14 would become:

$$\frac{\sum_{m=m_{min}(\omega)}^{m_{max}(\omega)} \overline{A_m^2(\omega)}}{\overline{p^2(\omega)}} = N_m(\omega) \int_{\gamma_{min}}^{\gamma_{max}} \frac{\overline{A_{\gamma_m}^2}}{\overline{p^2(\omega)}} f(\gamma_m) d\gamma_m = 1, \tag{4.16}$$

4.2. Noise metrics 49

where  $N_m(\omega)$  is the number of cut-on azimuthal mode orders at the analysis frequency, and  $f(\gamma)$  is the modal density of  $\gamma$  defined as,

$$f(\gamma) = \frac{1}{N_m(\omega)} \lim_{\Delta \gamma \to 0} \frac{N_m(\omega, \gamma + \Delta \gamma) - N_m(\omega, \gamma)}{\Delta \gamma},$$
(4.17)

which across the range of propagating modes between  $\gamma_{min}$  and  $\gamma_{max}$  is simply  $1/(\gamma_{max} - \gamma_{min})$  and satisfies  $\int_{\gamma_{min}}^{\gamma_{max}} f(\gamma) d\gamma = 1$ . From Eq. 4.16, we define  $\overline{a^2}(\gamma_m)$  as:

$$\overline{a^2}(\gamma_m) = \frac{\overline{A_{\gamma_m}^2}}{\overline{p^2}(\omega)/N_m(\omega)}$$
(4.18)

rendering it as a measure of the relative scale of the actual modal spectra,  $\overline{A_{\gamma_m}^2}$ , to the averaged modal spectra,  $\overline{p^2}(\omega)/N_m(\omega)$ . The frequency independence of the  $\overline{a^2}(\gamma)$  distribution is demonstrated using measured intra-stage noise data in Sec. 4.3, justifying the separability assumption of Eq. 4.5. We now aim to predict this  $\overline{a^2}(\gamma)$  distribution using the wall circular array.

In the high-frequency limit, the variables  $\gamma_m$  and  $\hat{\theta}$  may be treated as continuous. In terms of these two new variables, the pressure at  $\hat{\theta}$  may be expressed as the Fourier integral over  $\gamma$ ,

$$\hat{p}(\hat{\theta}) = \int_{-\infty}^{\infty} \hat{p}(\gamma) e^{j\gamma\hat{\theta}} d\gamma, \tag{4.19}$$

where  $\hat{p}(\gamma)$  is regarded as a continuous function of  $\gamma$  and is interpreted as the non-dimensional modal pressure in a unit  $\gamma$ -bandwidth. We may note that with this change of variables,  $\hat{p}(\hat{\theta})$  is not periodic like  $\hat{p}(\theta)$ . Therefore,  $\hat{p}(\gamma)$  is predicted at a desired value,  $\gamma = \gamma_b$ , by the inverse transform of a spatial block of N samples,  $\hat{p}(\hat{\theta}_e) = \left\{\hat{p}(\hat{\theta}_1), \hat{p}(\hat{\theta}_2), \ldots, \hat{p}(\hat{\theta}_N)\right\}$  for  $e = 1, 2, \ldots, N$ , at a given frequency ka as:

$$\hat{p}(\gamma_b) = \frac{1}{N} \sum_{e=1}^{N} \hat{p}(\hat{\theta}_e) e^{-j\gamma_b \hat{\theta}_e}.$$
(4.20)

For broadband noise, we are concerned with the time-averaged auto-spectra  $\overline{\hat{p}^2}(\gamma_b)$  obtained using the above equation as:

$$\overline{\hat{p}^2}(\gamma_b) = \lim_{T \to \infty} \frac{1}{T} E[\hat{p}(\gamma_b)\hat{p}^*(\gamma_b)] = \frac{1}{N^2} \sum_{e} \sum_{f} e^{-j\gamma_b \hat{\theta}_e} \eta(\hat{\theta}_e, \hat{\theta}_f) e^{j\gamma_b \hat{\theta}_f}, \tag{4.21}$$

where  $\eta(\hat{\theta}_e, \hat{\theta}_f) = \lim_{T \to \infty} \frac{1}{T} E\Big[\hat{p}(\hat{\theta}_e)\hat{p}^*(\hat{\theta}_f)\Big]$ . The predicted  $\gamma$ -spectrum is aliased at  $(\Delta \gamma)_{alias}$  intervals depending upon the sampling rate,  $\Delta \hat{\theta}_s = ka\Delta \theta_s$ , in the  $\hat{\theta}$  domain as:

$$\left(\Delta\gamma\right)_{alias} = \frac{2\pi}{ka\Delta\theta_s} = \frac{N}{ka'} \tag{4.22}$$

where  $\Delta\theta_s$  is the adjacent angular spacing between the circular microphones. A consequence of the finiteness in the  $\hat{\theta}$  domain is that the wavenumber resolution  $\Delta\gamma_b$  of the predicted  $\gamma$ -spectrum becomes:

$$\Delta \gamma_b = \frac{2\pi}{2\pi ka} = \frac{1}{ka}.\tag{4.23}$$

The upper limit  $\hat{\theta} = 2\pi ka$  is reduced in the use of partial arrays such as the semi-circular array used in the NASA SDT study described in Sec. 4.6. The wavenumber resolution for the estimate of  $\bar{p}^2(\gamma_b)$  therefore improves with increasing frequency. Incorporation of the high-ka approximation of Eq. 4.16 as well as the  $\Delta \gamma_b$  wavenumber resolution into Eq. 4.21 would result in:

$$\overline{\hat{p}^2}(\gamma_b)_{\Delta\gamma_b} \approx \int_{\gamma_{min}}^{\gamma_{max}} \overline{a^2}(\gamma) f(\gamma) \iota(\gamma, \gamma_b) d\gamma, \tag{4.24}$$

where  $\iota(\gamma,\gamma_b)=\left|\sum_{e=1}^N e^{j(\gamma-\gamma_b)\hat{\theta}_e}/N\right|^2$  is the response function of the inverse transform. We may note that the predicted  $\gamma$ -spectrum has been denoted in Eq. 4.24 as  $\overline{\hat{p}^2}(\gamma_b)_{\Delta\gamma_b}$  to indicate the  $\Delta\gamma_b$  bandwidth. We note here that  $\iota(\gamma,\gamma_b)$  attains the peak value of unity at  $\gamma=\gamma_b$  and decays sharply on either side. Therefore, the integration of Eq. 4.24 may be limited to within the  $\Delta\gamma_b$  bandwidth such that  $\overline{a^2}(\gamma)$  may be averaged out of the bandwidth as:

$$\overline{a^2}(\gamma_b) \approx \frac{\overline{\hat{p}^2}(\gamma_b)_{\Delta \gamma_b}}{\int_{\gamma_b - 0.5\Delta \gamma_b}^{\gamma_b + 0.5\Delta \gamma_b} f(\gamma) d\gamma}.$$
(4.25)

In practice, smooth estimates for the  $\gamma$ -spectrum can be obtained by averaging further over a broadband frequency range  $\Delta \omega = \omega_{max} - \omega_{min}$ ,

$$\langle \overline{a^2}(\gamma) \rangle_{\Delta\omega} = \frac{1}{\Delta\omega} \int_{\omega_{min}}^{\omega_{max}} \overline{a^2}(\gamma) d\omega.$$
 (4.26)

#### 4.2.3.1 Multi-frequency implementation

The method described above allows the estimation of  $\overline{p^2}(\gamma)$  based on the cross-spectrum at a single frequency of a number of microphones arranged circumferentially around the duct wall. An alternative implementation of Eq. 4.21 for the estimation of  $\overline{p^2}(\gamma)$  involves evaluating  $\eta$  ( $\hat{\theta}, \hat{\theta}'$ ) between just two microphones and integrating over frequency ka. In this two-microphone case, we assume that the pressures at different frequencies ka are uncorrelated, and also the pressures at the same frequency but at different  $\gamma$  values are uncorrelated resulting in  $\eta$  ( $\hat{\theta}, \hat{\theta}'$ ) =  $\eta$ ( $\Delta\hat{\theta}$ ) solely as a function of  $\Delta\hat{\theta} = ka\Delta\theta$ . The subsequent double summation over  $\hat{\theta}$  and  $\hat{\theta}'$  may therefore be reduced

4.2. Noise metrics 51

to a single integral over  $\Delta \hat{\theta}$  following the Wiener–Khinchin theorem (Battistelli (2021)),

$$\overline{\hat{p}^2}(\gamma_b) = \frac{1}{2\pi} \int_{-\infty}^{\infty} \eta \left(\Delta \hat{\theta}\right) e^{j\gamma_b \Delta \hat{\theta}} d(\Delta \hat{\theta}) \tag{4.27}$$

where the integration over  $\Delta \hat{\theta}$  is achieved by integrating across frequencies using the result  $d(\Delta \hat{\theta}) = 2\pi a \Delta \theta df/c$ .

As with the single-ka case, the mode amplitude distribution across  $\gamma$ ,  $\overline{a^2}(\gamma)$ , is related to the predicted mean squared pressure spectrum,  $\overline{\hat{p}^2}(\gamma)$ , as per Eq. 4.24. However, the response function  $\iota(\gamma, \gamma_b)$  in the multi-ka case reduces to the  $\delta$  function as:

$$\iota(\gamma, \gamma_b) = \frac{1}{2\pi} \int_{-\infty}^{\infty} e^{-j\Delta\hat{\theta}(\gamma - \gamma_b)} d(\Delta\hat{\theta}) = \delta(\gamma - \gamma_b), \qquad (4.28)$$

resulting in

$$\overline{a^2}(\gamma_b) = \frac{\overline{\hat{p}^2}(\gamma_b)}{f(\gamma_b)}.$$
(4.29)

Comparison between the predictions of  $\overline{a^2}(\gamma)$  obtained from both formulations of Eqs. 4.25 and 4.29 have indicated that the former approach provides a smoother estimate for  $\overline{a^2}(\gamma)$  since it involves the cross-spectrum from a larger number of microphones and therefore allows for better rejection of the high-frequency flow noise as well as ignoring the low-frequency hydrodynamic noise. Measurements of  $\overline{a^2}(\gamma)$  presented below will be based on the single frequency formulation of Eq. 4.21.

We may additionally note that the normalization condition of  $\overline{a^2}(\gamma)$ , as governed by Eqs. 4.16 and 4.18, is also satisfied following Parseval's theorem for discrete and continuous transforms,

$$\int_{-\infty}^{\infty} \overline{\hat{p}^2}(\gamma) d\gamma = \frac{1}{N} \sum_{e=1}^{N} \overline{\hat{p}^2}(\hat{\theta}_e) = \frac{1}{2\pi} \int_{-\infty}^{\infty} \eta(\Delta \hat{\theta}) d\Delta \hat{\theta} = 1.$$
 (4.30)

### 4.2.4 Normalized mean squared mode amplitude distribution, $\overline{a^2}(\zeta)$

The broadband noise metrics proposed in Secs. 4.2.1, 4.2.2, and 4.2.3 above relate to the behaviour of the sound field in the transverse  $r-\theta$  plane. This fourth noise metric relates to the behaviour of the sound field axially along the duct in the r-z plane. It specifies the distribution of the mean squared non-dimensional mode amplitude  $\overline{a^2}(\zeta_{mn}^\pm)$  as a function of the normalized modal axial wavenumber  $\zeta_{mn}=\kappa_{mn}/k$ . As with the high-frequency limiting approach adopted in the third metric, we treat  $\zeta$  as a continuous variable.

The rationale for the decomposition of the modal amplitudes in terms of  $\zeta$  is: (i) the mean squared mode amplitude spectrum  $\overline{a^2}(\zeta)$  collapses asymptotically in the high-frequency limit,(ii)  $\zeta$  corresponds to the axial phase speed of the mode normalized on the free space sound speed, (iii)  $\zeta$  can be used to distinguish upstream and downstream propagating duct modes, (iv) it tends to the cosine of the modal axial propagation angle in the low Mach number limit (Rice et al. (1979)).

Substitution of  $a_m(\omega) = \sum_n a_{mn}(\omega) e^{j\zeta_{mn}kz}$  into Eq. 4.13 renders a new modal expansion in terms of  $\hat{z} = kz$  and  $\zeta_{mn}$  pairs as follows:

$$\hat{p}(\hat{z}) = \sum_{m=m_{min}(\omega)}^{m_{max}(\omega)} \sum_{n=1}^{n_{max}(m,\omega)} a_{mn}(\omega) e^{jm\theta} e^{j\zeta_{mn}\hat{z}}, \tag{4.31}$$

which following the assumption of incoherent duct modes gives a mean squared value of

$$\overline{\hat{p}^2}(\hat{z}) = \sum_{m,n} \overline{a_{mn}^2}(\omega) = 1. \tag{4.32}$$

Substitution of Eq. 4.7 into Eq. 4.32 yields,

$$\frac{\sum_{m,n} \overline{A_{mn}^2}(\omega) \psi_{mn}^2(a)}{\overline{p^2}(\omega)} \approx \frac{\sum_{m,n} \overline{A_{mn}^2}(\omega)}{\overline{p^2}(\omega) / \langle \psi_{mn}^2(a) \rangle_{mn}} \approx 1, \tag{4.33}$$

where  $\langle \psi_{mn}^2(a) \rangle_{mn} = \sum_{m,n} \psi_{mn}^2(a)/N_\omega$  with  $N_\omega$  being the total number of cut-on modes at the analysis frequency. It may be easily shown that  $\sum_{m,n} \overline{A_{mn}^2}(\omega)$  is the mean squared pressure averaged across the duct cross-section, and therefore  $\langle \psi_{mn}^2(a) \rangle_{mn}$  is the ratio of the mean squared pressure at the duct wall to the area-averaged mean squared pressure, as shown by Joseph et al. (2003).  $\langle \psi_{mn}^2(a) \rangle_{mn}$  is roughly constant across frequencies, and following Joseph et al. (2003), we take  $\langle \psi_{mn}^2(a) \rangle_{mn} \approx 2$ .

In the high-ka limit,  $\hat{z}$  and  $\zeta$  may be treated as continuous variables, and therefore the double summation over the (m, n) modal indices in Eq. 4.33 may be approximated by a single integral over the propagating range of  $\zeta$ , similar to Eq. 4.16 as:

$$N_{\omega} \int_{\zeta_{min}}^{\zeta_{max}} \frac{\overline{A^2}(\zeta)}{\overline{p^2}(\omega)/\langle \psi_{2...}^2(a)\rangle_{min}} f(\zeta) d\zeta = 1, \tag{4.34}$$

where the cut-on bounds,  $\left[\zeta_{min},\zeta_{max}\right]$  converge asymptotically across frequencies, similar to the  $\gamma$ -distribution, and  $f(\zeta)$  is the modal density function in  $\zeta$  such that  $\int_{\zeta_{min}}^{\zeta_{max}} f(\zeta) d\zeta = 1$ . Using Eq. 4.34, we define  $\overline{A^2}_s = N_\omega^{-1} \overline{p^2}(\omega)/\langle \psi_{mn}^2(a)\rangle_{mn}$  as the modal average of the area-averaged pressure spectra. Hence, a simplified form of Eq. 4.34 can be used to

4.2. Noise metrics 53

define  $\overline{a^2}(\zeta)$  as:

$$\overline{a^2}(\zeta) = \frac{\overline{A^2}(\zeta)}{\overline{A^2}_s},\tag{4.35}$$

rendering it as a measure of the relative scale of the actual modal spectra,  $\overline{A^2}(\zeta)$ , to the modal average,  $\overline{A^2}_s$ , similar to the  $\overline{a^2}(\gamma)$  distribution defined in Eq. 4.18. The frequency independence of the  $\overline{a^2}(\zeta)$  modal distribution follows from the frequency independence of the  $\overline{a^2}(\gamma)$  distribution demonstrated in Sec. 4.3 below.

Following the arguments presented above for the  $\gamma$ -distribution and referring to Eq. 4.31, we may infer that the  $\overline{a^2}(\zeta)$  distribution may be predicted using the wall pressure information along the axial coordinate by the inverse transform of (i) the pressures sensed at an axial array of microphones,  $\hat{p}(\hat{z}_i)$  for  $i=1,2,\ldots,n_a$  at a single frequency, or (ii) the non-dimensional cross-spectrum,  $\eta(\Delta \hat{z})$  between any two pairs of axial microphones over a broad frequency range. Below, we present the multi-ka approach to predict the  $\overline{a^2}(\zeta)$  distribution.

Referring to Eq. 4.31, assuming uncorrelated duct mode amplitudes, the non-dimensional cross spectrum  $\eta$  ( $x_a$ ,  $x'_a$ ) of Eq. 4.6 between two axially spaced sensors at locations z and z' at the duct wall r = a is given by,

$$\eta\left(\mathbf{x}_{a}, \mathbf{x}_{a}^{\prime}\right) = \sum_{m=m_{min}(\omega)}^{m_{max}(\omega)} \sum_{n=1}^{n_{max}(m,\omega)} \overline{a_{mn}^{2}}(\omega) e^{-j\zeta_{mn}\hat{\omega}},\tag{4.36}$$

where  $\hat{\omega} = k(z'-z)$ . Eq. 4.36 on adopting the high-ka approximation would become,

$$\eta(\hat{\omega}) = \int_{\zeta_{min}}^{\zeta_{max}} \overline{a^2}(\zeta) f(\zeta) e^{-j\zeta\hat{\omega}} d\zeta, \tag{4.37}$$

Eq. 4.37 for  $\eta(\hat{\omega})$  exhibits a Fourier Transform of the weighted normalized mean squared mode amplitude distribution  $\overline{a^2}(\zeta)f(\zeta)$ , and hence,  $\overline{a^2}(\zeta)$  may therefore be obtained by the inverse Fourier transformation (IFT) of the non-dimensional pressure cross-spectrum (or the pressure coherence),  $\eta(\hat{\omega})$ , to give,

$$\overline{a^2}(\zeta) = \frac{1}{2\pi f(\zeta)} \int_{-\infty}^{\infty} \eta(\hat{\omega}) e^{j\zeta\hat{\omega}} d\hat{\omega}. \tag{4.38}$$

The foregoing formulation is a generalization of the two-microphone method of Joseph (2017) summarized in Appendix A.

# 4.3 Evidence for separability of the intra-stage broadband sound field

The usefulness of the decomposition of the intra-stage wall pressure into its  $\gamma$  and  $\zeta$  components derives from the assumption of the separability of Eq. 4.6 so that only the spatial distribution  $\eta$  ( $x_a$ ,  $x_a'$ ) of the sound field is required to fully characterize its broadband spectrum. To verify this important assumption, Fig. 4.2 below shows  $\overline{a^2}(\gamma)$  computed using Eq. 4.25 for the intra-stage noise data measured at approach for the NASA SDT fan rig from 60 equispaced microphones arranged over a half-circle. The spectra in Figs. 4.2a and 4.2b correspond to the *rotor-alone* and the OGV noise obtained by spectral subtraction.

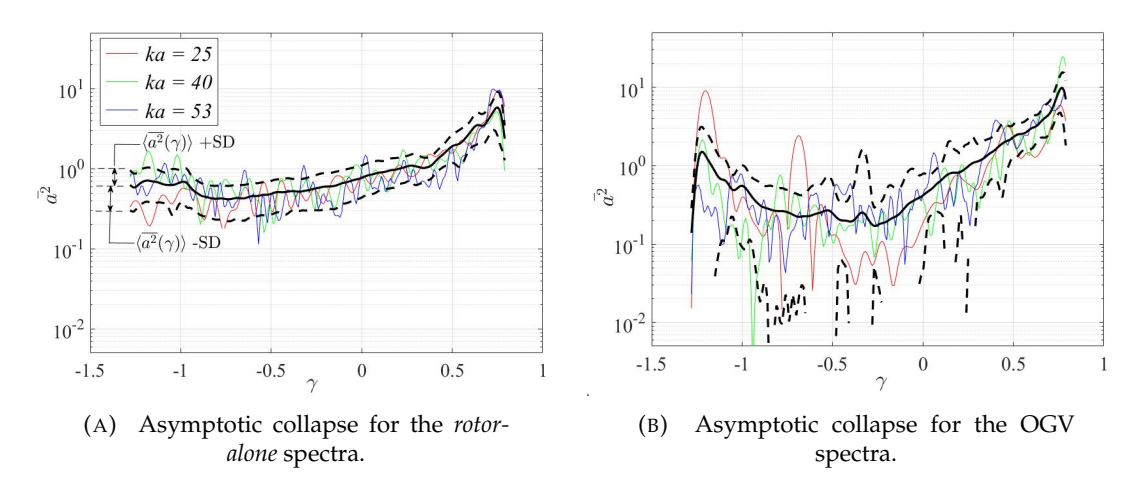


FIGURE 4.2: Evidence of separability of the *rotor-alone* and *OGV* noise spectra, demonstrated using the measured noise data of the NASA SDT fan rig at approach. Note that the solid black curve is the BB frequency-averaged  $\langle \overline{a^2}(\gamma) \rangle$  distribution.

Each figure shows the mean spectra  $\langle \overline{a^2}(\gamma) \rangle_{\Delta\omega}$  spectrum obtained from the average between ka=15 and ka=53 in increments of  $\Delta ka=0.04$  as the solid black line. Also, shown by the dashed black lines are the contours at  $\pm 1$  standard deviation (SD) from the  $\langle \overline{a^2}(\gamma) \rangle_{\Delta\omega}$ . The solid color curves show the spectra at the three discrete frequencies of ka=25,40, and 53, chosen to illustrate the behavior at individual frequencies.

The spectra  $\overline{a^2}(\gamma)$  due to the rotor can be observed to fluctuate by around 2 dB about the mean  $\langle \overline{a^2}(\gamma) \rangle_{\Delta\omega}$  across the range of  $\gamma$ . On the other hand, the spectra due to the OGV can be observed to exhibit greater levels of fluctuation about the mean, which in the range  $-0.6 < \gamma < -0.1$ , is generally small, the reason for which will be discussed below in Sec. 4.6.3. The combination of a relatively large standard deviation and lower mean implies that  $\overline{a^2}(\gamma)$  fluctuates close to 0 over this range of  $\gamma$ , which on a logarithmic scale, exhibits higher variability. This study has confirmed one of the main assumptions of this chapter of Eq. 4.5, i.e., that the frequency and spatial dependence

of the broadband sound field can be separated into a purely frequency-dependent term and another that varies only with space.

# 4.4 Limitations of the standard method for estimating *rotor-alone* noise by OGV removal

A common method of estimating the OGV noise spectrum is to subtract the rotor-alone noise spectrum, measured in the absence of the OGV, from the fan stage spectrum (Ganz et al. (1998)). This procedure is valid provided removing the OGV does not affect the rotor noise. However, we now demonstrate that this hypothesis is incorrect.

Figure 4.3a shows the noise spectra at the duct wall at cutback for the *stage*, the *rotor-alone*, and the *OGV* noise spectra obtained by spectral subtraction. Figure 4.3b shows the relative modal split  $\sigma_{+m}(\omega)$  for the three spectra obtained using Eq. 4.12.

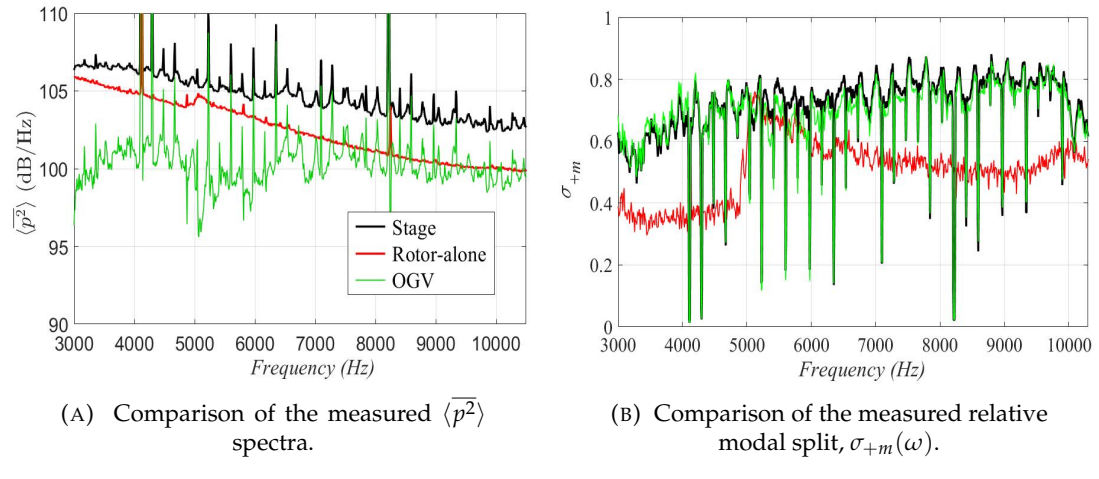


FIGURE 4.3: Comparison of the measured  $\langle \overline{p^2} \rangle$  spectra, and the modal split,  $\sigma_{+m}(\omega)$ , of the *stage*, *rotor-alone*, and *OGV* noise obtained using the NASA SDT rig at cutback.

The noise characteristics in these figure is inconsistent. Figure 4.3a shows that below about 5 kHz the rotor is the dominant noise source and above 8 kHz is comparable to the OGV. However, Fig. 4.3b shows clearly that  $\sigma_{+m}(\omega)$  for the stage and OGV is almost identical, suggesting that, in the presence of the OGV, the rotor-noise must be negligible, in contradiction to Fig. 4.3a. Removing the OGV therefore has a significant effect on the rotor noise, due to the effect of changes to the loading across the rotor by the OGV, indicating that the standard method for isolating the rotor-alone noise is not accurate. The impact on the fan aerodynamic performance is addressed in the paper by Hughes et al. (2002). However, we assume in the present work that, whilst the absolute levels of the rotor-alone noise measurements are not accurate, the relative mode amplitude distributions assessed using the normalized metrics are not significantly altered by removing the OGV. Evidence to support this assumption will be provided in Sec.

4.7 below, where we demonstrate that the effective rotor dipole orientation obtained from investigations on the NASA SDT noise data is also able to predict the measured  $\overline{a^2}(\zeta^+)$  distribution for the ACAT1 fan rig. As a corollary, the simple method of spectral subtraction predicts erroneous levels for the OGV. However, the normalized mode distribution metrics estimated using the measured noise data for the *stage* configuration are identical to those obtained using the *OGV* noise extracted by spectral subtraction.

### 4.5 Description of the three fan rigs

The noise metrics proposed above were measured on three turbofan rigs to establish the universality of the broadband sound field in the intra-stage. The three fan rigs under investigation below are the one-fifth scale fan rig of the NASA SDT (Premo and Joppa (2002); Hughes et al. (2002)), the one-third scale ACAT1 fan at ANECOM in Germany (Kissner et al. (2020); Guérin et al. (2020)), and the Rolls-Royce LSF rig also based at ANECOM. The SDT fan rig has the advantage of being modular so that the noise from the rotor may be measured independently of the fan stage. We now summarize the details for each fan rig, their associated acoustic instrumentation, and their respective flow profiles.

#### 4.5.1 The intra-stage geometry, and acoustic instrumentation

#### 4.5.1.1 The modular NASA 22-inch fan rig simulator

Under the AST (advanced subsonic technology) program, a one-fifth scale model turbofan was constructed in the 9-by-15-foot Low Speed Wind Tunnel (LSWT) at the NASA Glenn Research Center (Premo and Joppa (2002); Hughes et al. (2002)). The test section comprises only the fan stage with a central duct but no core duct, with the fan being driven by a turbo propulsion simulator to generate the air stream. The SDT fan rig was designed to be modular allowing it to be tested in two configurations – one involving the rotor alone, and the other involving both the rotor and the OGV, which we will refer to here as the *stage* configuration. The baseline configuration of the SDT comprises a rotor and OGV with 22 blades and 54 vanes, respectively. A top view and side view of a single rotor blade and OGV is shown below in Figs. 4.4a and 4.4b respectively, depicting the corresponding spanwise aerofoil sections. The axial and azimuthal flow directions,  $M_z$  and  $M_\theta$ , respectively, are also indicated.

The microphone array instrumentation in this rig comprises of an equi-spaced semicircular array of 60 Kulite transducers, which was nominally mounted half-way between the rotor and the OGV. Details of the acoustic measurements made could be found in Premo and Joppa (2002).

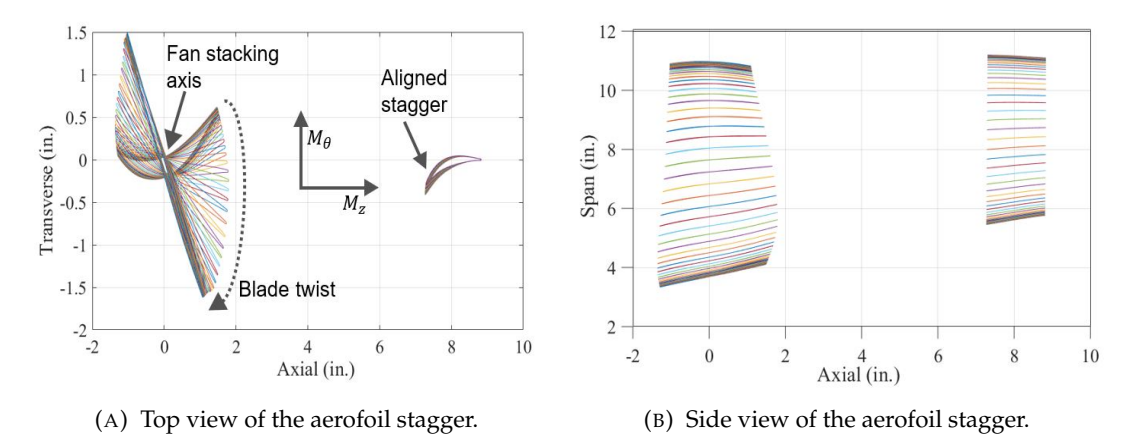


FIGURE 4.4: Staggered arrangement of the aerofoil sections of an isolated rotor blade and a stator vane for the baseline SDT fan stage.

#### 4.5.1.2 ACAT1 fan

Intra-stage broadband noise measurements were made within the framework of the TurboNoiseBB project on a scaled turbofan engine (the ACAT1 fan) in the UFFA test rig at AneCom Aero Test (ACAT), Wildau, Germany.

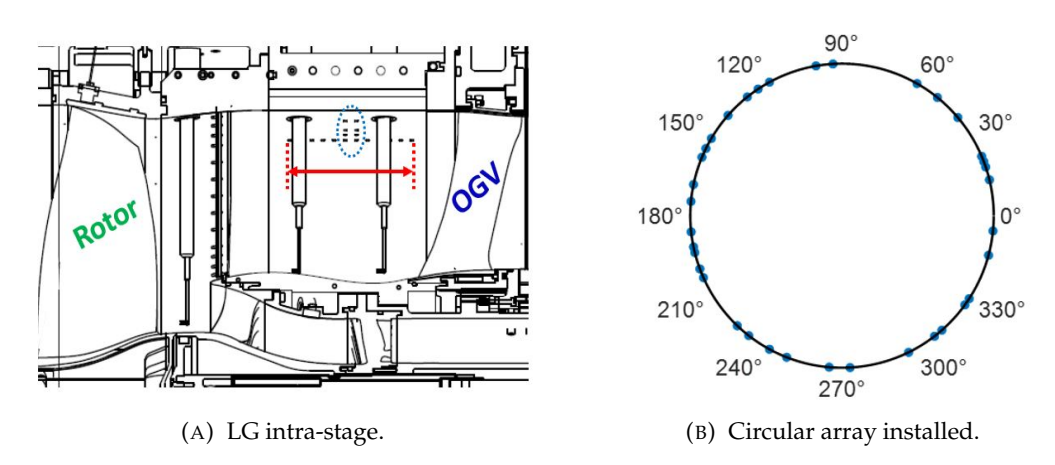


FIGURE 4.5: Schematic representation of the LG intra-stage of the ACAT1 fan instrumented with three hotwire probes, an axial array of twelve equispaced microphones, and two identical non-equispaced circular rings (separately shown on the right in (B)).

The ACAT1 fan rig is of diameter 34 *inches* and comprises a fan stage of 20 rotor blades and 44 stator vanes. Measurements presented in the current work relate to the long-gap (LG) configuration, shown in Fig. 4.5a, where the distance between the rotor trailing edge and OGV leading edge is roughly four times the rotor axial chord, at the high noise working line, at the cutback condition. Further information on the ACAT1 fan rig, the data post-processing, and the hardware instrumentation can be obtained from Behn and Tapken (2019); Kissner et al. (2020); Guérin et al. (2020); Tapken et al. (2019). Figure 4.5 depicts the LG intra-stage section with the location of the axial and circular

microphone arrays depicted by the red double arrow and dotted blue circle, respectively. The axial array comprises ten equally spaced microphones with an adjacent separation distance of 13.5 *mm*. Close to the mid-span of the axial array are mounted two identical circular rings, each comprising 36 non-equispaced microphones, as sketched in Fig. 4.5b.

#### 4.5.1.3 Rolls-Royce Low Speed Fan for Research (RR-LSF)

The third fan rig under investigation in the present work is the RR-LSF of Rolls-Royce PLC. This scaled turbofan has a shorter intra-stage than the LG ACAT1 fan with a length of 260 mm but a comparable tip-radius of 438 mm. The intra-stage instrumentation here comprises an axial array of 15 equi-spaced microphones separated by an adjacent spacing of 14.1 mm, and three circular arrays of 51 equally spaced microphones in each. One microphone ring is located just 48 mm from the rotor trailing edge and another at 15 mm from the OGV leading edge, while the third is positioned roughly midway. Figure. 4.6 below presents a schematic picture of the RR-LSF intra-stage along with its wall microphone array instrumentation.

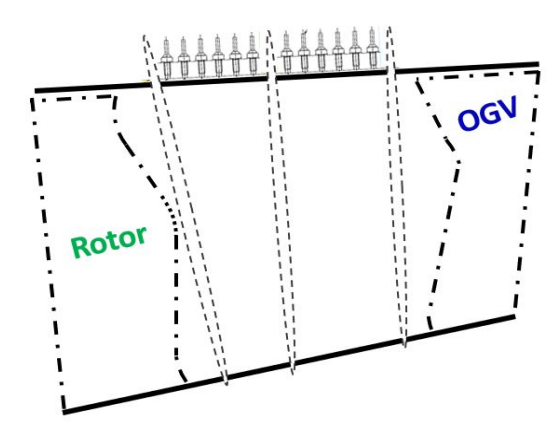


FIGURE 4.6: Schematic depiction of the RR-LSF intra-stage and its microphone array.

#### 4.5.2 Intra-stage flow profiles

We now compare the axial and azimuthal flow profiles measured in the intra-stage sections of the NASA SDT and ACAT1 fans. Laser Doppler Velocimetry (LDV) and hotwire measurements were made to obtain the mean flow velocities for the NASA SDT and the ACAT1 fan intra-stages, respectively. Figure 4.7 below presents a comparison of their axial and azimuthal Mach number profiles,  $M_z(r)$  and  $M_\theta(r)$ , at their corresponding approach and cutback operating points.

The radial flow component in the engine intra-stage is found to be negligible and hence the resulting flow field may be regarded as two-dimensional. Figure 4.7 reveals that the

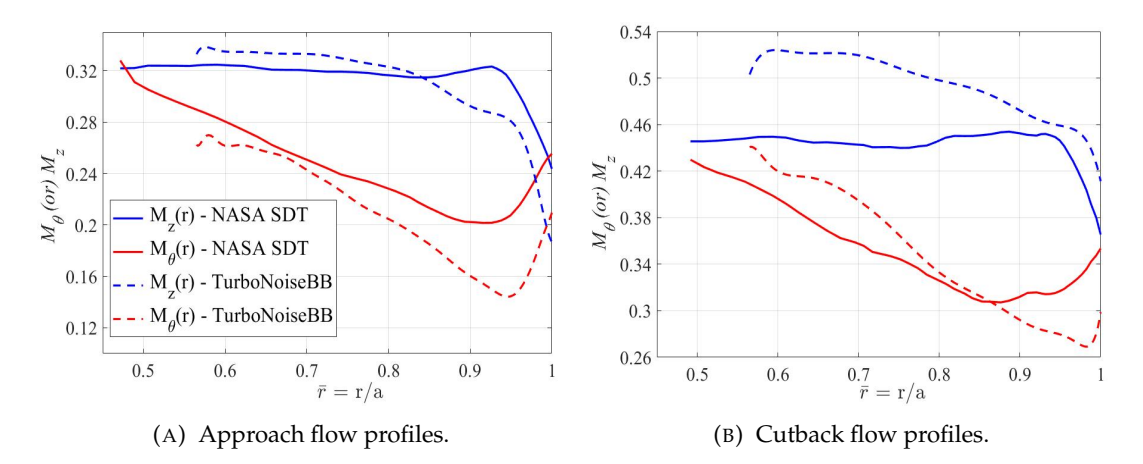


FIGURE 4.7: Comparison of the radial variation of the axial and the azimuthal mean flow Mach numbers for the NASA SDT and the ACAT1 intra-stages at their corresponding approach and cutback operating points.

axial flow profile is roughly constant over most of the annular region except around the tip (owing to the boundary layer (BL)) while the azimuthal flow decays from the hub to the tip with a slight increase in its Mach number near the tip. The mean flow profiles for the RR-LSF intra-stage were found to exhibit a similar behaviour but not included here for reasons of confidentiality. This similarity in the mean flow profiles is believed to be the reason why the broadband noise characteristics investigated below are found to be similar across the different engines and operating conditions.

#### 4.5.3 Test matrix

Intra-stage noise measurements were made across a range of aerodynamic operating conditions for the three fan rigs. In this chapter, we focus on the four operating conditions across the three turbofan rigs, presented in 4.1 below. Also shown, depending upon the microphone array geometry available in each intra-stage, are the mode distribution metrics measured in each fan rig for upstream and downstream modes.

	NASA SDT	ACAT1 fan	RR-LSF
Operating point	Approach (61.7%) & Cutback (87.5% design speed)	Cutback (80% design speed)	70% fan design speed
$\overline{a_m^2}(\omega)$	✓	-	-
$\sigma_{\pm m}(\omega)$	✓	-	-
$\overline{a^2}(\gamma)$	✓	-	✓
$\overline{a^2}(\zeta)$	-	✓	-

We may note here that the intra-stage instrumentation of the RR-LSF would allow the prediction of the  $\overline{a^2}(\zeta)$  distribution as well, but owing to brevity, we restrict ourselves to analysing its  $\overline{a^2}(\gamma)$  distribution in this chapter. We begin our analysis on the NASA SDT noise data and later assess their consistency with the metrics obtained on the other fan rigs.

### 4.6 NASA SDT modal spectra

#### 4.6.1 Wall pressure modal spectra

We first present the noise data measured for the *rotor-alone* and *stage* configurations. The OGV noise contribution is then predicted by subtracting the *rotor-alone* spectra from the fan stage spectra, as previously discussed in Sec. 4.4. The dimensional azimuthal modal spectra are measured by the discrete inverse Fourier Transform of the wall pressure,  $\overline{A_m^2}(\omega) = \overline{p^2}(\omega)N^{-2}\sum_{l=1}^N\sum_{s=1}^N e^{-jm\theta_l}\eta(\theta_l,\theta_s)e^{jm\theta_s}$ . Non-acoustic pressure fluctuations were removed from  $\overline{p^2}(\omega)\eta(\theta_l,\theta_s)$  by applying the robust principal component analysis (RPCA) method (Brunton and Kutz (2019)). Figure 4.8 shows the modal frequency spectra  $\overline{A_m^2}(\omega)$  for the *OGV* and *rotor-alone* noise data at approach.

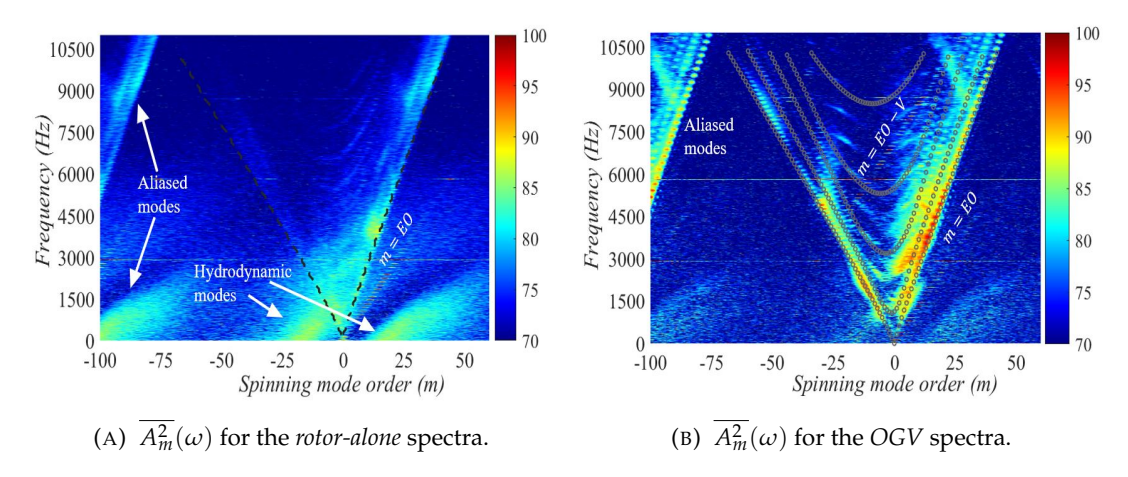


FIGURE 4.8: Measured wall pressure spectra versus *m* and frequency for the *rotor-alone* and the *OGV* noise at approach for the NASA SDT intra-stage.

The black dashed lines in Fig. 4.8a denote the cut-on m-bounds computed using GreenSwirl based on the rigid annular duct approximation. Within this mode triangle, the dispersion lines correspond to the different radial mode orders. These are illustrated in Fig. 4.8b for selected radials (n = 1, 2, 4, 6, 9), wherein the constituent grey circles correspond to the cut-on frequencies of the different (m, n) modes estimated using GreenSwirl. Also observed in the two figures above are the rotor-locked modes, m = EO (faintly observable outside of the mode triangle), the rotor-stator interaction modes m = EO - V (faintly observable inside the mode triangle in Fig. 4.8b), where

EO is the engine order and V is the number of stator vanes, and the aliased modes at the extreme |-m| mode orders. Despite the close proximity of the microphone ring to the rotor and OGV, cut-off modal amplitudes are generally negligible. The regions of high pressures below the  $1^{st}$  BPF ( $\sim 3~kHz$ ) are identified as non-acoustic (hydrodynamic) modes. These modes are conspicuous in the stage, and the rotor-alone spectra but absent in the OGV spectra suggesting that these high-pressure regions 'propagate' in the downstream direction.

# **4.6.2** Determining the equivalent point rotor $(\varphi_r)$ and OGV $(\varphi_o)$ dipole orientation

One of the objectives of this chapter is to demonstrate that the relative broadband mode distribution due to a rotor and OGV can be replicated by a point dipole source at  $2/3^{rd}$ the annular intra-stage gap at an appropriate orientation. In this section, we determine these effective dipole orientations by comparing the measured and numerically predicted noise metrics and choosing, by visual inspection, the dipole orientation providing the best agreement. Here we assume that the OGV broadband noise is generated by the interaction between rotor wake turbulence and the OGV leading edge, while the rotor self-noise is due to the interaction of the turbulent boundary layer passing over the rotor blades with their trailing edges. Hence, further verification of the validity of the effective singular dipole orientations is that these should be related to the physical metal angles of the rotor trailing edge and OGV leading edges. It is important to note that when comparing the measured and predicted mode distribution metrics to deduce the rotor dipole orientation it is necessary to include the Doppler frequency shift on the decaying source strength spectra,  $\hat{f}(\omega - m\Omega_r)$ , where  $\hat{f}(\omega)$  is predicted using the point source spectrum presented in Kim and George (1982). Central to the calculation of  $\hat{f}(\omega)$  in Kim and George (1982) is the calculation of the free stream velocity in the rotor reference frame. In the present work, the relative exit velocity  $W_1$  is calculated by constructing the flow velocity triangles comprising the measured axial  $U_z$ , azimuthal  $U_\theta$ , and rotor speeds  $\Omega_r$ , along the rotor blade span, as shown in Fig. 4.9 below. The effective free stream  $\overline{W_1}$  is then predicted from its area-averaged values. Additionally, we may note that the exit velocity  $W_1$  at  $2/3^{rd}$  span obtained from using the area-averaged value of  $U_z(r_s)$  and the radially averaged value of  $U_\theta(r_s)$  closely matches its  $\overline{W_1}$ . This exit velocity at  $2/3^{rd}$  span is therefore used in our analyses to compute the effective rotor dipole source strength using flat plate theory, such as Amiet (1976).

Figure 4.9 is a plot of the flow exit angles (estimated for the approach and the cutback profiles) compared against the rotor TE angle relating to the blade geometry of Fig. 4.4. The insert plot in Fig. 4.9 depicts a flow velocity triangle at the trailing edge of the blade camber line at a particular spanwise location used to estimate the exit flow angle. The deviation in the angles around the hub region is due to the extrapolation of

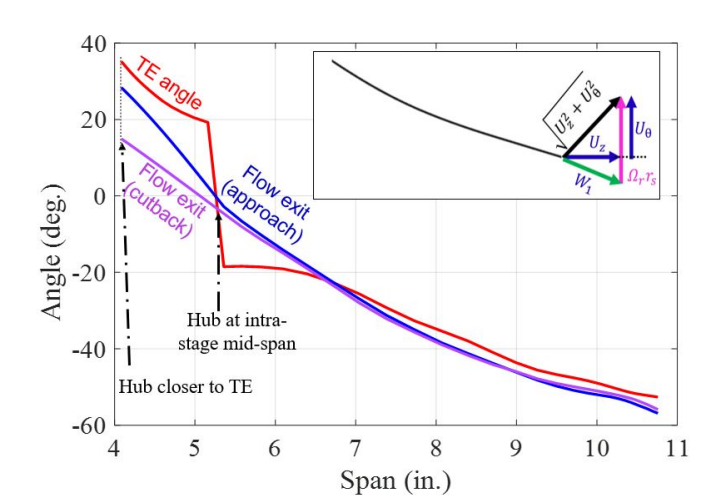


FIGURE 4.9: Comparison between the TE and flow exit angles along the rotor span.

the flow profiles from the measured values at mid-span. Note that the flow exit angles at approach and cutback are within 3° of the trailing edge angle. The flow deflection angle is therefore close to the blade twist at  $\sim 70^\circ$ , suggesting that the effective rotor dipole orientation is 20° relative to the duct axis. By contrast, the OGV leading edge angles are roughly 38° along the entire span and comparable to the OGV leading edge angle of the ACAT1 fan of 36° corresponding to a dipole orientation of 128°. From Appendices D and E, we may infer that the effective singular dipoles with appropriate  $\varphi_r \backslash \varphi_o$  orientations are aeroacoustically equivalent to a continuous distribution of BB noise source mechanisms along the fan blades and the stator vanes. This suggests that the rotor and the OGV may be suitably approximated by flat plates of stagger angles  $\chi_r = 70^\circ$  and  $\chi_o = 38^\circ$ , respectively, with the dipole loading acting normal as shown below in Fig. 4.10.

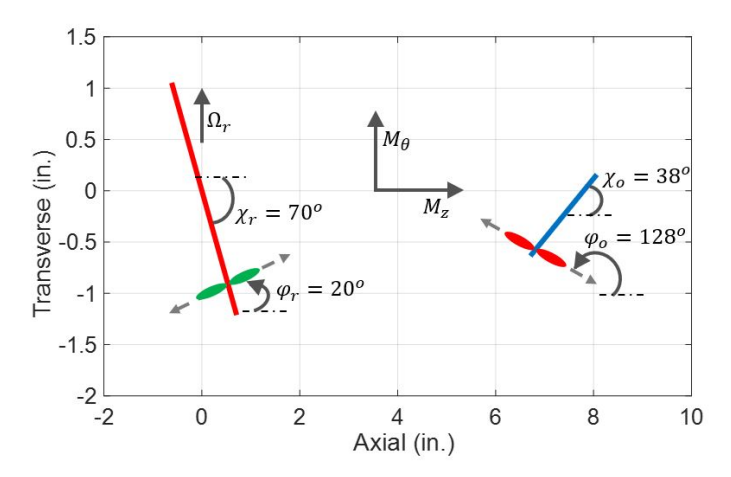


FIGURE 4.10: Aeroacoustic equivalence of the flat plate approximations for the rotor and OGV with the indicated dipole loading and flow directions.

These effective dipole angles will be used to compute the normalized noise metrics, which are then compared against the corresponding experimental results.

### **4.6.2.1** Measured vs computed $\overline{a_m^2}(\omega)$

The normalized mean squared spinning mode amplitudes  $\overline{a_m^2}(\omega)$  due to the *rotor-alone* and OGV were estimated using Eq. 4.11 from 3 kHz to 10 kHz ( $\sim$  1 BPF to 3 BPF). The spectra below about 1 BPF is ignored due to hydrodynamic noise contamination. Figure 4.11 below presents a comparison of the measured and predicted mode distribution  $(\overline{a_m^2}(\omega))$  for the rotor (Figs. 4.11a,4.11b) and OGV (Figs. 4.11c,4.11d), plotted against the frequency and the spinning mode index m, at the approach.

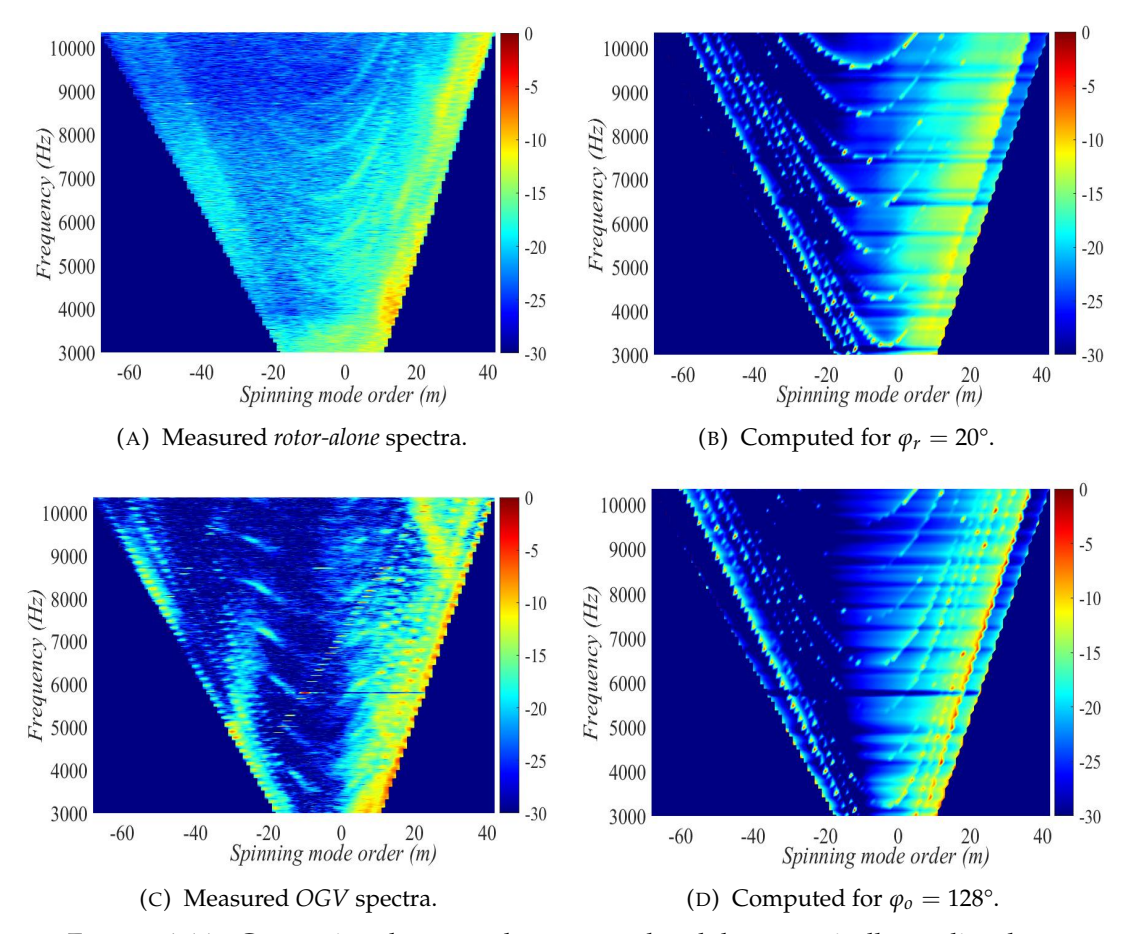


FIGURE 4.11: Comparison between the measured and the numerically predicted normalized Joppa plots for the rotor and OGV, based on the NASA SDT at the approach.

The comparison shows good overall general agreement between prediction and measurement, with both the *rotor-alone* and *OGV* spectra exhibiting higher mode amplitudes for the co-rotating modes (+m) spectra, particularly close to the cut-off boundary. The levels drop by more than 5 dB for the counter-rotating modes across a broad range of azimuthal mode orders m. The behavior observed in Figs. 4.11a was also reported in Ganz et al. (1998) and shown to be a characteristic of the modal distribution of rotor self-noise. The same modal asymmetry is also observed in the numerical distribution (Fig. 4.11b) computed for a single rotating dipole source at  $2/3^{rd}$  the annular intra-stage gap with an orientation of  $\varphi_r = 20^\circ$  relative to the engine axis.

The corresponding measured and predicted mode distribution  $\overline{a_m^2}(\omega)$  for the OGV are shown in Figs. 4.11c and 4.11d. Here, the different dispersion lines for the co-rotating modes can be observed to be more clearly delineated compared to the rotor self-noise in Figs. 4.11a,4.11b. Above about 8 kHz an additional line of high-pressure amplitude for the co-rotating modes is observed whose m-values reduce with increasing frequency. This phenomenon is not observed in the predictions (Fig. 4.11d), which may therefore suggest the presence of modal scattering. We also note in Fig. 4.11c, the presence of spurious modes in the vicinity of m=-30 across all frequencies, which are not present in the predictions, whose origins are not understood. We may note that similar levels of agreement are observed at the higher fan speeds but are not shown here for brevity.

In summary, therefore, the predicted distribution,  $\overline{a_m^2}(\omega)$ , is in good general overall agreement with the measurements thereby verifying the validity of the effective point source model in being able to reproduce the measured mode amplitude distribution in the engine intra-stage.

#### **4.6.2.2** Measured vs computed $\sigma_{+m}(\omega)$

We now compare in Fig. 4.12 the measured and predicted relative modal split  $\sigma_{+m}(\omega)$  for the rotor and OGV at approach, Figs. 4.12a,4.12b, and at cutback, Figs. 4.12c,4.12d, using Eq. 4.12. The predicted modal splits are presented at the effective dipole orientations of  $\varphi_r = 20^\circ$  and  $\varphi_o = 128^\circ$ . Also shown as the pale grey curves are the predicted modal splits at the incorrect dipole angles of  $\varphi_r = 90^\circ$  and  $\varphi_o = 105^\circ$  (normal to OGV stagger angle) to illustrate the sensitivity of  $\sigma_{+m}(\omega)$  to the dipole angle.

In summary, we may note that:

- 1. There is good general agreement between the measured modal split spectra and the predicted spectra based on a single dipole source at  $2/3^{rd}$  duct radius. The measured rotor spectra are generally smoother than their predicted counterparts, while the OGV spectra display similar levels of fluctuation.
- 2. The modal split is more sensitive to the choice of dipole orientation for the OGV at both fan speeds, whereas a greater discrepancy is observed for the rotor at higher fan speeds.
- 3. The modal split spectra for the rotor exhibit a stronger frequency dependence than the OGV which appears to be relatively independent of frequency.

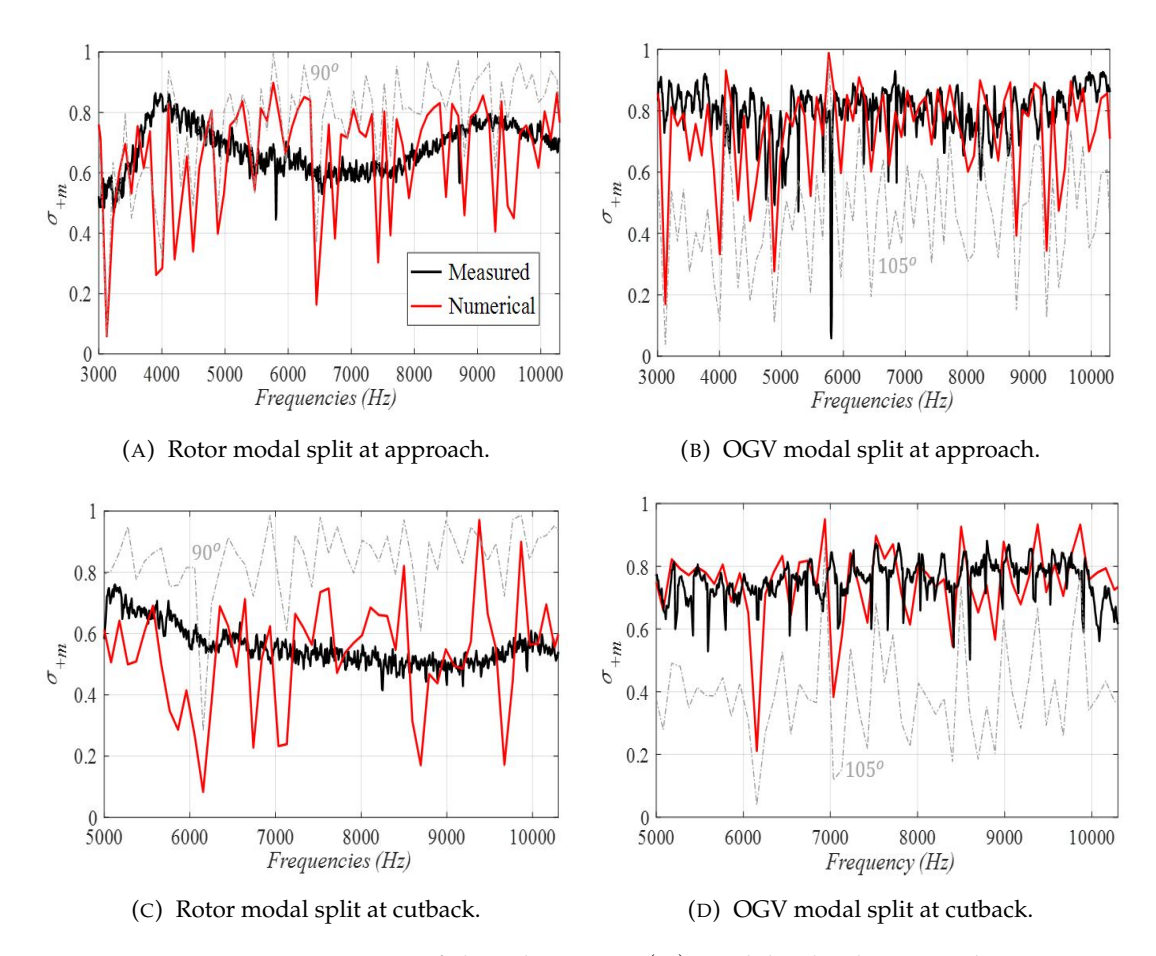


FIGURE 4.12: Comparison of the relative  $\sigma_{+m}(\omega)$  modal splits between the experimental and the numerical predictions for the rotor and OGV at the approach and cutback, based on the NASA SDT fan rig.

## **4.6.2.3** Measured vs computed $\langle \overline{a^2}(\gamma) \rangle$

We now provide an alternative representation of the intra-stage noise data by examination of its normalized spectra in terms of its  $\gamma$  distribution, where  $\gamma = m/ka$ , as outlined in Sec. 4.2.3. Figs. 4.13a,4.13b and 4.13c,4.13d below present the comparison between the  $\langle \overline{a^2}(\gamma) \rangle_{\Delta\omega}$  predictions obtained from the NASA SDT data at approach  $(\Delta\omega \sim 1^{st} \text{ to } 3^{rd} \text{ BPF})$  and cutback  $(\Delta\omega \sim 1^{st} \text{ to } 2^{rd} \text{ BPF})$  respectively, with the predictions obtained from *Greenswirl* at the effective dipole orientations of  $\varphi_r = 20^\circ$  and  $\varphi_o = 128^\circ$  for the rotor and OGV, respectively. Also shown as a faint green and blue line in Figs. 4.13a is the predictions for  $\varphi_r = 45^\circ$  and  $\varphi_r = 90^\circ$ , and as a faint grey line in Fig. 4.13b is the prediction for  $\varphi_o = 105^\circ$ , which have been included here to illustrate the sensitivity of the predicted mode distribution to dipole orientation.

From Fig. 4.13, we observe:

• Figs. 4.13a and 4.13c for the rotor angle indicate a closer general agreement between the predicted and measured  $\gamma$ -spectra than the corresponding modal split

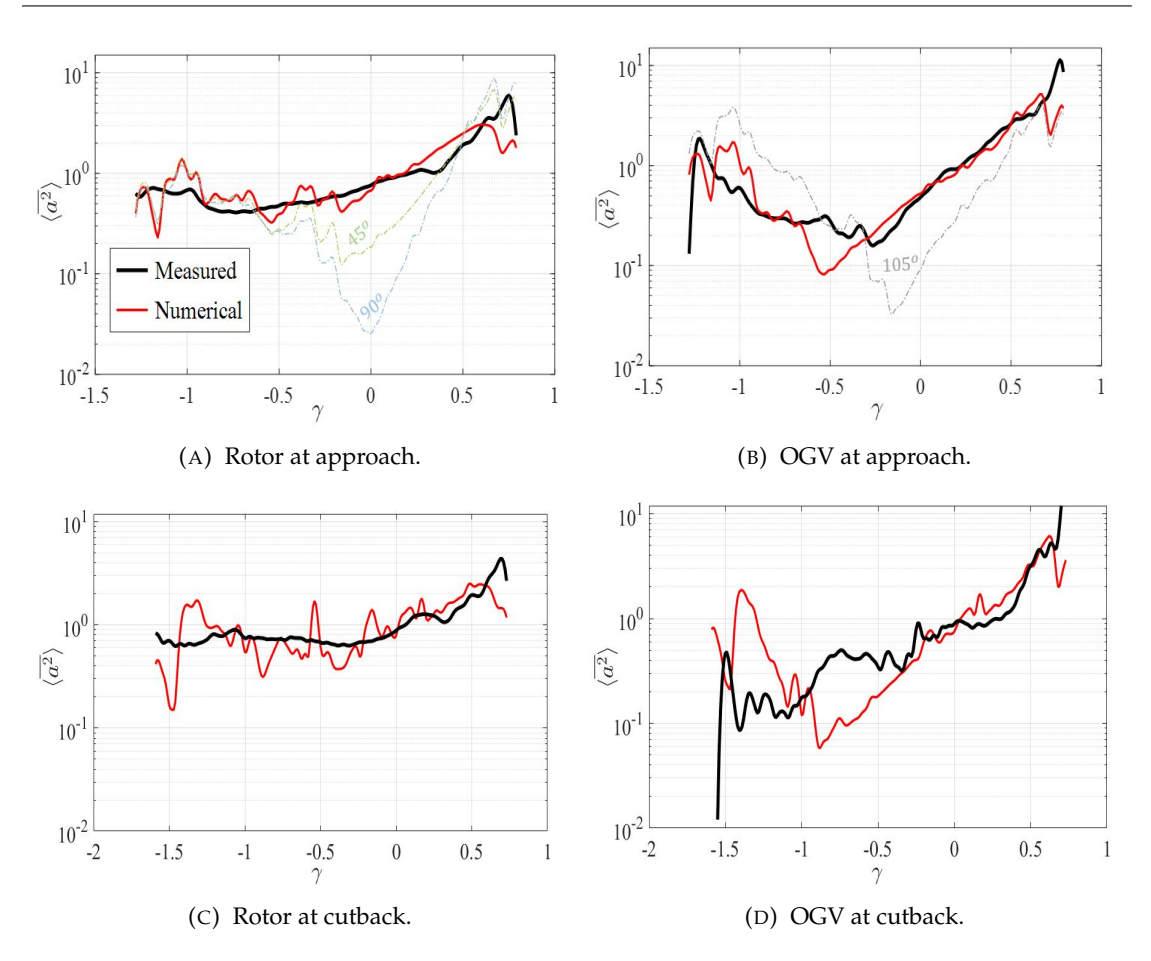


FIGURE 4.13: Comparison between the measured and the numerically predicted  $\langle \overline{a^2}(\gamma) \rangle$  distributions for the rotor and OGV at the approach and cutback, based on the NASA SDT fan rig.

 $\sigma_{+m}(\omega)$  in Fig. 4.12, which is due to the frequency-averaging of Eq. 4.26. Predictions obtained at the higher dipole orientations of  $\varphi_r = 45^\circ$  and  $\varphi_r = 90^\circ$  can be observed to deviate significantly from the measured spectra, indicating the sensitivity of  $\langle \overline{a^2}(\gamma) \rangle$  to  $\varphi_r$  and also providing further validation of the single source representation.

• Figs. 4.13b and 4.13d for the OGV angle indicate good levels of general agreement between the measured and predicted  $\gamma$ -spectra, although notable discrepancies can be observed for  $\gamma < 0$  at cutback. This discrepancy may be attributed to the presence of spurious modes observed in the Joppa plots of Fig. 4.11c for mode orders in the vicinity of m=-30, which are the dominant pressure contributions across the broader cut-on range of contra-rotating modes at cutback. These modes are not predicted by the numerical model.

Overall, from Figs. 4.11, 4.12, and 4.13, the single source representation can be seen to be in good general agreement with the measured data. More importantly, it demonstrates the usefulness of the two metrics,  $\sigma_{\pm m}(\omega)$  and  $\langle \overline{a^2}(\gamma) \rangle$ , for characterizing the

azimuthal modal distribution in high-frequency broadband sound fields. We now conclude this section by stating a simple relationship between the two as follows,

$$\langle \sigma_{+m} \rangle \approx \int_0^{\gamma_{max}} \langle \overline{a^2}(\gamma) \rangle f(\gamma) d\gamma.$$
 (4.39)

This relationship has been verified using the experimental data and found to be valid with 90 percent accuracy.

# 4.6.3 Interpretation of the modal pressure distributions due to rotor and OGV

The in-duct modal pressure distribution due to the rotor and OGV noise can be understood in terms of the various factors in the solution for the acoustic pressure due to a point dipole source. These factors account for the relationship between the three fundamental aeroacoustic components: the source, the observer, and the mean flow, as depicted schematically in Fig. 4.14 below.

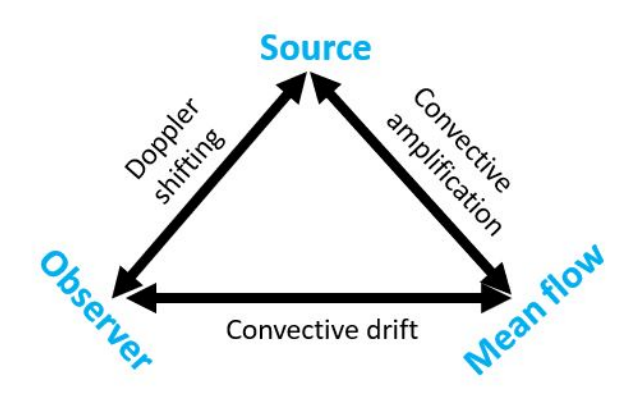


FIGURE 4.14: Various factors relating the three fundamental aeroacoustic components - the source, the observer, and the mean flow.

Referring to Fig. 4.14, the *convective drift* relative to the mean flow and the observer reference frame impacts the cut-on of the modes. For the engine intra-stage, this may be easily explained by considering the *rigid body swirl* model summarized in Sec. 3.3, wherein the effective propagation frequency, relative to the mean swirl, given by Eq. 3.29, is increased for the contra-rotating modes, spinning opposite to the direction of the mean swirl, and decreased for the co-rotating modes, spinning in the same direction as the mean swirl. On a crude approximation, based on the properties of Bessel's function, the cut-on *m*-bounds for a rigid body swirling flow could be defined as:

$$[m_{min}(\omega), m_{max}(\omega)] \approx \left[ -\frac{ka - 2\sqrt{1 - M_z^2}}{\sqrt{1 - M_z^2} - M_s}, \frac{ka - 2\sqrt{1 - M_z^2}}{\sqrt{1 - M_z^2} + M_s} \right],$$
 (4.40)

where  $M_s = \Omega a/c$  is the tip-swirl Mach number of the solid body rotation. The cut-on m-bounds of Eq. 4.40 were verified to be sufficiently accurate in an ideal rigid body swirling flow to within 3% deviation. Eq. 4.40 elucidates that in the absence of a swirling flow ( $M_s = 0$ ), a uniform axial flow broadens the cut-on m-range equally on both ends, whereas, in the presence of a swirling flow, the propagating range is broadened for the contra-rotating modes and shrunk for the co-rotating modes, as could be witnessed in the measured and predicted Joppa plots of Figs. 4.8 and 4.11. Consequently, at a given frequency ( $\omega$ ), we have a greater number of contra-rotating modes cut-on in a mean swirling flow than the co-rotating modes.

The influence of the two others factors, namely the *convective amplification* and the *Doppler shifting*, could be understood from the form of the dimensional mean squared amplitude  $\overline{A_m^2}(\omega)$  of a particular spinning mode at the duct wall, which may be written following Eqs. 4.3 and 4.4 as:

$$\overline{A_{m}^{2}}(\omega) = k^{2} \underbrace{E[|\hat{f}(\omega - m\Omega_{s})|^{2}]}_{Doppler} \underbrace{\sum_{n=1}^{n_{max}(m,\omega)}}_{N=1} \underbrace{\left|\overline{D_{mn}}(\varphi)\right|^{2}}_{Doppler} \left|\hat{G}_{mn}^{\pm}(x|y)\right|^{2}, \qquad (4.41)$$

$$Convective$$

$$shifting \qquad amplification$$

where  $\overline{D_{mn}}(\varphi) = -j(a/r_s)\gamma_m \sin\varphi - j\zeta_{mn}\cos\varphi$  is the normalized dipole directivity in terms of the normalized modal axial wavenumber,  $\zeta_{mn}(=\kappa_{mn}/k)$ , and normalized azimuthal wavenumber at the wall,  $\gamma_m(=m/ka)$ . For the rotating fan,  $\Omega_s = \Omega_r \ rad/s$ , and for the OGV,  $\Omega_s = 0$ . Below, we try to understand how the different factors influence the form of the  $\gamma$ -spectrum in Fig. 4.13 and the sensitivity of the modal split in Fig. 4.12 for the rotor and OGV.

#### 4.6.3.1 Rotor

The shape of the frequency-averaged  $\gamma$ -spectrum is predominantly determined by the magnitude-squared of the  $\overline{D_{mn}}(\varphi)$  term in Eq. 4.41. The shape of the  $\gamma$ -pressure spectrum is therefore governed by the relative balance between the wavenumber contributions  $\zeta_{mn}^+$  and  $\gamma_m^+$  to the modal pressure. This term varies between  $(\zeta_{mn}^+)^2$  and  $((a/r_s)\gamma_m)^2$  as the rotor dipole angle  $\varphi_r$  is varied between  $0^\circ$  and  $90^\circ$ , and therefore greatest variations in  $\langle \overline{a^2}(\gamma) \rangle$  are observed at  $\varphi_r = 90^\circ$  where the  $\langle \overline{a^2}(\gamma) \rangle$  exhibits a V-shape pattern with close to zero pressure at  $\gamma = 0$ , while the spectrum is relatively 'flat' for  $\varphi_r = 0^\circ$ . The *Doppler-frequency shifting* on the decaying source strength spectra (accounted in the rotor reference frame) favors the co-rotating modes. Combined, we may note that for the measured  $\langle \overline{a^2}(\gamma) \rangle$  distribution corresponding to  $\varphi_r = 20^\circ$ , we obtain a near-flat  $\gamma$ -spectrum across  $\gamma < 0$  with steadily rising pressures for  $\gamma > 0$ .

The increased sensitivity of the  $\sigma_{+m}(\omega)$  split to  $\varphi_r$  at higher flow speeds is related to the variations in the shape of the  $\gamma$ -spectrum and the increasing bias in the cut-on of contrarotating modes. Consequently, with a V-shape  $\langle \overline{a^2}(\gamma) \rangle$  profile at increasing  $\varphi_r$ , the relative pressure distribution is reduced across a broad cut-on range of contra-rotating modes  $(\gamma < 0)$  and the *Doppler-frequency shifting* results in an increased concentration of pressures close to the co-rotating cut-on boundary, resulting in the higher  $\sigma_{+m}(\omega)$  spectrum predicted in Figs. 4.12a and 4.12c.

#### 4.6.3.2 OGV

Referring to Eq. 4.41, the shape of the  $\gamma$ -spectrum for the OGV is uniquely dictated by  $\left|\overline{D_{mn}}(\varphi_o)\right|^2$ . From the OGV geometry in Fig. 4.4, we note that  $\varphi_o$  varies between 90° and 180° within which  $\cos\varphi_o$  takes on negative values and  $\sin\varphi_o$  takes on positive values. For upstream propagating modes,  $\zeta^-<0$ . Consequently, for  $\gamma>0$ , the axial and azimuthal components in  $\left|\overline{D_{mn}}(\varphi_o)\right|^2$  add up resulting in greater pressures for co-rotating modes, whereas, for the contra-rotating modes  $(\gamma<0)$ , the axial and azimuthal components in  $\left|\overline{D_{mn}}(\varphi_o)\right|^2$  possess opposite signs implying some cancellation. This convective amplification and diminution of the co- and contra-rotating modes could be observed in the predicted  $\langle \overline{a^2}(\gamma) \rangle$  distribution for  $\varphi_o=128^\circ$  in Figs. 4.13b and 4.13d. On the other hand, the predicted  $\langle \overline{a^2}(\gamma) \rangle$  distribution for  $\varphi_o=105^\circ$  reveals a sharp dip in the vicinity of  $\gamma=0$  with relatively higher pressure levels along the broader propagating range of contra-rotating modes. Consequently, with a greater number of cut-on contra-rotating modes, the pressure concentration in the +m modes is reduced resulting in a lower estimation of the  $\sigma_{+m}(\omega)$  spectrum for  $\varphi_o=105^\circ$ , as observed in Figs. 4.12b and 4.12d.

## 4.7 Investigations using the ACAT1 turbofan rig

# 4.7.1 Comparison between the measured and computed $\overline{a^2}(\zeta)$ distributions

The  $\overline{a^2}(\zeta)$  distribution is obtained using the ACAT1 intra-stage noise data at cutback by implementing the two-microphone method of Sec. 4.2.4 across pairs of axially-offset wall microphones. Fig. 4.15 below shows the measured  $\overline{a^2}(\zeta)$  distribution. Also, superimposed are the numerically computed distributions for upstream ( $\varphi_o = 128^\circ$ ) and downstream ( $\varphi_r = 20^\circ$ ) modes obtained using our equivalent point source model.

It may be worth reiterating here that the implementation of the two-microphone technique (Eq. 4.38) predicts the  $\overline{a^2}(\zeta)$  as a continuous distribution across the cut-on bounds of  $\zeta$ , spanning from the upstream modes (OGV) to the downstream modes (rotor).

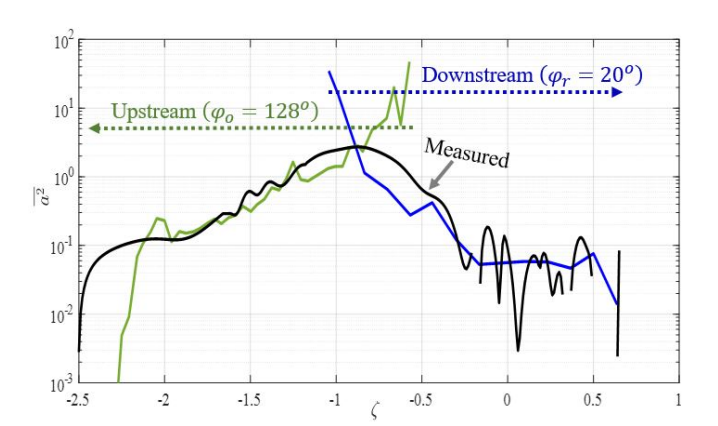


FIGURE 4.15:  $\overline{a^2}(\zeta)$  distribution obtained by the implementation of the two-microphone method on the measured ACAT1 intra-stage noise data at cutback. Note that the superimposed green and blue curves correspond to the theoretical distributions computed separately for the upstream ( $\varphi_0 = 128^\circ$ ) and downstream modes ( $\varphi_r = 20^\circ$ ) using our equivalent point source model.

Therefore, the measured  $\overline{a^2}(\zeta)$  distribution is normalized across a broader wavenumber domain, unlike the two separately predicted numerical contours. Since the primary objective here is the comparison of the relative (and not the absolute) pressure distribution to verify the appropriateness of the  $\varphi_r \setminus \varphi_0$  dipole orientations, the two normalized numerical contours have been suitably scaled to match the corresponding measured levels. The key aspect here is that by removing the dependency on  $(m, n, \omega)$ , the measured  $\overline{a^2}(\zeta)$  profile of Fig. 4.15 elegantly reveals the underlying structure of the BB multimodal sound field as a single contour with the direction of the modal propagation identified by the value of  $\zeta$ .

The comparison above exhibits a satisfying agreement between the measured and the numerical distributions except within the region of the modal overlap,  $\zeta \in [-1.1, -0.6]$ , within which the upstream and downstream modes are indistinguishable. As will be discussed further, this discrepancy within the modal overlap region is a phenomenon due to the swirling flow and does not imply any inconsistency of the empirically determined dipole orientations.

#### 4.7.1.1 The modal overlap

Referring to the two numerical contours in Fig. 4.15, the wavenumber domain  $\zeta \in [-1.1, -0.6]$  depicts a cross-over between the upstream and the downstream running modes. Outside of this region, we may note that  $\zeta$  is unique between the upstream and the downstream propagations. The cross-over domain showcases an overlap of the upstream and the downstream modes, wherein the two are indistinguishable in terms of  $\zeta$ . The comparison between the measured and the numerical modal distributions within the region of modal overlap reveals the potential consequences of this region.

We may note that each of the two numerical distributions depict a monotonic trend such that the region of modal overlap traps the dominant high-pressure modes due to both the rotor and the OGV. Within the modal overlap region, the measured  $\overline{a^2}(\zeta)$  profile is observed to deviate from a monotonic trend since it is a result of contributions from both the upstream and the downstream modes that are overlapping, which referring to the corresponding numerical contours, have varying relative magnitudes. Therefore, within the modal overlap, the upstream (OGV) and the downstream (rotor) modes are measured to the same levels, and consequently, the stronger modes (which in this case are the upstream modes) are underestimated and the weaker modes (in this case, the downstream modes) are overestimated, rendering the resulting predictions unreliable. Hence, even though, the modal overlap phenomenon prevails over a narrow  $\zeta$ -domain, its physical effect is not negligible and to reliably estimate the relative contributions of the fan and the OGV BB noise sources, the dominant high-pressure modes that are overlapping must be separated.

The modal analysis techniques (Joseph (2017); Lowis et al. (2010); Dougherty and Bozak (2018); Enghardt et al. (2007); Tapken et al. (2014)) have hitherto been developed and implemented under idealised stationary flow (or) uniform axial flow conditions, where the phenomenon of modal overlap doesn't occur. The presence of the modal overlap region was first reported in the work of Mathews et al. (2018) who studied the nature of the modal density functions,  $f(\zeta)$ , in complex sheared and swirling flows, and compared them against those of the conventional uniform axial flows. The present work corroborates the physical existence of this modal overlap region using actual intra-stage noise data and shows it as a potentially important region comprising dominant high-pressure modes that need to be separated, thereby emphasizing the need to develop sophisticated phased array techniques for use in the engine intra-stage to accomplish the desired source separation between the rotor and the OGV BB noise sources.

# 4.8 Investigations using the RR-LSF test rig

The axisymmetric circular array of 51 microphones in the acoustic instrumentation of the RR-LSF rig permits an unaliased detection of the cut-on m-orders upto the  $2^{nd}$  BPF( $\sim$  3000 Hz) at the operating condition considered with theoretically zero side-lobe error. The  $\langle \overline{a^2}(\gamma) \rangle$  distribution is then obtained using the single-ka implementation of Sec. 4.2.3 and averaged across the  $1^{st}$  BPF to the  $2^{nd}$  BPF. Fig. 4.16 below compares the measured  $\langle \overline{a^2}(\gamma) \rangle$  distribution against the corresponding numerically predicted distributions obtained using our equivalent point source model for the upstream ( $\varphi_o = 128^\circ$ ) and the downstream ( $\varphi_r = 20^\circ$ ) modes. Each of the two numerically predicted contours may be noted to depict a similar  $\gamma$ -spectrum as observed in Sec. 4.6.3 for the NASA SDT noise data.

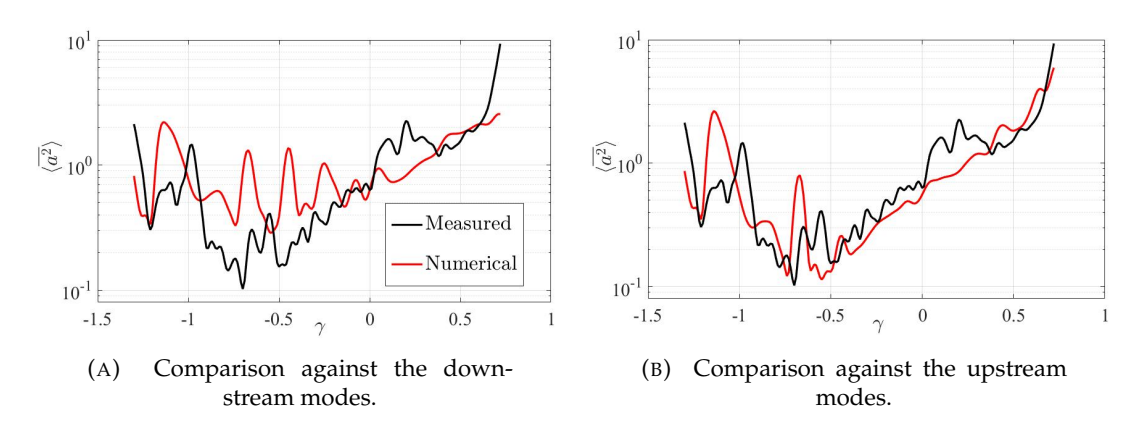


FIGURE 4.16: Comparison between the measured and the numerically predicted  $\langle \overline{a^2}(\gamma) \rangle$  distributions for the upstream ( $\varphi_o = 128^\circ$ ) and downstream ( $\varphi_r = 20^\circ$ ) modes considering the RR-LSF intra-stage.

It's worth mentioning here again that the RR-LSF rig was tested in the standard *stage* configuration involving both the rotor and the OGV. Also, it may be understood that in a  $\gamma$ -based analysis, we do not separate the upstream and the downstream modal distributions, unlike with the  $\overline{a^2}(\zeta)$  modal distributions, since  $\gamma$  corresponds to the circumferential phase speed and is same for both the upstream and downstream modes. However, the comparative study above clearly exhibits an excellent agreement of the measured contour with the numerically predicted  $\langle \overline{a^2}(\gamma) \rangle$  profile for the upstream modes clearly indicating that the relative pressure distribution across the constituent spinning modes, in the presence of both the rotor and the OGV, is solely dictated by the OGV. The following are the key takeaways from the foregoing analysis:

- The match with the computed  $\langle \overline{a^2}(\gamma) \rangle$  distribution for the upstream modes justifies the appropriateness of our equivalent point source model on a third engine. Overall, the successful validation across three turbofan intra-stages over a range of operating conditions substantiates that  $(\varphi_o, \varphi_r) = (128^\circ, 20^\circ)$  are universal engine constants.
- Although, a  $\gamma$ -based analysis doesn't perform any wave-splitting, it could potentially reveal the dominant BB noise component, which in the present test case is the OGV. This is the first time that an engine noise measurement, involving both the rotor and the OGV, has showcased the ponderance of the OGV LE interaction noise. To quantify the relative source levels however, we need to separate the upstream and the downstream contributions, which from referring to Fig. 4.15, calls for novel wave-splitting techniques.

### 4.9 Concluding remarks

The dominant broadband (BB) noise sources in the fan stage are the rotor self-noise at the trailing edges (TE) of the fan (rotor) blades and the rotor-stator interaction noise at the leading edges (LE) of the stator vanes (OGV). Noise measurements made in the engine intra-stage between the fan TE and the OGV LE permit an investigation into the broadband noise characteristics of the two sources. In the present work, we analyzed the noise data from three turbofan rigs, namely the NASA Fan Noise Source Diagnostic Test (NASA SDT), the ACAT1 fan of the TurboNoiseBB project, and the Rolls-Royce LSF (low speed fan for research), over different operating conditions, for a robust characterization of the intra-stage sound field. Using the measured noise data, it was shown that the relative spatial cross-spectrum between any two points on the duct wall is independent of frequency and reveals the underlying structure of the broadband multimodal sound field. This relative spatial cross-spectrum was characterized by developing suitable normalized mode distribution metrics based on the axial ( $\zeta$ ) and the azimuthal (m,  $\gamma$ ) wavenumbers, which were predicted using the available wall microphone arrays along the axial and azimuthal directions, respectively.

The theoretical component of our work involved the conceptualization of an equivalent point source model for the engine intra-stage with the rotor and the OGV BB noise sources effectively reduced to singular point dipoles of appropriate orientation relative to the engine axis, denoted by  $\varphi_r$  and  $\varphi_0$  respectively, at  $2/3^{rd}$  annulus position, each uni-directionally radiating the downstream modes and the upstream modes. The normalized mode distribution metrics measured using the intra-stage noise data of the three turbofan rigs were attempted to be replicated numerically using our point source model. The complete study revealed that dipole orientations of  $\varphi_r = 20^\circ$  and  $\varphi_0 = 128^\circ$  produce near-identical broadband noise characteristics as the measured distributions for the rotor and OGV, respectively. The consistency of the  $\varphi_r \setminus \varphi_0$  dipole orientations across the three turbofan rigs establishes the universality of the intra-stage broadband sound field. The establishment of an equivalent point source model for the engine intra-stage was useful in:

- the interpretation of the relative modal pressure distribution due to the fan and OGV,
- the illustration of the physical existence of the modal overlap region that entraps
  the high amplitude modes of the fan and OGV, which are inseparable using the
  existing phased array techniques, thereby calling for novel wave-splitting methods for the reliable source separation of the fan and OGV BB noise sources, and
- demonstrating the preponderance of the OGV as the dominant fan stage noise source for the first time using intra-stage measurements.

Furthermore, our empirically established point source model justifies some useful simplifications in our analysis such as mutually incoherent broadband modes and ignorance of any modal scattering from the rotor and OGV, and finds application in the development of source location techniques, liner design, and low-fidelity noise prediction models.

# **Chapter 5**

# Broadband acoustic mode detection in swirling flows

This chapter presents a systematic investigation into the development of phased array methods for use in the engine intra-stage to separate the relative contributions of the fan and OGV broadband noise sources. The currently available asymptotic (high-ka limit) modal analysis methods are one-dimensional (Lowis et al. (2010); Joseph (2017)), in the sense that these attempt to predict the BB modal amplitudes as a function of the normalized axial wavenumber  $(\zeta)$ , or the modal cut-on ratio  $(\alpha)$ , considering a uniform axial mean flow, making use of the wall pressures sensed along an axial array of microphones. However, the mean flow field in the engine intra-stage carries a comparable swirling flow component, and the work presented in the previous chapter demonstrated the physical existence of the modal overlap region (Sec. 4.7.1.1) which was shown to entrap the dominant high-amplitude modes of the fan and OGV, rendering it potentially important for the source separation of the intra-stage broadband noise. This chapter presents a theoretical and numerical investigation to understand the measurement challenges due to the modal overlap, its occurrence in a swirling flow, and developing robust techniques to separate the dominant modes from the overlap bandwidth and thence reliably estimate the relative source contributions.

We begin this chapter by investigating the phenomenon of modal overlap in a swirling flow in Sec. 5.1. It is shown that the modal overlap region presents a unique challenge to wave splitting in the engine intra-stage at higher fan speeds by rendering the existing 1-D modal analysis methods unsuitable for predicting the relative source contribution. The occurrence of the modal overlap region is then understood using the rigid body swirl model (Sec. 3.3) in Sec. 5.2, wherein it is shown that the  $\pm m$  modal grouping within the modal overlap region may be reasonably characterized by co-rotating (+m) upstream modes and contra-rotating (-m) downstream modes calling for 2-D wavenumber distribution approaches (based on m and  $\zeta$ ) as opposed to 1-D modal

analysis methods (based on  $\zeta$  alone). These 2-D modal analysis methods require 2-D microphone array geometries characterized by at least one circular ring (to decompose the m-orders) and more than one axial measurement position (to measure the relative axial phase difference). The development of these 2-D modal analysis techniques is enunciated in Secs. 5.3, which are then shown in Sec. 5.4 to effectively separate the dominant overlapping modes and reasonably predict the relative source contributions of the fan and OGV BB noise sources.

### 5.1 Modal overlap in a swirling flow

As discussed in Sec. 2.1.1, under uniform axial flow conditions, relevant to the engine intake and bypass ducts, a high-ka analysis typically involves studying the modes as a distribution over the cut-on ratio,  $\alpha$ , which is related to the Bessel eigenvalues. As summarized in Sec. 3.1.1, the normalized modal axial wavenumber  $\zeta$  is defined in terms of  $\alpha$  as per Eq. 3.10, from which we may note that in an ideal uniform flow, the wavenumber domain of  $\zeta$  is demarcated by the propagating limits,  $\left[\zeta_{min}, \zeta_{cut-off}\right] = \left[-1/(1-M_z), -M_z/\beta^2\right]$  for the upstream modes, and  $\left(\zeta_{cut-off}, \zeta_{max}\right] = \left(-M_z/\beta^2, 1/(1+M_z)\right]$  for the downstream modes, which have the corresponding  $\alpha$  ranges of [-1,0) and [0,1], respectively. Therefore, we may note that in a uniform axial flow,  $\zeta$  is unique between the upstream and downstream modes.

However, in a complex swirling flow, typical of the engine intra-stage, the governing equation is no longer a simple Bessel equation, and therefore, the eigenvalues here do not correspond to the stationary values of the Bessel's function. As summarized in Sec. 3.2, in a non-uniform swirling flow, the eigenvalue problem is only solved numerically with  $\zeta_{mn}$  being the desired solution. Recent work by Mathews et al. (2018) demonstrates that  $\alpha$  is ambiguous in its meaning and interpretation in non-uniform swirling flows prevalent in the engine intra-stage, rendering  $\zeta$  as the relevant parameter for modal measurements.

The propagating range of  $\zeta$  in a swirling flow differs from the theoretical cut-on bounds for an ideal uniform axial flow. As discussed in Chapter 4, the extreme cut-on bounds of  $\zeta$  denoted by  $[\zeta_{min}, \zeta_{max}]$  converge asymptotically across frequencies even in a non-uniform swirling flow. Our region of interest here is the modal overlap, which occurs in the vicinity of the inner cut-on bounds,  $\zeta_i^{\pm}$ , corresponding to the minimum and maximum  $\zeta$  values in the cut-on range of the downstream and upstream modes, respectively. Modal overlap occurs when:

$$\zeta_i^+ < \zeta_i^-, \tag{5.1}$$

with the overlap bandwidth,  $\Delta \zeta_o$ , defined as:

$$\Delta \zeta_o = \zeta_i^- - \zeta_i^+. \tag{5.2}$$

Fig. 5.1 below plots the computed  $\zeta_i^{\pm}$  cut-on bounds for the approach and cutback flow profiles of the ACAT1 fan, obtained using the *GreenSwirl* solver.

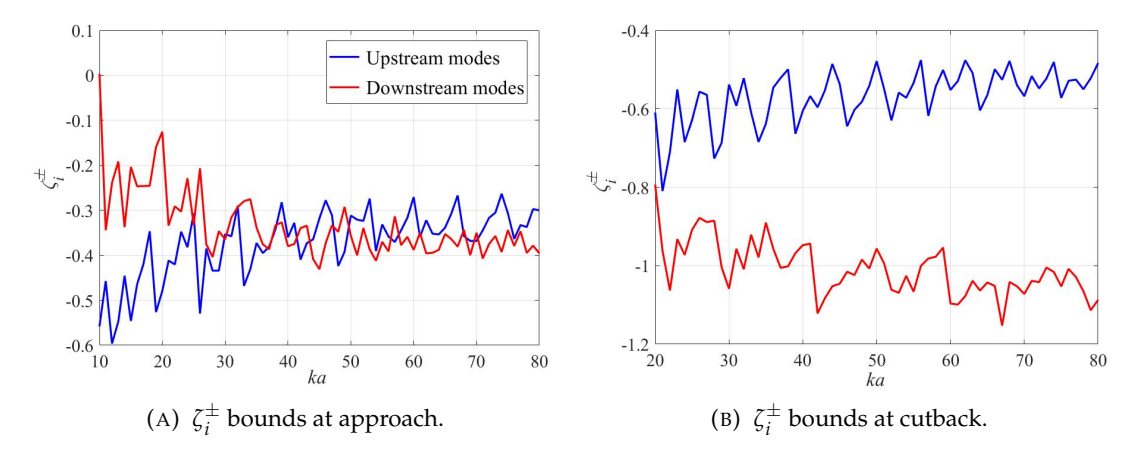


FIGURE 5.1: Spectral variation of the  $\zeta_i^{\pm}$  bounds for the approach and cutback flow profiles of the ACAT1 fan.

Referring to Fig. 5.1a for the approach flow profile, characterized by lower  $\overline{M_z}$  and  $\overline{M_\theta}$ , we may observe that close to ka=40, there is no modal overlap with  $\zeta_i^+>\zeta_i^-$  beyond which we observe a very narrow overlap region with  $\Delta\zeta_o<0.1$ . On the other hand, referring to Fig. 5.1b for cutback, characterized by higher  $\overline{M_z}$  and  $\overline{M_\theta}$ , the modal overlap is witnessed to be a regular phenomenon across the BB frequency range of interest with a broader bandwidth  $\Delta\zeta_o$ . It may be noted that the modal overlap region in Fig. 5.1b traps only about 5% – 6% of the total number of cut-on modes, but these are still consequential in rendering the existing 1-D modal analysis techniques unsuitable for implementation in the engine intra-stage, as will be shown in the next section.

# 5.1.1 Impact of the modal overlap on the mode detection capability of existing methods

The phenomenon of modal overlap was demonstrated using the measured intra-stage noise data at cutback in Fig. 4.15 by predicting the  $\overline{a^2}(\zeta)$  distribution using the two-microphone method (Joseph (2017)). To investigate the impact of the modal overlap, we attempted to replicate the corresponding measured  $\overline{a^2}(\zeta)$  distribution numerically using a synthesized dataset for the cutback swirling flow generated by the equivalent point source model of Sec. 4.1.2 by suitably altering the source strengths of the singular rotor and stator dipoles, whose orientations are fixed at  $\varphi_r = 20^\circ$  and  $\varphi_o = 128^\circ$ , respectively. The two 1-D modal analysis methods, namely the two-microphone technique and the axial beamformer, summarised in Appendix A, were implemented on

this synthesized dataset considering the microphone array geometry of the ACAT1 intra-stage and the  $\overline{a^2}(\zeta)$  distribution so obtained is compared against the measured distribution in Fig. 5.2 below. We may notice that except within the region of modal overlap,  $\zeta \in [-1.1, -0.5]$ , the two numerically predicted  $\overline{a^2}(\zeta)$  distributions excellently match the measurement.

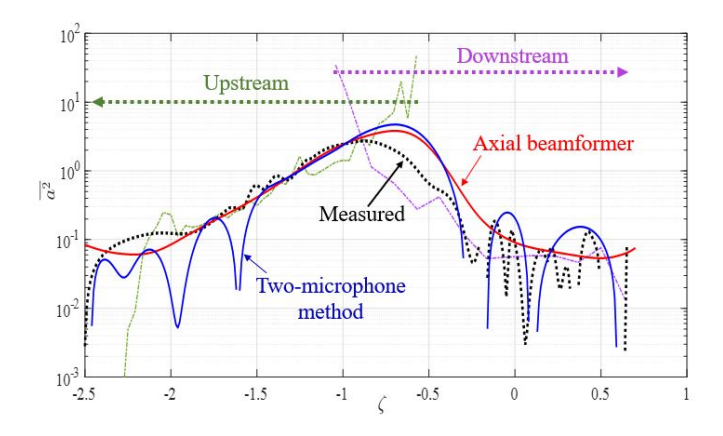


FIGURE 5.2: Comparison of the  $\overline{a^2}(\zeta)$  distributions numerically predicted by implementing the two-microphone and the axial beamformer methods on a synthesized dataset against the corresponding measured distribution obtained from the ACAT1 fan at cutback.

From the predicted  $\overline{a^2}(\zeta)$  distribution, we estimate the dimensional mean squared mode amplitude distribution,  $\overline{A^2}(\zeta)$ , using Eq. 4.35, which may be appropriately summed across the upstream and downstream modes to compute the relative source balance defined as  $10log_{10}\left(\sum \overline{A^2}(\zeta^-)/\sum \overline{A^2}(\zeta^+)\right)$ . The predictions within the modal overlap region are equally assigned to both the upstream and downstream modes. Fig. 5.3 below compares the relative source balance predicted using the two 1-D methods against the actual (target) relative balance of the synthesized dataset.

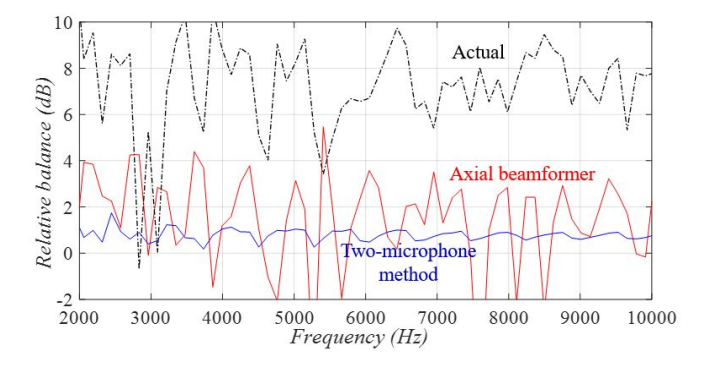


FIGURE 5.3: Comparison of the relative source balance predicted using the two 1-D techniques against the actual (target) relative balance, considering the synthesized dataset of the ACAT1 fan at cutback.

The actual relative balance indicates that the OGV noise dominates the fan by more than  $6 \, dB$  across the BB frequency range. However, the two 1-D techniques are observed to severely underestimate the relative source balance. The two-microphone

technique predicts a relative balance of less than 1 *dB* while the axial beamformer produces a fluctuating relative balance barely exceeding 2 *dB* across the broadband frequency range of interest. The comparative study above highlights the cruciality of separating the dominant overlapping modes of the fan and OGV to accomplish the desired wave splitting in the engine intra-stage at higher fan speeds.

# 5.2 Elucidation of the modal overlap phenomenon using the rigid body swirl model

Eq. 5.1 suggests that the modal overlap is a phenomenon wherein the downstream modal wavenumbers are more negative than the upstream modal wavenumbers. We now employ the rigid body swirl model, discussed in Sec. 3.3, and using a simple order of magnitude analysis, we explain that the *convective drift* due to the axial and azimuthal flows (Fig. 4.14) impacts the wavenumber negativities and eventually leads to the creation of the modal overlap region. Referring to the equations in Sec. 3.3, the Doppler-shifted  $\zeta_{mn}(\alpha_{mn})$  relation may be expressed as:

$$\zeta_{mn}^{\pm} \approx \underbrace{(1 - \epsilon_{m})}_{scaling} \left( -M_{z} \pm \underbrace{\sqrt{1 - \left(\frac{\beta \zeta_{mn}}{k \left(1 - \epsilon_{m}\right)}\right)^{2}}}_{cut\text{-on ratio, } \alpha_{mn}} \right), \tag{5.3}$$

where  $\zeta_{mn}$  are the stationary values of the Bessel function, and  $\varepsilon_m = m\Omega/\omega$  and  $\beta = \sqrt{1-M_z^2}$  account for the effects of the mean swirling flow and mean axial flow, respectively. It is worth mentioning here that when  $\Omega=0$  and  $M_z=0$ ,  $\zeta_{mn}^\pm=\alpha_{mn}^\pm$  and is negative for upstream modes and positive for downstream modes. Additionally, we may note that higher-order  $(\pm m,n)$  modes have a larger  $\zeta_{mn}$  and therefore possess smaller  $\alpha$ . Consequently, in the presence of a mean flow, referring to Eq. 5.3, we may understand that for these higher-order  $(\pm m,n)$  modes, when  $M_z>\alpha_{mn}$ , the convective drift due to the axial flow results in negative  $\zeta$  values for the downstream modes. Additionally, with  $\Omega\neq 0$ , the scaling factor, which accounts for the convective drift due to the swirling flow, shrinks or magnifies the corresponding  $\zeta^\pm$  negativity. In the following subsections, we demonstrate how this shift in the  $\zeta^\pm$  negativities of the higher-order  $(\pm m,n)$  modes brought about by the axial and azimuthal flows leads to the creation of the modal overlap.

#### 5.2.1 Higher order (+m, n) modes

For the co-rotating modes,  $0 \le \epsilon_m < 1$  and therefore the scaling factor,  $(1 - \epsilon_m) \le 1$ , which makes the inverse squared of the scaling factor inside the cut-on ratio in Eq. 5.3 to be greater than 1. Consequently, for a (+m,n) mode, the radical is real when  $(\beta \varsigma_{mn}/k)^2 < 1$ , which signifies a reduction in the number of cut-on co-rotating modes and a corresponding decrease in the extreme cut-on m-order.

We may note that for the higher-order (+m,n) modes, where the radical is smaller than  $M_z$ , the corresponding  $\zeta^{\pm}$  for the downstream and upstream modes is negative but the scaling factor reduces the negativity. As a result, the corresponding  $\zeta^{\pm}$  values are shifted right in the wavenumber domain, which implies that the upstream modes  $(\zeta^{-})$  approach the inner bound,  $\zeta_i^+$ , of the downstream wavenumber domain and thence vulnerable to falling within the overlap bandwidth  $\Delta \zeta_o$ , whilst the corresponding downstream modes  $(\zeta^+)$  are drifted further away thereby potentially avoiding any modal overlap.

#### 5.2.2 Higher order (-m, n) modes

For the contra-rotating modes,  $\epsilon_m < 0$ , making the scaling factor,  $(1 - \epsilon_m) > 1$ , which renders the inverse squared of the scaling factor inside the cut-on ratio in Eq. 5.3 to be lesser than 1. This means that for a (-m, n) mode, the radical is real even when  $(\beta \zeta_{mn}/k)^2 > 1$ , which signifies an increase in the number of cut-on contra-rotating modes and a corresponding increase in the extreme cut-on m-order.

For the higher-order (-m,n) modes, where the radical is smaller than  $M_z$ , the corresponding  $\zeta^\pm$  for the downstream and upstream modes is negative with the scaling factor now magnifying the negativity. As a result, the corresponding  $\zeta^\pm$  values are shifted left in the wavenumber domain, which implies that the upstream modes  $(\zeta^-)$  are drifted away from the inner bound,  $\zeta_i^+$ , of the downstream side, while the corresponding downstream modes  $(\zeta^+)$  approach the  $\zeta_i^-$  bound of the upstream wavenumber domain and are thus prone to lie within the overlap bandwidth. At higher fan speeds, typical of cutback/sideline, the cut-on m-bound is further widened, and the m-orders close to the cut-on limits would possess a very large scaling factor, which further enlarges the  $\zeta^\pm$  negativities as a result of which the corresponding downstream modes would cross over a broad range of  $\zeta^-$  values, whilst the corresponding upstream modes would be further drifted away from the inner cut-on bounds avoiding any modal overlap.

#### 5.2.3 Inferences and their validation

Using *GreenSwirl*, the eigenvalues  $\zeta_{mn}^{\pm}$  were calculated for the ACAT1 cutback flow profile across a wide frequency range up to ka=80 and the m orders of the upstream and downstream modes lying within the overlap bandwidth,  $\Delta \zeta_o$ , are depicted below in Fig. 5.4 by brown markers, and the m orders without any  $\zeta^{\pm}$  within  $\Delta \zeta_o$  are depicted by blue markers with the solid yellow line demarcating the cut-on limits.

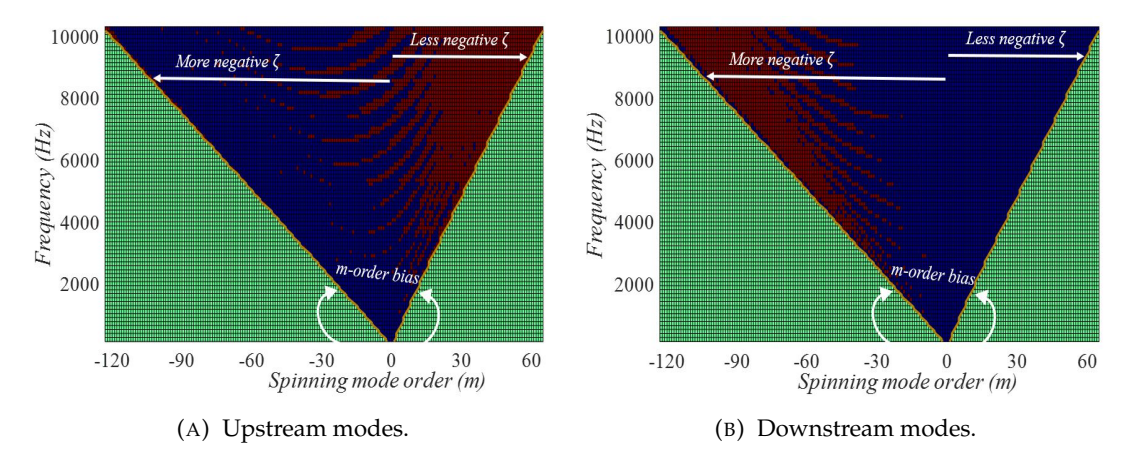


FIGURE 5.4: Spinning mode orders of the upstream and downstream cut-on modes within the modal overlap region, computed for the cutback flow profile of the ACAT1 fan.

It can be seen above that in the upstream propagation, the co-rotating (+m) modes (with reduced  $\zeta$  negativity) are predominantly entrapped within the modal overlap region compared to the contra-rotating (-m) modes. With a relatively narrower cut-on m-range of the co-rotating modes at higher flow levels, the broader overlap bandwidth eventually includes at least one higher order radial mode of almost every cut-on +m mode order. As a result, we notice in Fig. 5.4a that almost the complete +m range between ka=30 to 80 is impacted by the modal overlap. On the other hand, in the downstream propagation (5.4b), the overlapping modes are completely contra-rotating (with enlarged  $\zeta$  negativity). Overall, Fig. 5.4 corroborates our analysis in Secs. 5.2.1 and 5.2.2.

At lower levels of axial and swirling flows, the modal overlap is a sparse phenomenon and when present can be ideally characterized by co-rotating (+m) upstream modes and contra-rotating (-m) downstream modes. However, with the increase in the flow levels, as with the cutback flow profile, the bias in the cut-on of the  $\pm m$  mode orders becomes substantial, impacting the ideal  $\pm m$  grouping within the modal overlap region with some lower-order contra-rotating upstream modes now trapped within the  $\Delta\zeta_o$  bandwidth. This is because at higher flow levels,  $\Delta\zeta_o$  broadens as a result of the drifting of the  $\zeta^+$  values of the higher -m orders which cross-over a broader  $\zeta^-$  range of the upstream domain eventually entrapping some lower -m orders, as could be witnessed

in Fig. 5.4a. However, referring to the  $\overline{a_m^2}(\omega)$  (Sec. 4.6.2.1) and  $\overline{a^2}(\gamma)$  (Sec. 4.6.2.3) distributions for the rotor and OGV, it could be stated that these lower -m orders of the OGV are much weaker and it is essential to separate the dominant +m modes from the modal overlap. It may be additionally noted here that the dominant +m mode orders are easily transmitted through the fan blades and relevant in the intake far-field noise (Sijtsma (2010),Premo and Joppa (2002)).

The foregoing analysis therefore suggests that resolving the total pressure into +m and -m azimuthal mode orders is fundamental to separating the dominant +m modes from the  $\Delta\zeta_o$  bandwidth. Hence, 2-D wavenumber distribution approaches, based on the azimuthal number (m) and the axial wavenumber  $(\zeta)$ , should perform an effective wave splitting in the engine intra-stage compared to the current 1-D modal analysis methods that are based solely on  $\zeta$ . These 2-D methods require 2-D microphone array geometries characterized by at least one microphone ring (to decompose the m orders) and more than one axial measurement position (to measure the relative axial phase difference) and shall aim to predict the  $\overline{a^2}(\zeta_{\pm m})$  distributions separately for the +m modes and -m modes. In the following sections, we enunciate the development of such 2-D wavenumber distribution approaches and demonstrate their success in separating the dominant modes out of the modal overlap and thence reliably estimate the relative source contributions.

# 5.3 2-D wavenumber distribution approaches for enhanced wave splitting in a swirling flow

Referring to Eq. 4.31, we predict the normalized pressure distribution in  $\zeta$  by the inverse transform of the normalized pressures sensed at  $\hat{z}=kz$ . Following Sec. 4.2, this inverse transform could be performed by (i) sampling the pressures,  $\hat{p}(\hat{z}_i)$ , at numerous axial positions,  $i=\{1,2,\ldots,n_a\}$ , at a single frequency ka, or (ii) obtaining the normalized pressure spectrum,  $\eta(\hat{\omega})$ , between two axial positions, z and z', across a broad frequency range, with the non-dimensional frequency,  $\hat{\omega}=k(z'-z)$ . The former approach has been described in our thesis as the single-ka approach while the latter has been referred to as the multi-ka approach. We now extend these approaches to incorporate variable number of sensor rings,  $n_c$ , to allow separate prediction of the normalized pressure distribution,  $\overline{a^2}(\zeta_{\pm m})$ , for the co-rotating and contra-rotating modes.

#### 5.3.1 2-D multi-ka wavenumber distribution methods

In the multi-ka case,  $1 \le n_c \le 2$ . We consider the normalized pressure information at two axial positions, denoted as  $z_e$  and  $z_f$ , such that at least one of them comprises a

circular array of microphones. We predict the azimuthal constituents of the normalized cross-spectra of the pressures sensed at the two axial positions as:

$$\eta_m(\hat{\omega}) = \frac{1}{N_e N_f} \sum_{l=1}^{N_e} \sum_{g=1}^{N_f} e^{-jm\theta_{e(l)}} \eta(z_{e(l)}, z_{f(g)}) e^{jm\theta_{f(g)}}, \tag{5.4}$$

where  $N_e$  and  $N_f$  are the number of azimuthal sensor points at  $z_e = z$  and  $z_f = z'$ , respectively. It may be noted that  $N_f = N$  and  $N_e \in \{1, N\}$  with  $z_{f(g)}$  and  $z_{e(l)}$  denoting the positions of the different circumferential sensors, respectively. Referring to the modal expansion of Eq. 4.31, assuming incoherent modal amplitudes, Eq. 5.4 would be evaluated as:

$$\eta_m(\hat{\omega}) = \sum_n \overline{a_{mn}^2} e^{-j\zeta_{mn}\hat{\omega}}.$$
 (5.5)

From Eqs. 5.4 and 5.5, the azimuthal constituents of the corresponding auto-spectra may be obtained as:

$$\eta_m(0) = \frac{1}{N_e N_f} \sum_{l=1}^{N_e} \sum_{g=1}^{N_f} e^{-jm\theta_e(l)} \eta(z_{f(l)}, z_{f(g)}) e^{jm\theta_f(g)}, \tag{5.6}$$

for which the incoherent modal summation would be,

$$\eta_m(0) = \sum_n \overline{a_{mn}^2}. (5.7)$$

The individual azimuthal constituents are suitably summed across the co-rotating (+m) and contra-rotating (-m) mode orders as:

$$\eta^{\pm m}(\hat{\omega}) = \sum_{+m} \eta_m(\hat{\omega}),\tag{5.8}$$

and

$$\eta^{\pm m}(0) = \sum_{\pm m} \eta_m(0), \tag{5.9}$$

with the corresponding modal summations,

$$\eta^{\pm m}(\hat{\omega}) = \sum_{\pm m,n} \overline{a_{mn}^2} e^{-j\zeta_{mn}\hat{\omega}},\tag{5.10}$$

and

$$\eta^{\pm m}(0) = \sum_{\pm m,n} \overline{a_{mn}^2} = \sigma_{\pm m}(\omega), \tag{5.11}$$

respectively. The ratio of the cross-spectra and auto-spectra would yield the appropriate coherences for the co-rotating and contra-rotating modes between the two axial positions as:

$$C_{ef}^{\pm m}(\hat{\omega}) = \frac{\eta^{\pm m}(\hat{\omega})}{\eta^{\pm m}(0)} = \frac{\sum_{\pm m,n} \overline{a_{mn}^2} e^{-j\zeta_{mn}\hat{\omega}}}{\sigma_{\pm m}(\omega)}$$
(5.12)

The coherence,  $C_{ef}^{\pm m}$ , is observed to collapse across frequencies (ka) and separation distances  $(\Delta z_{ef} = z_f - z_e)$  as a function of  $\hat{\omega} = k\Delta z_{ef}$ . In the high-ka limit, the modal summation in Eq. 5.12 may be approximated as an integral over the propagating range of  $\zeta_{\pm m}$  for the co-rotating and contra-rotating modes as:

$$C_{ef}^{\pm m}(\hat{\omega}) = \int_{\zeta_{\pm m(min)}}^{\zeta_{\pm m(max)}} \overline{a^2}(\zeta_{\pm m}) f(\zeta_{\pm m}) e^{-j\zeta_{\pm m}\hat{\omega}} d\zeta_{\pm m}, \tag{5.13}$$

where we may note that the bounds  $\left[\zeta_{\pm m(min)},\zeta_{\pm m(max)}\right]$  converge asymptotically across frequencies with  $f(\zeta_{\pm m})$  being the corresponding modal density function in  $\zeta_{\pm m}$ . The normalized mean squared mode amplitude distribution,  $\overline{a^2}(\zeta_{\pm m})$ , may be estimated from the inverse transform of Eq. 5.13:

$$\overline{a^2}(\zeta_{\pm m}) = \frac{1}{2\pi f(\zeta_{\pm m})} \int_{-\infty}^{\infty} C_{ef}^{\pm m}(\hat{\omega}) e^{j\zeta_{\pm m}\hat{\omega}} d\hat{\omega}.$$
 (5.14)

Its worth mentioning here that the predicted  $\overline{a^2}(\zeta_{\pm m})$  distribution is ka-independent. Substituting  $\hat{\omega} = 0$  in Eq. 5.13 yields the normalization property of  $\overline{a^2}(\zeta_{\pm m})$ ,

$$\int_{\zeta_{\pm m(min)}}^{\zeta_{\pm m(max)}} \overline{a^2}(\zeta_{\pm m}) f(\zeta_{\pm m}) d\zeta_{\pm m} = 1, \tag{5.15}$$

which is separately satisfied for co-rotating and contra-rotating modes.

#### 5.3.2 2-D single-*ka* wavenumber distribution methods

In the single-ka case,  $1 \leq n_c \leq n_a$ . Here, we estimate the coherence function,  $\mathcal{C}_{if}^{\pm m}(\omega)$ , between the normalized pressures,  $\hat{p}(\hat{z}_i)$ , sensed along an axial array designated by  $\hat{z}_i = \{\hat{z}_1, \hat{z}_2, \dots, \hat{z}_{n_a}\}$ , and the individual circular arrays positioned at  $\hat{z}_f = \{\hat{z}_1, \hat{z}_2, \dots, \hat{z}_{n_c}\}$ . At a single frequency, we denote  $\mathcal{C}_{if}^{\pm m}(\omega)$  as  $\mathcal{C}_f^{\pm m}(\hat{z}_d)$ , where  $\hat{z}_d = \hat{z}_i - \hat{z}_f$  corresponds to the axial separation of the individual axial sensors from the circular array. Referring to Eq. 5.12, in the high-ka limit, the coherence  $\mathcal{C}_f^{\pm m}(\hat{z}_d)$  may be related to the normalized mean squared pressure,  $\overline{p^2}(\zeta_{\pm m})$ , by the Fourier integral,

$$C_f^{\pm m}(\hat{z}_d) = \int_{-\infty}^{\infty} \overline{\hat{p}^2}(\zeta_{\pm m}) e^{j\zeta_{\pm m}\hat{z}_d} d\zeta_{\pm m}, \qquad (5.16)$$

with  $\hat{z}_d$  and  $\zeta_{\pm m}$  forming the appropriate conjugate pairs. The inverse transform would predict the normalized mean squared pressure at the desired value,  $\zeta_{\pm m} = \zeta_b$  as:

$$\overline{\hat{p}_f^2}(\zeta_b) = \frac{1}{n_a} \sum_{i=1}^{n_a} C_f^{\pm m}(\hat{z}_d) e^{-j\zeta_b \hat{z}_d}.$$
 (5.17)

For the case of  $n_c > 1$ , we predict an averaged  $\langle \bar{p}^2(\zeta_b) \rangle$  across the different spatial blocks as:

$$\left\langle \overline{\hat{p}^2}(\zeta_b) \right\rangle = \frac{1}{n_c} \sum_{f=1}^{n_c} \overline{\hat{p}_f^2}(\zeta_b).$$
 (5.18)

In the high-ka limit, assuming incoherent duct modes, Eq. 5.18 would be evaluated as:

$$\left\langle \overline{\hat{p}^2}(\zeta_b) \right\rangle = \int_{\zeta_{\pm m(min)}}^{\zeta_{\pm m(max)}} \overline{a^2}(\zeta_{\pm m}) f(\zeta_{\pm m}) \iota\left(\zeta_{\pm m}, \zeta_b\right) d\zeta_{\pm m}, \tag{5.19}$$

where

$$\iota(\zeta_{\pm m}, \zeta_b) = \frac{1}{n_a n_c} \sum_{f=1}^{n_c} \sum_{i=1}^{n_a} e^{j(\zeta_{\pm m} - \zeta_b)\hat{z}_d}$$
 (5.20)

is the response function which governs the wavenumber resolution, the wavenumber aliasing, the compatible positioning of the sensor rings as well as the dynamic range of the  $\left\langle \overline{\hat{p}^2}(\zeta_b) \right\rangle$  prediction. The behavior of the response function for different numbers and positioning of the sensor rings is discussed in the next section. However, referring to Eq. 5.20, we may note that  $\iota\left(\zeta_{\pm m},\zeta_b\right)$  attains its peak value of unity at  $\zeta_{\pm m}=\zeta_b$ . Restricting the integration range in Eq. 5.19 to within the wavenumber resolution,  $\Delta\zeta_b$ , we obtain the normalized mean squared mode amplitude,  $\overline{a^2}(\zeta_b)$ , averaged out of the  $\Delta\zeta_b$  bandwidth as:

$$\overline{a^2}(\zeta_b) \approx \frac{\left\langle \overline{\hat{p}^2}(\zeta_b) \right\rangle}{\int_{\zeta_b - 0.5\Delta\zeta_b}^{\zeta_b + 0.5\Delta\zeta_b} f(\zeta_{\pm m}) d\zeta_{\pm m}}.$$
 (5.21)

The predicted  $\overline{a^2}(\zeta_{\pm m})$  distribution is generally ka-independent but with finer resolution at higher frequencies. However, a generalized broadband trend may be estimated by frequency-averaging, similar to Eq. 4.26, as:

$$\langle \overline{a^2}(\zeta_{\pm m}) \rangle = \frac{1}{\Delta \omega} \int_{\omega_{min}}^{\omega_{max}} \overline{a^2}(\zeta_{\pm m}) d\omega.$$
 (5.22)

#### 5.3.2.1 Response function of a generic $n_c$ -ring beamformer

After some algebraic manipulations, the response function of Eq. 5.20 may be shown to reduce to the product of two functions,

$$\iota\left(\zeta_{\pm m},\zeta_{b}\right) = \underbrace{\left(\frac{1}{n_{a}}\frac{\sin\left(0.5n_{a}\left(\zeta_{\pm m}-\zeta_{b}\right)k\Delta z\right)}{\sin\left(0.5\left(\zeta_{\pm m}-\zeta_{b}\right)k\Delta z\right)}\right)}_{Line\ array\ response\ function}\underbrace{\left(\frac{1}{n_{c}}\sum_{f=1}^{n_{c}}\left(e^{jk\left(\zeta_{\pm m}-\zeta_{b}\right)\left[\left(z_{1}-z_{f}\right)+\Delta z\left(n_{a}-1\right)0.5\right]}\right)\right)}_{Modulator\ function},$$

$$(5.23)$$

where  $\Delta z$  is the separation distance between the adjacent pair of axial microphones. Note that the response function of the classical axial beamformer (Lowis et al. (2010)) is the magnitude squared of the line array response function mentioned above. The modulator function accounts for the effects of the number of sensor rings and their relative positioning. It will be shown below to modulate the line array response and consequently influence the dynamic range of the beamformer.

Referring to Eq. 5.23, it may be readily inferred that a real value of the response function,  $\iota(\zeta_{\pm m}, \zeta_b)$ , is obtained when the summation of the sine terms in the modulator function equals zero. Since the arguments in the complex exponential of the modulator function are offset with respect to the mid-length of the array,  $\Delta z(n_a - 1)0.5$ , this compatibility function simplifies to,

$$\sum_{f=1}^{n_c} (z_f - z_1) = \frac{n_c(n_a - 1)\Delta z}{2}.$$
 (5.24)

The compatibility condition of Eq. 5.24 suggests that:

- (i) odd number of rings requires an odd number of axial microphones,  $n_a$ ,
- (ii) the circular rings should be symmetrically distributed about the mid-length of the array.

In the following sections, we demonstrate the behavior of the response function for 1-ring and 2-ring beamformers, developable using the ACAT1 intra-stage array instrumentation, to illustrate the effect of the modulator function on the wavenumber resolution and sidelobe contributions in the predicted  $\zeta_{\pm m}$  distribution.

#### 5.3.2.2 1-ring beamformer array

Referring to the ACAT1 intra-stage instrumentation, a compatible 1-ring beamformer is obtained with  $n_a=9$  with the single ring positioned at the mid-span of the array at  $z_f=z_5$ . For this 1-ring beamformer, the modulator function of Eq. 5.23 would evaluate to unity. Fig. 5.5 below depicts the response function of the chosen 1-ring beamformer steered to  $\zeta_b=-1$  at a frequency of ka=55. The beamwidth  $\Delta\zeta_b$  of the main lobe is obtained as the bandwidth corresponding to  $10log_{10}\iota=-3$  dB and is the wavenumber resolution of the predicted  $\zeta_{\pm m}$ -distribution.

The response function exhibits a peak value of unity at  $\zeta = \zeta_b$  with an alternating pattern of positive and negative sidelobes on either side. This alternating sidelobe pattern is crucial in canceling out the sidelobe contributions and focusing the predictions within the main lobe beamwidth,  $\Delta \zeta_b$ .

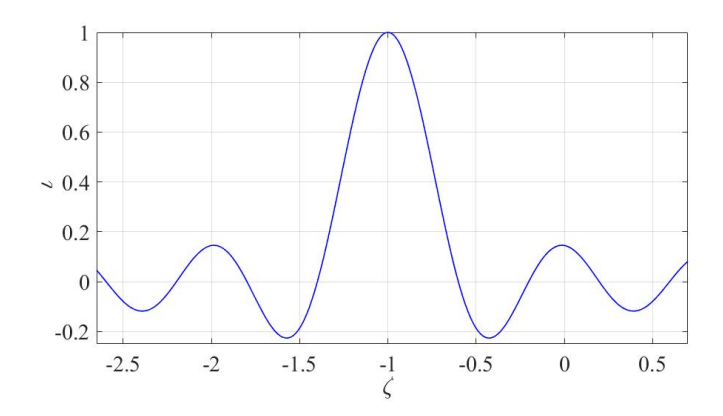


FIGURE 5.5: Behavior of the response function of the chosen 1-ring beamformer.

## 5.3.2.3 2-ring beamformer arrays

For  $n_c = 2$ , the compatibility condition of Eq. 5.24 becomes,

$$(z_{f(1)} - z_1) + (z_{f(2)} - z_1) = (n_a - 1) \Delta z, \tag{5.25}$$

leading to  $(n_a-1)/2$  and  $n_a/2$  symmetric two-ring array configurations for odd and even  $n_a's$ , respectively. Considering the ACAT1 intra-stage instrumentation, Fig. 5.6 below plots the response function of two compatible 2-ring beamformers steered to  $\zeta_b=-1$  at a frequency of ka=55 with the case of two close-by rings at  $z_{f(1)}=z_5$  and  $z_{f(2)}=z_6$  in 5.6a, and two farthest rings at  $z_{f(1)}=z_1$  and  $z_{f(2)}=z_{10}$  in 5.6b. To enable an appreciation of the behavior of the individual response functions, the corresponding line array response, and modulator functions have also been superimposed.

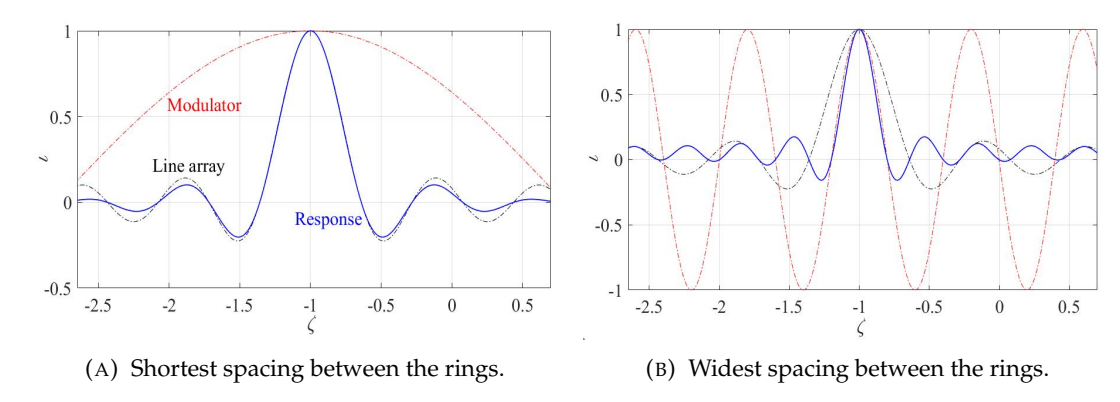


FIGURE 5.6: Behavior of the response function of the 2-ring beamformer with the shortest and widest spacing between the rings.

Referring to the above plots, we may notice that with the two rings close by in Fig. 5.6a, the resolution  $\Delta \zeta_b$  of the beamformer is broader with the sidelobes now depicting an alternating positive and negative pattern, as in Fig. 5.5. On the other hand, with the widest ring spacing in Fig. 5.6b, we obtain a narrower main lobe at the cost of positive sidelobes. This contrasting behavior may be understood by considering the modulator

function of Eq. 5.23, which for  $n_c=2$ , simplifies to  $\cos(0.5k\,(\zeta_{\pm m}-\zeta_b)\,(z_{f(2)}-z_{f(1)}))$  having a half-wavelength given by  $2\pi\,\Big(k(z_{f(2)}-z_{f(1)})\Big)^{-1}$ . Therefore, it could be easily inferred that for the widest ring separation with  $z_{f(2)}-z_{f(1)}=(n_a-1)\Delta z$ , the modulator, and line array response functions have nearly the same half-wavelengths. Consequently, the two functions are almost nearly in phase, making their product positive, which explains the positive sidelobes as well as the narrowing of the main lobe in Fig. 5.6b. On the other hand, with the shortest ring separation, the half-wavelength of the modulator function is much longer, and so we don't loose the alternating sidelobe pattern. Also, a broader modulator function reduces the sidelobe peaks.

The foregoing analysis could be extended to a variable number of sensor rings. For a cage array with  $n_c = n_a$ , the modulator function becomes the same as the line array response function eventually yielding an identical response function as the classical axial beamformer. This explains that the sidelobe levels come down with an increase in  $n_c$ . Hence, with a reduced  $n_c$ , the quality of predictions of the  $\overline{a^2}(\zeta_{\pm m})$  distributions is dependent on the sidelobe cancelation than sidelobe attenuation. In the next section, we illustrate the application of the different 2-D wavenumber distribution approaches on the synthesized dataset of the ACAT1 fan at cutback and assess the quality of their predictions.

## 5.4 Assessment of the mode detection capability of the 2-D wavenumber distribution approaches

The 2-D techniques compatible with the ACAT1 intra-stage array geometry are 1) the two-ring method, 2) 1-ring-1-mic method, and 3) 1-ring beamformer. The 2-ring beamformer, despite finding the necessary instrumentation with  $n_c=2$  and  $n_a=10$ , is incompatible on the ACAT1 intra-stage owing to the incompatible placement of the two rings on the given microphone array geometry at  $z_{f(1)}=z_6$  and  $z_{f(2)}=z_7$  instead of at  $z_{f(1)}=z_5$  and  $z_{f(2)}=z_6$ , referring to Sec. 5.3.2.3. However, for illustration, we demonstrate the mode detection capability of the 2-ring beamformer along with the three compatible 2-D methods. The first two methods listed are the multi-ka methods elaborated in Sec. 5.3.1 with the 1-ring-1-mic method and the two-ring method corresponding to  $n_c=1$  and  $n_c=2$ , respectively. The four methods were implemented on the synthesized dataset of the ACAT1 fan at cutback. Since the purpose of this numerical study is to assess the wave splitting of the different 2-D methods, the circular arrays considered in each of the methods are assumed to be made up of an infinite number of sensing points to be able to estimate the azimuthal mode order spectra up to the highest frequency of interest.

## 5.4.1 2-D multi-ka techniques

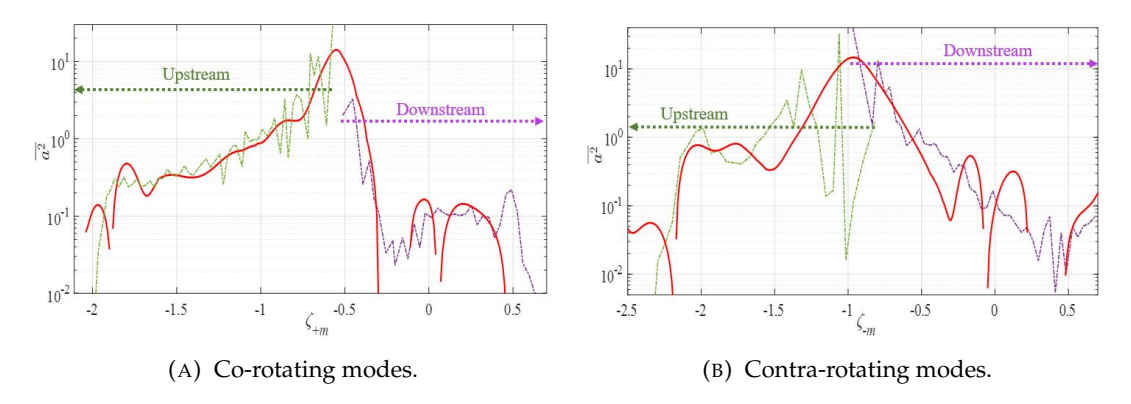


FIGURE 5.7:  $\overline{a^2}(\zeta_{\pm m})$  distributions obtained by implementing the multi-ka methods on the synthesized dataset of the ACAT1 fan at cutback.

Since the two multi-ka methods have a similar mode detection approach, their  $\overline{a^2}(\zeta_{\pm m})$  predictions are identical. Fig. 5.7 shows the predicted  $\overline{a^2}(\zeta_{\pm m})$  distribution for the co-rotating and contra-rotating modes. Also, superimposed are the corresponding theoretical distributions computed separately for the upstream and downstream modes, shown as the green and violet contours, respectively, which have been suitably scaled to match the predicted levels. The comparison reveals a good general overall agreement for both the co-rotating and contra-rotating modes.

The region of interest here is  $\zeta_{\pm m} \in [-1.1, -0.5]$ , which is the wavenumber domain of the modal overlap in Fig. 5.2. For the co-rotating modes (Fig. 5.7a), we notice that there is no modal overlap with  $\zeta_{+m}$  being distinguishable between the upstream and downstream propagations. Consequently, we capture the correct trend of the  $\overline{a^2}(\zeta_{+m})$  distribution consistent with the individual contours. In the case of the -m modes (Fig. 5.7b), there is a very thin region of modal overlap within which the upstream modes are weaker, as discussed in Sec. 5.2.3, and therefore the predictions for these weaker contra-rotating upstream modes are ignored. Overall, our 2-D approach is shown to effectively separate the high-amplitude +m modes from the region of modal overlap and predict their levels to reasonable accuracy.

## 5.4.2 2-D single-*ka* beamformers

#### 5.4.2.1 1-ring beamformer

Fig. 5.8 plots the  $\langle \overline{a^2}(\zeta_{\pm m}) \rangle$  distribution averaged across the frequency range from ka = 15 to ka = 80, predicted using the 1-ring beamformer with  $n_a = 9$  and  $n_c = 1$ .

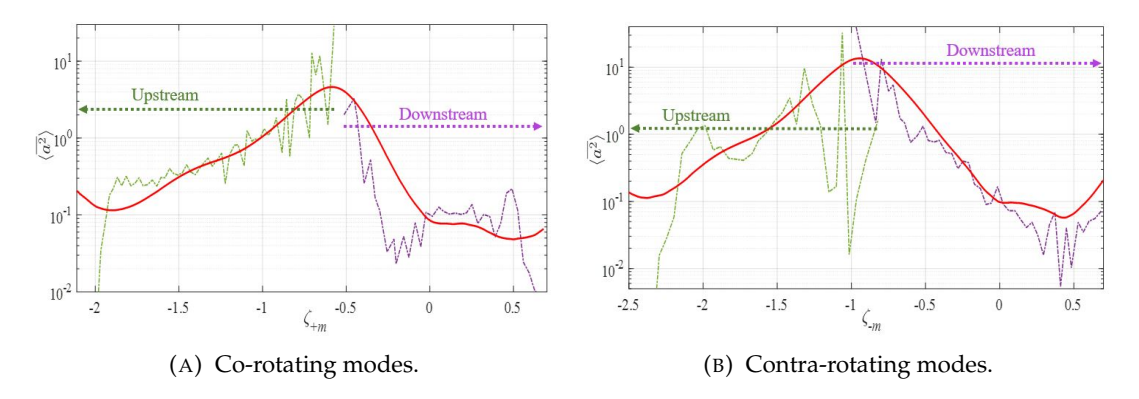


FIGURE 5.8:  $\langle \overline{a^2}(\zeta_{\pm m}) \rangle$  distributions obtained by implementing the *1-ring* beamformer on the synthesized dataset of the ACAT1 fan at cutback.

The wavenumber resolution of the predicted  $\zeta_{\pm m}$ -distribution improves with increasing frequencies, and number of axial sensing positions,  $n_a$ . However, our chosen 1-ring beamformer accomplishes a good wave splitting as in Fig. 5.7.

## 5.4.2.2 2-ring beamformer

Fig. 5.9 plots the  $\langle \overline{a^2}(\zeta_{\pm m}) \rangle$  distribution averaged across the frequency range from ka=15 to ka=80, predicted using the 2-ring beamformer with  $n_a=10$  and  $n_c=2$ . Note that Fig. 5.9 also demonstrates a comparison between the predictions obtained with the widest and shortest ring separation.

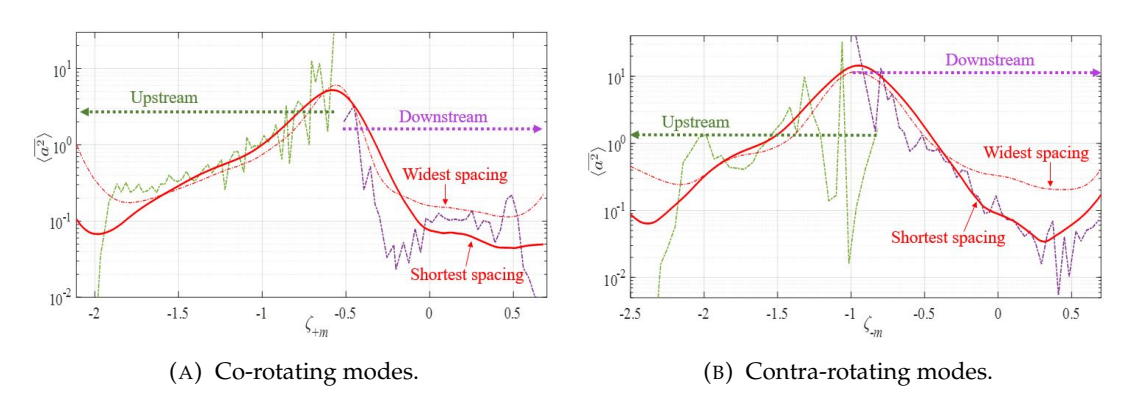


FIGURE 5.9:  $\langle a^2(\zeta_{\pm m}) \rangle$  distributions obtained by implementing the 2-*ring* beamformer on the synthesized dataset of the ACAT1 fan at cutback.

The effect of the sidelobe cancelation in the configuration with the shortest ring separation (refer to Fig. 5.6a) is evident in the predictions for the weaker (downstream) modes. With the widest ring spacing (Fig. 5.6b), the positive sidelobes add up on the weaker downstream side, overpredicting their corresponding levels.

# 5.4.3 Comparison of the relative source balance predicted using the 2-D multi-*ka* and single-*ka* techniques

Fig. 5.10 compares the relative source balance predicted by the 1-ring-1-mic method and the 1-ring beamformer on the synthesized dataset of the ACAT1 fan at cutback.

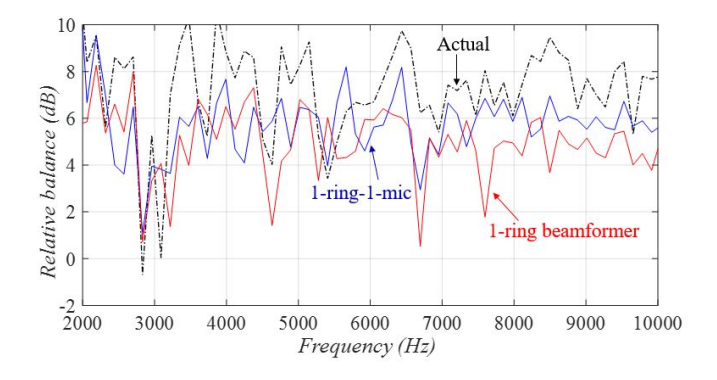


FIGURE 5.10: Comparison of the relative source balance predicted using the 2-D techniques against the actual (target) relative balance, considering the synthesized dataset of the ACAT1 fan at cutback.

We may note that both the single-ka and multi-ka approaches estimate a relative balance of about 5 dB or more across the BB frequency range with the multi-ka methods predicting comparatively better at higher frequencies. Overall, the 2-D methods reveal an improvement in the predictions over the 1-D methods in Fig. 5.3 by separating the dominant +m modes from the region of modal overlap and estimating the preponderance of the OGV over the rotor in the synthesized dataset.

Additionally, we may note that the 2-ring beamformer with the shortest ring spacing predicts a comparable relative balance as the chosen 1-ring beamformer. With the two rings far apart, the relative balance was about 2 dB lesser across the whole frequency range.

## 5.5 Concluding remarks

The problem of broadband acoustic mode detection in the swirling flows of engine intra-stage was systematically studied. A numerical test case was synthesized to obtain a near-identical  $\zeta$ -based relative mode amplitude distribution as the measurement obtained using the ACAT1 intra-stage noise data at cutback by the application of one of the currently available 1-D modal analysis methods originally developed under ideal uniform axial flow conditions. Previous work had demonstrated the physical existence of the modal overlap region in the measured  $\zeta$ -distribution at cutback within which the downstream and upstream modes are indistinguishable in terms of their  $\zeta$ , each of them carrying the dominant high amplitude modes of the fan and OGV, respectively.

Using the synthesized dataset, the existing 1-*D* modal analysis methods were shown to deliver erroneous predictions of the relative source contributions at higher fan speeds owing to the increasing bandwidth of the modal overlap region.

The occurrence of the modal overlap region was subsequently elucidated using the rigid body swirl model by a simple order of magnitude analysis to reveal that the *convective drift* due to the axial and azimuthal flows impacts the cut-on of the duct modes and their wavenumber negativities, eventually leading to the creation of the modal overlap region at higher fan speeds. The study revealed that the  $\pm m$  modal grouping within the modal overlap bandwidth may be reasonably characterized by co-rotating (+m) upstream modes and contra-rotating (-m) downstream modes, thereby calling for 2-D modal analysis methods (based on m and  $\zeta$ ), as opposed to 1-D modal analysis methods (based on  $\zeta$  alone), to accomplish the desired wave splitting in the engine intra-stage.

These 2-*D* modal analysis methods require 2-*D* microphone array geometries characterized by at least one circular ring (to decompose the *m*-orders) and more than one axial measurement position (to measure the relative axial phase difference). A generalized framework for developing these 2-*D* modal analysis methods was presented enabling the development of suitable measurement techniques in any given intra-stage microphone array geometry. Three potential 2-*D* techniques compatible with the intra-stage array geometry of the ACAT1 fan were implemented on the synthesized dataset and shown to deliver reliable predictions of the relative source contributions, identifying the OGV as the preponderant noise source.

# Chapter 6

# Estimation of the relative balance between the rotor and OGV broadband noise

This chapter investigates the measured intra-stage noise data of the ACAT1 fan at approach, and the RR-LSF at 70% fan speed, to separate the relative BB noise contributions of the fan and OGV. A systematic investigation of the intra-stage pressure measurements is presented by analyzing the relative importance of secondary noise sources for the two turbofan rigs with differing intra-stage lengths. Across both fan rigs, a short correlation length scale turbulent flow noise structure is detected to dominate the pressure coherence between adjacent axial microphones, consequently rendering the single-ka modal analysis methods, effective in principle, unreliable for practical implementation. The multi-ka modal analysis methods on the other hand are shown to effectively decorrelate the turbulent flow noise structure by taking the cross-pressure spectra across larger separation distances and extracting the acoustical modal distributions to reliably measure the relative source contributions of the fan and OGV. The final predictions obtained for the ACAT1 intra-stage noise data at approach reveal the OGV to be dominant by about 8 dB across the BB frequency range. This is the first time that a source breakdown of the engine noise data is accomplished without removing the OGV.

# 6.1 Investigation of the relative importance of secondary noise sources

In addition to the cut-on acoustic modes, the microphone pressure signal is contaminated by contributions from numerous secondary noise sources. In this section, we

investigate the influence of these secondary noise sources in the modal analysis of the intra-stage noise data of the ACAT1 fan at approach and RR-LSF rig at 70% fan speed. These secondary noise sources have been classified hereunder:

- Acoustic near-field,
- Rotor hydrodynamic near-field,
- Nearly convected hydrodynamic disturbances,
- Incoherent boundary layer noise, and
- Turbulent flow noise.

#### 6.1.1 Acoustic near-field

The influence of the cut-off (evanescent) acoustic modes was investigated numerically using the equivalent point source model of Sec. 4.1.2, assuming a rigid body swirling flow with averaged  $\overline{M}_z$  &  $\overline{M}_\theta$  values, whilst considering the length-to-diameter ratio and microphone array geometry of the two intra-stages. Since the cut-off acoustic modes are evanescent, their contributions are higher at positions closer to the source planes. Owing to their varying magnitudes across the r-z plane, the cut-off modes increasingly decorrelate the pressures between two points with the widening of their axial separation distance, as shown below in Fig. 6.1, where the magnitude of the pressure coherence is considered between the closest microphone position to the OGV (dominant source) and microphone locations farther upstream. Note that  $\Delta z$  here denotes the adjacent separation distance between the axial microphones.

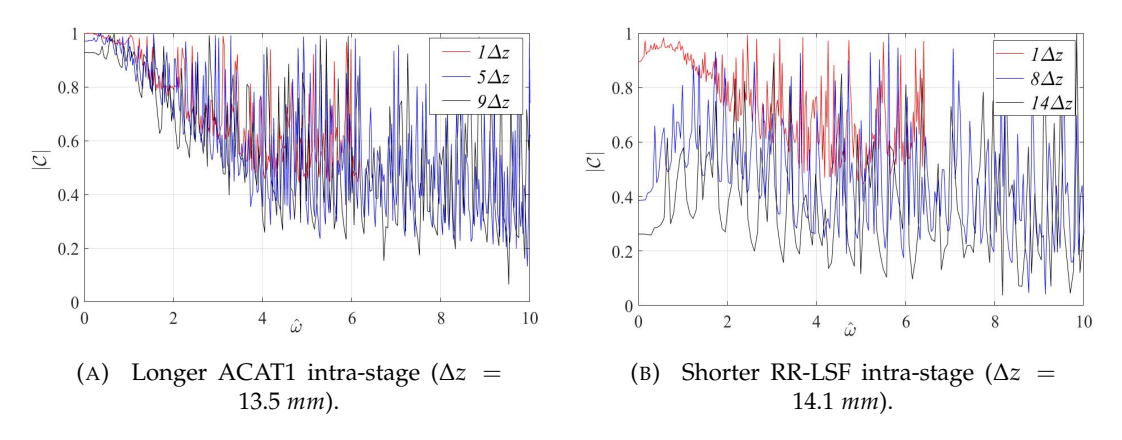


FIGURE 6.1: Illustration of the impact of acoustic near-field using computed pressure coherences of synthesized datasets for the (a) ACAT1 and (b) RR-LSF intra-stages.

The above figure conveys that the cut-off modes add on to incoherent acoustic noise, and their decorrelation effect is significant for the shorter LSF intra-stage and imperceptible for the longer ACAT1 intra-stage. Referring to the intra-stage array geometry

of the two rigs in Sec. 4.5, the measurement array of the ACAT1 LG configuration is positioned sufficiently away from the fan and OGV sources to allow their cut-off modes to decay considerably before reaching the measurement positions.

## 6.1.2 Rotor hydrodynamic near-field

Pressure coherence was measured between different pairs of axial microphones for the ACAT1 and RR-LSF intra-stages. It was observed that for the shorter LSF intra-stage, the magnitude of the pressure coherence for the same separation distance diminished for microphone pairs closer to the fan, as illustrated below in Fig. 6.2a for  $2\Delta z$  separation distance. Note that the legend "1-3" here denotes the coherence between the first and third axial microphones from the fan's proximity. The improvement in coherence away from the fan is attributed to the decay of its hydrodynamic near-field. For the longer ACAT1 intra-stage, the difference in the pressure coherence was imperceptible owing to the microphone array being sufficiently distanced from the fan and hence not shown here. Fig. 6.2b illustrates the influence of the rotor hydrodynamic near-field in

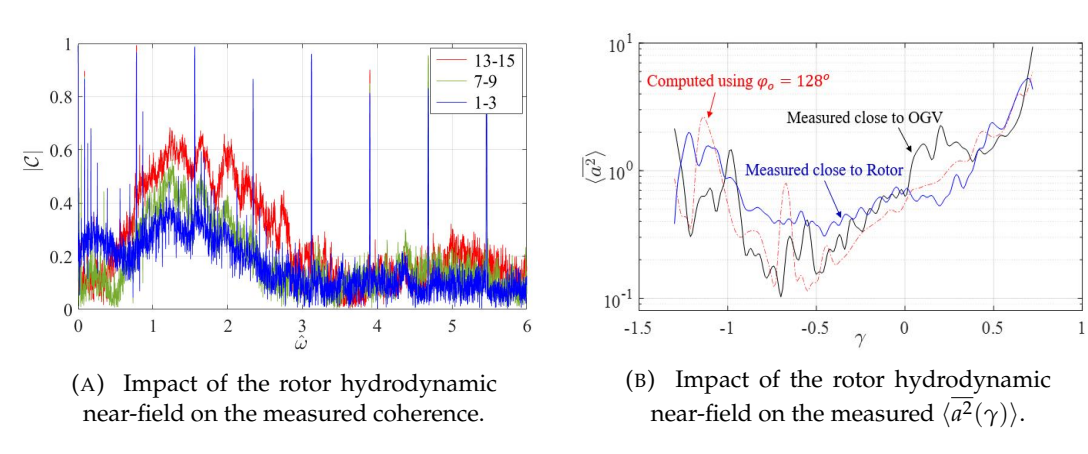


FIGURE 6.2: Impact of the rotor hydrodynamic near-field on the measured coherence and the  $\langle \overline{a^2}(\gamma) \rangle$  distribution of the shorter RR-LSF intra-stage.

measuring the behavior of the sound field along the  $r-\theta$  plane in the LSF intra-stage, wherein we compare the  $\langle \overline{a^2}(\gamma) \rangle$  distributions measured using the microphone rings closer to the fan and OGV against the theoretical distribution computed for the OGV considering a dipole orientation of  $\varphi_0=128^\circ$ . The mismatch between the  $\langle \overline{a^2}(\gamma) \rangle$  measured close to the fan and the theoretical distribution in  $\gamma \in (-1,-0.25)$  is the result of the pseudo-noise contribution of the hydrodynamic near-field.

## 6.1.3 Nearly convected hydrodynamic disturbances

Fig. 6.3 plots the modal spectra measured in terms of the axial wavenumber  $\kappa$  across the broadband frequency range by implementing the classical axial beamformer technique

(Lowis et al. (2010)) on the axial microphone arrays of the ACAT1 and LSF intra-stages.

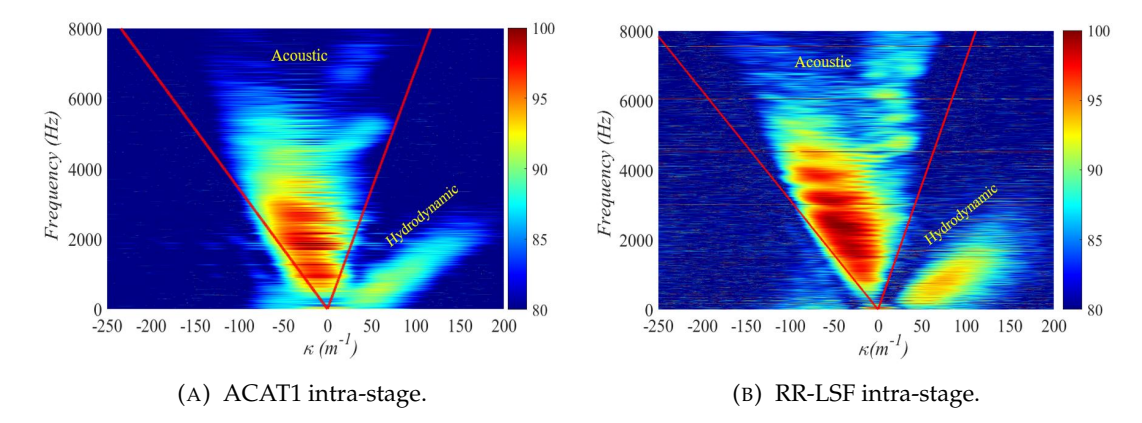


FIGURE 6.3: Measured axial wavenumber spectra of the (a) ACAT1 and (b) RR-LSF intra-stages delineating the propagating acoustic and hydrodynamic regimes.

The two plots above reveal an interesting similarity in modal distribution across the two intra-stages. The red lines in the plots demarcate the corresponding cut-on acoustic limits predicted using *GreenSwirl*. The pressure disturbance outside of this region corresponds to the nearly convected hydrodynamic modes having an axial phase velocity of about  $0.8\overline{U_z}$ . For both the intra-stages, we may notice that the nearly convected hydrodynamic modes are prevalent only up to the  $1^{st}$  BPF, wherein these are still at least 5 dB weaker than the acoustic modes.

## 6.1.4 Incoherent boundary layer noise

The turbulent boundary layer (BL) noise is incoherent between the different microphones. Therefore, when multiple microphones are used, the phase-delay-and-sum between the numerous microphones would effectively suppress the incoherent BL noise and enhance the acoustic coherence of the spectral measurements. The array gain of a

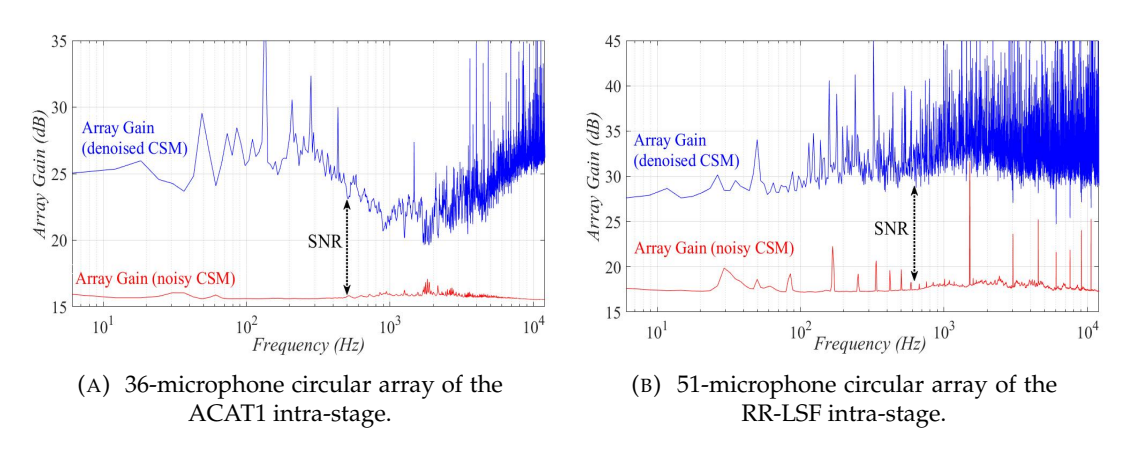


FIGURE 6.4: Measured array gains (in dB) of the circular microphone arrays of the (a) ACAT1 and (b) RR-LSF intra-stages.

N-microphone array is defined as the ratio of the auto-power spectra of a single microphone to the Fourier-transformed spectra of a NxN cross-spectral matrix (CSM). Fig. 6.4 plots the array gain for the circular array measurements of the ACAT1 (6.4a) and LSF (6.4b) intra-stages, which is roughly  $10log_{10}N$  (Sijtsma and Zillmann (2007)). The incoherent BL noise populates along the diagonal elements of the CSM, and may be effectively isolated by diagonal removal (Sijtsma and Zillmann (2007)), or the method of robust principal component analysis (Brunton and Kutz (2019)) applied in the present study. The array gain is noted to improve significantly with the denoising of the CSM in both Figs. 6.4a and 6.4b. The signal-to-noise ratio (SNR) is defined as the difference between the array gains of the denoised and noisy CSM.

The incoherent BL noise was found to be consequential in impacting the measurements at a single axial plane instead of between multiple axial planes. Fig. 6.5 compares the measured  $\langle \overline{a^2}(\gamma) \rangle$  distribution obtained with and without denoising the CSM of the 51-microphone circular array of the LSF intra-stage against the corresponding theoretical distribution computed using  $\varphi_o = 128^\circ$ . The pseudo-noise contribution is evident across a broad range of contra-rotating modes ( $\gamma < 0$ ).

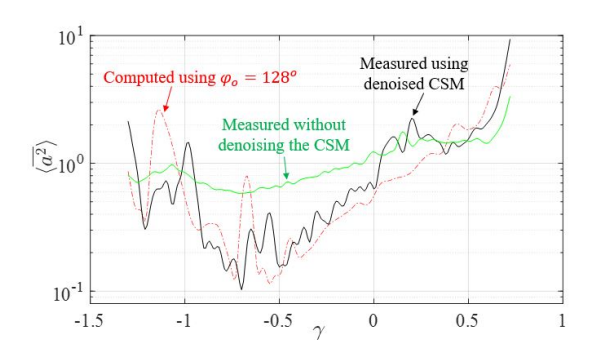


FIGURE 6.5: Impact of the incoherent boundary layer noise on the  $\langle \overline{a^2}(\gamma) \rangle$  distribution obtained using the 51-microphone circular array of the RR-LSF intra-stage.

## 6.1.5 Turbulent flow noise

Fig. 6.6 compares the magnitude of the pressure coherence for different pairs of axial microphones, labeled by their separation distances, for the ACAT1 (6.6a) and LSF (6.6b) intra-stages. The study across the two intra-stages reveals that the coherence decays drastically from  $1\Delta z$  to  $2\Delta z$  separation, gradually collapsing as a function of  $\hat{\omega} = k(z'-z)$  at increasing separation distances. The present investigation therefore detects the presence of a turbulent flow noise structure that has a short correlation length scale of the order of  $\Delta z$  separation distance, which decorrelates with increasing axial spacing to consequently render acoustics-dominated coherence. The source of this turbulence is unknown, but could either be the rotor wakes or the tip vortices.

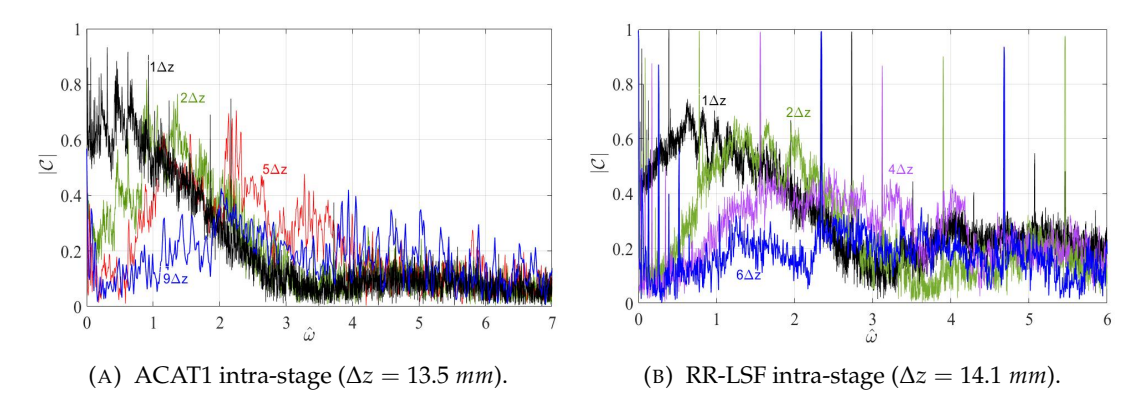


FIGURE 6.6: Impact of the turbulent flow noise structure on the measured wall pressure coherence across different microphone-pair spacing, demonstrated on the (a) ACAT1 and (b) RR-LSF intra-stages.

Overall, a holistic analysis of the different secondary noise sources bears out that the turbulent flow noise of short correlation length scale is singularly influential in affecting the pressure measurements across the r-z plane, which are crucial to predicting the relative mode amplitude distribution and thence the relative source contributions. In the following section, we illustrate that this turbulent flow noise structure inevitably renders the single-ka modal analysis methods, effective in principle, unreliable for practical implementation. We go on to demonstrate that the multi-ka modal analysis methods allow an effective decorrelation of this turbulent flow noise structure (as already demonstrated in Fig. 6.6) to extract the acoustical modal distributions used to estimate the relative source contributions.

# 6.2 Application of the different phased array techniques on the ACAT1 intra-stage noise data at approach

In this section, we consider the intra-stage noise data of the ACAT1 fan at approach, and demonstrate the influence of the turbulent flow noise phenomenon of Sec. 6.1.5 on the single-ka and multi-ka modal analysis methods. The multi-ka methods considered here are the two-microphone method (Sec. 4.2.4) and the 1-ring-1-mic method (Sec. 5.3.1), and the single-ka method considered is the classical axial beamformer (Lowis et al. (2010)).

## 6.2.1 Application of the two-microphone method

The pressure coherences measured across the different separation distances in Fig. 6.6a are inverse transformed as per Eq. 4.38 to predict the non-dimensional  $\overline{a^2}(\zeta)$  distribution, plotted in Fig. 6.7a. Also, plotted alongside is the phase of the complex coherence

in Fig. 6.7b. We note in Fig. 6.7b that the coherence between the adjacent microphones

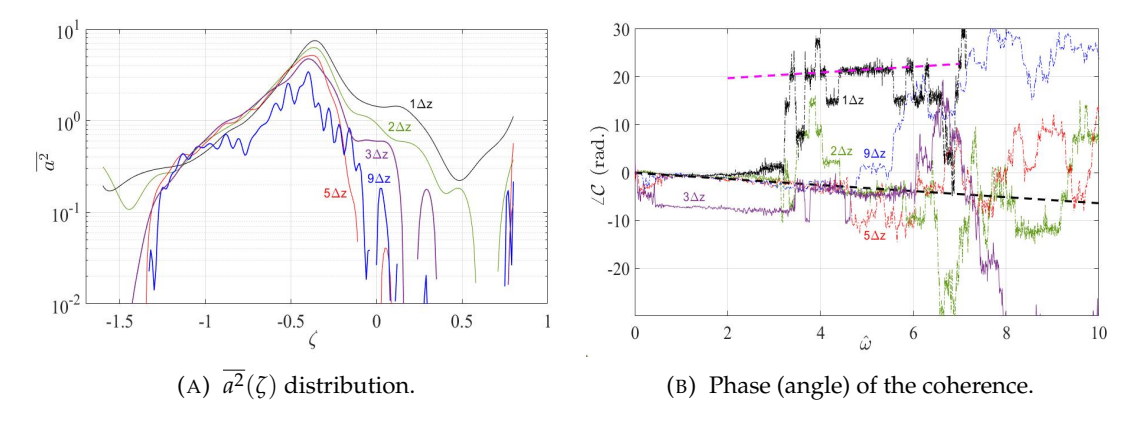


FIGURE 6.7: Results obtained by applying the two-microphone method across different microphone-pair spacing on the ACAT1 intra-stage noise data at approach.

has a constant phase (slope) of  $\zeta=0.6$  across the broadband frequency range, as indicated by the dashed magenta line. On the other hand, the coherence at larger separation distances has a phase of  $\zeta=-0.64$ , as indicated by the dashed black line. Note that the coherence at larger separation distances collapses as a function of  $\hat{\omega}$  except for  $2\pi$  unwrapping issues. The differing phase of the coherence between adjacent microphones indicates the dominance of the turbulent flow noise structure of comparable correlation length scale, as discussed in Sec. 6.1.5. Fig. 6.7a reveals the gradual collapse of the measured  $\overline{a^2}(\zeta)$  distribution at increasing separation distances.

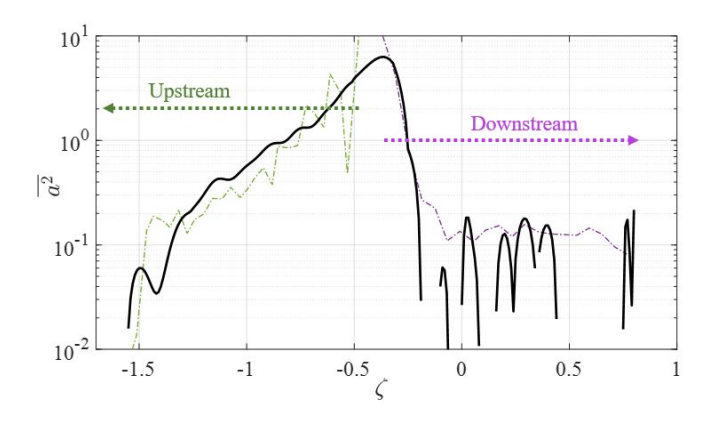


FIGURE 6.8: Spatially averaged  $\overline{a^2}(\zeta)$  distribution obtained by the implementation of the two-microphone method on the ACAT1 intra-stage noise data at approach. Note that the superimposed green and violet curves correspond to the theoretical distributions computed separately for the upstream and downstream modes respectively.

Referring to Fig. 6.7a, it is interesting to note that the pseudo-noise contribution is prevalent from the vicinity of  $\zeta=0$ , corresponding to the downstream modes, with the predictions for the upstream wavenumbers (the dominant side) almost unaffected. Importantly, Fig. 6.7 suggests that the  $\overline{a^2}(\zeta)$  predictions may be selectively averaged across the larger separation distances to avoid the influence of the pseudo-noise as well as wholly predict the relative mode amplitude distribution across the complete

propagating range of  $\zeta$  spanning from the upstream modes to downstream modes, as shown in Fig. 6.8 by the black curve. Also, superimposed are the corresponding theoretical modal distributions computed separately for the upstream modes ( $\varphi_0 = 128^\circ$ ) and downstream modes ( $\varphi_r = 20^\circ$ ) using our equivalent point source model, which are shown as the pale green and violet curves, respectively. The match between the measured and theoretical modal distributions is convincing to justify the extraction of the acoustical information from the flow-noise-contaminated pressure measurements.

## 6.2.2 Application of the axial beamformer method

The axial beamformer method is a one-dimensional single-ka modal analysis approach, and referring to Sec. 5.3.2, it may be inferred that the method involves a phase-delay-and-sum of the pressure coherences between the individual microphones of an axial array and a reference sensor belonging to the array. Consequently, the single-ka modal analysis framework doesn't allow spatial filtering, permitted with the multi-ka approach, resulting in the predicted modal distribution being significantly contaminated by the turbulent flow noise, as shown below in Fig. 6.9, wherein we plot the  $\langle \overline{a^2}(\zeta) \rangle$  distributions averaged across the low-frequency range between 2-3 kHz and high-frequency range between 7-10 kHz, which were found to match well with the  $\overline{a^2}(\zeta)$  distributions predicted using the two-microphone method for  $3\Delta z$  and  $1\Delta z$  separation distances, respectively, also included in the figure for comparison.

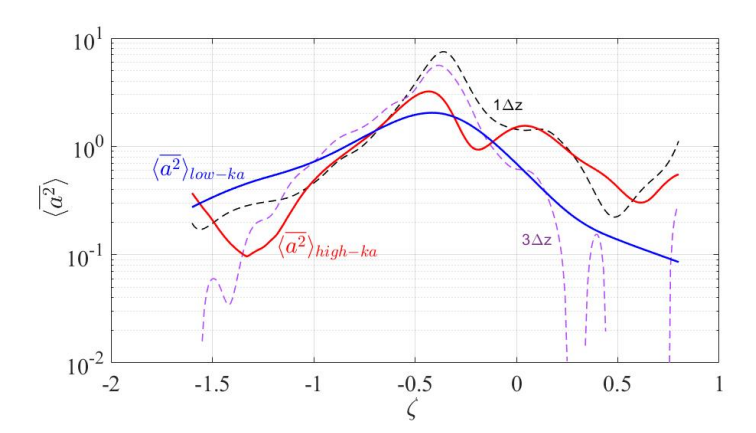


FIGURE 6.9:  $\langle a^2(\zeta) \rangle$  distributions, averaged across lower and higher frequencies, obtained by the implementation of the axial beamformer on the ACAT1 intra-stage noise data at approach compared against the corresponding  $\overline{a^2}(\zeta)$  distributions predicted using the two-microphone method for  $1\Delta z$  and  $3\Delta z$  spacing.

Referring to Fig. 6.7a, we may note that the turbulent flow noise structure is effectively decorrelated only beyond  $4\Delta z$  separation distance. So, the relative mode amplitude distribution predicted using the axial beamformer, or any other single-ka modal analysis technique, is heavily contaminated by the short-correlation-length-scale turbulent flow noise structure, rendering these methods, albeit effective in principle, unsuitable for practical implementation.

## 6.2.3 Application of the 1-ring-1-mic method

Following the arguments presented above, the only 2-D method that is compatible with the ACAT1 intra-stage instrumentation and allows for effective spatial filtering is the 1-ring-1-mic method. We note here that an excellent collapse was observed in the measured  $\overline{a^2}(\zeta_{\pm m})$  modal distributions obtained for axial separation distances of  $4\Delta z$  and beyond between the microphone ring and the reference microphone. However, for brevity, we only include the spatially-filtered-and-averaged  $\overline{a^2}(\zeta_{\pm m})$  modal distribution for the co-rotating and contra-rotating modes in Fig. 6.10, plotted as the black curves, with the corresponding theoretical modal distributions for fan and OGV also superimposed as the pale violet and green curves, respectively, to facilitate a comparative study. An excellent agreement between the measured and theoretical modal distributions may be observed across both upstream and downstream modes.

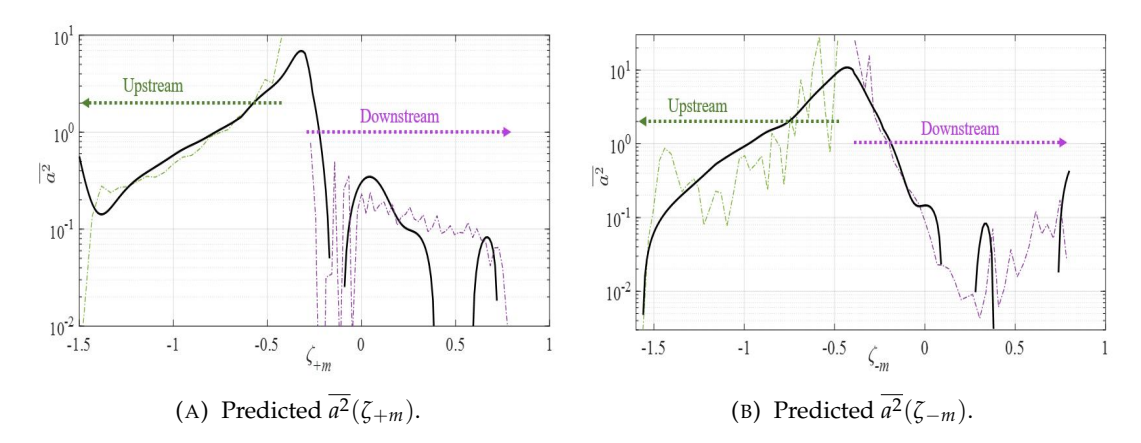


FIGURE 6.10:  $\overline{a^2}(\zeta_{\pm m})$  distributions predicted by implementing the 1-ring-1-mic method on the measured ACAT1 intra-stage noise data at approach. Note that the superimposed green and violet curves correspond to the theoretical distributions computed separately for the upstream and downstream modes respectively.

Referring to the arguments presented in Sec. 4.6.3, for a dipole orientation of  $\varphi_r = 20^{\circ}$  for the downstream modes:

- For contra-rotating modes, the axial and azimuthal components in the magnitude-squared of the dipole directivity term add up for  $\zeta_{-m} < 0$ , while the two possess opposite signs for  $\zeta_{-m} > 0$  implying some cancelation. Consequently, in Fig. 6.10b for the downstream modes, we notice the lowest pressure in the vicinity of  $\zeta_{-m} = 0.4$  beyond which the relative modal amplitude distribution steadily rises.
- For co-rotating modes, the axial and azimuthal components in the magnitude-squared of the dipole directivity term add up for  $\zeta_{+m} > 0$ , while the two possess opposite signs for  $\zeta_{+m} < 0$  implying some cancelation. Correspondingly, in Fig.

6.10a, for the downstream modes, we witness a dip in the relative mode amplitude distribution in the vicinity of  $\zeta_{+m}=-0.1$  and higher mode amplitudes across  $\zeta_{+m}>0$ .

The matching between the measured and theoretical modal distributions, particularly for the weaker downstream modes, indicates that the mode amplitude predictions here are not influenced by any modal scattering phenomenon.

## 6.3 Investigations using the RR-LSF intra-stage noise data

The arguments presented in Sec. 6.2 above apply equally to the RR-LSF intra-stage noise data. Hence, for completeness, in this section, we demonstrate the application of the 1-*ring*-1-*mic* method on the measured intra-stage noise data of the RR-LSF rig at 70% fan speed. Considering the axisymmetric geometry of the microphone ring, we note here that the predicted azimuthal mode order spectra are aliased beyond the  $2^{nd}$  BPF. However, the aliasing effects are significant across the weaker contra-rotating *m*-orders, and therefore the dominant +m mode orders could be usefully decomposed across the broadband frequency range of interest.

## 6.3.1 Application of the 1-ring-1-mic method

Fig. 6.11 plots the measured  $a^2(\zeta_{+m})$  modal distribution as the black curve, with the corresponding theoretical modal distributions for the fan and OGV superimposed as the pale violet and green curves, respectively. The comparative study demonstrates a convincing match between the measured and theoretical modal distributions on the LSF intra-stage.

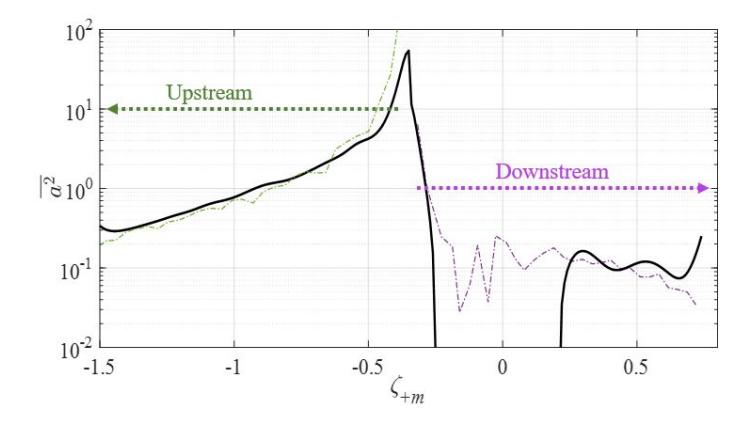


FIGURE 6.11:  $a^2(\zeta_{+m})$  predicted by implementing the 1-ring-1-mic method on the measured LSF intra-stage noise data. Note that the superimposed green and violet curves correspond to the theoretical distributions computed separately for the upstream and downstream modes respectively

It may be noted here that from the net summation,  $\sum_{+m} \overline{A^2}(\zeta_{+m}, \omega)$ , for the co-rotating modes, the contribution due to the contra-rotating modes may be estimated using the relative modal split,  $\sigma_{\pm m}(\omega)$ , calculated based on the equivalent point source model with appropriate dipole orientations, thereby overcoming the measurement limitations due to aliasing.

## 6.4 Source separation of the fan BB noise of the ACAT1 intrastage at approach

From the predicted non-dimensional mean squared mode amplitude distributions,  $\overline{a^2}(\zeta)$  and  $\overline{a^2}(\zeta_{\pm m})$ , the dimensional mean squared mode amplitude distributions may be suitably estimated and appropriately summed across the upstream and downstream modes to determine the relative source balance defined as  $10log_{10}\left(\sum \overline{A^2}(\zeta^-)/\sum \overline{A^2}(\zeta^+)\right)$ . Sec. 6.4.1 below compares the relative source balance estimated using the different phased array techniques on the ACAT1 intra-stage noise data at approach, and Sec. 6.4.2 subsequently presents the final BB noise breakdown estimated using the multi-ka methods.

# 6.4.1 Comparison of the relative source balance predicted using the different methods

Fig. 6.12 below presents the relative source balance estimated using the different 1-D (6.12a) and 2-D (6.12b) modal analysis methods. We may readily note that at approach, with negligible modal overlap (refer to Fig. 5.1), the corresponding 1-D and 2-D modal analysis methods predict almost the same relative balance.

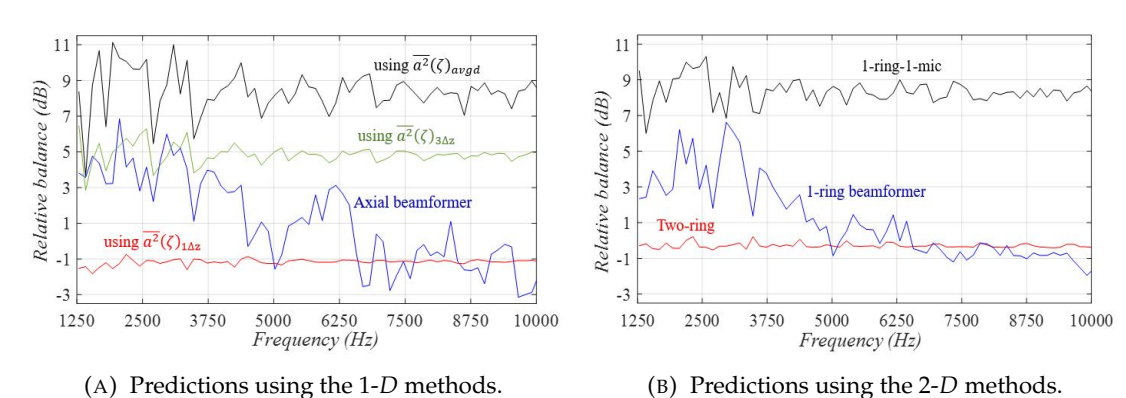


FIGURE 6.12: Comparison of the relative source balance predicted using the different 1-*D* and 2-*D* phased array techniques on the ACAT1 intra-stage noise data at approach.

Fig. 6.12 summarizes this chapter's overall investigations. The lower limit of the relative balance is about -1 dB, estimated using the two-microphone and two-ring methods implemented across the separation distance of  $1\Delta z$ . In Fig. 6.12a, note that the relative source balance estimated by the axial beamformer technique drops from about 5 dB at the lower frequencies, comparable with the predictions of the two-microphone method across  $3\Delta z$  separation distance, to around -1 dB at the higher frequencies. This behavior may be understood from Fig. 6.9. A similar trend in the estimated relative balance could also be observed with the 1-ring beamformer in Fig. 6.12b. Finally, the relative source balance estimated by the spatially-filtered-and-averaged  $\overline{a^2}(\zeta)$  and  $\overline{a^2}(\zeta_{\pm m})$  modal distributions of Figs. 6.8 and 6.10, respectively, is about 8 dB across the broadband frequency range.

#### 6.4.2 Final noise breakdown

The broadband noise levels of the fan and OGV predicted using the appropriate spatially-filtered-and-averaged  $\overline{a^2}(\zeta)$  and  $\overline{a^2}(\zeta_{\pm m})$  modal distributions of the two-microphone and 1-*ring*-1-*mic* methods are close to within 1 dB. Fig. 6.13 plots the broadband noise spectra of the two sources estimated using the multi-ka methods. This is the first time that a source breakdown of the fan BB noise has been accomplished without removing the OGV.

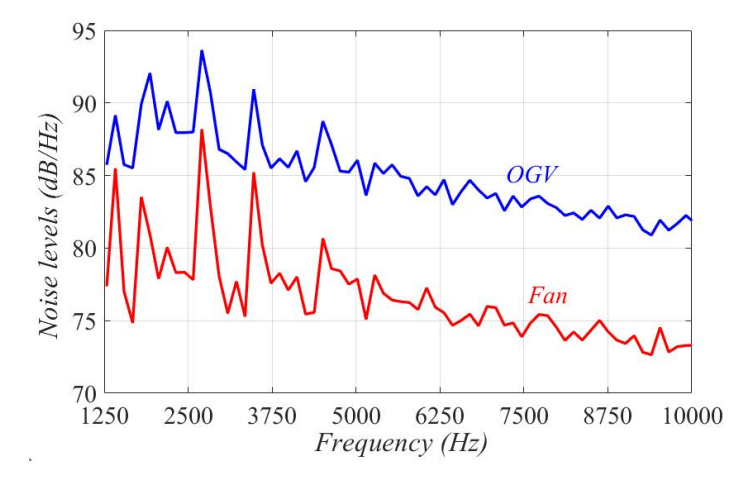


FIGURE 6.13: Predicted broadband noise levels of the fan and the OGV using the measured ACAT1 intra-stage noise data at approach ( $ref.: 20 \mu Pa$ ).

## 6.5 Concluding remarks

This chapter investigated the measured intra-stage noise data of the ACAT1 fan at approach, and the RR-LSF rig at 70% fan speed, to separate the relative BB noise contributions of the fan and OGV. The work presented a systematic investigation of the relative influence of different secondary noise sources across the two intra-stages, classified as i)

Acoustic near-field, ii) Rotor hydrodynamic near-field, iii) Nearly convected hydrodynamic disturbances, iv) Incoherent boundary layer noise, and v) Turbulent flow noise. The complete analysis revealed that the turbulent flow noise of short correlation length scale dominates the pressure coherence between adjacent axial microphones, eventually rendering the single-ka modal analysis methods, effective in principle, unreliable for practical implementation. The multi-ka modal analysis methods, on the other hand, were shown to permit an effective decorrelation of this turbulent flow noise structure by taking the cross-pressure spectra across larger separation distances and extracting the acoustical modal distributions to reliably measure the relative source contributions of the fan and OGV. The final predictions obtained for the ACAT1 intra-stage noise data at approach revealed the OGV to be dominant by about 8 dB across the BB frequency range. This is the first time that a source breakdown of the engine noise data has been accomplished without removing the OGV.

# Chapter 7

# Source separation of the fan broadband noise at higher engine speeds

In this chapter, we consider the measured intra-stage noise data of the ACAT1 fan at cutback to demonstrate the source separation at higher fan speeds. Work presented in Chapter 5 considered the synthesized dataset of the ACAT1 fan at cutback to numerically show that the two-dimensional modal analysis methods are more effective than the standard one-dimensional methods at separating the dominant high-amplitude modes of the fan and the OGV to accomplish the desired wave splitting at higher fan speeds. This chapter implements the 1-*ring*-1-*mic* method developed in Chapter 5 on the measured noise data, and the mode amplitude distributions so obtained are shown to be in excellent agreement with the corresponding numerical predictions. The final predictions obtained for the ACAT1 intra-stage noise data at cutback reveal the OGV to be dominant by about 6 *dB*, as demonstrated using the corresponding synthesized dataset.

# 7.1 Primary investigations of the ACAT1 intra-stage noise data at cutback

Following the arguments presented in Chapter 6, we note that the coherence measured between the adjacent axial microphones in an intra-stage is dominated by a turbulent flow noise structure, which eventually renders the single-ka modal analysis methods, effective in principle, unsuitable for practical implementation. This aspect is demonstrated in Fig. 7.1 for the cutback noise data, where we plot the pressure coherence measured between the different pairs of axial microphones. Note the drastic decay in

the magnitude of the coherence from  $1\Delta z$  separation distance and the gradual collapse at higher separation distances in Fig. 7.1a. Alongside, in Fig. 7.1b, note that the phase (or slope) of the complex coherence is constant at  $\zeta=0.5$  across the BB frequency range for  $1\Delta z$  separation distance, as indicated by the dashed magenta line, whilst the phase at larger separation distances collapses across frequencies and microphone-pair spacing as a function of  $\hat{\omega}=k(z'-z)$  (except for the  $2\pi$  unwrapping issues) with a constant value of  $\zeta=-1.3$ , as indicated by the black dashed line.

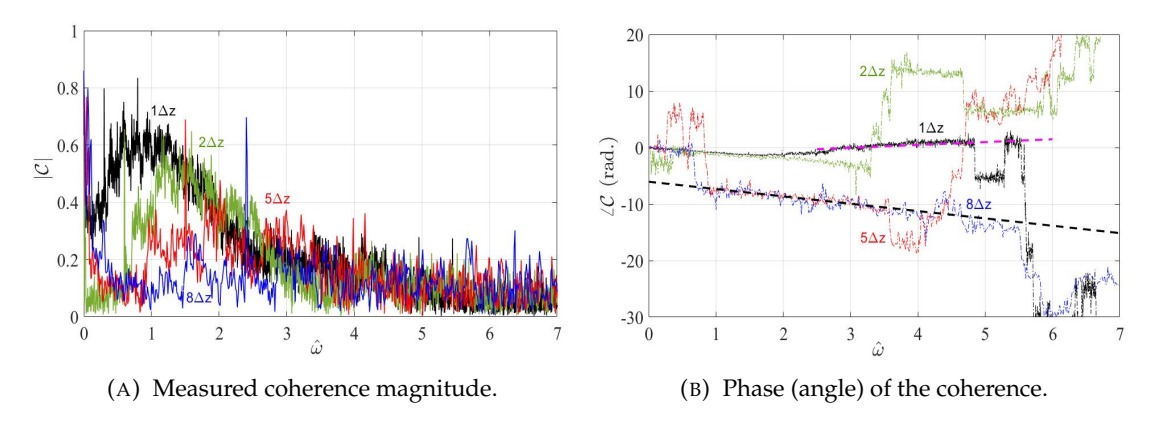


FIGURE 7.1: Coherence measured across different microphone-pair spacing on the ACAT1 intra-stage noise data at cutback.

## 7.1.1 Two-microphone technique, and the modal overlap

The measured coherences of Fig. 7.1 are inverse transformed as per Eq. 4.38 to predict the corresponding non-dimensional mean squared mode amplitude distribution,  $\overline{a^2}(\zeta)$ , plotted in Fig. 7.2a.

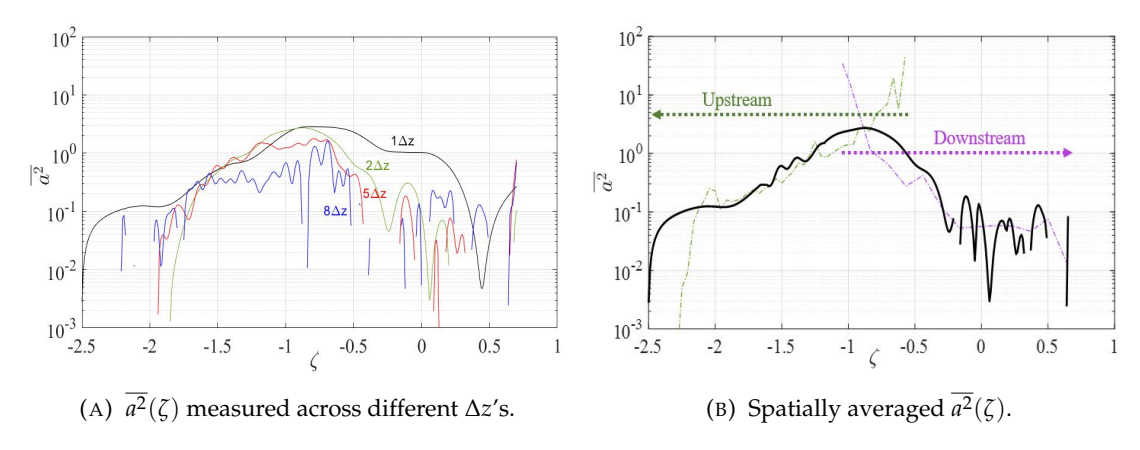


FIGURE 7.2:  $\overline{a^2}(\zeta)$  distribution predicted by the implementation of the two-microphone method on the ACAT1 intra-stage noise data at cutback. Note that the superimposed green and violet curves in (b) correspond to the theoretical distributions computed separately for the upstream and downstream modes respectively.

Note the collapse in the  $\overline{a^2}(\zeta)$  distributions beyond the  $1\Delta z$  separation distance, which are spatially averaged to predict a continuous contour shown alongside in Fig. 7.2b,

with the corresponding theoretical mean squared mode amplitude distributions for the fan and OGV superimposed as the pale violet and green curves, respectively. Note that Fig. 7.2b was referred to in Chapter 4, based on which a synthesized dataset was generated using our equivalent point source model and used for the numerical investigations in Chapter 5. Referring to Fig. 7.2b,  $\zeta \in [-1.1, -0.5]$ , is the region of modal overlap within which the dominant high-amplitude modes of the fan and OGV are indistinguishable in terms of  $\zeta$  and thus predicted to the same levels irrespective of their actual relative magnitudes, leading to erroneous predictions of the relative source contributions using the standard 1-D modal analysis methods. Application of the 2-D modal analysis methods was shown in Chapter 5 to separate the dominant modes trapped within the overlap bandwidth and accomplish the desired wave splitting. From our foregoing discussion, we note that the 1-ring-1-mic method, which is a 2-D multi-ka modal analysis method, shall allow the spatial-filtering-and-averaging of the predicted modal distributions (like Fig. 7.2) to avoid the confounding influence of the pseudonoise as well as separate the dominant modes from the overlap bandwidth.

# 7.2 Application of the 1-ring-1-mic method to separate the fan and OGV modes

Fig. 7.3 plots the  $\overline{a^2}(\zeta_{\pm m})$  modal distributions predicted using the 1-*ring*-1-*mic* method on the measured noise data as the black curves, compared against the corresponding numerical distributions predicted using the method on the synthesized dataset, shown as the pale red curves. An excellent agreement between the measured and numerical  $\overline{a^2}(\zeta_{\pm m})$  predictions may be observed across both upstream and downstream modes.

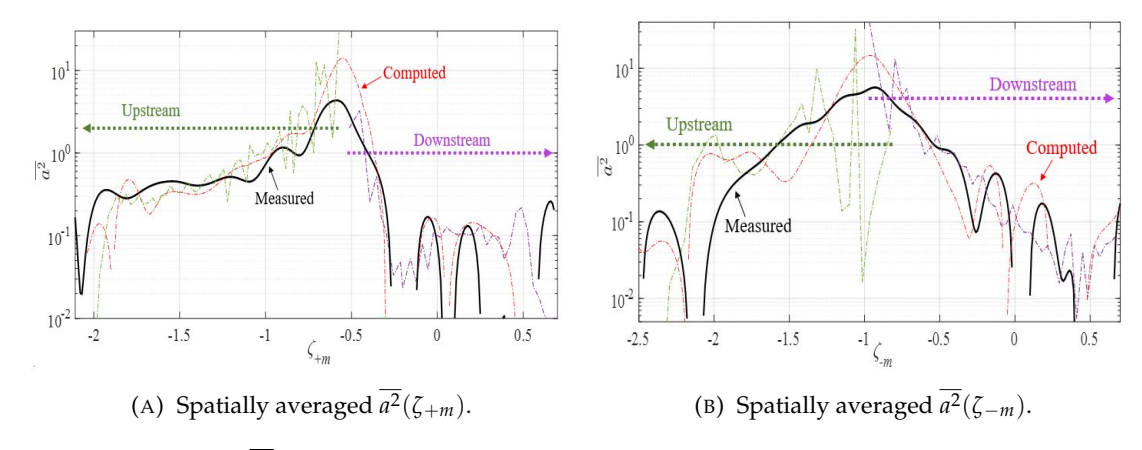


FIGURE 7.3:  $a^2(\zeta_{\pm m})$  distributions predicted using the 1-*ring*-1-*mic* method on the ACAT1 intra-stage noise data at cutback compared against the corresponding numerically computed distributions obtained using the synthesized dataset. Note that the superimposed pale green and violet curves correspond to the theoretical modal distributions computed separately for the upstream and downstream modes, respectively.

## Fig. 7.3 reveals some important features:

- For  $\zeta_{+m} \in [-1.1, -0.5]$  in Fig. 7.3a, we note that the measured mode amplitude distribution depicts a steadily rising trend, consistent with the corresponding numerical as well as theoretical modal distributions, indicating that the dominant co-rotating modes of the OGV are now separated from the overlap bandwidth of Fig. 7.2b. On the other hand, for  $\zeta_{-m} \in [-1.1, -0.5]$  in Fig. 7.3b, we witness a steadily decaying trend. Therefore, the two-dimensional approach of the 1-*ring*-1-*mic* method has been shown on the measured data to separate the dominant co-rotating modes of the OGV from the overlap bandwidth and accomplish the appropriate wave split-up.
- The presence of the low-pressure dip in  $\zeta_{+m} < 0$  and  $\zeta_{-m} > 0$  for the downstream modes in Figs. 7.3a and 7.3b, respectively, could be understood as the effect of *convective amplification* for a rotor dipole of orientation,  $\varphi_r = 20^\circ$ , following the arguments presented in Sec. 6.2.3.

## 7.3 Source separation of the fan BB noise of the ACAT1 intrastage at cutback

## 7.3.1 Predicted relative source balance

The acoustical modal distributions predicted in Fig. 7.3 are used to suitably estimate the dimensional mean squared mode amplitude distributions,  $\overline{A^2}(\zeta_{\pm m}^\pm)$ , which may be appropriately summed across the upstream and downstream modes to determine the relative source balance. Fig. 7.4 plots the relative balance estimated with and without using the  $\sigma_{+m}(\omega)$  modal split on the measured distributions, and compares them with the computed and target relative balance obtained using the synthesized dataset.

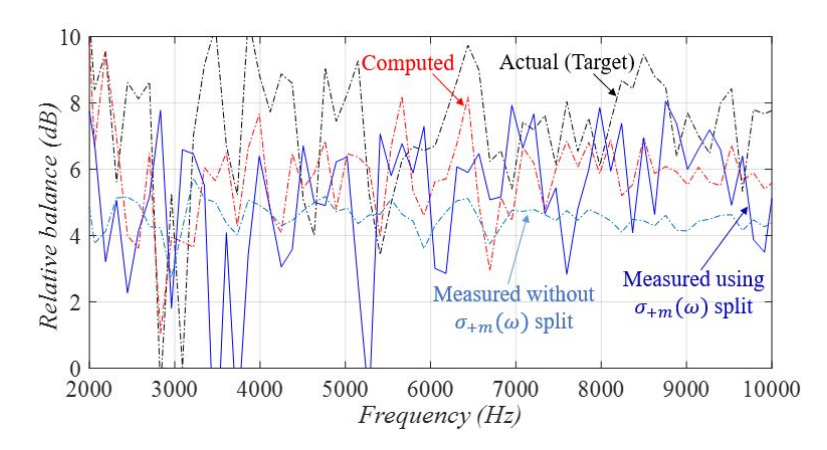


FIGURE 7.4: Comparison between the measured and numerically predicted relative source balance for the ACAT1 intra-stage noise data at cutback.

The comparative study in Fig. 7.4 shows the relative balance estimated using the theoretical  $\sigma_{+m}(\omega)$  modal split on the measured  $\overline{a^2}(\zeta_{+m})$  modal distributions matches well with the computed relative balance obtained by implementing the 1-*ring*-1-*mic* method on the synthesized dataset. On the other hand, the relative balance obtained directly using the measured  $\overline{a^2}(\zeta_{\pm m})$  modal distributions of Fig. 7.3 is underestimated.

Referring to Sec. 4.5.1.2, we note that the sparse circular array of the ACAT1 intra-stage permits an unaliased detection of the higher *m*-orders beyond the Nyquist criterion,  $-N/2 < m \le N/2$ , unlike an equispaced circular array, but at the cost of sidelobe noise additions. Therefore, even though, the dynamic range of the circular array of Fig. 4.5b is about 11 dB for  $\Delta m \in [1,500]$ , the sidelobe contributions from the dominant co-rotating modes add up to the levels of the weaker contra-rotating modes. Referring to Appendix F, we note that at cutback, the difference between  $\sigma_{+m}^+(\omega)$  and  $\sigma_{-m}^-(\omega)$ is much greater than at approach. Consequently, the sidelobe noise additions across the broader m-range of contra-rotating modes at cutback overestimate the total noise levels,  $\sum \overline{A^2}(\zeta_{-m}^+) + \sum \overline{A^2}(\zeta_{+m}^+)$ , for the downstream modes, thereby predicting a reduced relative source balance, as depicted by the pale blue curve in Fig. 7.4. With the use of the theoretical  $\sigma_{+m}^{\pm}(\omega)$  values, computed based on our equivalent point source model for  $\varphi_0 = 128^{\circ}$  and  $\varphi_r = 20^{\circ}$ , on the measured  $\sum \overline{A^2}(\zeta_{+m}^{\pm})$  to predict the total levels of the contra-rotating modes,  $\sum \overline{A^2}(\zeta_{-m}^{\pm})$ , we greatly reduce the impact of the sidelobe contributions, and the relative balance so estimated is found to be about 2 dB greater beyond 5 kHz, closely matching with the relative source balance computed using the synthesized dataset. Comparison against the result predicted using the synthesized dataset demonstrates that the use of theoretical  $\sigma_{+m}(\omega)$  modal split values effectively minimizes the impact of the sidelobe noise without the use of any deconvolution (Sijtsma and Brouwer (2018)) or sparsity-based reconstruction (Pereira and Jacob (2022)) algorithms. Overall, the 1-ring-1-mic method, along with the prior knowledge of the  $\sigma_{+m}^{\pm}(\omega)$  modal splits, has been shown here to predict an accurate relative source balance at higher fan speeds, overcoming the inherent challenges due to the modal overlap and sidelobe noise.

## 7.3.2 Final noise breakdown

The broadband noise levels of the fan and OGV predicted by the appropriate combination of the theoretical  $\sigma_{+m}^{\pm}(\omega)$  split and the spatially-filtered-and-averaged  $\overline{a^2}(\zeta_{+m})$  modal distribution of Fig. 7.3a is shown in Fig. 7.5, wherein the OGV noise is dominant by about 6 dB across the broadband frequency range. In contrast to the predicted BB noise spectra at approach in Fig. 6.13, we notice fairly flat noise spectra at cutback.

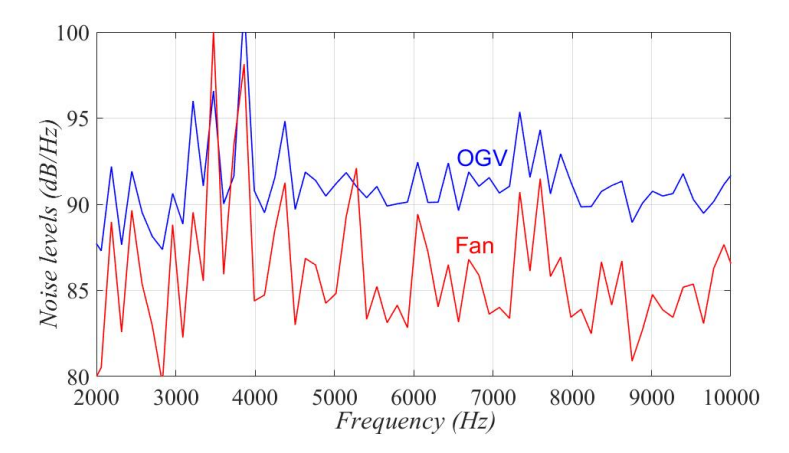


FIGURE 7.5: Predicted broadband noise levels of the fan and the OGV using the measured ACAT1 intra-stage noise data at cutback ( $ref.: 20 \mu Pa$ ).

## 7.4 Concluding remarks

This chapter demonstrated the source separation of the fan BB noise at higher engine speeds using the measured intra-stage noise data of the ACAT1 fan at cutback. Work presented in Chapter 5 considered the synthesized dataset of the ACAT1 fan at cutback to investigate the region of modal overlap, and developed suitable 2-D phased array methods to separate the dominant high-amplitude modes of the fan and OGV entrapped within the overlap bandwidth to accomplish the desired wave splitting. This chapter presented a comparative study between the measured and numerical results for the ACAT1 intra-stage at cutback. In summary,

- we implemented the 1-ring-1-mic method, developed in Chapter 5, on the measured noise data at cutback, and the modal distributions so obtained were shown to be in excellent agreement with the corresponding numerical predictions, thereby demonstrating the separation of the high-amplitude modes of the OGV from the overlap bandwidth and accomplishing the appropriate wave split-up.
- the sidelobe noise due to a sparse circular array is more impactful at higher fan speeds owing to the increase in the m-order bias and the variation between the  $\sigma_{+m}^{\pm}(\omega)$  spectrum of the fan and OGV, resulting in the relative source balance being underestimated by about 2 dB compared to the numerical predictions. The use of the theoretical  $\sigma_{+m}(\omega)$  split in conjunction with the measured modal distributions for the co-rotating modes was shown to reduce the impact of the sidelobe noise additions, bypassing the use of any deconvolution or sparsity-based reconstruction algorithms, eventually estimating a relative source balance consistent with the numerical results.
- almost flat noise spectra were predicted at cutback with the OGV being dominant by about 6 *dB*.

# **Chapter 8**

# Modal axial group velocity in ducted swirling flows and its relevance to intra-stage noise measurements

In this final chapter, we investigate the concept of the modal axial group velocity in ducted swirling flows, and its relevance to noise measurements in the engine intrastage. The modal axial group velocity has so far been an analytical construct in duct acoustics and not much use has been made of it to study the modal propagation. As far as the aeroengine is concerned, the duct mode analyses have predominantly focused on the engine intake and bypass sections, which support a uniform axial flow assumption, with the cut-on ratio ( $\alpha$ ) serving as the fundamental modal analysis parameter that is i) directly linked to the modal eigenvalues, ii) defines the modal axial wavenumber, and iii) its sign corresponds to the direction of modal energy propagation. The presence of the swirling flow component in the engine intra-stage brings in numerous complications:

- i the cut-on ratio  $(\alpha)$  is no longer the fundamental modal analysis parameter with the eigenvalue being the normalized axial wavenumber  $(\zeta)$  that is numerically estimated. Recent work (Mathews et al. (2018)) has borne out that the relationship between  $\alpha$  and  $\zeta$  in a swirling flow is many-to-many, rendering  $\alpha$  to be ambiguous in its definition and interpretation.
- ii the acoustic energy is not conserved in a swirling flow, and the suitability of any approximate expression of the modal sound power is debatable.

In long ducts (or waveguides), the sound power is transmitted in the axial direction, and the modal axial group velocity ( $\mu$ ) corresponds to the modal energy velocity (or signal velocity) such that the modes with positive axial group velocity are downstream

propagating and the modes with negative axial group velocity are upstream propagating. In this chapter, we develop a theoretical interpretation of  $\mu$  using the ideal rigid body swirl model and test its suitability in realistic intra-stage swirling flows at varying Mach numbers. The axial group velocity is shown here to be a more relevant modal analysis parameter than the cut-on ratio in a swirling flow. Regarding the intra-stage noise measurements,  $\mu$  is found to be unsuitable for duct mode measurements. However, the extent of its definiteness in a swirling flow governs the relevancy of defining modal sound powers based on which modal sound power distributions have been estimated for measured intra-stage noise data.

# 8.1 Theoretical interpretation of the axial group velocity in a swirling flow

The modal axial group velocity is defined as:

$$\mu_{mn}^{\pm} = \frac{d\omega}{d\kappa_{mn}^{\pm}},\tag{8.1}$$

and is different from the modal axial phase velocity which is simply,  $\omega/\kappa_{mn}^{\pm}$ . Referring to Sec. 3.3, in the rigid body swirl (RBS) model, we assume a 2-D flow field made up of a uniform axial flow and a rigid body swirl, with the modal propagation studied in a coordinate system rotating with the fluid, which results in a Doppler shift in the modal propagation frequency. Developing upon the rigid body swirl model, the Doppler-shifted modal dispersion relation would be obtained as:

$$\kappa_{mn}^2 + \varsigma_{mn}^2 = \left(k_{\varepsilon} - M_z \kappa_{mn}\right)^2, \tag{8.2}$$

which on differentiation would yield the normalized axial group velocity,  $\vartheta_{mn}$ , as:

$$\vartheta_{mn} = \frac{\mu_{mn}}{c} = \frac{\zeta_{mn}}{1 - \epsilon_m - M_z \zeta_{mn}} + M_z. \tag{8.3}$$

 $\mu_{mn}$  derived in Eq. 8.3 is the length of the axial projection of the resultant wave vector as illustrated in Fig. 8.1 following Rice et al. (1979), wherein the modal wavefront is locally approximated as a plane wave propagating obliquely within the duct. The normal vector to the wavefront propagates at the sound speed, c, with  $\phi_i$  defining the propagation angles to the duct axis, which are the directional cosines,

$$\cos\phi_i = \frac{c_i}{c}.\tag{8.4}$$

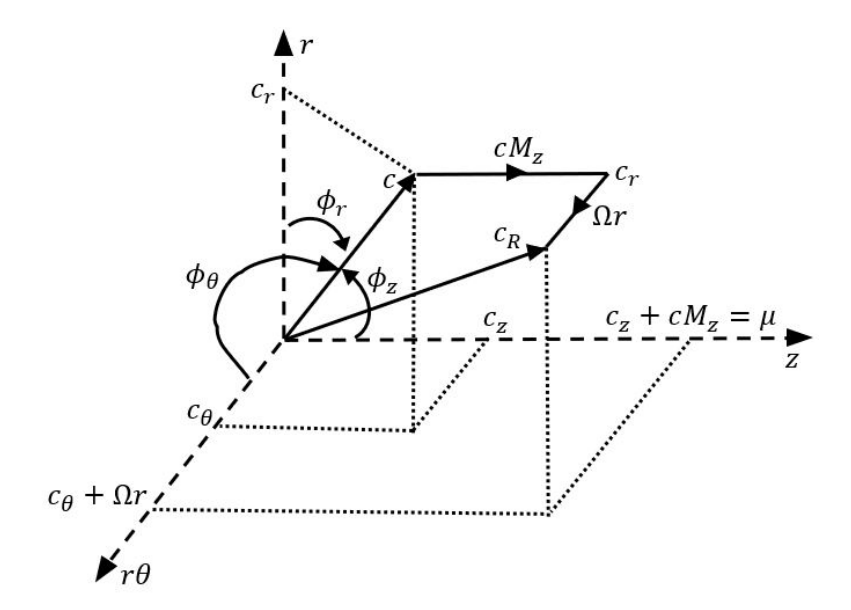


FIGURE 8.1: Geometry of the local wave propagation vectors.

Referring to the wave vector equation of 8.2, we obtain the axial propagation angle as the directional cosine,

$$\cos\phi_z = \frac{c_z}{c} = \frac{\kappa_{mn}}{k_e - M_z \kappa_{mn}},\tag{8.5}$$

which from Eq. 8.3 simplifies to,

$$\cos\phi_z = \frac{\zeta_{mn}}{1 - \epsilon_m - M_z \zeta_{mn}} = \vartheta_{mn} - M_z. \tag{8.6}$$

Referring to Fig. 8.1, the resultant direction of propagation is along  $c_R$  and not c, the axial component of which is the axial group velocity,

$$c_z + cM_z = c\cos\phi_z + cM_z = \mu_{mn}. \tag{8.7}$$

We may therefore infer that:

- $\vartheta_{mn} = \mu_{mn}/c$  is the length of the normalized axial component of the resultant wave vector, as indicated in Fig. 8.1. It therefore corresponds to the speed of modal energy transmission along the duct.
- $\vartheta$  is bounded between  $[-1+M_z,0]$  for the upstream modes and  $(0,1+M_z]$  for the downstream modes, which may be understood from Eq. 8.6.
- $\vartheta$  solely defines the modal axial propagation such that the modes with larger  $\vartheta$  propagate at small angles to the duct axis, while the modes with smaller  $\vartheta$  propagate at large angles to the duct axis. Hence, as  $\vartheta \to 0$ , the resultant vector  $c_R$  is at right angles to the duct axis.

The appropriateness of the foregoing physical interpretation of  $\theta$  in a swirling flow is governed by the extent of validity of Eq. 8.3 relating  $\theta_{mn}$  to  $\zeta_{mn}$ . Following the first point above, we may note that the definiteness (i.e.: how clearly and unambiguously defined) of the axial group velocity of the duct modes in a swirling flow is directly linked to the definiteness of their modal sound powers.

It may be noted here that for the case of uniform axial flow, the Doppler shifted modal propagation frequency in the moving reference frame would be  $\omega - U_z \kappa_{mn}$ . It may be noted here that for no-flow and uniform axial flow, the governing equation is the classical Bessel equation. Therefore, the cut-on axial and azimuthal wavenumbers as well as the combined radial-transverse wavenumber ( $\varsigma_{mn}$  in Eq. 8.2) are consistent between the moving and stationary reference frames. However, in the presence of a swirling flow component, the differential equation governing the radial propagation is no longer the Bessel equation (Posson and Peake (2013)). Therefore, the calculations based on the RBS approximation (which assumes a Bessel equation) throw up greater errors, especially at higher flow Mach numbers. The comparative study presented in Appendix C demonstrates that in the idealized case of a rigid body swirl and a uniform axial flow, the calculations based on the RBS approximation reasonably predict the number of cut-on modes, modal wavenumbers (axial as well as azimuthal), and mode amplitude distributions, for mean flow Mach numbers of interest. It may also be noted here that except for a few lower-order (m, n) modes, the radial mode shape variation could be reasonably approximated by the linear combination of the classical Bessel functions. On the other hand, for non-uniform swirling flows, we observe greater deviations, which further increase with increasing flow Mach numbers. However, we note that our principal objective here is not to approximate the eigenvalue calculations in a swirling flow but to rather test the suitability of Eq. 8.3 considering the numerically estimated modal wavenumbers from GreenSwirl. In Sec. 8.2 that follows, we demonstrate that for ideal rigid body swirling flows, Eq. 8.3 is excellently satisfied even at very high Mach numbers, thereby justifying our theoretical interpretation of  $\vartheta$ . In the same section, we also demonstrate that  $\vartheta$  is a more definite parameter than the classical  $\alpha$  in a swirling flow. We then test the applicability of Eq. 8.3 for realistic intra-stage swirling flows in Sec. 8.3, following which in Sec. 8.4 we discuss the suitability of  $\vartheta$  as a mode measurement parameter in the engine intra-stage. We conclude this chapter with Sec. 8.5 where we discuss the correspondence of  $\vartheta$  with modal sound power, and plot the modal sound power distributions estimated for the measured intra-stage noise data.

## 8.2 Investigations considering simple rigid body swirling flows

The flow profiles considered for study in this section are the RBS equivalent of the measured intra-stage flow profiles of the ACAT1 fan, wherein the axial flow is radially uniform with the area-averaged axial Mach number  $\overline{M}_z$  and the swirling flow is a solid

body swirl with angular velocity as defined in Eq. 3.33. For these ideal rigid body swirling flows, we verify the suitability of Eqs. 8.3 and 3.32 for predicting the actual  $\vartheta(\zeta)$  and  $\alpha(\zeta)$  behaviors, respectively. Note that  $\zeta_{mn}$  is numerically predicted using *GreenSwirl* for any arbitrary swirling flow.

## 8.2.1 $\vartheta$ versus $\zeta$ behavior

For an arbitrary swirling flow,  $\vartheta_{mn}$  is numerically estimated using Eq. 8.1 as:

$$\mu_{mn} = \left(\lim_{\Delta\omega \to 0} \frac{\Delta\kappa_{mn}}{\Delta\omega}\right)^{-1},\tag{8.8}$$

by computing the  $\kappa_{mn}$  at two very close frequencies ( $\Delta\omega=0.008\ rad/s$ ). Fig. 8.2 compares the  $\vartheta(\zeta)$  behavior predicted numerically using Eq. 8.8 with the analytical  $\vartheta(\zeta)$  predictions obtained using Eq. 8.3 at a selected analysis frequency for the upstream (Fig. 8.2a) and downstream (Fig. 8.2b) modes. Note that in Figs. 8.2a and 8.2b, the dashed blue line denotes the  $\vartheta(\zeta)$  relationship for a uniform axial flow obtained by setting  $\epsilon_m=0$  in Eq. 8.3. For a better illustration, the numerical predictions are selectively plotted for co-rotating and contra-rotating modes using green and red circles, respectively. An excellent match between the analytical and numerical predictions may be seen in Fig. 8.2.

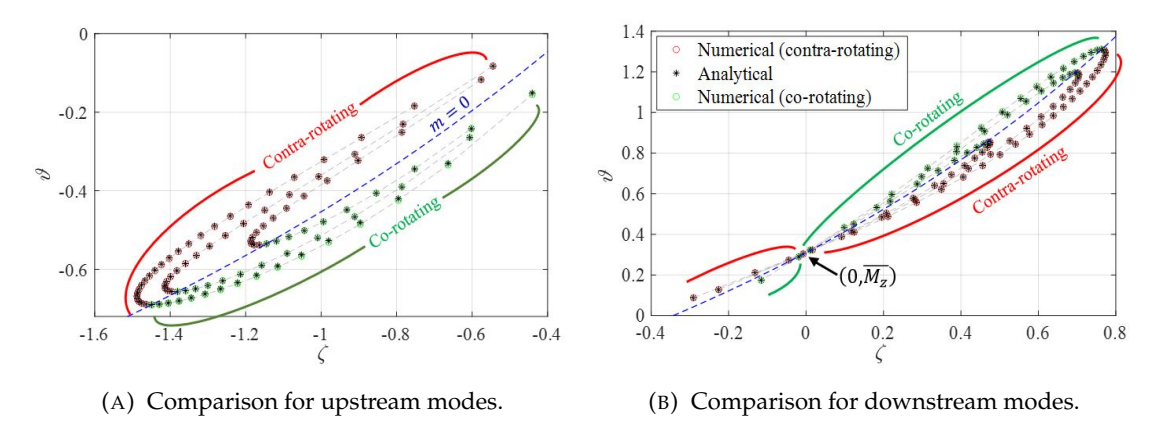


FIGURE 8.2: Comparison between the analytical and numerical  $\vartheta$  predictions for an ideal solid body swirling flow with M=0.31 and  $\Omega=195.7$  rad/s.

Fig. 8.2 depicts some interesting features of the  $\vartheta(\zeta)$  distribution in a swirling flow:

- The different loops in the  $\vartheta(\zeta)$  distribution correspond to a radial mode order (n) with the outermost loop (with the most number of modes) corresponding to the first radial mode order (n = 1).
- The co-rotating and contra-rotating modes are distributed on either side of the uniform flow  $\vartheta(\zeta)$  curve.

- The axisymmetric modes (m = 0) lie on the uniform flow curve, which may be understood since  $\epsilon_m = 0$  for m = 0. Hence, for any radial loop, the constituent m orders follow the arithmetic progression starting from the uniform flow curve such that the higher m orders have a low  $|\vartheta|$ .
- $(\zeta, \vartheta) = (0, \overline{M_z})$  is a pivotal point about which the co-rotating and contra-rotating modes switch sides, as indicated in Fig. 8.2b.

For ideal rigid body swirling flows, the analytical  $\vartheta(\zeta)$  relation of Eq. 8.3 is found to deliver an excellent agreement even at very high Mach numbers as shown in Fig. 8.3. Overall, the comparative studies in this section demonstrate the appropriateness of the theoretical interpretation of  $\vartheta$  developed in Sec. 8.1 for ideal rigid body swirling flow.

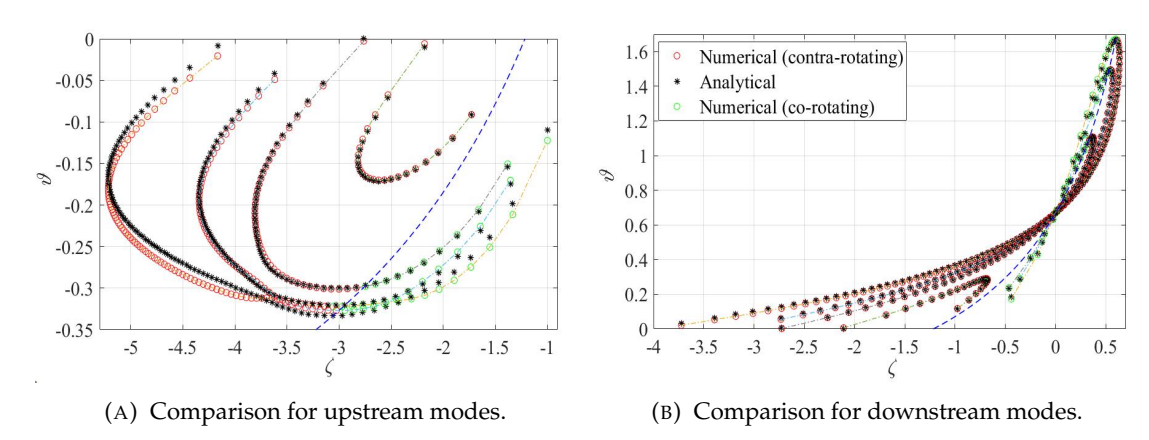


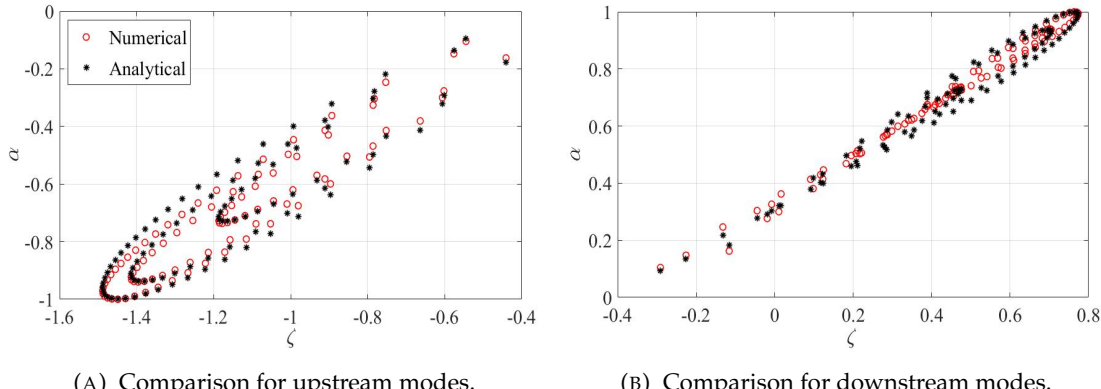
Figure 8.3: Comparison between the analytical and numerical  $\vartheta$  predictions for an ideal solid body swirling flow with M=0.67 and  $\Omega=447.5$  rad/s.

#### 8.2.2 $\alpha$ versus $\zeta$ behavior

For an arbitrary swirling flow, the cut-on ratio is only arbitrarily defined following Mathews et al. (2018) as:

$$\alpha_{mn} = \pm \sqrt{1 - \left(\frac{\omega_{mn}}{\omega}\right)^2},\tag{8.9}$$

where the cut-on frequency  $\omega_{mn}$  is numerically computed using *GreenSwirl* following the method of Mathews et al. (2018). The corresponding analytical predictions of  $\alpha_{mn}$  are obtained by substituting the numerical  $\zeta_{mn}$  values in the Doppler shifted equation of 3.32. Figs. 8.4 and 8.5 compare the analytical and numerical  $\alpha(\zeta)$  behavior for two different rigid body swirling flow profiles at a selected frequency. We witness a generally poor agreement with the discrepancy aggravated at higher flow Mach numbers.



- (A) Comparison for upstream modes.
- (B) Comparison for downstream modes.

FIGURE 8.4: Comparison between the analytical and numerical  $\alpha$  predictions for an ideal solid body swirling flow with M = 0.31 and  $\Omega = 195.7$  rad/s.

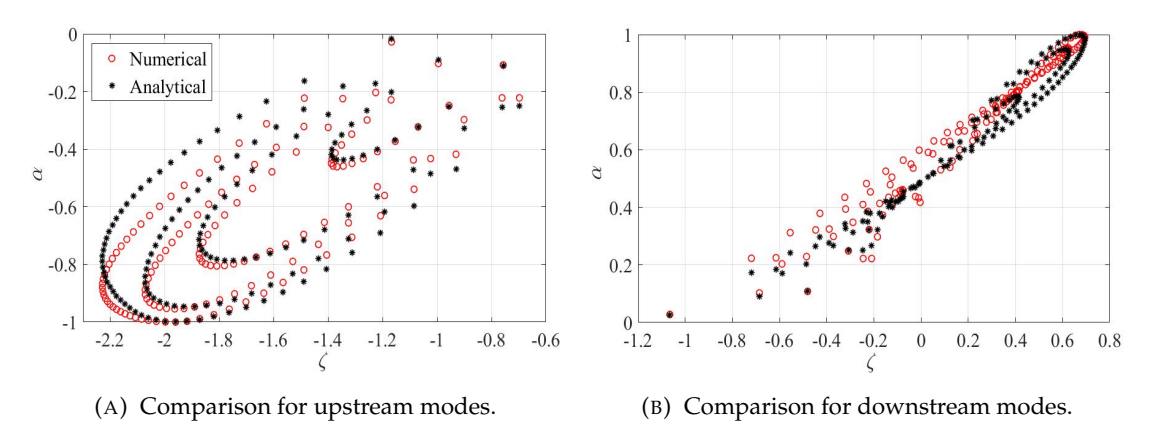


FIGURE 8.5: Comparison between the analytical and numerical  $\alpha$  predictions for an ideal solid body swirling flow with M = 0.49 and  $\Omega = 326.9$  rad/s.

## Ambiguity in the usage of $\alpha$ in a swirling flow

Referring to Figs. 8.2, 8.3, 8.4, and 8.5, we may note that even in an ideal rigid body swirling flow, the RBS approximation doesn't predict the actual  $\alpha(\zeta)$  behavior. We reiterate here that in the presence of a swirling flow component, the governing differential equation is no longer the classical Bessel equation and therefore only solved numerically with  $\zeta_{mn}$  being the eigenvalues. Therefore, unlike in an ideal uniform axial flow, wherein the cut-on frequencies (and thence the cut-on ratio) are directly related to the eigenvalues based on the Bessel functions  $(\zeta_{mn})$ ,  $\omega_{mn}$  is not directly predicted from the eigenvalues in a swirling flow and thus  $\alpha_{mn}$  is only arbitrarily defined. It may be worth noting here that even though the radial mode shape variation could be reasonably approximated by the linear combination of the classical Bessel functions, the relationship between the cut-on frequencies and modal wavenumbers is still ambiguous, as a result of which the use of the Doppler-shifted  $\alpha(\zeta)$  relation of Eq. 3.32 is erroneous even in an ideal rigid body swirling flow. The present analysis, therefore, corrects Morfey (1971a) that in a subsonic fluid rotation (Eq. 3.34),  $\omega_{mn}$  may not be easily estimated by a mere Doppler-frequency correction.

However,  $\vartheta_{mn}$ , is always a derived modal parameter and defined independently of the cut-on frequencies. Also, when the modal dispersion relation of Eq. 8.2 is differentiated to yield the group velocity expression, the dependence on the  $\zeta_{mn}$  Bessel eigenvalues is done away with, consequently reducing the order of error in the RBS approximation. The present work therefore clarifies Mathews et al. (2018) that it is not the deviation from the one-to-one relationship (uniform flow) with  $\zeta$  but rather the existence of a suitable expression relating to  $\zeta$  that renders  $\vartheta$  as a definite parameter over  $\alpha$  in a swirling flow. Additionally, we may note here that for modes with  $\vartheta^{\pm} \to 0$ , their corresponding  $\alpha^{\pm} \to 0$ . Therefore, referring to Fig. 8.1,  $\vartheta \to 0$  is the cut-off point at which the resultant vector  $c_R$  is at right angles to the duct axis.

## 8.3 Investigations considering realistic intra-stage swirling flows

In the engine intra-stage, the radial variation of the axial mean flow profile is almost flat, and the comparative studies conducted by removing the swirling flow component revealed an excellent agreement with the analytical predictions obtained using  $\overline{M_z}$ . The complexity here arises from the non-uniform swirling flow component (with radially varying  $\Omega$ ) which mostly resembles a free vortex. An RBS equivalent may be obtained by using a suitable mean angular velocity  $\overline{\Omega}$  in the  $\vartheta(\zeta)$  expression of Eq. 8.3, which in our present study, is either computed as the angular momentum average of  $\Omega(r)$  as per Eq. 3.33, or as the radial average of  $\Omega(r)$ . The choice of  $\overline{\Omega}$  is done to obtain the best match with the actual  $\vartheta(\zeta)$  behavior.

The suitability of the  $\vartheta(\zeta)$  expression of Eq. 8.3 was verified across the approach and cutback flow profiles of the ACAT1 intra-stage. We may note here that the  $\overline{\Omega}$  used for the co-rotating and contra-rotating modes need not be the same. At approach,  $\overline{\Omega}$  predicted as the radial average was found to deliver a very good match for both co-rotating and contra-rotating modes, whereas at cutback, the angular momentum average of Eq. 3.33 yielded a good match for the co-rotating modes and the radial average yielded a better match for the contra-rotating modes. For illustration, Fig. 8.6 presents the comparative study for the cutback profile at a chosen frequency.

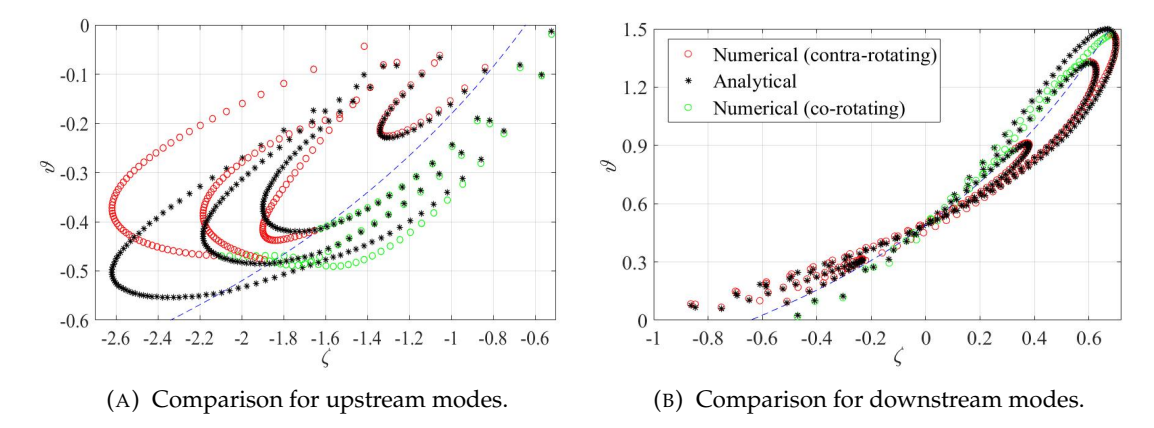


FIGURE 8.6: Comparison between the analytical and numerical  $\vartheta$  predictions for the cutback flow profile of the ACAT1 intra-stage.

In the comparative study of Fig. 8.6:

- the RBS approximation of Eq. 8.3 predicts to the actual  $\vartheta(\zeta)$  to within 10% deviation for the co-rotating modes in both upstream and downstream propagations.
- for the upstream contra-rotating modes, the predictions are poor across the lower-order radials, and get progressively better with increasing radial order to within 15% deviation. On the other hand, a reasonably good match is exhibited for all the downstream contra-rotating modes.

As expected, the discrepancy between the analytical and numerical  $\vartheta(\zeta)$  behavior was observed to be reduced at approach with the  $\vartheta$  for all the modes predicted to within 15% deviation.

Referring to the  $\overline{a^2}(\zeta_{-m})$  predictions in Fig. 7.3b of Chapter 7, we note that at cutback, the upstream modes with  $\zeta_{-m}^- < -1.8$  are very weak and therefore unimportant. Hence, from an intra-stage noise point of view, the severe mismatch in  $\zeta_{-m}^- < -1.8$  in Fig. 8.6a is not influential. Therefore, leaving apart a few contra-rotating m orders close to the cut-on bound, the  $\vartheta$  predictions using the RBS approximation of Eq. 8.3 are reasonably accurate in the flow Mach numbers of interest.

### 8.4 $\vartheta$ in the measurement of intra-stage duct mode amplitudes

We now explore the suitability of  $\vartheta$  as a mode measurement parameter in a high-frequency BB sound field in the engine intra-stage.

### 8.4.1 Modal distribution function in $\vartheta$

In the high-ka limit, we now regard the in-duct sound field as a continuum of modes distributed over  $\vartheta$  instead of  $\zeta$ . Central to this asymptotic limit is the knowledge of the modal density function,  $f(\vartheta)$ . Extending upon the governing equations of the rigid body swirl model of Secs. 3.3 and 8.1, the modal density function in  $\vartheta$  which satisfies between the limits,  $\int_{-1+\overline{M_z}}^{1+\overline{M_z}} f(\vartheta) d\vartheta = 1$  is:

$$f(\vartheta) = \left| \frac{\vartheta}{1 - \overline{M_z}^2 + \vartheta \overline{M_z}} \right| \left( \frac{\beta}{1 - \overline{M_z}^2 + \vartheta \overline{M_z}} \right)^2. \tag{8.10}$$

Eq. 8.10 indicates that  $f(\theta)$  is independent of the swirling flow component and is unchanged as in an ideal uniform axial flow. The density function was numerically computed for different swirling flow profiles and found to collapse excellently with the theoretical density function of Eq. 8.10. As an illustration, Fig. 8.7 plots the numerically predicted density function  $f(\theta)$  estimated for the set of co-rotating modes, contra-rotating modes, and the complete set of modes, each of which is observed to match well with the theoretical density function of Eq. 8.10.

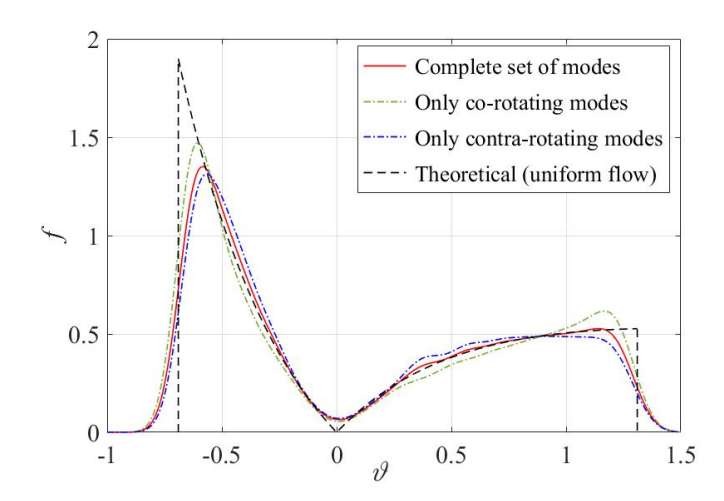


FIGURE 8.7: Modal distribution function in  $\vartheta$ , computed for the approach flow profile of the ACAT1 intra-stage.

The plot of  $f(\vartheta)$  reveals that:

- there are very few modes in the vicinity of the cut-off point,  $\vartheta = 0$ .
- the modal density function is not symmetric with the downstream modes (positive  $\theta's$ ) depicting a relatively flat likelihood over a wide range of  $\theta$ , while the upstream modes (negative  $\theta's$ ) depict a continuously rising density function peaking at the extreme limit  $-1 + \overline{M_z}$ .

### 8.4.2 Acoustic mode detection in $\vartheta$

To extend the asymptotic mode detection methods, originally developed in  $\zeta$ , in terms of  $\vartheta$ , we approximate the many-to-many  $\vartheta(\zeta)$  relationship in a swirling flow by an averaged one-to-one contour as:

$$\zeta = \frac{\left(\vartheta - \overline{M_z}\right)\left(1 - \overline{\epsilon_m}\right)}{1 - \overline{M_z}^2 + \overline{M_z}\vartheta},\tag{8.11}$$

where  $\overline{\epsilon_m}$  is chosen appropriately for the co-rotating and contra-rotating modes to capture their averaged  $\vartheta(\zeta)$  behavior. We may note that the analytical  $\vartheta(\zeta)$  relation of Eq. 8.11 is non-linear even in an ideal uniform axial flow ( $\epsilon_m = 0$ ). Consequently, the framework of the 2-D multi-ka methods developed in Sec. 5.3.1 is unsuitable for mode detection in  $\vartheta$ , leaving us with the 2-D single-ka methods.

Using appropriate synthesized datasets, the 2-D single-ka methods were first verified for their suitability towards a  $\vartheta$ -based modal analysis. It was observed that the methods work well across the narrow cut-on range of co-rotating (+m) modes across the different flow Mach numbers of interest, while across the broader cut-on range of contrarotating (-m) modes, the methods were found to deliver mismatched predictions, which aggravated at higher flow speeds, owing to the oversimplification of the broader loopy  $\vartheta(\zeta)$  behavior by an averaged one-to-one contour of Eq. 8.11. In this thesis, we avoid the inclusion of the detailed study conducted using the numerical datasets for brevity, and the readers are referred to the conference paper by Venkateswaran et al. (2022) for more information. In this section, we directly present our studies conducted using the measured intra-stage noise data of the ACAT1 fan at approach.

Referring to the intra-stage array geometry of the ACAT1 fan, the 1-ring beamformer method was extended in terms of  $\vartheta$  by defining the steering vector using Eq. 8.11 to cover the propagating range,  $\left[-1+\overline{M_z},\ 1+\overline{M_z}\right]$ . The modal density functions,  $f(\vartheta_{\pm m})$ , were estimated using Eq. 8.10 to account for the distribution of modes across the propagating range of  $\vartheta_{\pm m}$ . Fig. 8.8 plots the broadband frequency-averaged non-dimensional mean squared  $\langle \overline{a^2}(\vartheta_{\pm m})\rangle$  modal distribution predicted using the 1-ring beamformer method on the measured intra-stage noise data at approach as the solid black curve. Also, included for comparison are the corresponding theoretical modal distributions computed separately for the upstream and downstream modes using our equivalent point source model of Sec. 4.1.2, shown as the pale green and violet curves, respectively. The theoretical modal distributions are scaled in accordance with the corresponding  $\zeta$ -based theoretical distributions superimposed in Fig. 6.10.

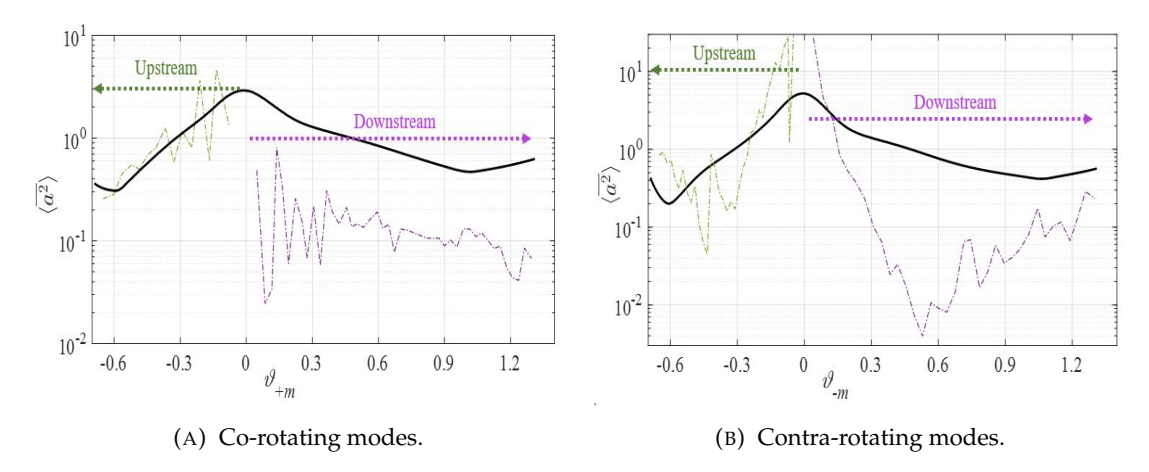


FIGURE 8.8:  $\langle \overline{a^2}(\vartheta_{\pm m}) \rangle$  distributions obtained using the 1-ring beamformer technique on the measured intra-stage noise data of the ACAT1 turbofan at approach.

We may note that the  $\vartheta$ -based mode distribution of Fig. 8.8 facilitates a direct and seamless interpretation of the relative modal levels of the fan  $(\vartheta>0)$  and OGV  $(\vartheta<0)$  sources. The predicted  $\langle \overline{a^2}(\vartheta^-)\rangle$  distribution for the OGV is observed to match reasonably well with its corresponding theoretical modal distribution for both the co-rotating and contra-rotating modes. The mismatch observed with the downstream modes is due to the pseudo-noise contributions of the turbulent flow noise structure (refer to Chapter 6), which couldn't be decorrelated using a single-ka modal analysis approach. Consequently, the comparative study in Fig. 8.8 shows that for practical purposes,  $\vartheta$  is not a suitable parameter for modal measurements in the engine intra-stage.

### 8.5 Correspondence of $\vartheta$ with the modal sound power distributions in the engine intra-stage

In Sec. 8.1, we had shown that  $\vartheta$  is the length of the axial projection of the resultant wave vector,  $c_R$ , and therefore corresponds to the speed of the modal energy transmission. Consequently, the definiteness of the concept of  $\vartheta$  governs the suitability of defining approximate modal sound powers in a swirling flow. In this section, we make use of appropriate pressure-power relationships to produce modal sound power distribution plots for measured intra-stage noise data.

### 8.5.1 Modal sound power in a swirling flow

A generalized acoustic energy conservation equation could be written, following Morfey (1971b) and Goldstein (1976), as:

$$\frac{\partial E}{\partial t} + \nabla \cdot \mathbf{I} = E_s,\tag{8.12}$$

where E is the acoustic energy per unit volume,  $I = (I_z, I_r, I_\theta)$  is the acoustic intensity vector, and  $E_s$  is the source (or sink) term accounting for any dissipation or interaction with the vorticity disturbances. In a ducted waveguide carrying a mean flow that is homentropic and irrotational,  $E_s = 0$ , and therefore the sound power transmitted is predicted as the cross-sectional integral of the axial acoustic intensity,  $I_z$ , for which Morfey (1971b) gives a generalized expression as:

$$I_z = \overline{p'u'} + \frac{\overline{U_z}}{\rho_0 c^2} \overline{p'p'} + \frac{\overline{U_z}^2}{c^2} \overline{p'u'} + \rho_0 \overline{U_z} \overline{u'u'} + \frac{\overline{U_z} \overline{U_\theta}}{c^2} \overline{p'w'} + \rho_0 \overline{U_\theta} \overline{u'w'}, \tag{8.13}$$

where the overline ( ¯ ) denotes a time-averaging operation.

For the engine intra-stage, we assume a homentropic swirling flow, and consequently, the  $E_s$  term in Eq. 8.12 would account for the non-uniformity (radial gradients) in mean flow as well as the coupling between acoustics and vorticity disturbances, the form of which may be referred to from Goldstein (1976) and Posson and Peake (2012). As a result, the acoustic energy is no longer conserved in the intra-stage, putting into question the reliability of any suitable definition of modal sound power. We may note that the analytical RBS model is idealistic with potentially zero dissipation in an energy conservation sense. Referring to the comparative studies in Secs. 8.2 and 8.3, we may note that the discrepancy between the analytical and numerical predictions of  $\vartheta$  could be attributed to the unaccounted dissipation effects. However, for the intra-stage swirling flow profiles of the ACAT1 fan at approach and cutback, the analytical  $\vartheta$  predictions (and thence the theoretical interpretation) were observed to be reasonably accurate, except for the lower radial order modes of the OGV at cutback. The fact that the physical intelligibility of the concept of  $\vartheta$  governs the relevancy of defining modal sound powers  $(\overline{W_{mn}})$  provides confidence in defining an approximate  $\overline{W_{mn}}$  for the intra-stage duct modes.

Below, we present calculations of the modal sound power distributions in a swirling flow based on the generalized definition of Eq. 8.13 (Posson and Peake (2012), Morfey (1971b)) and RBS approximation (Morfey (1971a)). We subsequently show that the two calculations produce a near-identical broadband sound power distribution for the measured intra-stage noise data of the ACAT1 fan at approach and cutback. Assuming incoherent duct modes, the total sound power at an analysis frequency is  $\overline{W} = \sum_{m,n} \overline{W_{mn}}$ , where the modal power is predicted as  $\overline{W_{mn}} = F_{mn} \overline{A_{mn}^2}$ . Referring to Eq. 8.13, the factor

 $F_{mn}$  accounts for the relationship between the acoustic pressure and particle velocity components, the form of which is different between the two calculation procedures.

### 8.5.1.1 Calculations based on a generalized definition of the acoustic intensity

We define the relationship between the perturbation pressure and velocity components as:

$$u_{mn} = p_{mn}\hat{u}_{mn},$$

$$w_{mn} = p_{mn}\hat{w}_{mn}.$$
(8.14)

where  $p_{mn}$ ,  $u_{mn}$ , and  $w_{mn}$  are the individual modal components of the total pressure  $p(x, \omega)$ , axial acoustic particle velocity, and tangential acoustic particle velocity, respectively.  $\hat{u}_{mn}$  and  $\hat{w}_{mn}$  for a swirling flow may be written following Posson and Peake (2012) as:

$$\hat{u}_{mn} = \frac{-1}{\rho_0(r)D_{mn}(r)} \left[ \frac{dU_z}{dr} \frac{d\psi_{mn}}{dr} + \left( \frac{\kappa_{mn}D_{mn}(r)}{\Lambda_{mn}(r)} + B_m(r) \frac{dU_z}{dr} \right) \right], \tag{8.15}$$

and

$$\hat{w}_{mn} = \frac{-1}{\rho_0(r)D_{mn}(r)} \left[ \frac{d(rU_\theta)}{rdr} \frac{d\psi_{mn}}{dr} + \left( \frac{mD_{mn}(r)}{r\Lambda_{mn}(r)} + B_m(r) \frac{d(rU_\theta)}{rdr} \right) \right], \tag{8.16}$$

where

$$\Lambda_{mn} = \kappa_{mn}U_z + \frac{mU_\theta}{r} - \omega; \quad D_{mn} = \Lambda^2 - \frac{2U_\theta}{r^2} \frac{d(rU_\theta)}{dr}; \quad B_m = \frac{2mU_\theta}{\Lambda_{mn}r^2} - \frac{U_\theta^2}{rc^2}.$$

Note that the mean flow quantities and sound speed in Eq. 8.13 are radially varying in this calculation procedure. Eq. 8.14 may be substituted into Eq. 8.13 with the  $\hat{u}_{mn}$  and  $\hat{w}_{mn}$  quantities evaluated as per Eqs. 8.15 and 8.16, respectively, to suitably estimate the  $F_{mn}$  factor, which may be integrated along the radius to estimate  $\overline{W}_{mn}$ .

### 8.5.1.2 Calculations based on the RBS approximation

Based on the rigid body swirl model, the  $F_{mn}$  factor may be derived as:

$$F_{mn} = \frac{\omega}{2\omega_{\epsilon}} S \left[ \rho_0 c \overline{M_z} \, \tilde{h}_{mn}^2 + \frac{\overline{M_z}}{\rho_0 c} + \left( 1 + \overline{M_z}^2 \right) \tilde{h}_{mn} \right], \tag{8.17}$$

where *S* is the cross-sectional area, and  $\tilde{h}_{mn}$  is defined as:

$$\tilde{h}_{mn} = \frac{\kappa_{mn}}{\omega \vartheta_{mn}},\tag{8.18}$$

with  $\theta_{mn}$  given by:

$$\vartheta_{mn} = \rho_0 \left[ \frac{\omega_{\epsilon}}{\omega} - \overline{M}_z \, c \frac{\kappa_{mn}}{\omega} \right], \tag{8.19}$$

where the uniform mean density  $(\rho_o)$  and sound speed (c) are chosen based on a reference condition. The modal wavenumbers (axial and azimuthal) in Eqs. 8.17-8.19 are suitably predicted using *GreenSwirl* for the actual swirling flow profile, while the Doppler-corrected frequency,  $\omega_{\epsilon}$ , is predicted using  $\overline{\Omega}$  used in the analytical  $\theta$  calculations in Sec. 8.3.

### 8.5.2 Modal sound power distributions for the ACAT1 intra-stage noise data at approach and cutback

The mean squared modal amplitudes,  $\overline{A^2}(\zeta_{\pm m})$ , predicted by implementing the 1-ring-1-mic method on the measured intra-stage noise data of the ACAT1 fan at approach and cutback were suitably used to estimate the modal sound power distributions,  $\overline{W}(\zeta_{\pm m})$ , from which the normalized modal sound power distributions,  $\overline{W}(\zeta_{\pm m})$ , were calculated, which collapse asymptotically across the ka-range, and satisfy  $\int_{\zeta_{\pm m}} \overline{W}(\zeta_{\pm m}) f(\zeta_{\pm m}) d\zeta_{\pm m} = 1$  for the co-rotating (+m) and contra-rotating (-m) modes separately.

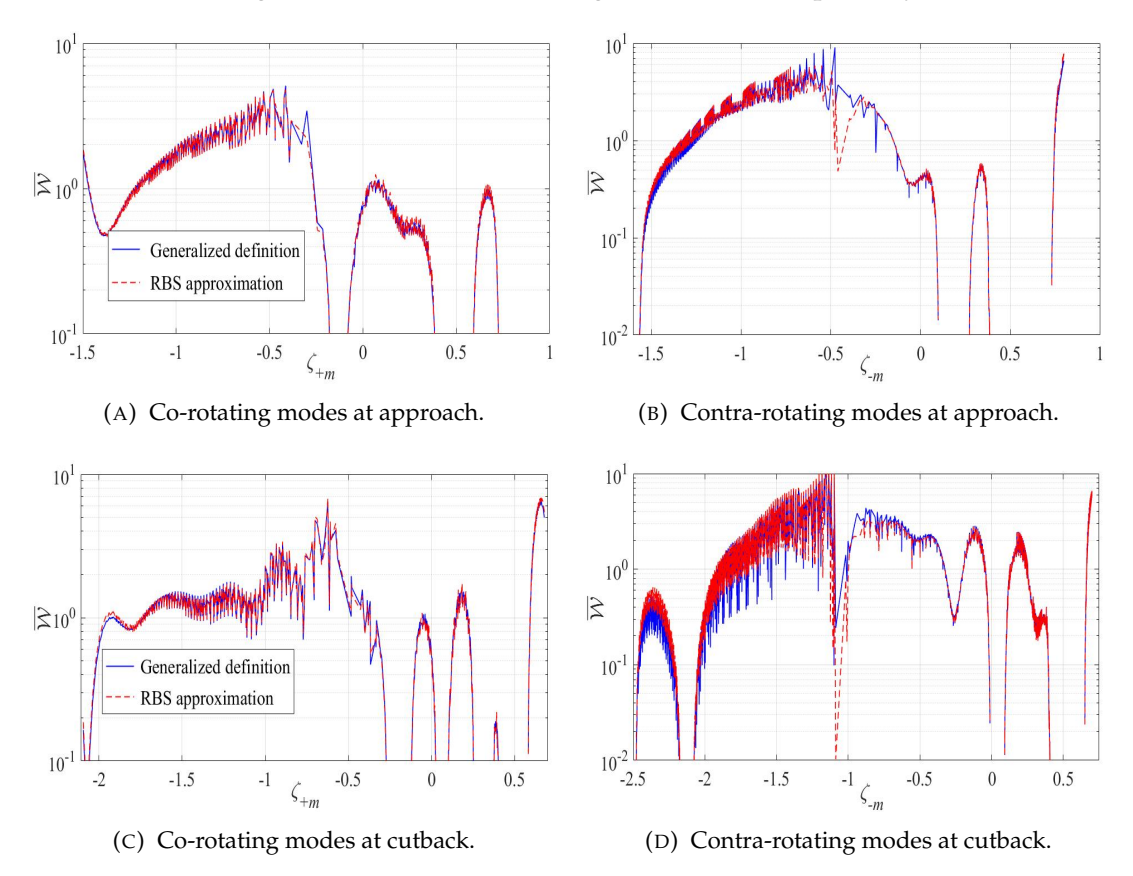


FIGURE 8.9: Normalized modal sound power distributions obtained using the measured intra-stage noise data of the ACAT1 turbofan at approach and cutback.

Fig. 8.9 demonstrates an excellent agreement between the  $\overline{\mathcal{W}}(\zeta_{\pm m})$  distributions predicted at approach (8.9a, 8.9b) and cutback (8.9c, 8.9d) using the two different calculation procedures of Secs. 8.5.1.1 and 8.5.1.2. We may notice that the matching is almost identical for the co-rotating modes (Figs. 8.9a and 8.9c), whereas for the contra-rotating modes (Figs. 8.9b and 8.9d), the match is near-identical for the fan modes with the OGV modes showing conspicuous discrepancy at cutback for  $\zeta_{-m}^- < -1.5$ . Overall, the consistency between the two calculations is convincing enough to justify the meaning-fulness of the estimated  $\overline{\mathcal{W}}(\zeta_{\pm m})$  distributions. Interestingly, Atassi (2003) shows that the coupling between the acoustic and vorticity waves is weak in the high-frequency limit such that sound power can be considered continuous in a general sense.

Comparison between the corresponding  $\overline{a^2}(\zeta_{\pm m})$  modal distributions and the  $\overline{\mathcal{W}}(\zeta_{\pm m})$  distributions measured at approach and cutback reveals that:

- (i) The modal sound power distribution of the rotor is comparatively uniform to its mode amplitude distribution.
- (ii) In the case of OGV, the co-rotating modes at cutback reveal an almost uniform modal power distribution, unlike their mode amplitude counterpart. With OGV being the dominant noise source, and the bulk of its power concentrated in the +m modes, we may say that the cutback noise data reasonably demonstrates a uniform modal power distribution.
- (iii) The approach noise data however shows a deviation from the equal-power-permode concept.

### 8.6 Concluding remarks

The modal axial group velocity  $(\mu)$  has been an analytical construct in duct acoustics. However, physically, it corresponds to the speed of modal energy transmission along the duct. In this chapter, we investigated the concept of  $\vartheta(=\mu/c)$  in the context of ducted swirling flows and its relevance to intra-stage noise measurements. In our present work,

- we developed a theoretical interpretation of  $\vartheta$  based on the ideal rigid body swirl model. An analytical expression relating  $\vartheta$  to the axial phase velocity (or  $\zeta$ ) was derived, the suitability of which was verified across ideal rigid body swirling flows (to exceptional agreement) as well as realistic intra-stage swirling flows (to reasonably good agreement at approach and cutback conditions).
- we demonstrated  $\theta$  as a relevant modal analysis parameter to the classical cut-on ratio  $(\alpha)$  in a swirling flow.

- we subsequently investigated the suitability of  $\vartheta$  as a mode detection parameter. The applicability of  $\vartheta$  was found to be limited in modal detection, and when tested using measured intra-stage noise data, a  $\vartheta$ -based modal analysis was shown to be ineffective at countering the pseudo-noise due to turbulent structures in the flow field.
- modal sound power distributions were estimated for measured intra-stage noise data at approach and cutback using expressions based on the ideal rigid body swirl model (Morfey (1971a)) and the generalized definition of acoustic intensity (Morfey (1971b)). The two calculation procedures delivered near-identical BB modal power distributions, with the results estimated at cutback reasonably demonstrating a uniform modal power distribution in contrast to the approach, which showcased a deviation from the equal-power-per-mode concept.

### Chapter 9

### Conclusions and future work

### 9.1 Conclusions

The broadband (BB) noise generated in the fan stage is a significant contributor to the total engine noise. The dominant BB noise sources within the fan stage are the rotor self-noise at the trailing edges (TE) of the fan blades (rotor), and the rotor-stator interaction noise at the leading edges (LE) of the stator vanes (OGV). Despite more than 50 years of research, the fan BB noise has not been properly understood, and the relative balance between its rotor and stator origins has never been established. In this thesis, we considered the noise measurements made in the intra-stage region between the fan TE and OGV LE to identify and reveal the fundamental characteristics of the fan BB noise, and develop measurement techniques to separate the relative source contributions of its rotor and stator components. A knowledge of the relative source balance shall facilitate the development of suitable noise mitigation strategies to target the dominant BB noise source. Also, an understanding of intra-stage BB noise is relevant for future UHBR turbofans with a reduced length of the intake section and a longer intra-stage, which could potentially be installed with sound absorption liners (Maldonado (2016)).

We began our research in Chapter 4 with a robust characterization of the BB intrastage sound field using the noise data from three turbofan rigs, namely the NASA SDT, the ACAT1 fan, and the RR-LSF, over a range of operating conditions. Using the measured noise data, it was shown that the relative spatial cross-spectrum between any two points on the duct wall is independent of frequency and reveals the underlying structure of the broadband multimodal sound field. This relative spatial cross-spectrum was characterized by developing suitable normalized mode distribution metrics based on the axial ( $\zeta$ ) and the azimuthal (m,  $\gamma$ ) wavenumbers, which were predicted using the axialable wall microphone arrays along the axial and azimuthal directions, respectively. A theoretical noise model for the intra-stage (referred to as the equivalent point source model in the main text) was developed with the fan and the OGV BB noise

sources effectively reduced to singular point dipoles of appropriate orientation relative to the engine axis, denoted by  $\varphi_r$  and  $\varphi_o$  respectively, at  $2/3^{rd}$  annulus position, each uni-directionally radiating the downstream modes and the upstream modes. The complete study revealed that dipole orientations of  $\varphi_r = 20^\circ$  and  $\varphi_o = 128^\circ$  produce near-identical broadband noise characteristics as the measured distributions for the rotor and OGV, respectively. The consistency of the empirically determined source parameters across the three turbofan rigs over different operating conditions establishes the universality of the intra-stage broadband sound field and justifies the secondary importance of any modal scattering phenomenon. The establishment of a theoretical noise model for the engine intra-stage was useful in:

- the interpretation of the relative modal pressure distribution due to the fan and OGV,
- the illustration of the physical existence of the modal overlap region in a swirling flow that entraps the high amplitude modes of the fan and OGV, which are inseparable using the existing 1-D phased array techniques, thereby calling for novel wave-splitting methods for the reliable source separation of the fan and OGV BB noise sources, and
- demonstrating the preponderance of the OGV as the dominant fan stage noise source for the first time using intra-stage measurements.

Our empirically validated point source model is invaluable in the development of source location techniques, liner design, and low-fidelity noise prediction models.

Chapters 5-7 were focused on the source separation of the intra-stage BB noise. Chapter 5 presented a systematic investigation into the problem of BB acoustic mode detection in the swirling flows. Using a numerically synthesized dataset for the ACAT1 intrastage noise data at cutback, the existing 1-D modal analysis methods were shown to deliver erroneous predictions of the relative source contributions at higher fan speeds owing to the increasing bandwidth  $(\Delta \zeta_o)$  of the modal overlap region. Using the rigid body swirl model, a simple order-of-magnitude analysis elucidated that the phenomenon of modal overlap is the result of the convective drift due to the axial and azimuthal flows, which impacts the cut-on of the duct modes and their wavenumber negativities, eventually leading to  $\zeta_i^+ < \zeta_i^-$  at higher fan speeds. The study revealed that the  $\pm m$  modal grouping within the  $\Delta \zeta_0$  bandwidth may be reasonably characterized by co-rotating (+m) upstream modes and contra-rotating (-m) downstream modes, thereby calling for 2-D modal analysis methods (based on m and  $\zeta$ ), as opposed to 1-D modal analysis methods (based on  $\zeta$  alone), to accomplish the desired wave splitting in the engine intra-stage. These 2-D modal analysis methods require 2-D microphone array geometries characterized by at least one circular ring (to decompose the *m*-orders)

9.1. Conclusions 133

and more than one axial measurement position (to measure the relative axial phase difference). A generalized framework for developing these 2-*D* modal analysis methods was presented enabling the development of suitable measurement techniques in any given intra-stage microphone array geometry. Three potential 2-*D* techniques compatible with the intra-stage array geometry of the ACAT1 fan were implemented on the synthesized dataset and shown to deliver reliable predictions of the relative source contributions, identifying the OGV as the preponderant noise source.

In Chapter 6, we investigated the measured intra-stage noise data of the ACAT1 fan at approach, and the RR-LSF rig at 70% fan speed, to separate the relative BB noise contributions of the fan and OGV. Using the measured data from two turbofan rigs having different intra-stage lengths, we systematically investigated the relative influence of the secondary noise sources in an engine intra-stage, classified as: i) Acoustic near-field, ii) Rotor hydrodynamic near-field, iii) Nearly convected hydrodynamic disturbances, iv) Incoherent boundary layer noise, and v) Turbulent flow noise. The complete analysis revealed that the turbulent flow noise structure having a short correlation length scale dominates the pressure coherence between the adjacent axial microphones, eventually rendering the single-ka modal analysis methods, effective in principle, unreliable for practical implementation. The multi-ka modal analysis methods, on the other hand, were shown to permit an effective decorrelation of this turbulent flow noise structure by taking the cross-pressure spectra across larger separation distances and extracting the acoustical modal distributions to reliably measure the relative source contributions of the fan and OGV. The final predictions obtained for the ACAT1 intra-stage noise data at approach revealed the OGV to be dominant by about 8 dB across the BB frequency range. This is the first time a source breakdown of the engine noise data was accomplished without removing the OGV.

Chapter 7 presented a comparative study between the results obtained by implementing the 1-ring-1-mic method on the measured and numerically synthesized (Chapter 5) datsets of the ACAT1 intra-stage at cutback to demonstrate the source separation at higher fan speeds. The comparative study demonstrated that the 2-D approach of the 1-ring-1-mic method effectively separates the high-amplitude modes of the OGV from the  $\Delta\zeta_0$  bandwidth in the measured noise data to accomplish the appropriate wave split-up. Additionally, the sidelobe noise due to the sparse circular array was observed to be impactful at higher fan speeds owing to the increase in the *m*-order bias and the variation between the  $\sigma_{+m}^{\pm}(\omega)$  spectrum of the fan and OGV, resulting in the relative balance being underestimated by about 2 dB compared to the numerical predictions. The use of the theoretical  $\sigma_{+m}(\omega)$  split in conjunction with the measured mode amplitude distributions for the co-rotating modes was shown to reduce the impact of the sidelobe noise additions, bypassing the use of any deconvolution or sparsity-based reconstruction algorithms, eventually estimating a relative source balance consistent

with the numerical results with the OGV being dominant by about 6 dB. Unlike the approach, we predicted almost flat noise spectra at cutback.

In Chapter 8, we investigated the concept of the modal axial group velocity in the context of ducted swirling flows, and its relevance to intra-stage noise measurements.  $\vartheta$  has so far been an analytical construct in duct acoustics. However, it physically corresponds to the speed of modal energy transmission along the duct. In our present work,

- we developed a theoretical interpretation of  $\vartheta$  based on the ideal rigid body swirl model. An analytical expression relating  $\vartheta$  to the axial phase velocity (or  $\zeta$ ) was derived, the suitability of which was verified across ideal rigid body swirling flows (to exceptional agreement) as well as realistic intra-stage swirling flows (to reasonably good agreement at approach and cutback conditions).
- we demonstrated  $\vartheta$  as a relevant modal analysis parameter to the classical cut-on ratio  $(\alpha)$  in a swirling flow.
- we subsequently investigated the suitability of  $\vartheta$  as a mode detection parameter. The applicability of  $\vartheta$  was found to be limited in modal detection, and when tested using measured intra-stage noise data, a  $\vartheta$ -based modal analysis was shown to be ineffective at countering the pseudo-noise due to turbulent structures in the flow field.
- modal sound power distributions were estimated for measured intra-stage noise data at approach and cutback using expressions based on the ideal rigid body swirl model (Morfey (1971a)) and the generalized definition of acoustic intensity (Morfey (1971b)). The two calculation procedures delivered near-identical BB modal power distributions, with the results estimated at cutback reasonably demonstrating a uniform modal power distribution in contrast to the approach, which showcased a deviation from the equal-power-per-mode concept.

### 9.2 Avenues for future research

The research and analysis presented in our thesis could be extended to further develop our understanding of fan broadband noise, as well as investigate the implementation of suitable noise abatement technologies. Below, we propose some relevant areas of research:

### 9.2.1 Investigating the modal transmission from the intra-stage region to the intake and bypass sections

In our present research, we have justified that the unidirectional source radiation of the downstream and upstream modes solely corresponding to the fan and OGV, respectively, without any significant modal scattering, is reasonably applicable for an intrastage BB noise analysis. In the current trend of HBR turbofans, the rotor-stator interaction noise mechanism at the leading edge of the OGV was found to dictate the intrastage modal spectrum and possess a characteristic modal structure. From the measurements of the spinning mode order spectra across the different turbofan rigs presented in Premo and Joppa (2002) (on the NASA SDT rig), Sijtsma (2010), and Pereira and Jacob (2022) (on the ACAT1 fan rig), we may notice a similar universality in the intake and bypass modal spectra. However, it may be interesting to note from the published results that the characteristic modal structure measured in the intake and bypass ducts differ from the intra-stage section.

Following Sijtsma (2010), we may understand that the co-rotating modes of the OGV face less shielding from the fan blades and dominate the measured intake mode spectrum. From the latest results presented in Pereira and Jacob (2022) on the ACAT1 fan rig, we may notice that the BB spectra differ between the co-rotating and contra-rotating modes in the engine intake. The intake spectrum for the contra-rotating modes revealed spectral humps, centered at the BPFs, characteristic of the rotor tip-BL interaction noise while the co-rotating modes may be attributed to being predominantly corresponding to the LE interaction noise mechanism at the OGV. On the other hand, the bypass modal spectra across all the rigs were shown to reveal a near-symmetric azimuthal pressure distribution. Understanding the modal transmission from the intra-stage to the intake and bypass ducts shall therefore aid in the understanding of the measured modal spectra in the intake and bypass.

### 9.2.2 A targeted intra-stage liner design

The bulk of the total power due to the OGV is concentrated in its +m modes, with the m-orders close to the cut-off boundary being stronger. It may be noted that these +m modes may be narrow cut-on in number in the engine intra-stage but are relevant in the intake far-field noise. Also, an interesting thing to note here is that, unlike the -m modes, the cut-on m-bounds of the co-rotating modes do not vary significantly across the different fan speeds. Therefore, for a future UHBR turbofan, research works (similar to Maldonado (2016), Palani (2022)) could be directed at a systematic intra-stage liner design to have an optimum impedance to effectively mitigate the higher m orders of the upstream propagating co-rotating modes for the high-frequency BB noise, whilst also attenuating the low-frequency tonal modes.

### 9.2.3 Suitable surface treatments of the OGV to mitigate its dominant corotating modes

The normalized mode distribution metrics, presented in Chapter 4, could be similarly obtained for the OGVs with surface treatments such as LE serrations (Chaitanya Paruchuri (2017)), soft vanes (Fernandez et al. (2016)), and *lean* and *sweeps* (Premo and Joppa (2002) and Walsh (2016)), which may facilitate the improvisation of such surface treatments to mitigate the dominant +m mode orders. Also, it may be interesting to investigate if the effective dipole orientation ( $\varphi_0$ ) varies with surface treatments.

### Appendix A

### Brief summary of the two existing asymptotic wavenumber distribution approaches

The working principles of the axial beamformer (Lowis et al. (2010)) and the two-microphone method (Joseph (2017); Melling et al. (2017)) have been summarized below. Since we are primarily interested in the modal analysis in swirling flows, we present a modified formulation of the two techniques with the normalized axial wavenumber ( $\zeta$ ) as the modal analysis parameter instead of the cut-on ratio ( $\alpha$ ).

### A.1 The axial beamformer

The axial beamformer method (Lowis et al. (2010)) implements the conventional delayand-sum algorithm (de Santana (2017)) with a  $\zeta$ -based steering vector,  $\varrho(\zeta_b)$ , on a linear array of  $N_a$  equispaced wall microphones to yield the beamformer output:

$$\mathcal{B}(\zeta_b, \omega) = \frac{1}{N_a} \sum_{i=1}^{N_a} p(z_i, \omega) \varrho^*(\zeta_b, z_i) = \frac{1}{N_a} \sum_{i=1}^{N_a} p(z_i, \omega) e^{-jk\zeta_b z_i}, \tag{A.1}$$

where  $z_i$  denotes the axial position of the individual microphones. We are interested in the cross-spectra and auto-spectra of microphone pressures for fan broadband noise. So from Eq. A.1, the mean squared beamformer output may be obtained from the cross-spectral matrix (CSM) of the wall microphone pressures as:

$$\mathcal{Z}(\zeta_b, \omega) = \lim_{T \to \infty} \frac{1}{T} E\left[\mathcal{B}\mathcal{B}^*\left(\zeta_b, \omega\right)\right] = \frac{1}{N_a^2} \sum_{i=1}^{N_a} \sum_{f=1}^{N_a} \varrho^*(\zeta_b, z_i) E\left[p(z_i)p^*(z_f)\right] \varrho(\zeta_b, z_f), \tag{A.2}$$

where  $E[\ ]$  denotes the expectation, and T is the total duration over which the Fast Fourier transform (FFT) of the pressure time series is done. For a random BB signal with uncorrelated duct modes, the power spectral density (PSD) of the beamformer output may be expressed as:

$$\mathcal{Z}(\zeta_b,\omega) = \sum_{m,n} E[A_{mn}(\zeta_{mn},\omega)A_{mn}^*(\zeta_{mn},\omega)]|\psi_{mn}(a)|^2|\iota_{mn}(\zeta_{mn}-\zeta_b)|^2, \tag{A.3}$$

where

$$\iota_{mn}(\zeta_{mn} - \zeta_b) = \frac{1}{N_a} \sum_{i=1}^{N_a} e^{jk(\zeta_{mn} - \zeta_b)z_i}$$
(A.4)

is the response function of the beamformer for each (m, n) mode. For cut-on modes, this is simply a summation of a complex exponential series yielding the magnitude:

$$|\iota_{mn}(\zeta_{mn} - \zeta_b)| = \frac{1}{N_a} \left| \frac{\sin(0.5N_a(\zeta_{mn} - \zeta_b)k\Delta z)}{\sin(0.5(\zeta_{mn} - \zeta_b)k\Delta z)} \right|,\tag{A.5}$$

where  $\Delta z$  is the separation distance between the adjacent microphones. At suitably high ka's, we replace the (m,n) modal summation by an integration over the cut-on range of  $\zeta$  such that Eq. A.3 becomes:

$$\mathcal{Z}(\zeta_b,\omega) \approx 2N_\omega \int_{\zeta_{min}}^{\zeta_{max}} E[|A(\zeta,\omega)|^2] f(\zeta) |\iota(\zeta-\zeta_b)|^2 d\zeta, \tag{A.6}$$

where  $N_{\omega}$  is the number of cut-on modes (upstream + downstream) at the analysis frequency  $(\omega)$ , and  $f(\zeta)$  is the modal density function. Eq. A.6 incorporates the modal averaging,  $\langle |\psi_{mn}(a)|^2 \rangle_{m,n} \approx 2$ , following Joseph et al. (2003); Lowis et al. (2010) to remove the radial mode order dependency and obtain a  $\zeta$ -only dependent integral equation. Eq. A.6 indicates that the mean squared beamformer output is a convolution of the  $f(\zeta)$ -weighted mean squared mode amplitude distribution by the response function. We may note from Eq. A.5 that the beamformer response function is characterized by a peak (main) lobe at  $\zeta = \zeta_b$  with a value of unity and a multitude of sidelobes on either side of the main lobe. The beamformer's resolution is defined by its beamwidth,  $\Delta \zeta_b$ , which is half the angle between the first zero crossings on either side of the main lobe at  $\zeta = \zeta_b$  obtained as:

$$0.5N_a(\Delta\zeta_b)k\Delta z = \pi$$

$$\implies \Delta\zeta_b = \frac{2\pi}{N_ak\Delta z} = \frac{\lambda}{N_a\Delta z} \simeq \frac{\lambda}{L_a},$$
(A.7)

where  $L_a$  is the length of the axial array. By assuming that the level of the sidelobes is sufficiently smaller than the main lobe peak value of unity, the integration of Eq. A.6 could be effectively limited to within the beamwidth,  $\Delta \zeta_b$ , as:

$$\mathcal{Z}(\zeta_b,\omega) \approx 2N_\omega E[|A(\zeta_b,\omega)|^2] \int_{\zeta_b-0.5\Delta\zeta_b}^{\zeta_b+0.5\Delta\zeta_b} f(\zeta)d\zeta,$$
 (A.8)

where the mean squared amplitude,  $E[|A(\zeta_b,\omega)|^2]$ , is averaged over the beamwidth  $(\Delta \zeta_b)$  and thus taken out of the integral. Therefore, when the beamformer's lookup is steered to cover the complete propagating range of  $\zeta$ , we effectively predict the weighted moving average of the mean squared modal pressure amplitudes at each steered value. Eq. A.8 finally yields:

$$E[|A(\zeta_b,\omega)|^2] \approx \frac{\mathcal{Z}(\zeta_b,\omega)}{2N_\omega \int_{\zeta_b-0.5\Delta\zeta_b}^{\zeta_b+0.5\Delta\zeta_b} f(\zeta)d\zeta}.$$
 (A.9)

### A.2 The two-microphone method

The two-microphone method predicts the mean squared mode amplitude distribution from the measurements of the complex coherence function between the acoustic pressures sensed at two closely spaced axial positions on the duct wall. We first estimate the pressure cross-spectral density between the two sensing points spaced apart by a small distance  $\Delta z_{ab}$  as:

$$S_{ab}(\omega) = \lim_{T \to \infty} \frac{1}{T} E[p(\mathbf{x}_a) p^*(\mathbf{x}_b)], \tag{A.10}$$

where  $x_a$  and  $x_b$  only differ in their *z*-coordinates. Assuming incoherent duct modes, Eq. A.10 may be expressed as:

$$S_{ab}(\omega) = \sum_{m,n} E[|A_{mn}|^2] |\psi_{mn}(a)|^2 e^{-jk\zeta_{mn}\Delta z_{ab}}.$$
 (A.11)

The two-microphone technique assumes a separability of modal amplitudes such that:

$$E[|A_{mn}(\omega,\zeta_{mn})|^2] = S(\omega)\overline{a^2}(\zeta_{mn}), \tag{A.12}$$

where  $S(\omega)$  is a frequency-dependent term encapsulating the source strength, and  $\overline{a^2}(\zeta)$  is the relative mean squared mode amplitude distribution that is frequency-independent. Using the high-ka modal continuum hypothesis, we approximate Eq. A.11 as:

$$S_{ab}(\omega) \approx 2N_{\omega}S(\omega) \int_{\zeta} \overline{a^2}(\zeta)f(\zeta)e^{-jk\zeta\Delta z_{ab}}d\zeta.$$
 (A.13)

The split between  $S(\omega)$  and  $\overline{a^2}(\zeta)$  terms in Eq. A.12 is arbitrary. Therefore, for convenience, we suitably normalize the  $\overline{a^2}(\zeta)$  distribution such that:

$$\int_{\zeta} \overline{a^2}(\zeta) f(\zeta) d\zeta = 1. \tag{A.14}$$

When  $\Delta z_{ab} = 0$ , Eqs. A.13 & A.14 would relate the auto spectral density,  $S_{aa}(\omega)$ , and  $S(\omega)$  as:

$$S_{aa}(\omega) \approx 2N_{\omega}S(\omega).$$
 (A.15)

Substitution of Eq. A.15 into Eq. A.13 would relate the normalized  $\overline{a^2}(\zeta)$  distribution to the pressure coherence,  $C_{ab}(\hat{\omega})$ , as:

$$C_{ab}(\hat{\omega}) = \frac{S_{ab}(\omega, \Delta z_{ab})}{\sqrt{S_{aa}S_{bb}}} \approx \int_{\zeta} \overline{a^2}(\zeta) f(\zeta) e^{-j\hat{\omega}\zeta} d\zeta, \tag{A.16}$$

where  $\hat{\omega} = k\Delta z_{ab}$  is a non-dimensional frequency that encapsulates the  $\omega$  and  $\Delta z_{ab}$  dependence. Eq. A.16 reveals a Fourier transform (FT) relationship between  $C_{ab}(\hat{\omega})$  and  $f(\zeta)$ -weighted  $\overline{a^2}(\zeta)$  functions with  $\hat{\omega}$  and  $\zeta$  forming the appropriate FT pairs. The inverse Fourier transform (IFT) of Eq. A.16 shall yield the normalized  $\overline{a^2}(\zeta)$  distribution from the complex coherence function as:

$$\overline{a^2}(\zeta) = \frac{1}{2\pi f(\zeta)} \int_{-\infty}^{\infty} C_{ab}(\hat{\omega}) e^{j\zeta\hat{\omega}} d\hat{\omega} = \frac{1}{\pi f(\zeta)} \int_{0}^{\infty} C_{ab}(\hat{\omega}) e^{j\zeta\hat{\omega}} d\hat{\omega}, \tag{A.17}$$

from which the dimensional mean squared mode amplitude distribution,  $E[|A(\zeta,\omega)|^2]$ , may be obtained using Eqs. A.12 and A.15.

### Appendix B

### Numerical procedure to calculating the eigenmodes, and Green's function in a ducted swirling flow

### **B.1** Numerical eigenmodes

To calculate the eigenmodes numerically, the Euler equations are linearized for small amplitude perturbations resulting in:

$$\frac{1}{c_{+}^{2}} \frac{D_{0} p_{+}'}{D t_{+}} + \frac{\rho_{+}^{0} M_{\theta}^{2}}{r_{+} c_{+}^{2}} v_{+}' + \rho_{+}^{0} \left(\nabla_{+} \cdot u_{+}'\right) = 0$$

$$\rho_{+}^{0} \left(\frac{D_{0} u_{+}'}{D t_{+}} + v_{+}' \frac{d M_{z}}{d r_{+}}\right) + \frac{\partial p_{+}'}{\partial z_{+}} = 0$$

$$\rho_{+}^{0} \left(\frac{D_{0} v_{+}'}{D t_{+}} - 2 \frac{M_{\theta} w_{+}'}{r_{+}}\right) - \frac{M_{\theta}^{2} \rho_{+}'}{r_{+}} + \frac{\partial p_{+}'}{\partial r_{+}} = 0$$

$$\rho_{+}^{0} \left(\frac{D_{0} w_{+}'}{D t_{+}} + \frac{v_{+}'}{r_{+}} \frac{d}{d r_{+}} (r_{+} M_{\theta})\right) + \frac{1}{r_{+}} \frac{\partial p_{+}'}{\partial \theta} = 0$$
(B.1)

We solve for time-harmonic perturbations, which are expressed in terms of temporal and spatial Fourier transforms as:

$$\{u'_{+}, v'_{+}, w'_{+}, p'_{+}\} (z_{+}, r_{+}, \theta_{+}, t_{+}) = \int \sum_{m} \int \{U'_{+}(r_{+}), V'_{+}(r_{+}), W'_{+}(r_{+}), P'_{+}(r_{+})\} e^{j\tau_{+}z_{+}} d\tau_{+} e^{jm\theta} e^{-j\omega_{+}t_{+}} d\omega_{+}.$$
(B.2)

We solve for the set of linearized Euler equations for the axial wavenumber  $\tau_{t}(=\tau_{mn})$ , which is the eigen value of the problem. Appropriate Fourier transformation of Eq. B.1

results in the final eigen value problem:

$$-\frac{M_{z}}{c_{+}^{2}}\frac{\overline{\Lambda}}{\underline{U}}jU'_{+} + \left[\frac{M_{z}}{c_{+}^{2}\underline{U}}\frac{dM_{z}}{dr_{+}} - \frac{1}{r_{+}\underline{U}} - \frac{M_{\theta}^{2}}{Ur_{+}c_{+}^{2}}\right]V'_{+} - \frac{1}{\underline{U}}\frac{dV'_{+}}{dr_{+}} - \frac{m}{r_{+}\underline{U}}jW'_{+} + \frac{j\overline{\Lambda}}{c_{+}^{2}\rho_{+}^{0}\underline{U}}P'_{+} = (\tau_{+})jU'_{+}$$
(B.3a)

$$\frac{\overline{\Lambda}}{M_z}V'_{\dagger} - 2\frac{M_{\theta}}{r_{\dagger}M_z}jW'_{\dagger} + \frac{j}{\rho_{\dagger}^0M_z}\frac{dP'_{\dagger}}{dr_{\dagger}} - \frac{jM_{\theta}^2}{\rho_{\dagger}^0M_zr_{\dagger}c_{\dagger}^2}P'_{\dagger} = (\tau_{\dagger})V'_{\dagger}$$
(B.3b)

$$-\frac{1}{M_{z}} \left[ \frac{M_{\theta}}{r_{+}} + \frac{dM_{\theta}}{dr_{+}} \right] V'_{+} + \frac{\overline{\Lambda}}{M_{z}} j W'_{+} - \frac{jm}{r_{+} \rho_{+}^{0} M_{z}} P'_{+} = (\tau_{+}) j W'_{+}$$
 (B.3c)

$$\frac{\rho_{+}^{0}\overline{\Lambda}}{\underline{U}}U'_{+}+j\frac{\rho_{+}^{0}}{\underline{U}}\left[\frac{dM_{z}}{dr_{+}}-\left(1+\frac{M_{\theta}^{2}}{c_{+}^{2}}\right)\frac{M_{z}}{r_{+}}\right]V'_{+}-\frac{j\rho_{+}^{0}M_{z}}{\underline{U}}\frac{dV'_{+}}{dr_{+}}+\frac{m\rho_{+}^{0}M_{z}}{r_{+}\underline{U}}W'_{+}-\frac{M_{z}\overline{\Lambda}}{c_{+}^{2}\underline{U}}P'_{+}=(\tau_{+})P'_{+}$$
(B.3d)

where  $\overline{\Lambda} = \omega_{\dagger} - \frac{mM_{\theta}}{r_{\dagger}}$  is the reduced frequency and  $\underline{U} = 1 - \frac{M_{z}^{2}}{c_{\dagger}^{2}}$  is the local compressibility factor. Referring to Eq. 3.20, the boundary conditions for the eigen value problem would be:

$$Z(h)\frac{\omega V'_{+}(h)}{M_{z}(h)} + \frac{\overline{\Lambda}(h)P'_{+}(h)}{M_{z}(h)} - \tau_{+}P'_{+}(h) = 0,$$

$$Z(1)\frac{\omega V'_{+}(1)}{M_{z}(1)} + \frac{\overline{\Lambda}(1)P'_{+}(1)}{M_{z}(1)} - \tau_{+}P'_{+}(1) = 0,$$
(B.4)

which for rigid ducts reduces to  $V'_{t}(h) = V'_{t}(1) = 0$ .

The eigen value problem is solved using Chebfun (Driscoll et al. (2014)) in MATLAB, which avoids having to discretize the derivatives. The outputs obtained are the axial wavenumber,  $\tau_{\dagger} = \tau_{mn}$  (eigenmodes), and the normalized radial eigen function,  $\psi_{mn}(r_{\dagger})$ .

### **B.2** Numerical Green's function

We may rewrite Eq. 3.27 in the conventional form as:

$$\mathcal{G}_m = \sum_n \mathcal{G}_{mn} \tag{B.5}$$

such that

$$\mathcal{G}_{mn} = \pm \frac{2\pi j}{4\pi^2} \operatorname{Res} \left( g_m \left( r_{\dagger} | r_{\dagger}^s; \tau_{\dagger}(n), \omega \right) e^{j\tau_{\dagger}(n)(z_{\dagger} - z_{\dagger}^s)} \right), \tag{B.6}$$

where the  $\pm$  would correspond to downstream (+) and upstream (-) propagation. The contribution from each acoustic eigenmode is given as:

$$\mathcal{G}_{mn} = \pm \frac{i\omega_{+}}{4\pi^{2}} e^{j\tau_{mn}(z_{+}-z_{+}^{s})} \frac{1}{r_{+}^{s} \frac{\partial W}{\partial \tau}(\tau_{mn})} \begin{cases} g_{1}(r_{+}^{s}, \tau_{mn})g_{2}(r_{+}, \tau_{mn}) & r_{+} \leq r_{+}^{s}, \\ g_{1}(r_{+}, \tau_{mn})g_{2}(r_{+}^{s}, \tau_{mn}) & r_{+} > r_{+}^{s}. \end{cases}$$
(B.7)

where  $r_{+}^{s}$  is the normalized radial source position, and W( $r_{+}^{s}$ ,  $\tau_{+}$ ) is the Wronskian of the two functions  $g_{1}(r_{+}, \tau_{+})$  and  $g_{2}(r_{+}, \tau_{+})$ . The two functions,  $g_{1}(r_{+}, \tau_{+})$  and  $g_{2}(r_{+}, \tau_{+})$ , satisfy the second order ordinary differential equation:

$$\mathcal{A}(r_{+},\tau_{mn})\frac{d^{2}g_{i}}{dr_{+}^{2}}(r_{+},\tau_{mn}) + \mathcal{H}(r_{+},\tau_{mn})\frac{dg_{i}}{dr_{+}}(r_{+},\tau_{mn}) - \mathcal{P}(r_{+},\tau_{mn})g_{i}(r_{+},\tau_{mn}) = 0, \quad (B.8)$$

where i = 1, 2 corresponding to  $g_1$  and  $g_2$ , respectively. The coefficients are defined as:

$$\mathcal{A}(r_{+}, \tau_{+}) = \Phi^{2}(r_{+}, \tau_{+}) \left( \mathcal{U}_{\theta}(r_{+}) - \Phi^{2}(r_{+}, \tau_{+}) \right), \tag{B.9}$$

$$\mathcal{H}(r_{+}, \tau_{+}) = \Phi^{2}(r_{+}, \tau_{+}) \left[ \left( \mathcal{U}_{\theta}(r_{+}) - \Phi^{2}(r_{+}, \tau_{+}) \right) \left( \frac{1}{r_{+}} - \frac{1}{\rho_{+}^{0}(r_{+})} \frac{d\rho_{+}^{0}(r_{+})}{dr_{+}} \right) + \frac{\partial}{\partial r_{+}} \left( \Phi^{2}(r_{+}, \tau_{+}) - \mathcal{U}_{\theta}(r_{+}) \right) \right], \tag{B.10}$$

$$\mathcal{P}(r_{+}, \tau_{+}) = Y \left( \mathcal{U}_{\theta}(r_{+}) - \Phi^{2} \right) \left[ Y + \Phi \left( \frac{1}{r_{+}} - \frac{1}{\rho_{+}^{0}(r_{+})} \frac{d(\rho_{+}^{0}(r_{+}))}{dr_{+}} \right) \right] - \Phi \left( \Phi^{2} - \mathcal{U}_{\theta}(r_{+}) \right) \frac{dY}{dr_{+}} + \left( \mathcal{U}_{\theta}(r_{+}) - \Phi^{2} \right)^{2} \left[ \frac{\Phi^{2}}{c_{+}^{2}} - \tau_{+}^{2} - \frac{m^{2}}{r_{+}^{2}} \right] + Y \frac{d}{dr_{+}} \left( \Phi \left( \Phi^{2} - \mathcal{U}_{\theta}(r_{+}) \right) \right), \tag{B.11}$$

where 
$$\Phi(r_{t}, \tau_{t}) = \omega_{t} - \tau_{t} M_{z}(r_{t}) - \frac{m M_{\theta}(r_{t})}{r_{t}}$$
 and  $Y(r_{t}, \tau_{t}) = \frac{M_{\theta}^{2}(r_{t})}{r_{t}c_{t}^{2}} \Phi(r_{t}, \tau_{t}) + \frac{2m M_{\theta}(r_{t})}{r_{t}^{2}}$ .

From the acoustic analogy of Posson and Peake (2013), we have  $\rho_+^0 \mathcal{R}(v_+') = \mathcal{T}(p_+')$  on ignoring the source terms. Using this in Myer's boundary condition of Eq. 3.20 results in:

$$\frac{dg_i(r_+^i, \tau_{mn})}{dr_+} = \hat{f}_i(r_+^i, \tau_{mn})g_i(r_+^i, \tau_{mn}), \tag{B.12}$$

where  $r_1^i$  takes on values of 1 and h corresponding to  $g_i = g_1$  and  $g_i = g_2$ , respectively. Note that we choose  $g_1(1, \tau_{mn}) = g_2(h, \tau_{mn}) = 1$  for convenience and that  $\hat{f}_i(r_+^i, \tau_{mn})$  in the above equation may be easily determined from Eq. 3.20. The functions  $g_1, g_2$  and their Wronskian, W, are calculated numerically using Chebfun in Matlab (Driscoll et al. (2014)). Referring to Eq. B.7, we are only left with calculating the derivative,  $(\partial W/\partial \tau_+)_{\tau_+=\tau_{mn}}$ , for which we need  $\partial g_i/\partial \tau_+$ , which are obtained by differentiating the second-order differential equation of Eq. B.8 with respect to  $\tau_+$  to give:

$$\mathcal{A}(r_{+}, \tau_{mn}) \frac{d^{2}}{dr_{+}^{2}} \left( \frac{\partial g_{i}}{\partial \tau_{+}} \right) + \mathcal{H}(r_{+}, \tau_{mn}) \frac{d}{dr_{+}} \left( \frac{\partial g_{i}}{\partial \tau_{+}} \right) - \mathcal{P}(r_{+}, \tau_{mn}) \frac{\partial g_{i}}{\partial \tau_{+}} \\
= \frac{\partial \mathcal{P}}{\partial \tau_{+}} (r_{+}, \tau_{mn}) g_{i} - \frac{\partial \mathcal{H}}{\partial \tau_{+}} (r_{+}, \tau_{mn}) \frac{dg_{i}}{dr_{+}} - \frac{\partial \mathcal{A}}{\partial \tau_{+}} (r_{+}, \tau_{mn}) \frac{d^{2}g_{i}}{dr_{+}^{2}}.$$
(B.13)

We may note that the right-hand side of Eq. B.13 is now known. By differentiating the boundary conditions of Eq. B.12 with respect to  $\tau_{+}$ , we can suitably solve Eq. B.13 to calculate the required derivatives  $\partial g_{i}/\partial \tau_{+}$ .

### Appendix C

### Assessment of the suitability of the rigid body swirl model

As a primary test, the analytical predictions of the rigid body swirl (RBS) model (Sec. 3.3) were compared against the corresponding numerical predictions of *GreenSwirl* for several idealized rigid body swirling flow profiles characterized by a uniform axial flow  $(M_z)$  and solid body swirl  $(\Omega (rad/s))$ . As already mentioned, studying the sound propagation in a moving reference frame is ideally expected to yield the same modal wavenumbers and pressure amplitudes. Therefore, the accuracy of the analytical approximation was compared for the estimations of (i) the cut-on *m*-range, (ii) the number of propagating modes,  $N_{\omega}$ , (iii) the accuracy of the  $\zeta_{mn}^{\pm}$  wavenumbers, (iv) the mode amplitude distribution,  $\overline{A^2}(\zeta)$ , and (v) the radial mode shape function,  $\psi_{mn}(r)$ . We note here again that the RBS approximation ignores the radial variations in the sound speed and mean flow variables, and the coupling between the acoustics and vorticity fields. Therefore, the Doppler-frequency correction is not representative of the actual swirling flow physics, resulting in a discrepancy between the analytical and numerical calculations, which were found to increase with increasing  $M_z$  and  $\Omega$  of the RBS flow profiles. In this section, we present the comparative studies for an RBS flow profile with  $M_z = 0.45$  and  $\Omega = 380 \ rad/s$ , with the Mach numbers chosen to be comparable to the cutback condition of a modern HBR turbofan.

### **C.1** Comparison of the cut-on m-range, and $N_{\omega}$

Table C.1 below shows that the analytical approximation closely estimates the cut-on m-range with the limit for the contra-rotating mode orders slightly overestimated.  $N_{\omega}$  is the number of propagating modes in individual directions and is estimated to within 1% deviation.

ka -	<i>m</i> -range		$N_{\omega}$	
	Numerical	Analytical	Numerical	Analytical
18	-36:11	-37:11	111	112
37	-78:25	-80:25	437	440
60	-130:41	-133:41	1109	1112
75	-165:52	-168:52	1705	1715

TABLE C.1: Comparison between the analytical and numerical estimations of the cuton *m*-range and  $N_{\omega}$  for  $M_z=0.45$  and  $\Omega=380$  rad/s.

### C.2 Accuracy of the $\zeta_{mn}$ estimations

From the analytical and numerical  $\zeta_{mn}$  estimations, the mean relative error  $(\overline{\Delta\zeta})$  in  $\zeta$  was computed by averaging the relative errors  $(\Delta\zeta)$  at a particular m-order across the constituent radial modes (n). Fig. C.1 plots the computed  $\overline{\Delta\zeta}$  error contours for the upstream and downstream modes as a function of  $\epsilon_m = m\Omega/\omega$ . It may be noted here that the  $\overline{\Delta\zeta}$  contours collapse asymptotically across the high frequencies for a given RBS flow profile.

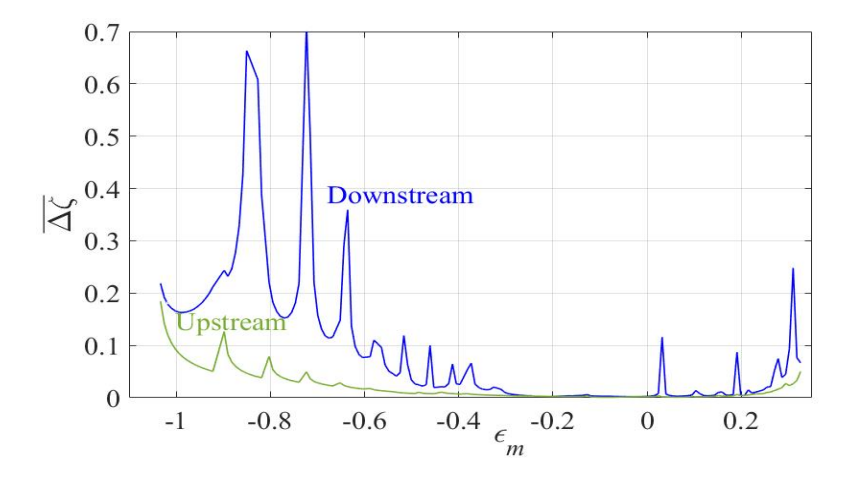


FIGURE C.1:  $\overline{\Delta \zeta}$  *vs*  $\epsilon_m$  for the RBS profile under consideration.

The  $\Delta\zeta$  contours for a particular radial order depicted the highest relative errors in the vicinity of the highest cut-on m-order (or,  $\epsilon_m$ ) for both the upstream and downstream modes, which result in the peakiness in the averaged  $\overline{\Delta\zeta}$  contours. Fig. C.1 reveals that the relative errors are comparatively greater for the downstream modes. However, for our RBS profile under consideration, the analytical RBS approximation estimates the  $\zeta_{mn}$  values of more than 85% of the cut-on modes to within 10% deviation.

### **C.3** Mode amplitude distributions, $\overline{A^2}(\zeta)$

Fig. C.2 compares the analytical and numerical calculations of the dimensional mean squared mode amplitude distribution,  $\overline{A^2}(\zeta_{\pm m})$ , for the co-rotating and contra-rotating modes. For a better visual interpretation, the comparison is shown separately for the upstream (Figs. C.2a and C.2c) and downstream (Figs. C.2b and C.2d) modes. A good general overall agreement between the analytical and numerical estimations could be observed in Fig. C.2.

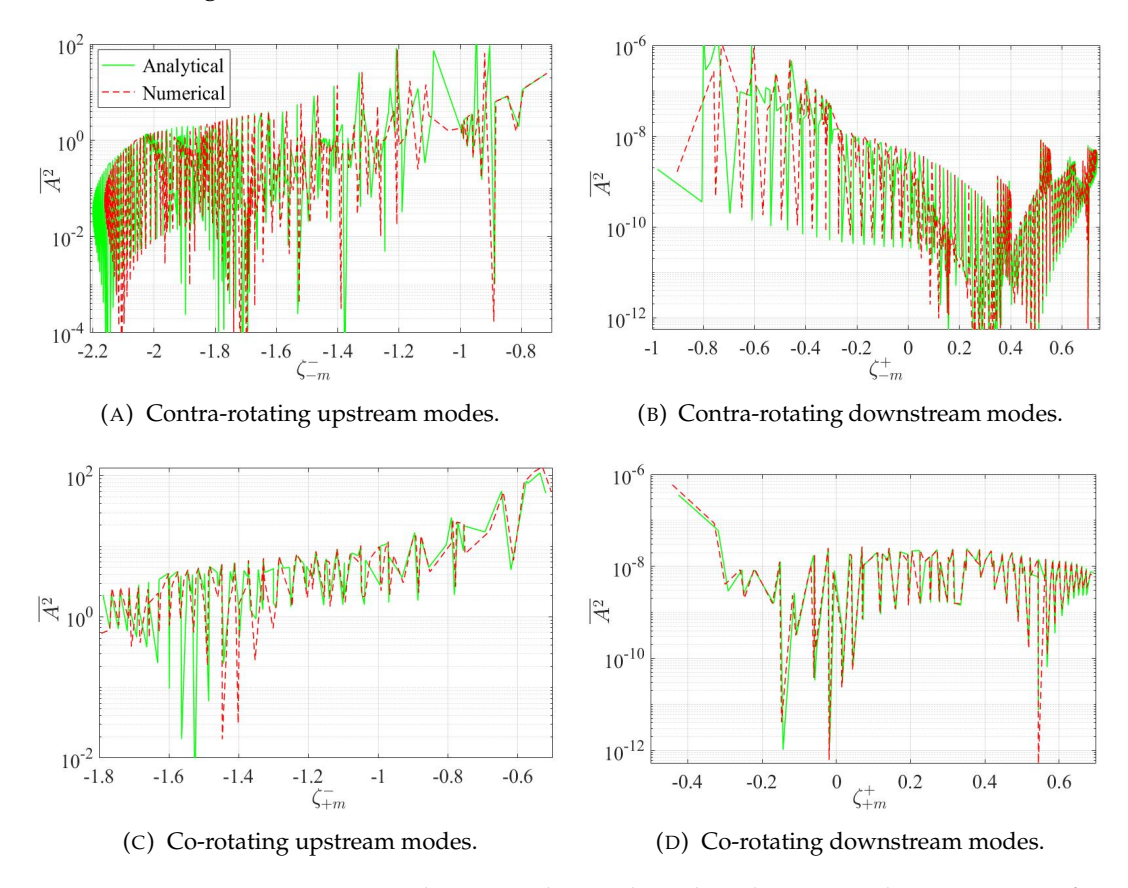


FIGURE C.2: Comparison between the analytical and numerical estimations of  $\overline{A^2}(\zeta_{\pm m})$  mode amplitude distributions at ka=37 for the RBS profile under study.

### **C.4** Radial mode shape variation, $\psi_{mn}(r)$

The radial mode shapes,  $\psi_{mn}(r)$ , computed using *GreenSwirl* were found to reasonably match with the classical Bessel mode shapes, except for the lower (m, n) mode orders. Fig. C.3 presents the comparison of  $\psi_{mn}(r)$  mode shapes for selected (m, n) mode orders in their upstream and downstream propagations. Note that the analytical  $\psi_{mn}(r)$  mode shapes are the same in both upstream and downstream propagations.

From the comparative study in Fig. C.3, we may observe that the upstream modes show relatively greater deviations, contrary to Fig. C.1. The first radial order of lower

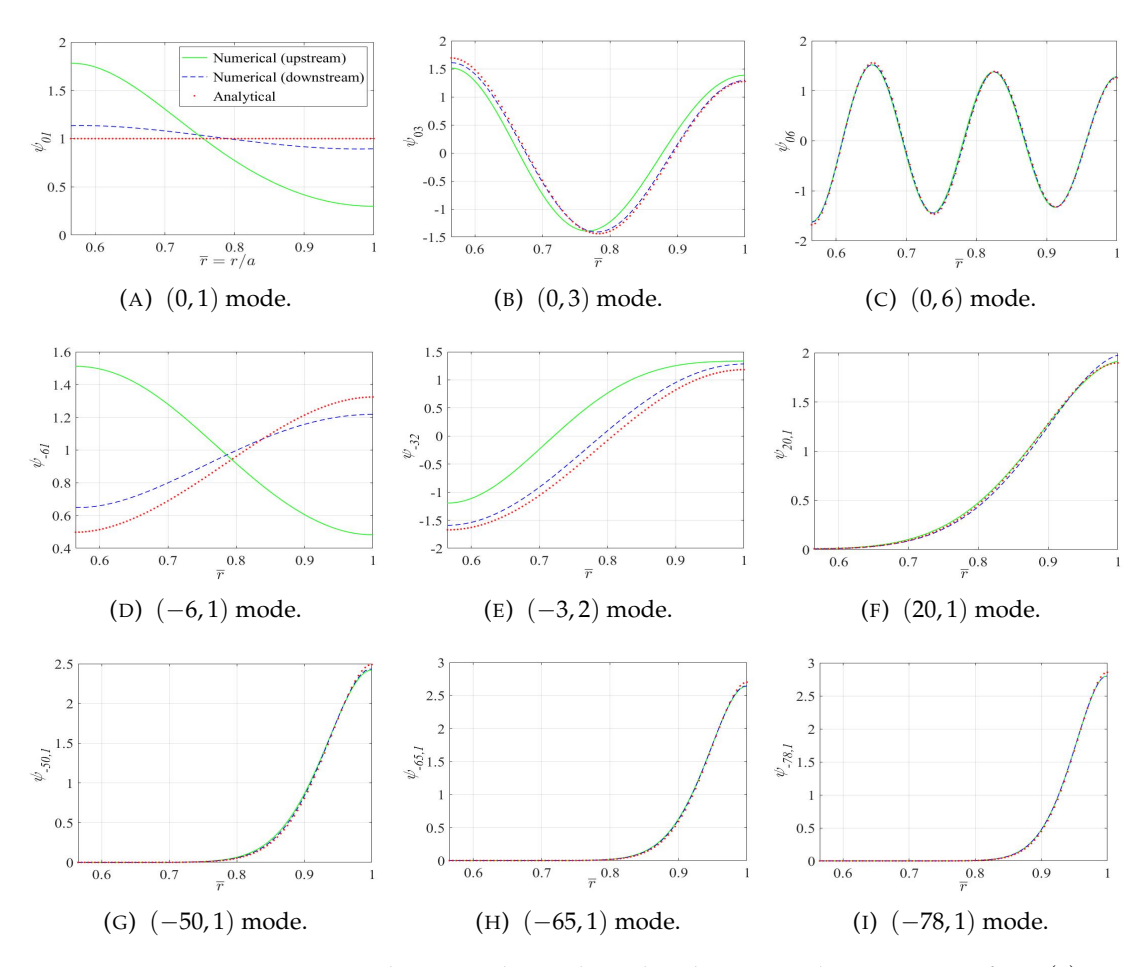


FIGURE C.3: Comparison between the analytical and numerical estimations of  $\psi_{mn}(r)$  mode shape variation for selected (m, n) mode orders for our RBS profile under investigation.

order m's depicts the highest discrepancy (Figs. C.3a and C.3d). The radial variation is near-identical to the classical linear combination of Bessel functions at increasing m and/or n mode orders. Overall, leaving apart a few modes, the radial variation is nearly representable by the linear combination of Bessel functions for ideal rigid body swirling flows.

Overall, the comparative studies presented in this section demonstrate that for idealized rigid body swirling flows the analytical RBS approximation is fairly accurate in predicting the number of cut-on modes, their modal wavenumbers, mode shape variations, and their pressure mode amplitude distributions. We emphasize here that the objective is not to approximate the eigenvalue calculations for realistic intra-stage swirling flows but to rather employ the RBS model to understand the characteristics of the modal distributions in swirling flows.

### Appendix D

# Aeroacoustic equivalence of a single source at the two-thirds annulus position to an incoherent distribution of sources

Referring to Eqs. 2.1 and 2.2, the wall pressure spectra at  $x_a = (z, a, \theta)$  at an analysis frequency  $(\omega)$  due to a distribution of point sources along a duct cross-section,  $y_s = (r_s, \theta_s)$ , could be written as:

$$S_{\omega} = E[pp^{*}]$$

$$= \sum_{m,n} \sum_{m',n'} \iint \iint E[A_{mn}(\omega, \mathbf{y}_{s}) A^{*}_{m'n'}(\omega, \mathbf{y}'_{s})] \psi_{mn}(a) \psi^{*}_{m'n'}(a) e^{j(m-m')\theta} e^{j(\kappa_{mn} - \kappa_{m'n'})(z-z_{s})} r_{s} r'_{s} dr_{s} dr'_{s} d\theta_{s} d\theta'_{s}.$$
(D.1)

Referring to Eq. 4.3, the (m,n) mode amplitude due to a dipole source at  $y_s$  with strength,  $\hat{f}(\omega)$ , may be expressed as:

$$A_{mn}(\omega, \mathbf{y}_s) = \hat{f}(\omega, \mathbf{y}_s) D_{mn}(\varphi) \mathring{A}_{mn}(\omega, \mathbf{y}_s), \qquad (D.2)$$

where  $D_{mn}(\varphi)$  is the dipole directivity, and  $\mathring{A}_{mn}(\omega, y_s)$  is the mode amplitude due to a unit-strength monopole. To evaluate the integral of Eq. D.1, we need to know the variation of the modal amplitudes as a function of the source coordinates. It may be noted that the source strength may be considered unity for simplification, or predicted using standard blade loading expressions (Amiet (1976), Kim and George (1982)). The dipole directivity may be easily evaluated across the radial source coordinate using Eq. 4.4, and therefore the challenge in the integration lies in the knowledge of the cross-sectional variation of  $\mathring{A}_{mn}$ .

For a singular source radiating in a swirling flow, *GreenSwirl* is used to predict the multimodal sound field from which the individual mode amplitudes are estimated by the method of least squares fitting (Moore (1979)). Predicting the sound field for a planar distribution of sources in a swirling flow would be computationally expensive using *GreenSwirl*. Since, the present objective is to demonstrate that a singular dipole source at the  $2/3^{rd}$  annulus position produces a comparable  $\langle \overline{a^2}(\gamma) \rangle$  modal distribution as that of an incoherent distribution of dipoles, we resort to a first-approximation approach for a quicker calculation. Referring to the standard Green's function for a ducted uniform axial flow (Glegg and Devenport (2017)), the  $\mathring{A}_{mn}$  at a different source coordinate  $y_s' = (r_s', \theta_s')$  may be obtained as:

$$\mathring{A}_{mn}(\omega, \mathbf{y}_s') \approx \mathring{A}_{mn}(\omega, \mathbf{y}_s) \frac{\psi_{mn}^*(r_s') e^{-jm\theta_s'}}{\psi_{mn}^*(r_s) e^{-jm\theta_s}}.$$
 (D.3)

The computation of the modal eigenfunctions across the duct cross-section is quick using *GreenSwirl*. For illustration in this section, we consider the approach condition of the NASA SDT rig to verify the suitability of the approximation of Eq. D.3 by comparing the  $\langle \overline{a^2}(\gamma) \rangle$  modal distribution that is directly computed for a dipole source at  $r_s = 0.63a$  ( $\sim 1/3^{rd}$  annulus position) against the corresponding distribution predicted using the approximation of Eq. D.3 on the synthesized sound fields due to singular dipoles at  $r_s = 0.82a$  ( $\sim 2/3^{rd}$  annulus position) and  $r_s = 0.94a$  (close to blade tip). Fig. D.1 presents the comparative study justifying the suitability of the approximation of Eq. D.3 for the rotor dipole ( $\varphi_r = 20^\circ$ ) and the stator dipole ( $\varphi_o = 128^\circ$ ). Compared with the corresponding mean distributions plotted in Fig. E.1, it is interesting to note that the above approximation suitably alters the relative modal pressure distribution to produce a convincing match with the original computed  $\langle \overline{a^2}(\gamma) \rangle$  distribution for  $r_s = 0.63a$ . Thus, we now have a good approximation of the variation of the mode amplitudes as a function of the source coordinates to evaluate the integral of Eq. D.1.

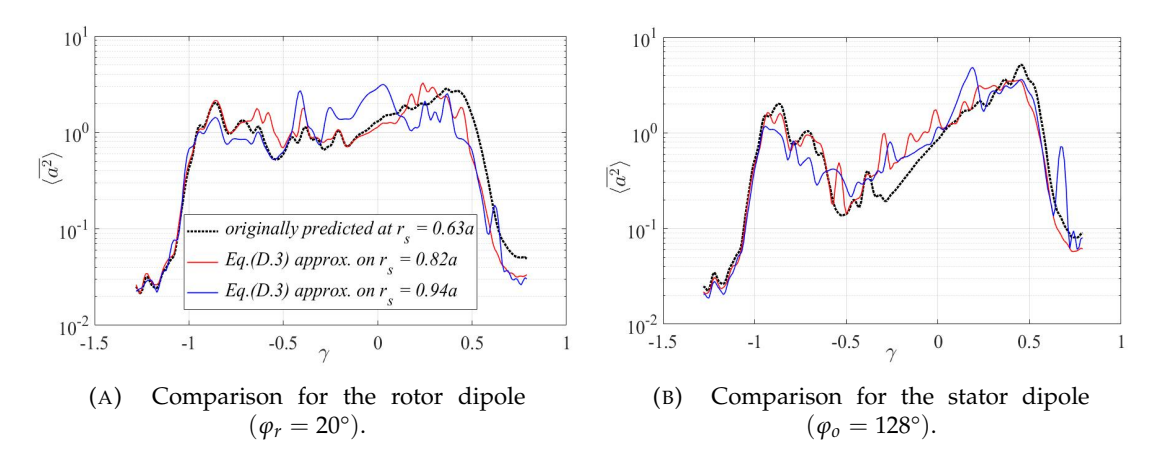


FIGURE D.1: Comparison of the original computed  $\langle \overline{a^2}(\gamma) \rangle$  distribution for  $r_s = 0.63a$  with the corresponding distributions calculated using the approximation of Eq. D.3 on the synthesized sound fields due to dipole sources at  $r_s = 0.82a$  and  $r_s = 0.94a$ .

Referring to Eqs. D.1 and D.2, we write the source loading spectra in the variable separable form as:

$$E[\hat{f}\hat{f}^*(\omega, \mathbf{y}_s, \mathbf{y}_s')] = E[\hat{f}\hat{f}^*(\omega, r_s, r_s')]E[\hat{f}\hat{f}^*(\omega, \theta_s, \theta_s')]. \tag{D.4}$$

Therefore, the double integral along the azimuthal source coordinates in Eq. D.1 would be evaluated as  $\iint E[\hat{f}\hat{f}^*(\omega,\theta_s,\theta_s')]e^{-jm\theta_s}e^{jm'\theta_s'}d\theta_sd\theta_s'$ . Assuming that the blade-to-blade loading is uncorrelated, the expectation of the azimuthal loading spectra would be  $E[\hat{f}\hat{f}^*(\omega,\theta_s,\theta_s')] = E[|\hat{f}(\omega,\theta_s)|^2]\delta\left(\theta_s-\theta_s'\right)$ . By assuming  $E[|\hat{f}(\omega,\theta_s)|^2]$  to be unity (to simplify the calculations), the double integral along the azimuthal source coordinates would reduce to  $\int E[|\hat{f}(\omega,\theta_s)|^2]e^{j(m'-m)\theta_s}d\theta_s = 2\pi\delta\left(m-m'\right)$ , suggesting that an uncorrelated blade-to-blade loading transforms to incoherent spinning modes.

With non-orthogonal duct modes in a swirling flow, the wall pressure spectra would include the cross-terms between the different radial modes within a spinning mode order. Posson and Peake (2012) demonstrates that the cross product between the (m,n)and (m, n') modes may be neglected on a first approximation. Further, assuming an uncorrelated source loading along the radial coordinate, the integral of Eq. D.1 may be further simplified. Since the present study deals with the normalized  $\langle a^2(\gamma) \rangle$  modal distributions, the impact of the spanwise (and chordwise) correlations would be absorbed in the frequency dependence such that the relative (normalized) pressure distribution characteristics are essentially the same. Also, it may be understood that a single effective dipole source inherently includes a spanwise-averaged correlation (Kim and George (1982)). Fig. D.2 compares the  $\langle \overline{a^2}(\gamma) \rangle$  modal distributions for a single effective dipole source at the  $2/3^{rd}$  annulus position  $(r_{2/3})$  versus an incoherent distribution of dipoles with the dipole orientations fixed at  $\varphi_r = 20^{\circ}$  for the downstream modes and  $\varphi_0 = 128^{\circ}$  for the upstream modes. A convincing match could be witnessed across both the upstream and downstream propagations. Note that the corresponding measured distributions are superimposed as the dotted black curve for better illustration.

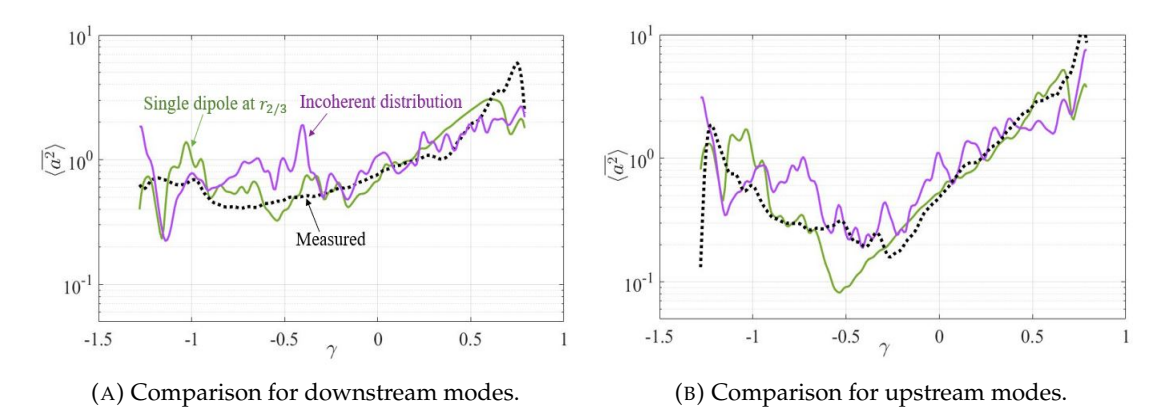


FIGURE D.2: Comparison between the  $\langle \overline{a^2}(\gamma) \rangle$  distributions for a single effective dipole source at  $r_s = r_{2/3}$  and an incoherent distribution of dipoles, considering the NASA SDT intra-stage at approach.

### Appendix E

### Sensitivity of the modal pressure distribution characteristics to the radial source position

In Chapter 4, we illustrated the empirical determination of the effective dipole orientations  $(\varphi_r/\varphi_o)$  by fixing the singular dipole sources at  $2/3^{rd}$  the annulus position, i.e.:  $r_s=r_{2/3}$ . In this section, we consider the NASA SDT fan rig at the approach condition to demonstrate that the two-thirds annulus position, which for NASA SDT intra-stage is  $r_{2/3}=0.82a$ , is the effective source position by computing the  $\langle \overline{a^2}(\gamma) \rangle$  modal distributions at two other radial source positions,  $r_s=0.63a$  and  $r_s=0.94a$ , and comparing the different numerical distributions against the corresponding measured distributions. Fig. E.1 presents the comparative study for both the upstream  $(\varphi_o=128^\circ)$  and downstream  $(\varphi_r=20^\circ)$  modes.

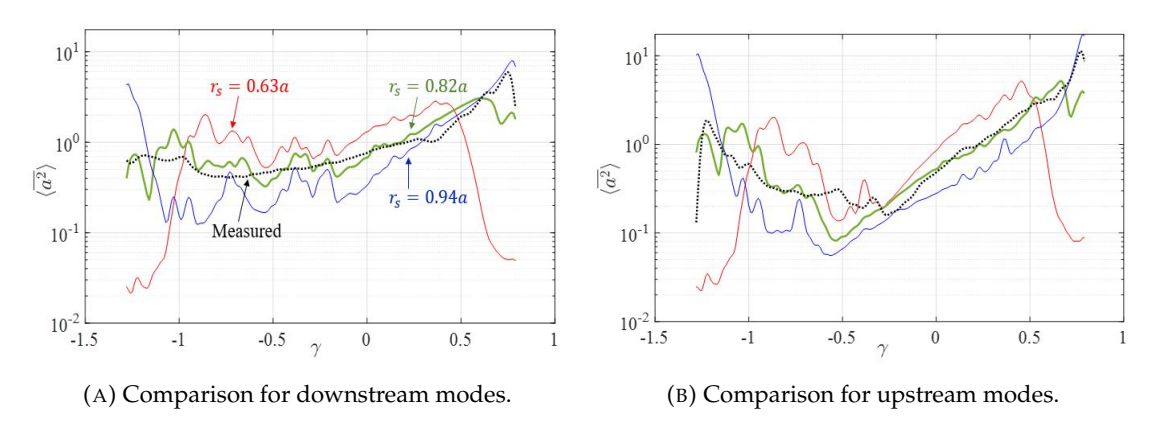


FIGURE E.1: Comparison of the computed  $\langle \overline{a^2}(\gamma) \rangle$  distributions at three different source positions against the corresponding measured distribution for the NASA SDT intra-stage at approach.

Fig. E.1 demonstrates that across both the upstream and downstream modes, the deviations amongst the different computed  $\langle \overline{a^2}(\gamma) \rangle$  distributions show a consistent pattern. When the source is closer to the hub (b=0.471a), the modes in the vicinity of the cuton  $\pm m$  limits are weakly excited and as a result, the normalized pressure distribution is raised elsewhere. With the source closer to the tip, the modes near the cut-on m limits are strongly excited resulting in the lowering of the normalized pressure distribution across the intermediate m orders. Overall, the comparative study illustrates that the two-thirds annulus position,  $r_s = r_{2/3}$ , is ideal for our equivalent point source model.

### Appendix F

## Relative modal splits, $\sigma_{+m}^{\pm}(\omega)$ , at the approach and cutback conditions for the ACAT1 intra-stage

The relative modal splits,  $\sigma_{+m}^{\pm}(\omega)$ , were computed for the downstream (+) and upstream (-) modes using Eq. 4.12 of Sec. 4.2.2 using appropriate synthesized sound fields, generated from our equivalent point source model of Sec. 4.1.2 with  $\varphi_r=20^\circ$  (rotor) and  $\varphi_o=128^\circ$  (OGV), for the ACAT1 intra-stage at its approach and cutback operating points. Fig. F.1 plots and compares the computed  $\sigma_{+m}^{\pm}(\omega)$  modal splits at the approach and cutback conditions across the BB frequency range of interest.

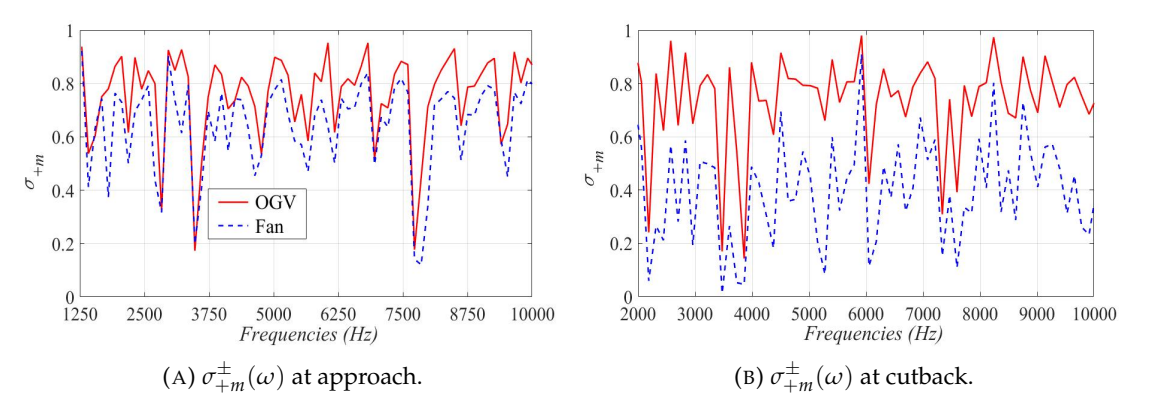


Figure F.1: Relative modal splits,  $\sigma^{\pm}_{+m}(\omega)$ , computed for the approach and cutback conditions of the ACAT1 intra-stage.

Fig. F.1 demonstrates that for the OGV about 80% of its total mean squared pressure is concentrated in its co-rotating modes at both approach and cutback. For the fan, however, we notice a reduction in its  $\sigma_{+m}(\omega)$  spectrum with increasing fan speeds due to the increasing m-order bias with a broader cut-on azimuthal range for the contrarotating modes.

### References

- R. K. Amiet. Acoustic radiation from an airfoil in a turbulent stream. *Journal of Sound and Vibration*, 1975.
- R. K. Amiet. Noise due to turbulent flow past a trailing edge. *Journal of Sound and Vibration*, 1976.
- R. Jeremy Astley. *Encyclopedia of Aerospace Engineering*, chapter Propulsion System Noise: Turbomachinery. John Wiley & Sons, Ltd., 2010.
- O.V. Atassi. Computing the sound power in non-uniform flow. *Journal of Sound and Vibration*, 2003.
- Elia Stefano Battistelli. Experimental Astrophysics. Institute of Physics Publishing, 2021.
- Maximilian Behn and Ulf Tapken. Investigation of Sound Generation and Transmission Effects Through the ACAT1 Fan Stage using Compressed Sensing-based Mode Analysis. In 25<sup>th</sup> AIAA/CEAS Aeroacoustics Conference, 2019.
- Maximilian Behn, Roman Kisler, and Ulf Tapken. Efficient Azimuthal Mode Analysis using Compressed Sensing. In 22<sup>nd</sup> AIAA/CEAS Aeroacoustics Conference, 2016.
- Jeffrey J. Berton. System noise prediction of the DGEN 380 turbofan engine. In 21<sup>st</sup> AIAA/CEAS Aeroacoustics Conference, 2015.
- U. Bolleter and M. Crocker. Theory and measurement of modal spectra in hard-walled cylindrical ducts. *Journal of the Acoustical Society of America*, 1972.
- Thomas F. Brooks and William M. Humphreys. A deconvolution approach for the mapping of acoustic sources (DAMAS) determined from phased microphone arrays. *Journal of Sound and Vibration*, 2006.
- Thomas F. Brooks, D. Stuart Pope, and Michael A. Marcolini. Airfoil Self-Noise and Prediction. Technical report, NASA, 1989.
- Harry H. Brouwer and Pieter Sijtsma. Phased array beamforming to identify broadband noise sources in the interstage section of a turbofan engine. In 25<sup>th</sup> AIAA/CEAS Aeroacoustics Conference, 2019.

Steven L. Brunton and J. Nathan Kutz. *Data Driven Science Engineering - Machine Learning, Dynamical Systems, and Control.* Cambridge University Press, 2019.

- Sergi Pallejà Cabré. Fan proximity acoustic treatments for improved noise suppression in turbofan engines. PhD thesis, University of Southampton, 2021.
- Chaitanya Paruchuri. *Aerofoil geometry effects on turbulence interaction noise*. PhD thesis, University of Southampton, 2017.
- A. J. Cooper and N. Peake. Upstream-radiated rotor-stator interaction noise in mean swirling flow. *Journal of Fluid Mechanics*, 2005.
- Leandro de Santana. Fundamentals of acoustic beamforming. In *Design and Operation* of Aeroacoustic Wind Tunnel Tests for Group and Air Transport, 2017.
- Robert Dougherty. Mutual Incoherence of Broadband Duct Acoustic Modes. In 22<sup>nd</sup> *AIAA/CEAS Aeroacoustics Conference*, 2016.
- Robert P. Dougherty and Richard Bozak. Two-dimensional Modal Beamforming in Wavenumber Space for Duct Acoustics. In 2018 AIAA/CEAS Aeroacoustics Conference, 2018.
- Ann P. Dowling and Yasser Mahmoudi. Combustion noise. *Proceedings of the Combustion Institute*, 2015.
- T. A. Driscoll, N. Hale, and L. N. Trefethen. *Chebfun guide*. Pafnuty Publications, Oxford, 2014.
- Lars Enghardt, Axel Holewa, and Ulf Tapken. Comparison of Different Analysis Techniques to Decompose a Broad-band Ducted Sound Field in its Mode Constituents. In 13<sup>th</sup> AIAA/CEAS Aeroacoustics Conference, 2007.
- Edmane Envia. Fan Noise Reduction: An Overview. *International Journal of Aeroacoustics*, 2002.
- F. Farassat, Douglas Nark, and Russell Thomas. The detection of radiated modes from ducted fan engines. In 7<sup>th</sup> AIAA/CEAS Aeroacoustics Conference and Exhibit, 2001.
- Hamilton Fernandez, Douglas Nark, and Dale Van Zante. Aircraft Noise Reduction Subproject Overview, April 2016. Acoustics Technical Working Group Meeting, NASA LaRC.
- Ulrich W. Ganz, Paul D. Joppa, Timothy J. Patten, and Daniel F. Scharpf. Boeing 18-inch fan rig broadband noise test. Technical report, NASA, 1998.
- Paul Rodriguez Garcia. Exploring and developing processing techniques for the extraction of aircraft combustion noise. In 20<sup>th</sup> International Conference on Sound & Vibration, 2013.

Stewart Glegg and William Devenport. *Aeroacoustics of low Mach number flows: fundamentals, analysis, and measurement.* Academic Press, 2017.

- Stewart Glegg and Cyrille Jochault. Broadband Self-Noise from a Ducted Fan. *AIAA Journal*, 1998.
- Marvin E. Goldstein. Aeroacoustics. McGraw-Hill Inc., US, 1976.
- S. Guérin, U. Michel, H. Siller, U. Finke, and G. Saueressig. Airbus A319 Database from Dedicated Flyover Measurements to Investigate Noise Abatement Procedures. In 11<sup>th</sup> AIAA/CEAS Aeroacoustics Conference, 2005.
- Sébastien Guérin, Carolin Kissner, Pascal Seeler, Ricardo Blázquez, Pedro Carrasco Laraña, Hélène de Laborderie, Danny Lewis, Paruchuri Chaitanya, Cyril Polacsek, and Johan Thisse. ACAT1 Benchmark of RANS-Informed Analytical Methods for Fan Broadband Noise Prediction: Part II—Influence of the Acoustic Models. *Acoustics*, 2020.
- C. J. Heaton and N. Peake. Journal of Fluid Mechanics. *Algebraic and exponential instability of inviscid swirling flow*, 2006.
- L. Heidelberg and D. Hall. Inlet acoustic mode measurements using a continuously rotating rake. *Journal of Aircraft*, 1995.
- G.F. Homicz and J.A. Lordi. A note on the radiative directivity patterns of duct acoustic modes. *Journal of Sound and Vibration*, 1975.
- Christopher E. Hughes, Robert J. Jeracki, Richard P. Woodward, and Christopher J. Miller. Fan Noise Source Diagnostic Test: Rotor Alone Aerodynamic Performance Results. In *Eighth Aeroacoustics Conference*, June 2002.
- Florence V. Hutcheson and Thomas F. Brooks. Measurement of trailing edge noise using directional array and coherent output power methods. *International Journal of Aeroacoustics*, 2002.
- J. Cuenca and R. Hallez and B. Peeters. Angular and radial acoustic mode detection in large cylindrical ducts by sequential measurements using a single ring of microphones. In 20<sup>th</sup> International Congress on Sound and Vibration, 2013.
- P. D. Joppa. Acoustic mode measurements in the inlet of a turbofan engine. *Journal of Aircraft*, 1987.
- P. Joseph, C.L. Morfey, and C.R. Lowis. Multi-mode sound transmission in ducts with flow. *Journal of Sound and Vibration*, 2003.
- P. F Joseph. A two-microphone method for the determination of the mode amplitude distribution in high-frequency ducted broadband sound fields. *The Journal of the Acoustical Society of America*, 2017.

Phillip Joseph and Christopher L. Morfey. Multimode radiation from an unflanged, semi-infinite circular duct. *The Journal of the Acoustical Society of America*, 1999.

- Andrew Kempton. Acoustic liners for modern aero-engines, October 2011. 15th CEAS-ASC Workshop and 1st Scientific Workshop of X-Noise EV Acoustic Liners and Associated Propagation Techniques.
- Y. Kim and P. A. Nelson. Optimal regularisation for acoustic source reconstruction by inverse methods. *Journal of Sound and Vibration*, 2004.
- Y. N. Kim and A. R. George. Trailing-edge noise from hovering rotors. *AIAA Journal*, 1982.
- Carolin Kissner, Sébastien Guérin, Pascal Seeler, Mattias Billson, Paruchuri Chaitanya, Pedro Carrasco Laraña, Hélène de Laborderie, Benjamin François, Katharina Lefarth, Danny Lewis, Gonzalo Montero Villar, and Thomas Nodé-Langlois. ACAT1 Benchmark of RANS-Informed Analytical Methods for Fan Broadband Noise Prediction—Part I—Influence of the RANS Simulation. *Acoustics*, 2020.
- James J. Kramer. The NASA quiet engine. Technical report, NASA, 1971.
- V. Ram Kumar, Phillip. F. Joseph, and Chaitanya Paruchuri. Estimation of the relative balance between the rotor and the ogv broadband noise. In *AIAA AVIATION 2023 Forum*, 2023.
- C. R. Lowis and P. Joseph. A Focused Beamformer Technique for Separating Rotor and Stator-Based Broadband Sources. In 12th AIAA/CEAS Aeroacoustics Conference, 2006.
- C.R. Lowis, P.F. Joseph, and A.J. Kempton. Estimation of the far-field directivity of broadband aeroengine fan noise using an in-duct axial microphone array. *Journal of Sound and Vibration*, 2010.
- Ana Luisa Pereira Maldonado. *On the Prediction of the Effect of Interstage Liners in Turbo- fan Engines*. PhD thesis, University of Southampton, 2016.
- V. Masson, H. Posson, M. Sanjose, S. Moreau, and M. Roger. Fan-OGV interaction broadband noise prediction in a rigid annular duct with swirling and sheared mean flow. In 22<sup>nd</sup> AIAA/CEAS Aeroacoustics Conference, 2016.
- Vianney Masson, James R. Mathews, Stéphane Moreau, Hélène Posson, and Edward J. Brambley. The impedance boundary condition for acoustics in swirling ducted flow. *Journal of Fluid Mechanics*, 2018.
- J. R. Mathews and N. Peake. The acoustic Green's function for swirling flow in a lined duct. *Journal of Sound and Vibration*, 2017.
- James R. Mathews. *Mathematical modelling of noise generation in turbofan aeroengines using Green's functions*. PhD thesis, University of Cambridge, 2016.

J.R. Mathews, J. Chen, and P. Joseph. Modal cut-on ratio in ducts with realistic flow profiles and its application to acoustic mode detection. *Journal of Sound and Vibration*, 2018.

- A. McAlpine, P.J.G. Schwaller, M.J. Fisher, and B.J. Tester. "buzz-saw" noise: Prediction of the rotor-alone pressure field. *Journal of Sound and Vibration*, 2012.
- Jonathan Melling, Jian Chen, and Phillip Joseph. Experimental investigation of a new two-microphone method for the determination of broadband noise radiation from ducts. *Applied Acoustics*, 2017.
- J. M. Mendoza, T. F. Brooks, and W. M. Humphreys Jr. An aeroacoustic study OF a leading edge slat configuration. *International Journal of Aeroacoustics*, 2002.
- C. J. Moore. Measurement of Radial and Circumferential Modes in annular and circular fan ducts. *Journal of Sound and Vibration*, 1979.
- C.L. Morfey. Sound transmission and generation in ducts with flow. *Journal of Sound and Vibration*, 1971a.
- C.L. Morfey. Acoustic energy in non-uniform flows. *Journal of Sound and Vibration*, 1971b.
- Bruce L. Morin. Broadband Fan Noise Prediction System for Turbofan Engines, Volume 2: BFaNS User's Manual and Developer's Guide. Technical report, Pratt & Whitney, 2010.
- M. L. Munjal. Acoustics of Ducts and Mufflers. John Wiley &) Sons Ltd, 2014.
- Stefan Oerlemans and Pieter Sijtsma. Acoustic Array Measurements of a 1:10.6 Scaled Airbus A340 Model. In *10th AIAA/CEAS Aeroacoustics Conference*, 2004.
- Suresh Palani. *Novel acoustic liners for broadband sound attenuation*. PhD thesis, University of Southampton, 2022.
- A. Pereira and Marc C. Jacob. Modal analysis of in-duct fan broadband noise via an iterative Bayesian inverse approach. *Journal of Sound and Vibration*, 2022.
- Lourenço Tércio Lima Pereira, Francesco Avallone, Daniele Ragni, and Fulvio Scarano. A parametric study of serration design for trailing—edge broadband noise reduction. *Applied Acoustics*, 2023.
- H. Posson and N. Peake. Acoustic analogy in swirling mean flow applied to predict rotor trailing-edge noise. In 18<sup>th</sup> AIAA/CEAS Aeroacoustics Conference, 2012.
- H. Posson and N. Peake. The acoustic analogy in an annular duct with swirling mean flow. *Journal of Fluid Mechanics*, 2013.

John Premo and Paul Joppa. Fan Noise Source Diagnostic Test - Wall Measured Circumferential Array Mode Results. In 8<sup>th</sup> AIAA/CEAS Aeroacoustics Conference Exhibit, 2002.

- E.R. Rademaker, P. Sijtsma, and B.J. Tester. Mode detection with an optimised array in a model turbofan engine intake at varying shaft speeds. In 7<sup>th</sup> AIAA/CEAS Aeroacoustics Conference, 2001.
- John A. Reed, Mark G. Turner, Andrew Norris, and Joseph P. Veres. Towards an Automated Full-Turbofan Engine Numerical Simulation. In 16<sup>th</sup> International Symposium on Airbreathing Engines, 2003.
- E. J. Rice. Acoustic liner optimum impedance for the spinning modes with mode cut-off ratio as the design criterion. In 3<sup>rd</sup> AIAA/CEAS Aeroacoustics Conference, 1976a.
- E. J. Rice. Inlet noise suppressor design method based upon the distribution of acoustic power with mode cutoff ratio. *Advances in Engineering Science*, 1976b.
- E. J. Rice. Modal density function and number of propagating modes in ducts. In *Meeting of the Acoustical Society of America*, November 1976c.
- E. J. Rice, M. F. Heidmann, and T. G. Sofrin. Modal propagation angles in a cylindrical duct with flow and their relation to sound radiation. In 17<sup>th</sup> Aerospace Sciences Meeting, 1979.
- Edward J. Rice. Multimodal Far-Field Acoustic Radiation Pattern Using Mode Cutoff Ratio. *AIAA Journal*, 1978.
- Sjoerd W. Rienstra. Fundamentals of duct acoustics, November 2015. VKI Lecture Series 2016-02. Notes of course "Progress in Simulation, Control and Reduction of Ventilation Noise".
- Arthur V. Saule. Modal structure inferred from static far-field noise directivity. In 3<sup>rd</sup> *Aeroacoustics Conference*, 1976.
- P. Sijtsma. Using Phased Array Beamforming to Locate Broadband Noise Sources inside a Turbofan Engine. In *AARC Engine Noise Phased Array Workshop*, 2006.
- P. Sijtsma and J. Zillmann. In-Duct and Far-Field Mode Detection Techniques. In 13<sup>th</sup> AIAA/CEAS Aeroacoustics Conference, 2007.
- P. Sijtsma, H. Brouwer, and M. Snellen. Beamforming in an annular duct with swirling flow. In *AIAA AVIATION 2023 Forum*, 2023.
- Pieter Sijtsma. Using phased array beamforming to identify broadband noise sources in a turbofan engine. *International Journal of Aeroacoustics*, 2010.
- Pieter Sijtsma. Circular Harmonics Beamforming with Multiple Rings of Microphones. In 18th AIAA/CEAS Aeroacoustics Conference, 2012.

Pieter Sijtsma. CLEAN Based on Spatial Source Coherence. *International Journal of Aeroacoustics*, 2017.

- Pieter Sijtsma and Harry Brouwer. Deconvolution of azimuthal mode detection measurements. *Journal of Sound and Vibration*, 2018.
- Pieter Sijtsma, Stefan Oerlemans, and Hermann Holthusen. Location of rotating sources by phased array measurements. In 7th AIAA/CEAS Aeroacoustics Conference and Exhibit, 2001.
- Samuel Sinayoko, Phillip Joseph, and Alan McAlpine. Multimode radiation from an unflanged, semi-infinite circular duct with uniform flow. *The Journal of the Acoustical Society of America*, 2010.
- Ramesh Raja Subramanyam, Suresh Palani, Paruchuri Chaitanya, and Sergi Pallejà Cabré. On the noise reduction mechanisms of over-tip liners. *Journal of the Acoustical Society of America*, 2024.
- D. L. Sutliff, K. E. Konno, and L. J. Heidelberg. Duct Mode Measurements on the TFE731-60 Full Scale Engine. In 8<sup>th</sup> AIAA/CEAS Aeroacoustics Conference Exhibit, 2012.
- Daniel Sutliff, Daniel Tweedt, E. Brian Fite, and Edmane Envia. Low-Speed Fan Noise Reduction with Trailing Edge Blowing. In 8<sup>th</sup> AIAA/CEAS Aeroacoustics Conference & Exhibit, 2002.
- Ulf Tapken, Roland Bauers, Lars Neuhaus, Nicholas Humphreys, Alec Wilson, Christian Stoehr, and Matthias Beutke. A New Modular Fan Rig Noise Test and Radial Mode Detection Capability. In 17<sup>th</sup> AIAA/CEAS Aeroacoustics Conference, 2012.
- Ulf Tapken, Dominic Gutsche, and Lars Enghardt. Radial mode analysis of broadband noise in flow ducts using a combined axial and azimuthal sensor array. In 20<sup>th</sup> AIAA/CEAS Aeroacoustics Conference, 2014.
- Ulf Tapken, Maximilian Behn, Mirko Spitalny, and Benjamin Pardowitz. Radial mode breakdown of the ACAT1 fan broadband noise generation in the bypass duct using a sparse sensor array. In 25<sup>th</sup> AIAA/CEAS Aeroacoustics Conference, 2019.
- R. H. Thomas, F. Farassat, L. R. Clark, C. H. Gerhold, J. J. Kelly, and L. E. Becker. A mode detection method using the azimuthal directivity of a turbofan model. In 5<sup>th</sup> AIAA/CEAS Aeroacoustics Conference and Exhibit, 1999.
- J. M. Tyler and T. G. Sofrin. Axial flow compressor noise studies. *SAE Transactions*, 1962.
- Ram Kumar Venkateswaran, Phillip Joseph, and Chaitanya C. Paruchuri. Modal axial group velocity in ducted swirling flows and its application to the detection of broadband acoustic modes. In 28<sup>th</sup> AIAA/CEAS Aeroacoustics Conference, 2022.

Ram Kumar Venkateswaran, Phillip Joseph, and Chaitanya C. Paruchuri. Characterizing Fan Broadband Noise Using Engine Intra-Stage Measurements. In 30<sup>th</sup> AIAA/CEAS Aeroacoustics Conference, June 2024.

- Joe Walsh. Progress in Engine Noise Reduction and Future Challenges. In *Greener by Design Conference*, October 2016.
- Dale E. Van Zante, Gary G. Podboy, Christopher J. Miller, and Scott A. Thorp. Testing and Performance Verification of a High Bypass Ratio Turbofan Rotor in an Internal Flow Component Test Facility. In *Turbo Expo 2007*, 2007.
- Dale Van Zante, Doughlas Nark, and Hamilton Fernandez. Propulsion noise reduction research in the nasa advanced air transport technology project. In *International Society of Air Breathing Engines*, 2017.